

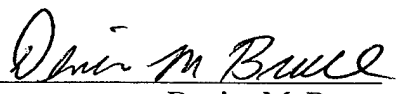
DYNAMIC TENSILE TESTING OF SHEET STEELS
&
INFLUENCE OF STRAIN RATE ON STRENGTHENING
MECHANISMS IN SHEET STEELS

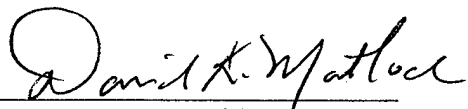
by
Denise M. Bruce

A thesis submitted to the Faculty and the Board of Trustees of the Colorado School of Mines in partial fulfillment of the requirements for the degree of Doctor of Philosophy (Metallurgical and Materials Engineering).

Golden, Colorado

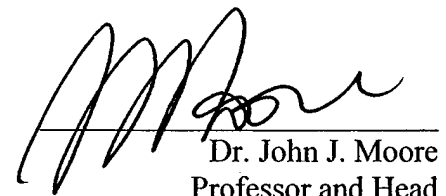
Date 3 Jul 2003

Signed: 
Denise M. Bruce

Approved: 
Dr. David K. Matlock
Thesis Advisor

Golden, Colorado

Date 7/8/03.


Dr. John J. Moore
Professor and Head
Department of Metallurgical
and Materials Engineering

The views expressed in this article are those of the author and do not reflect the official policy or position of the United States Air Force, Department of Defense, or the U.S. Government

ABSTRACT

The capability to conduct dynamic tensile testing of sheet steels was established and the influence of strain rate on strengthening mechanisms in sheet steels was investigated in this work. Several different automotive sheet steels were studied, including interstitial free (IF) steel, high strength low alloy (HSLA) steel, dual phase steel and transformation induced plasticity (TRIP) steel.

A method was developed to acquire accurate load and strain data over the strain rate range from 0.001 s^{-1} to 500 s^{-1} using a servo-hydraulic tensile test machine. Tensile samples were instrumented with high-elongation strain gages to collect gage section strain information at all strain rates. At low strain rates (less than 10 s^{-1}), a piezoelectric load washer was used to gather load data, while a strain gage mounted directly on the grip section of each tensile sample was used to collect load data for strain rates above 10 s^{-1} . These measurement techniques enabled creation of accurate stress-strain curves with the ability to distinguish yielding and strain hardening behavior for all strain rates. Stress-strain data for the entire range of strain rates were used to compare differences in material behavior with changing strain rate and to evaluate material suitability for high-rate applications.

The tensile test methods developed were used to investigate the effects of strain rate on various strengthening mechanisms in sheet steels. IF steels with controlled variations in cold work, grain size and solid solution strengthening were obtained and samples tested over the strain rate range from 0.001 s^{-1} to 500 s^{-1} . It was found that cold work and grain size strengthening were essentially independent of strain rate, while solid solution strengthening was a strong function of strain rate. The strengthening increment due to solute addition diminished with increasing strain rate. The cold work and grain size results were predicted by considering increasing strain rate as analogous to decreasing temperature and using the concepts of thermal activation of dislocation

motion in BCC materials. The solid solution softening result was consistent with some empirical evidence of solute softening with decreasing temperature in iron alloys.

The Zerilli-Armstrong constitutive model relating flow stress to temperature, strain rate, strain, and grain size was modified to include variables for cold work and solute additions. The model was found to provide good correlation with experimental data gathered on IF steels with variations in cold work, grain size and solute content. It is anticipated that this model may be applied to other sheet steels if the grain size, cold work, solute content, and quasi-static flow curve are known.

The effects of strain rate on a TRIP steel with controlled variations in retained austenite stability were also examined, and it was found that the differences in flow behavior diminished with increasing strain rate. A comparison of the same TRIP steel with the other sheet steels studied revealed that the TRIP steel did not strengthen as much at high rates as some other low carbon steels. This difference was attributed to the reduction of transformation of retained austenite to martensite at high strain rates due to adiabatic heating.

TABLE OF CONTENTS

ABSTRACT	iii
LIST OF FIGURES	x
LIST OF TABLES	xxiii
ACKNOWLEDGMENTS	xxvii
CHAPTER 1: INTRODUCTION	1
CHAPTER 2: BACKGROUND INFORMATION: DYNAMIC TENSILE TESTING.....	13
2.1 High-Rate Tensile Testing Apparatus and Procedures.....	13
2.2 Problems Associated With Dynamic Tensile Testing on Servo-Hydraulic Machines.....	16
2.2.1 Load Cell Ringing.....	16
2.2.2 Elastic and Plastic Stress Waves.....	22
2.2.3 Adiabatic Heating.....	24
2.2.4 Data Collection Issues.....	26
2.2.4.1 High Rate Data Acquisition.....	27
2.2.4.2 Time Delays Due to Stress Wave Velocities.....	28
CHAPTER 3: BACKGROUND INFORMATION: STRENGTHENING MECHANISMS.....	29
3.1 Fundamentals of Strengthening in BCC Metals.....	29
3.2 Influence of Strain Rate and Temperature on BCC Iron.....	31
3.3 Work Hardening.....	34

3.4	Influence of Strain Rate and Temperature on Work Hardened BCC Metals.....	36
3.5	Solid Solution Strengthening.....	39
3.6	Influence of Strain Rate and Temperature on Solution Strengthened BCC Iron.....	44
3.7	Grain Size Strengthening.....	47
3.8	Influence of Strain Rate and Temperature on Grain Size Strengthening in BCC Iron.....	50
3.9	Precipitation Strengthening in Steel.....	54
3.10	Multiphase Strengthening in Dual Phase and Transformation Induced Plasticity (TRIP) Steels.....	56
3.10.1	Strengthening in Dual Phase Steels.....	57
3.10.2	Strengthening in TRIP Steels.....	58
3.11	Influence of Strain Rate and Temperature on Dual Phase Steels.....	61
3.12	Influence of Strain Rate and Temperature on TRIP Steels.....	64
3.13	Modeling of Flow Behavior with Strain Rate and Temperature.....	68
3.13.1	Empirical Relationships.....	69
3.13.2	Dislocation Mechanics.....	70
3.13.3	Yield Strength Models.....	75
3.13.3.1	Brunner-Diehl BCC Model.....	75
3.13.3.2	Hahn Yield Drop Model.....	77
3.13.4	Flow Curve Models.....	78
3.13.4.1	Johnson-Cook Model.....	78
3.13.4.2	Zerilli-Armstrong Model.....	81
3.13.4.3	Mechanical Threshold Stress (MTS) Model.....	84
3.13.4.4	Comparison of Flow Curve Models.....	86

CHAPTER 4: EXPERIMENTAL PROCEDURES.....	87
4.1 MTS High Rate Testing System.....	87
4.1.1 Strain Measurement.....	89
4.1.2 Load Measurement.....	91
4.2 Test Sample Details.....	98
4.3 Data Collection & Reduction Methods.....	99
4.3.1 Conversion of Raw Data Into Stress-Strain Curves.....	100
4.3.2 Interpreting Anomalous Strain and Load Data.....	111
4.3.3 Determination of Mechanical Properties.....	114
4.4 Validation of High-Rate Test Methods.....	117
4.4.1 Comparison of Screw-Driven and High-Rate Tensile Test Machine Results.....	117
4.4.2 Geometry Change Effects.....	118
4.4.3 Accuracy of Low-Strain Region of the Stress-Strain Curve.....	119
4.4.4 Repeatability of Tests.....	120
4.5 Presentation of Results.....	120
4.6 Strengthening Mechanisms: Cold Work.....	121
4.7 Strengthening Mechanisms: Solid Solution Strengthening.....	123
4.7.1 IF Steel.....	123
4.7.2 HSLA Steel.....	124
4.8 Strengthening Mechanisms: Grain Size.....	125
4.8.1 First Grain Size Study.....	126
4.8.2 Second Grain Size Study.....	127
4.9 Strengthening Mechanisms: Multiphase TRIP Steel.....	129
4.10 Multiphase Strengthening Mechanisms: Comparison of Dual Phase to TRIP Steel.....	130

CHAPTER 5: RESULTS & DISCUSSION: DYNAMIC TENSILE TESTING.....	131
5.1 Validation of High-Rate Test Methods.....	131
5.1.1 Comparison of Screw-Driven and High-Rate Tensile Test Machine Results.....	131
5.1.2 Geometry Change Effects.....	132
5.1.3 Accuracy of Low-Strain Region of the Stress-Strain Curve.....	139
5.1.4 Repeatability of Tests.....	142
5.1.5 Discussion of High Rate Test Validation Results.....	143
5.2 Mechanical Properties as a Function of Strain Rate.....	144
5.2.1 Stress-Strain Curves.....	145
5.2.2 Strain Rate Sensitivity of Material Properties.....	148
5.2.3 Material Comparison for High Rate Applications.....	153
5.2.4 Discussion of Mechanical Property Results.....	160
CHAPTER 6: RESULTS & DISCUSSION: STRENGTHENING MECHANISMS.....	162
6.1 Strengthening by Cold Work.....	162
6.2 Solid Solution Strengthening.....	166
6.2.1 IF Steel.....	166
6.2.2 HSLA Steel.....	169
6.3 First Grain Size Study.....	171
6.4 Second Grain Size Study.....	179
6.5 Discussion of Cold Work, Solid Solution and Grain Size Strengthening Results.....	185
6.6 Multiphase Strengthening: Effect of Retained Austenite Stability in a TRIP Steel.....	188
6.7 Multiphase Strengthening: Comparison of Dual Phase to TRIP Steel.....	192
6.8 Constitutive Equation for IF Steels Strengthened by Cold Work, Solid Solution Strengthening and Grain Refinement.....	201

6.9	Constitutive Equation for HSLA Steels.....	211
6.10	Summary of Strengthening Mechanism Results.....	212
6.11	Relationships Between Dynamic Test Methodology and Strengthening Mechanism Investigation.....	214
CHAPTER 7: CONCLUSIONS.....		216
7.1	Dynamic Tensile Testing Conclusions.....	216
7.2	Strengthening Mechanisms Conclusions.....	217
7.2.1	Single Phase Ferrite Low Carbon Sheet Steels.....	217
7.2.2	Multiphase Transformation Induced Plasticity (TRIP) Steels.....	218
7.3	Suggestions for Future Work.....	218
CHAPTER 8: REFERENCES.....		220
APPENDIX A: NATURAL FREQUENCY CALCULATION FOR TENSILE SAMPLE.....		233
APPENDIX B: TENSILE SAMPLE DIMENSIONS.....		235
APPENDIX C: DETERMINATION OF CONSTANTS FOR THE MODIFIED ZERILLI-ARMSTRONG EQUATION.....		237

LIST OF FIGURES

Figure 1.1: Optical micrographs of IF-1 steel, single phase ferrite, 2% nital etch. (a) 10 μm grains. (b) 25 μm grains. (c) 65 μm grains. (d) 135 μm grains.	6
Figure 1.2: Optical micrographs of IF steels, single phase ferrite, 2% nital etch. (a) IF-2. (b) IF-3. (c) IF-4.	7
Figure 1.3: Optical micrographs of IF-5 steel, single phase ferrite, 2% nital etch. (a) 10 μm grains. (b) 14 μm grains. (c) 36 μm grains. (d) 130 μm grains.	8
Figure 1.4: Optical micrographs of (a) ULC-C (single phase ferrite), (b) ULC-D (single phase ferrite) and (c) dual phase (light = ferrite, dark = martensite) steel. 2% nital etch.	9
Figure 1.5: Optical micrographs of HSLA steels. Light colored phase is ferrite and dark colored phase in pearlite. (a) HSLA-1, 2% nital etch. (b) HSLA-2, sodium metabisulfite etch. (c) HSLA-3, sodium metabisulfite etch.	10
Figure 1.6: Optical micrographs of TRIP steels, sodium metabisulfite etch. White phase is retained austenite, gray phase is ferrite and dark colored phases are bainite and/or martensite. (a) TRIP-1. (b) TRIP-3: LS. (c) TRIP-3: HS.	11
Figure 2.1: Schematic classification of testing techniques according to strain rate [1 (p. 299)].	14
Figure 2.2: Schematic drawing of high-rate servo-hydraulic tensile test machine.	17
Figure 2.3: Oscilloscope record of load cell force versus time during a dynamic tension test depicting the phenomenon of ringing [23].	18
Figure 2.4: Spring and mass vibration system [24].	19
Figure 2.5: Single bar vibration system.	20

Figure 3.1:	Temperature dependence of yield and flow stresses in Fe-0.15%Ti tested at strain rate of $2.5 \times 10^{-4} \text{ s}^{-1}$ [34 (p. 23)].	32
Figure 3.2:	True stress-strain curves at four different strain rates for an interstitial free steel tested in compression at room temperature [43].	32
Figure 3.3:	Variation of lower yield stress of mild steel with strain rate at different constant temperatures [replotted from 42].	33
Figure 3.4:	(a) Schematic stress-strain curve for a fully annealed material. (b) Predicted stress-strain curves for the same material as in (a) but cold-worked to the strain levels “1” and “2” as shown in (a).	37
Figure 3.5:	True stress at yield versus temperature for an IF steel pre-strained to six different levels at room temperature. All tests conducted at a strain rate of 0.04 s^{-1} [54].	38
Figure 3.6:	True stress at 0.02 true strain versus strain rate for an IF steel quasi-statically pre-strained to five different levels. All tests conducted at room temperature [38].	39
Figure 3.7:	Strength increase, $\Delta\sigma$, of steel versus solute content. Solid lines represent substitutional atoms in the iron solvent lattice, while the dashed line represents interstitial atoms. [41 (p. 465)].	40
Figure 3.8:	Correlation of solid solution strengthening of iron-base binary alloys at 298K with size misfit parameter [replotted from 34 (p. 119)].	43
Figure 3.9:	Change in yield strength ($\Delta\sigma$) from pure iron to alloy (1.5 atomic %) versus temperature for several solute elements. The curves show both solid solution strengthening and softening. [34 (p. 117)].	45
Figure 3.10:	Critical resolved shear stress versus temperature for pure iron (designated by “ZrH ₂ -purified”) and an iron-carbon alloy (designated by “185 at ppm C”) [50].	46
Figure 3.11:	Dislocation pile-up model of grain size strengthening [43 (p. 182)]. Slip begins in grain “1”. As dislocations pile-up at the grain boundary, the stress concentration eventually activates slip in grain “2”.	48

Figure 3.12: Effect of grain size and strain rate on the lower yield stress of pure iron [replotted from 36].	52
Figure 3.13: Effect of grain size and temperature on the upper (σ_U) and lower (σ_L) yield strengths of Armco iron with composition (wt. pct.) of 0.03C-0.005Si-0.08Mn-0.007P-0.03S-0.03Ni. [69].	53
Figure 3.14: Effect of grain size and strain rate on the yield strength of a ferritic single phase steel with composition (wt. pct.) of 0.003C-1.5Si-2.0Mn-0.01P [35].	54
Figure 3.15: Illustration of dislocation bowing around precipitate particles under applied shear stress, τ [adapted from 39 (p. 209)].	55
Figure 3.16: Schematic free energy versus composition curves for austenite (A) and martensite (M) at different temperatures, where $T_1 > T_2 > T_3$.	60
Figure 3.17: Schematic free energy versus temperature curves for austenite (A) and martensite (M).	61
Figure 3.18: Influence of strain rate and volumetric fraction of martensite on tensile strength of dual phase steel [35].	63
Figure 3.19: Influence of strain rate and volumetric fraction of martensite on yield strength of dual phase steel [35].	63
Figure 3.20: Nominal stress-strain curves at two different strain rates for (a) mild steel, (b) solution-hardened steel, and (c) dual phase steel. [35]	64
Figure 3.21: Schematic drawing of critical stress for martensite formation versus temperature for a TRIP steel.	65
Figure 3.22: Volume fraction of martensite formed during straining of 304 stainless steel at room temperature in uniaxial tension at high (10^3 s^{-1}) and low (10^{-3} s^{-1}) strain rates [adapted from 96].	68
Figure 3.23: Movement of an array of dislocations causing shear strain $\gamma = \tan \theta$ [adapted from 1 (p. 331)].	70

Figure 3.24: (a) Schematic drawing of thermal energy used to overcome short-range obstacles. $T_3 > T_2 > T_1 > T_0$. Cross-hatched areas show thermal energy contributions. (b) Stress required to overcome a short-range obstacle as a function of temperature. [1 (p. 341)]	73
Figure 3.25: Divergent stress-strain curves predicted by isothermal use of the Johnson-Cook equation (Equation 3.52). $\dot{\epsilon}_1 > \dot{\epsilon}_2 > \dot{\epsilon}_3$	81
Figure 4.1: Photographs of the MTS servo-hydraulic high rate testing system. a) Entire system. b) Loading assembly. c) Test sample.	88
Figure 4.2: Photograph of two copper tensile samples. The upper sample is shown prior to testing and the lower sample is shown after testing to fracture with approximately 50% elongation.	89
Figure 4.3: Engineering strain versus time plots for TRIP-1 steel. a) Low-rate test: gage length = 50.8 mm, actuator velocity = 6 mm/s, strain rate = 0.12 s^{-1} b) High-rate test: gage length = 12.7 mm, actuator velocity = 8 m/s, strain rate = 630 s^{-1}	91
Figure 4.4: Engineering stress-strain curves for HSLA-1 steel calculated using load data from the piezoelectric load washer at four strain rates. Increasing strain rate increases ringing amplitude while ringing frequency remains approximately constant. All tests run using 25.4 mm gage length samples with actuator velocities of 0.025 mm/s, 250 mm/s, 2.5 m/s and 13.5 m/s used to achieve strain rates of 10^{-3} , 10, 100 and 530 s^{-1} , respectively.	92
Figure 4.5: Load versus time plot for two frequency response tests. One test ("High Mass") was conducted with the upper grip installed, while the other ("Low Mass") was conducted without the upper grip installed. The plot shows the higher mass test resulted in larger amplitude, lower frequency oscillations.	93
Figure 4.6: Load versus time plot for two HSLA-1 steel tensile samples with different gage lengths. One sample (solid line) had a gage length of 25.4 mm and the other sample had a gage length of 12.7 mm. The smaller gage length sample provided a higher strain rate even with a lower actuator velocity. The lower actuator velocity resulted in lower amplitude oscillations in the load washer data.	95

Figure 4.7: Schematic drawing of tensile sample with strain and load measurement strain gages attached.	96
Figure 4.8: Load versus time plot for TRIP-2 steel tensile test at an engineering strain rate of 110s^{-1} . Load data from a piezoelectric load washer are compared with load data gathered using a grip section strain gage. Sample gage length was 25.4 mm and actuator velocity was 2.8 m/s.	96
Figure 4.9: Load versus time plot for TRIP-2 steel tensile test at an engineering strain rate of 240s^{-1} . Load data from a piezoelectric load washer lags load data gathered using a grip section strain gage by about 50 μs . Tensile sample gage length = 25.4 mm and actuator velocity = 6.1 m/s. ..	98
Figure 4.10: Engineering strain versus time for two dual phase steel tensile tests. a) Low rate test with gage length = 25.4 mm and actuator velocity = 25 mm/s. b) High rate test with gage length = 25.4 mm and actuator velocity = 2.7 m/s.	101
Figure 4.11: Linear portion of the engineering strain versus time plots from Figure 4.10 for two dual phase steel tensile tests. In each figure, the dashed line is the linear curve fit. a) Low rate test with gage length = 25.4 mm and actuator velocity = 25 mm/s. b) High rate test with gage length = 25.4 mm and actuator velocity = 2.7 m/s.	102
Figure 4.12: Engineering stress versus engineering strain for the grip section of a dual phase steel low rate test. The slope of the plot gives the material's elastic modulus. Sample gage length = 25.4 mm and actuator velocity = 25 mm/s.	104
Figure 4.13: Load versus time plots comparing piezoelectric load washer, grip section strain gage and data-averaged load washer data for a dual phase steel high rate test. Tensile sample gage length = 25.4 mm and actuator velocity = 2.7 m/s. (a) Elastic modulus of 192 GPa used to calculate grip section strain gage loads. (b) Elastic modulus of 189 GPa used to calculate grip section strain gage loads.	106
Figure 4.14: Engineering stress-strain curves for dual phase steel tensile tests at two different strain rates. a) Low rate test with gage length = 25.4 mm and actuator velocity = 25 mm/s. b) High rate test with gage length = 25.4 mm and actuator velocity = 2.7 m/s.	110

Figure 4.15: True stress-strain curves for dual phase steel tensile tests at two different strain rates. a) Low rate test with gage length = 25.4 mm and actuator velocity = 25 mm/s. b) High rate test with gage length = 25.4 mm and actuator velocity = 2.7 m/s.	111
Figure 4.16: Tensile test results for IF-1 steel sample with gage length of 25.4 mm run using an actuator velocity of 27 mm/s. a) Engineering stress-strain curve showing yield point elongation (YPE) up to nearly 0.07 strain. b) Engineering strain versus time plot showing difference in strain rates for YPE region and the rest of the test.	112
Figure 4.17: Load versus time plots comparing piezoelectric load washer and grip section strain gage data. a) Grip section strain gage partial debond location shown by arrow. TRIP-1 steel with tensile sample gage length = 12.7 mm and actuator velocity = 350 mm/s. b) Tensile sample grip section experiences plastic deformation. Dual phase steel with tensile sample gage length = 25.4 mm and actuator velocity = 2.7 m/s.	113
Figure 4.18: Figure 4.17 data re-plotted using data-averaged load washer signal after the grip section strain gage data becomes unreliable. a) TRIP-1 steel with tensile sample gage length = 12.7 mm and actuator velocity = 350 mm/s. b) Dual phase steel with tensile sample gage length = 25.4 mm and actuator velocity = 2.7 m/s.	114
Figure 4.19: True stress-strain curves for dual phase steel tensile tests at two different strain rates. Low rate test used sample gage length = 25.4 mm and actuator velocity = 25 mm/s. High rate test used sample gage length = 25.4 mm and actuator velocity = 2.7 m/s.	116
Figure 4.20: True stress-strain plots on a log-log scale for dual phase steel tensile tests at two different strain rates. The slope of each plot is the strain hardening exponent. Low rate test used sample gage length = 25.4 mm and actuator velocity = 25 mm/s. High rate test used sample gage length = 25.4 mm and actuator velocity = 2.7 m/s.	116
Figure 5.1: Comparison of low-rate true stress-strain curves for tensile tests run on screw-driven MTS and high-rate MTS tensile test machines at identical crosshead/actuator speeds for a) ULC-D steel with gage length of 76 mm and b) HSLA-1 steel with gage length of 50.8 mm. Results in both cases are similar.	132

Figure 5.2:	True stress-strain curves for HSLA-1 steel. Each plot shows two different gage lengths tested at similar strain rates.	134
Figure 5.3:	True stress-strain curves for HSLA-2 steel. Each plot shows two different gage lengths tested at similar strain rates.	134
Figure 5.4:	True stress-strain curves for TRIP-1 steel tested with two different gage lengths at similar strain rates.	135
Figure 5.5:	Engineering stress-strain curves for HSLA-2 steel. Each plot shows two different gage lengths tested at similar strain rates.	135
Figure 5.6:	Engineering stress-strain curves for TRIP-1 steel tested with two different gage lengths at similar strain rates.	136
Figure 5.7:	Engineering stress-strain curves for five different steels with different sheet thicknesses.	137
Figure 5.8:	Load versus engineering strain curves for the five different steels with different sheet thicknesses shown in Figure 5.7.	139
Figure 5.9:	True stress-strain curves up to 0.05 true strain for copper samples tensile tested at six different strain rates. All curves show continuous-yielding behavior. All samples had 25.4 mm gage lengths.	140
Figure 5.10:	True stress-strain curves up to 0.05 true strain for IF-1 steel samples tensile tested at three different strain rates. All curves show upper and lower yield points. All samples had 25.4 mm gage lengths.	141
Figure 5.11:	True stress-strain curves up to 0.05 true strain for HSLA-1 steel samples tensile tested at three different strain rates. All curves show upper and lower yield points. All samples had 25.4 mm gage lengths.	141
Figure 5.12:	True stress-strain curves up to 0.05 true strain for ULC-D steel samples tensile tested at three different strain rates. All curves show upper and lower yield points. All samples had 76 mm gage lengths.	142
Figure 5.13:	Repeatability study of engineering stress-strain curves for HSLA-2 steel samples tensile tested at five different strain rates. Two tests were run at each of the strain rates 0.014 s^{-1} and 235 s^{-1} , while three tests were run for each of the other strain rates.	143

Figure 5.14: Engineering and true stress-strain curves for HSLA-1 steel samples tensile tested at five different strain rates. All sample gage lengths were 50.8 mm, except for the 95 s ⁻¹ test which used 12.7 mm gage length. Actuator speeds were 0.50 mm/s, 5.0 mm/s, 50 mm/s, 500 mm/s and 2.5 m/s, respectively, to achieve the indicated strain rates of 0.013, 0.097, 1.4, 10 and 95 s ⁻¹	146
Figure 5.15: Engineering and true stress-strain curves for HSLA-2 steel samples tensile tested at five different strain rates. Sample gage lengths were 50.8 mm for the three lowest rate tests and 25.4 mm for the two highest rate tests. Actuator speeds were 0.5 mm/s, 50 mm/s, 375 mm/s, 5.0 m/s and 10 m/s, respectively, to achieve the indicated strain rates of 0.014, 1.4, 6.4, 235 and 420 s ⁻¹	147
Figure 5.16: Engineering and true stress-strain curves for dual phase steel samples tensile tested at five different strain rates. All sample gage lengths were 25.4 mm. Actuator speeds were 0.025 mm/s, 25 mm/s, 250 mm/s, 2.5 m/s and 12.5 m/s, respectively, to achieve the indicated strain rates of 8.9x10 ⁻⁴ , 0.92, 7.8, 110 and 490 s ⁻¹	147
Figure 5.17: Engineering and true stress-strain curves for IF-1 steel samples tensile tested at five different strain rates. All sample gage lengths were 25.4 mm. Actuator speeds were 0.025 mm/s, 25 mm/s, 250 mm/s, 2.5 m/s and 12.5 m/s, respectively, to achieve the indicated strain rates of 1.0x10 ⁻³ , 1.0, 15, 100 and 500 s ⁻¹	148
Figure 5.18: Strain rate sensitivities of yield and tensile strengths for (a) HSLA-2 steel, and (b) dual phase steel.	149
Figure 5.19: Strain hardening exponent versus logarithm of strain rate for HSLA-2 and dual phase steels. Strain hardening exponents calculated from 0.002 true strain up to the uniform strain limit.	151
Figure 5.20: Comparison of area under the engineering stress-strain curve up to 10% strain versus logarithm of strain rate for HSLA-2 and dual phase steels.	152

Figure 5.21: Engineering stress-strain curves for HSLA-2 and dual phase (DP) steels. (a) Low-rate tests. Sample gage lengths: HSLA-2 = 50.8 mm, DP = 25.4 mm. Actuator speeds: HSLA-2 = 50 mm/s, DP = 25 mm/s. (b) High-rate tests. Sample gage lengths: HSLA-2 = 25.4 mm, DP = 25.4 mm. Actuator speeds: HSLA-2 = 11.2 m/s, DP = 11.2 m/s.	153
Figure 5.22: Dynamic strength minus static strength versus static strength plots for (a) yield strength and (b) tensile strength. Dynamic strength values determined at strain rate of about 100 s^{-1} and static values determined at strain rate of about 0.01 s^{-1} . In both (a) and (b), the IF-1 steel has $10 \mu\text{m}$ grain size.	155
Figure 5.23: Strain rate sensitivities of yield and tensile strengths for (a) HSLA-1 steel, and (b) dual phase steel.	156
Figure 5.24: Strain hardening exponent versus logarithm of strain rate for HSLA-1 and dual phase steels. Strain hardening exponents were calculated for entire flow curve between 0.02 true strain and uniform strain limit for dual phase and beyond the yield point elongation up to the uniform strain limit for HSLA-1 steel.	157
Figure 5.25: Comparison of area under the engineering stress-strain curve up to 10% strain versus logarithm of strain rate for HSLA-1 and dual phase steels.	158
Figure 5.26: Engineering stress-strain curves for HSLA-1 and dual phase (DP) steels. (a) Low-rate test. Sample gage lengths: HSLA-1 = 50.8 mm, DP = 25.4 mm. Actuator speeds: HSLA-1 = 50 mm/s, DP = 25 mm/s. (b) High-rate test. Sample gage lengths: HSLA-1 = 12.7 mm, DP = 25.4 mm. Actuator speeds: HSLA-1 = 1.25 m/s, DP = 2.5 m/s.	158
Figure 5.27: True stress-strain curves for IF-1 and IF-2 steels. All sample gage lengths were 25.4 mm. (a) Quasi-static tests. Actuator speed = 0.025 mm/s. (b) Dynamic tests. Actuator speed = 2.5 m/s.	159
Figure 6.1: Stress-strain curves at a strain rate of about 0.001 s^{-1} for IF-2 steel with five different pre-strain levels. a) Engineering stress-strain curves. b) True stress-strain curves with pre-strained results offset by the appropriate amount.	162

Figure 6.2:	Stress-strain curves at a strain rate of about 9 s^{-1} for IF-2 steel with five different pre-strain levels. a) Engineering stress-strain curves. b) True stress-strain curves with pre-strained results offset by the appropriate amount.	164
Figure 6.3:	Stress-strain curves at a strain rate of about 150 s^{-1} for IF-2 steel with five different pre-strain levels. a) Engineering stress-strain curves. b) True stress-strain curves with pre-strained results offset by the appropriate amount.	165
Figure 6.4:	a) Flow stress at 0.02 true strain versus strain rate for an IF steel with five different amounts of pre-strain. b) Flow stress at 0.02 true strain versus pre-strain amount for an IF steel at three different strain rates.	165
Figure 6.5:	Engineering stress-strain curves for IF steels tested at five different strain rates. a) IF-3 steel (0.2 Mn, 0.01 P). b) IF-4 steel (0.9 Mn, 0.09 P).	166
Figure 6.6:	(a) Yield strength and (b) tensile strength as functions of alloying additions to an IF steel [replotted from 127].	167
Figure 6.7:	a) Flow stress at 0.02 true strain versus strain rate for two IF steels with different solute content. b) Flow stress at 0.02 true strain versus IF steel designation at four different strain rates. “3” is the IF-3 steel composition (0.2 Mn, 0.01 P) and “4” is the IF-4 steel composition (0.9 Mn, 0.09 P).	168
Figure 6.8:	Yield strength versus strain rate for two HSLA steels with different solute content.	170
Figure 6.9:	a) Yield strength (modified for HSLA-2) versus strain rate for two HSLA steels with different solute content. b) Yield strength (modified for HSLA-2) versus IF steel designation at four different strain rates. “1” is the HSLA-1 steel composition (lower solute content) and “2” is the HSLA-2 steel composition (higher solute content).	171
Figure 6.10:	True stress-strain curves at two strain rates for IF-1 steel with four different grain sizes. All sample gage lengths were 25.4 mm. Actuator speed for low strain rate was 0.025 mm/s and was 1.0 m/s for high strain rate. Arrows indicate heights of upper yield points for low-rate stress-strain curves.	173

Figure 6.11: Flow stress at 0.05 true strain as a function of (grain diameter) ^{-1/2} for IF-1 steel tensile tested at five different strain rates. All sample gage lengths were 25.4 mm. Actuator speeds were 0.025, 2.5, 25, 250 and 1000 mm/s for strain rates of 0.001, 0.1, 1, 10 and 35 s ⁻¹ , respectively. ..	174
Figure 6.12: Flow stress versus (grain diameter) ^{-1/2} for IF-1 steel tested at five different strain rates. a) Yield stress, b) Flow stress at 0.05 true strain, c) Flow stress at 0.10 true strain, and d) Flow stress at 0.15 true strain. All sample gage lengths were 25.4 mm. Actuator speeds were 0.025, 2.5, 25, 250 and 1000 mm/s for strain rates of 0.001, 0.1, 1, 10 and 35 s ⁻¹ , respectively.	175
Figure 6.13: Strain rate sensitivities of (a) σ_0 and (b) k for the data presented in Table 6.3.	176
Figure 6.14: True stress-strain curves at five different strain rates for IF-1 steel with 135 mm grain size. All sample gage lengths were 25.4 mm.	178
Figure 6.15: Quasi-static engineering stress-strain curves for IF-1 and IF-5 steels with grain size of about 135 mm.	180
Figure 6.16: Yield strength as a function of (grain diameter) ^{-1/2} . All sample gage lengths were 25.4 mm. Actuator speed was 0.025 mm/s. (a) All quasi-static IF-5 steel sample results. 10 μ m grain size samples do not follow the expected Hall-Petch trend. (b) IF-5 steel results (without 10 μ m data) compared to IF-1 steel results. The k_y values are similar.	181
Figure 6.17: Flow stress versus (grain diameter) ^{-1/2} for IF-5 steel tested at five different strain rates. a) Yield stress, b) Flow stress at 0.05 true strain, c) Flow stress at 0.075 true strain, and d) Flow stress at 0.10 true strain. All sample gage lengths were 25.4 mm. Actuator speeds were 0.025 mm/s, 25 mm/s, 750 mm/s, 5.0 m/s and 10.0 m/s for strain rates of 0.001, 1, 30, 200 and 400 s ⁻¹ , respectively.	182
Figure 6.18: Strain rate sensitivities of (a) σ_0 and (b) k for the data presented in Table 6.4.	184
Figure 6.19: Comparison of the strain rate sensitivities of (a) σ_0 and (b) k for IF-1 and IF-5 steels at 0.05 true strain.	185

- Figure 6.20: Static-to-dynamic strength increment versus static strength for six different steels. Dynamic yield strength measured at strain rate of approximately 100 s^{-1} . IF-2 data point based on 0% pre-strain. IF-1 data point based on $10 \mu\text{m}$ grain size. 187
- Figure 6.21: Static-to-dynamic strength increment versus static strength for four different IF steels. IF-1 steel data points for different amounts of tensile pre-strain (cold work). IF-2 and IF-5 steel data points for different grain sizes. IF-3 and IF-4 steel data points are from the solid solution strengthening experiment. Strain rates and true strain values used for data points are given in Table 6.5. 187
- Figure 6.22: True stress-strain curves at two different strain rates for (a) LS and (b) HS TRIP-3 steel. Sample gage length was 50.8 mm and actuator speed was 0.25 mm/s for both low-rate tests. Gage length was 25.4 mm and actuator speed was 6.0 m/s for the high-rate tests. 189
- Figure 6.23: True stress-strain curves comparing LS and HS heat treatments for TRIP-3 steel at three different strain rates. a) Sample gage length = 50.8 mm and actuator speed = 0.50 mm/s. b) Sample gage length = 50.8 mm and actuator speed = 500 mm/s. c) Sample gage length = 25.4 mm and actuator speed = 6.0 m/s. 190
- Figure 6.24: True stress-strain curves comparing TRIP-3 LS and HS with dual phase steel at quasi-static strain rates. For both TRIP-3 steels, sample gage length = 50.8 mm, actuator speed = 0.50 mm/s and strain rate = 0.012 s^{-1} . For the dual phase steel, sample gage length = 25.4 mm, actuator speed = 0.025 mm/s and strain rate = $8.9 \times 10^{-4} \text{ s}^{-1}$ 193
- Figure 6.25: Strain rate sensitivity plots for both yield and tensile strengths for (a) TRIP-3 LS steel, (b) TRIP-3 HS steel and (c) dual phase steel. 195
- Figure 6.26: Engineering stress-strain curves for HSLA-2 and TRIP-3 HS steels at two different strain rates. (a) Gage length = 50.8 mm and actuator speed = 0.50 mm/s. (b) Gage length = 25.4 mm and actuator speed = 250 mm/s. (c) Gage length = 25.4 mm and actuator speed = 6.2 m/s. 198

Figure 6.27: Area under the engineering stress-strain curve versus engineering strain for HSLA-2 and TRIP-3 HS steels at two different strain rates. (a) Gage length = 50.8 mm and actuator speed = 0.50 mm/s. (b) Gage length = 25.4 mm and actuator speed = 250 mm/s. (c) Gage length = 25.4 mm and actuator speed = 6.2 m/s.	200
Figure 6.28: True stress-strain curves for IF-1 steel at three different strain rates compared with Modified Zerilli-Armstrong model at same strain rates using the constants shown in Table 6.12. (a) 10 μm grain size, (b) 25 μm grain size, and (c) 135 μm grain size.	206
Figure 6.29: True stress-strain curves for IF-2 steel at four different strain rates compared with Modified Zerilli-Armstrong model at same strain rates using the constants shown in Table 6.12. (a) 0% pre-strain, (b) 2% pre-strain and (c) 5% pre-strain.	207
Figure 6.30: True stress-strain curves for IF-2 steel at four different strain rates compared with Modified Zerilli-Armstrong model at same strain rates using the constants shown in Table 6.12. (a) 10% pre-strain and (b) 18% pre-strain.	208
Figure 6.31: True stress-strain curves for (a) IF-3 steel and (b) IF-4 steel at four different strain rates compared with Modified Zerilli-Armstrong model at same strain rates using the constants shown in Table 6.12.	208
Figure 6.32: Lower yield strength as a function of strain rate for IF-1 (10 μm grain size) steel compared to the Hahn model using the constants shown in Table 6.13.	210
Figure 6.33: True stress-strain curves for (a) HSLA-1 steel and (b) HSLA-2 steel at four different strain rates compared with Modified Zerilli-Armstrong model at same strain rates using the constants shown in Table 6.14.	212
Figure C1: True stress-strain curves for IF-2 steel with 0% pre-strain at four different strain rates compared with Modified Zerilli-Armstrong model at same strain rates.	241

LIST OF TABLES

Table 1.1: Material designation and chemical composition (wt. pct.) for each material used in this thesis. “NR” means the element was not reported. “IF” indicates interstitial free steel, “ULC” indicates ultra-low carbon steel, “HSLA” indicates high strength low alloy steel, “DP” indicates dual phase steel and “TRIP” indicates transformation induced plasticity steel.	3
Table 1.2: Sheet thickness and process history for each material in Table 1.1.	4
Table 1.3: Quasi-static tensile properties for each material in Table 1.1. The yield strength is given as the lower yield point for materials exhibiting yield point elongation and is the 0.2% offset stress for continuous-yielding materials.	5
Table 1.4: Materials used for each test conducted for this thesis.	12
Table 3.1: Constants for the Brunner-Diehl model for pure α -iron [48].	76
Table 3.2: Constants for the Hahn model for 1020 steel [104]. m_L is for strain rates less than 1 s^{-1} , while m_H is used for strain rates between 1 and 1000 s^{-1}	78
Table 3.3: Material and constitutive constants for the Johnson-Cook equation (Equation 3.52) for various Armco iron and 1006 steel [105].	80
Table 3.4: Constants for the Zerilli-Armstrong equation (Equation 3.57) for iron [107].	82
Table 3.5: Constants for the modified Zerilli-Armstrong equation (Equation 3.58) for carbon-chromium-molybdenum steel with quasi-static yield strength of 800 MPa [108].	83
Table 4.1: Nominal dimensions of dual phase (DP) steel tensile samples.	100
Table 4.2: True uniform strain limits based on different calculation methods for two different rate tensile tests on dual phase steel.	109

Table 4.3: Mechanical properties of dual phase steel for two different strain rates.	117
Table 4.4: Nominal dimensions of ULC-D and HSLA-1 steels used for low-rate tensile test comparison between screw-driven and high-rate machines.	118
Table 4.5: Nominal dimensions of steel samples used for geometry comparison tensile tests.	119
Table 4.6: Nominal dimensions of 11000-H00 Cu used for tensile tests.	120
Table 4.7: Nominal dimensions of IF-2 steel tensile samples (before pre-strain).	122
Table 4.8: Statistical analysis of pre-strain data for IF-2 tensile samples.	122
Table 4.9: Test matrix for IF-2 steel tensile tests.	123
Table 4.10: Nominal dimensions of IF-3 and IF-4 steel tensile samples.	124
Table 4.11: Test matrix for IF-3 and IF 4 steel tensile samples used for solid solution strengthening study.	124
Table 4.12: Nominal dimensions of HSLA-1 and HSLA-2 steel tensile samples.	125
Table 4.13: Test matrix for HSLA-1 and HSLA-2 steel tensile samples used for solid solution strengthening study.	125
Table 4.14: Heat treat procedures used on the IF-1 steel for the first grain size study.	126
Table 4.15: Nominal dimensions of IF-1 steel tensile samples used for the first grain size study.	127
Table 4.16: Test matrix for IF-1 steel tensile samples used for first grain size study. ...	127
Table 4.17: Heat treat procedures used on IF-5 steel for the second grain size study. ...	128
Table 4.18: Nominal dimensions of IF-5 steel tensile samples used for the second grain size study.	128
Table 4.19: Test matrix for IF-5 steel tensile samples used for second grain size study.	128

Table 4.20: Heat treatment details for TRIP-3 steel processed to achieve two different retained austenite stabilities.	129
Table 4.21: Nominal dimensions of TRIP-3 steel tensile samples used for the TRIP austenite stability study.	129
Table 4.22: Test matrix for TRIP-3 steel tensile samples used for the TRIP austenite stability study.	130
Table 4.23: Nominal dimensions of dual phase (DP) steel tensile samples.	130
Table 4.24: Test matrix for dual phase steel tensile samples used for comparison to TRIP-3 steels.	130
Table 5.1: Sheet thickness, gage length, strain rate, actuator speed, yield strength, and load at yield for each of five materials used to compare “noisiness” of stress-strain curves in Figures 5.7 and 5.8.	137
Table 5.2: Logarithmic strain rate sensitivities (β) for the HSLA-2 and dual phase steel data in Figure 5.18.	150
Table 5.3: Logarithmic strain rate sensitivities (β) for the HSLA-1 and dual phase steel data in Figure 5.23.	157
Table 6.1: Logarithmic strain rate sensitivities (β) for the IF-3 and IF-4 steel data shown in Figure 6.7a.	169
Table 6.2: Logarithmic strain rate sensitivities (β) for HSLA-1 and HSLA-2 steel data shown in Figure 6.8.	171
Table 6.3: Hall-Petch parameters, σ_0 (MPa) and k (MPa $\sqrt{\text{mm}}$), for each flow stress and strain rate shown in Figure 6.12.	176
Table 6.4: Hall-Petch parameters, σ_0 (MPa) and k (MPa $\sqrt{\text{mm}}$), for each flow stress and strain rate shown in Figure 6.17.	183
Table 6.5: Strain rates and true strain values used for flow stress measurements in Figure 6.21.	188
Table 6.6: Work hardening exponents, n , for low and high strain values for each tensile test shown in Figures 6.23a and 6.23b.	191

Table 6.7: Work hardening exponents, n , for low and high strain values for the quasi-static tensile tests shown in Figure 6.24.	193
Table 6.8: Logarithmic strain rate sensitivities (β) for the TRIP-3 and dual phase steel data in Figure 6.25.	196
Table 6.9: Logarithmic strain rate sensitivities (β) for TRIP-3 HS and HSLA-2 steels.	197
Table 6.10: Area under the engineering stress-strain curve up to 10% engineering strain for TRIP-3 HS and HSLA-2 steels at three different strain rates as shown in Figures 6.26 and 6.27.	201
Table 6.11: Quasi-static solid solution strengthening increment for several IF steels. ..	203
Table 6.12: Constants for the modified Zerilli-Armstrong (MZA) equation (Equation 6.2) for IF steels.	204
Table 6.13: Constants for the Hahn model for IF-1 steel with 10 μm grain size. m_L was for strain rates up to 1 s^{-1} , while m_H was used for strain rates above 1 s^{-1} . Model constants given by Hahn [104] for 1020 steel are shown for comparison.....	210
Table 6.14: Constants for the modified Zerilli-Armstrong (MZA) equation (Equation 6.2) for HSLA steels.	211
Table C1: Constants required for the modified Zerilli-Armstrong (MZA) equation (Equation 6.2) for IF steels.	238
Table C2: Constants for the modified Zerilli-Armstrong (MZA) equation (Equation 6.2) for IF steels determined prior to fitting the model to experimental data.	240
Table C3: Final constants for the modified Zerilli-Armstrong (MZA) equation (Equation 6.2) for IF steels.	242

ACKNOWLEDGMENTS

This project was funded by AISI/DOE Project 9904, “Constitutive Behavior of High Strength Multiphase Sheet Steels Under High Strain Rate Deformation Conditions.” I would like to thank the following sponsor companies for their support of this project: AK Steel Corporation, Bethlehem Steel Corporation, DaimlerChrysler Corporation, Ispat Inland Inc., LTV Steel Company, MTS Systems Corporation, National Steel Corporation, Rouge Steel Company, and US Steel Company.

I would also like to thank the following:

- The Department of Engineering Mechanics at the United States Air Force Academy for their sponsorship of my education and for the use of their laboratory equipment.
- My advisor, Dr. David Matlock, and members of my thesis committee, Dr. John Speer, Dr. Greg Shoales and Dr. Marty Mataya for guidance and support.
- Dr. Ildong Choi of the Korea Maritime University for providing TRIP steel tensile samples.
- Mimi Martin, Rachel Cohen, Steve Donelson, Matt Ruggerio, Ty Colman and Mike Morimoto for their help.
- Special thanks to my husband, . for his endless patience and encouragement.

The views expressed in this thesis are those of the author and do not reflect the official policy or position of the United States Air Force, Department of Defense, or the U.S. Government.

CHAPTER 1

INTRODUCTION

The mechanical response of materials subjected to various strain rates is important for many applications ranging from metal forming operations to automobile collisions to military projectile effectiveness. To understand the mechanical properties under various strain rates requires test equipment capable of imposing those strain rates and measuring relevant quantities, such as load and deformation.

High strength steels are designed for a range of applications and employ a combination of strengthening mechanisms, which may include cold work, grain size, dispersion, solid solution strengthening, strain aging and multiphase strengthening. Designing structures for use in high strain rate environments using high strength sheet steels requires knowledge of their mechanical properties over the range of strain rates they are expected to encounter. While any potential material could be tested over a range of strain rates, it would be more efficient to understand how the strengthening mechanisms used in the steel are affected by strain rate, and predict its high-rate properties accordingly.

The two primary goals of this thesis program were to develop dynamic tensile test capability for sheet steels and to determine the effects of strain rate on various strengthening mechanisms used in sheet steels. The tests discussed in this thesis focus on acquiring tensile mechanical properties of sheet steels at strain rates ranging from “quasi-static” up to about 500 s^{-1} , with the primary industrial application being accurate property data for these steels to use in automobile crash simulations. Sheet steels designed to isolate various strengthening mechanisms including cold work, grain size and solid solution strengthening were tested over this strain rate range. Tensile properties were determined and analyzed with the goal of developing a model for predicting high-rate flow stress values based on quasi-static properties and microstructure.

This thesis is divided into two major sections: 1) dynamic tensile testing of sheet steels and 2) effects of strain rate on selected strengthening mechanisms of importance in sheet steels. Background information and literature review for each major section are contained in Chapters two and three. Chapter four describes the experimental procedures used for all testing. Chapter five contains results and discussions of the dynamic tensile testing section and Chapter six covers results and discussions for the strengthening mechanisms section. Chapter seven summarizes conclusions and recommendations for further work.

A wide range of materials was used to conduct experiments to validate the dynamic tensile test procedures and to conduct the strengthening mechanisms experiments. A list of all the material designations along with each chemical composition is shown in Table 1.1. Table 1.2 lists sheet thickness and process history for each material, while Table 1.3 gives their quasi-static tensile properties. Figures 1.1 through 1.6 show optical micrographs of each material. Table 1.4 lists the various tests conducted and the materials used for each test.

Table 1.2: Sheet thickness and process history for each material in Table 1.1.

Designation	Sheet Thickness (mm)	Process History
IF-1	2.0 - 4.1	Commercial Product: Heat treated to achieve various grain sizes -- details contained in Table 4.14 (Section 4.8.1)
IF-2	0.76	Commercial Product: Pre-strained to various amounts -- details contained in Section 4.6
IF-3	1.42	Commercial Product: As-received
IF-4	1.40	Commercial Product: As-received
IF-5	1.99	Commercial Product: Cold-rolled from 4.69 mm sheet and heat treated to achieve various grain sizes -- details contained in Table 4.17 (Section 4.8.2)
ULC-C	0.72	Commercial Product: As-received
ULC-D	0.72	Commercial Product: As-received
HSLA-1	1.6	Commercial Product: As-received
HSLA-2	3.2	Commercial Product: As-received
HSLA-3	1.2	Commercial Product: As-received
DP	1.4	Commercial Product: As-received, 15 volume percent martensite
TRIP-1	2.7	Commercial Product: As-received
TRIP-3	0.83	Laboratory Produced: Heat-treated to achieve different stability levels of retained austenite -- details contained in Section 4.9
11000-H00	3.2	Commercial Product: As-received

Table 1.3: Quasi-static tensile properties for each material in Table 1.1. The yield strength is given as the lower yield point for materials exhibiting yield point elongation and is the 0.2% offset stress for continuous-yielding materials.

Designation	Yield Strength (MPa)	Tensile Strength (MPa)	% Elongation (in 50.8 mm gage length unless otherwise noted)
IF-1 (as received)	250	300	50% (25.4 mm gage length)
IF-2 (as received)	135	290	42%
IF-3	195	290	42%
IF-4	240	335	36%
IF-5 (as received)	380	485	40%
ULC-C	380	405	21% (76 mm gage length)
ULC-D	325	390	27% (76 mm gage length)
HSLA-1	335	415	30%
HSLA-2	530	600	20%
HSLA-3	480	605	22%
DP	330	600	25%
TRIP-1	635	820	25%
TRIP-3: LS	395	700	20%
TRIP-3: HS	405	655	23%
11000-H00	80	235	50%

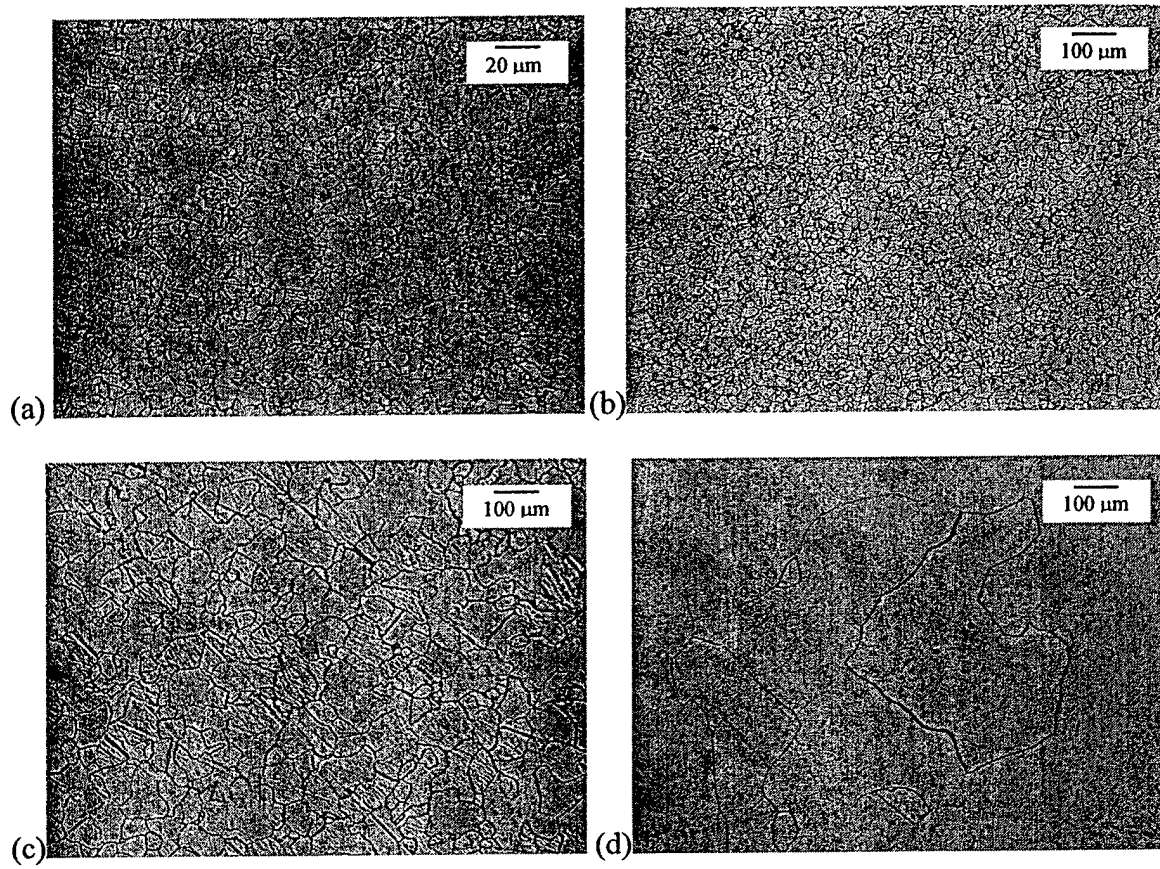


Figure 1.1: Optical micrographs of IF-1 steel, single phase ferrite, 2% nital etch.
(a) 10 μm grains. (b) 25 μm grains. (c) 65 μm grains. (d) 135 μm grains.

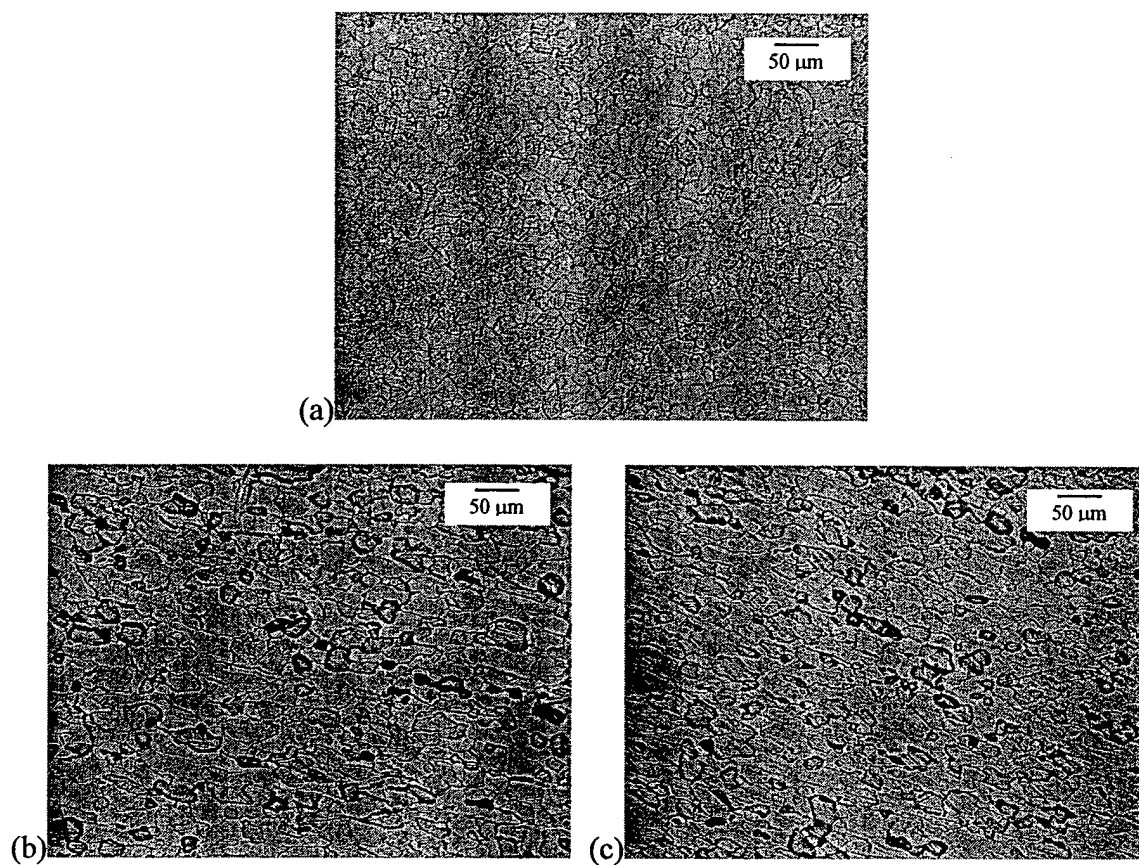


Figure 1.2: Optical micrographs of IF steels, single phase ferrite, 2% nital etch.
(a) IF-2. (b) IF-3. (c) IF-4.

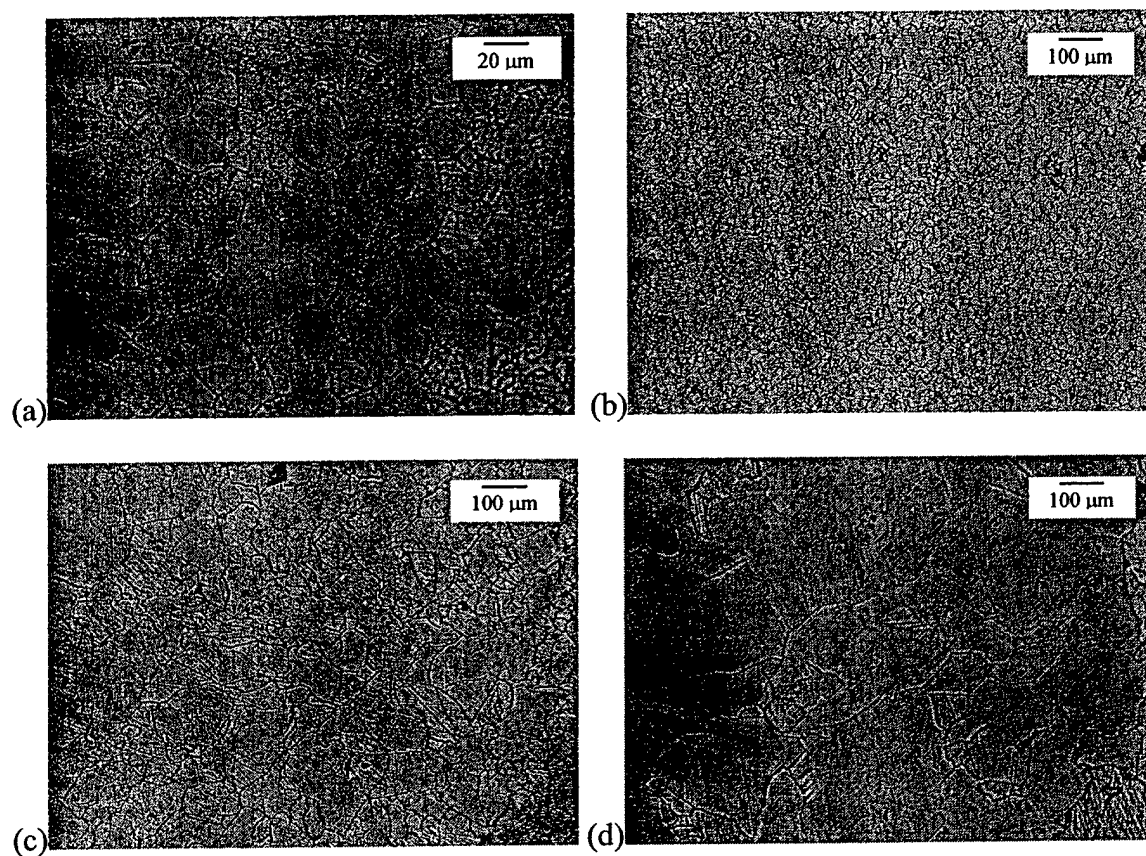


Figure 1.3: Optical micrographs of IF-5 steel, single phase ferrite, 2% nital etch.
(a) 10 μm grains. (b) 14 μm grains. (c) 36 μm grains. (d) 130 μm grains.

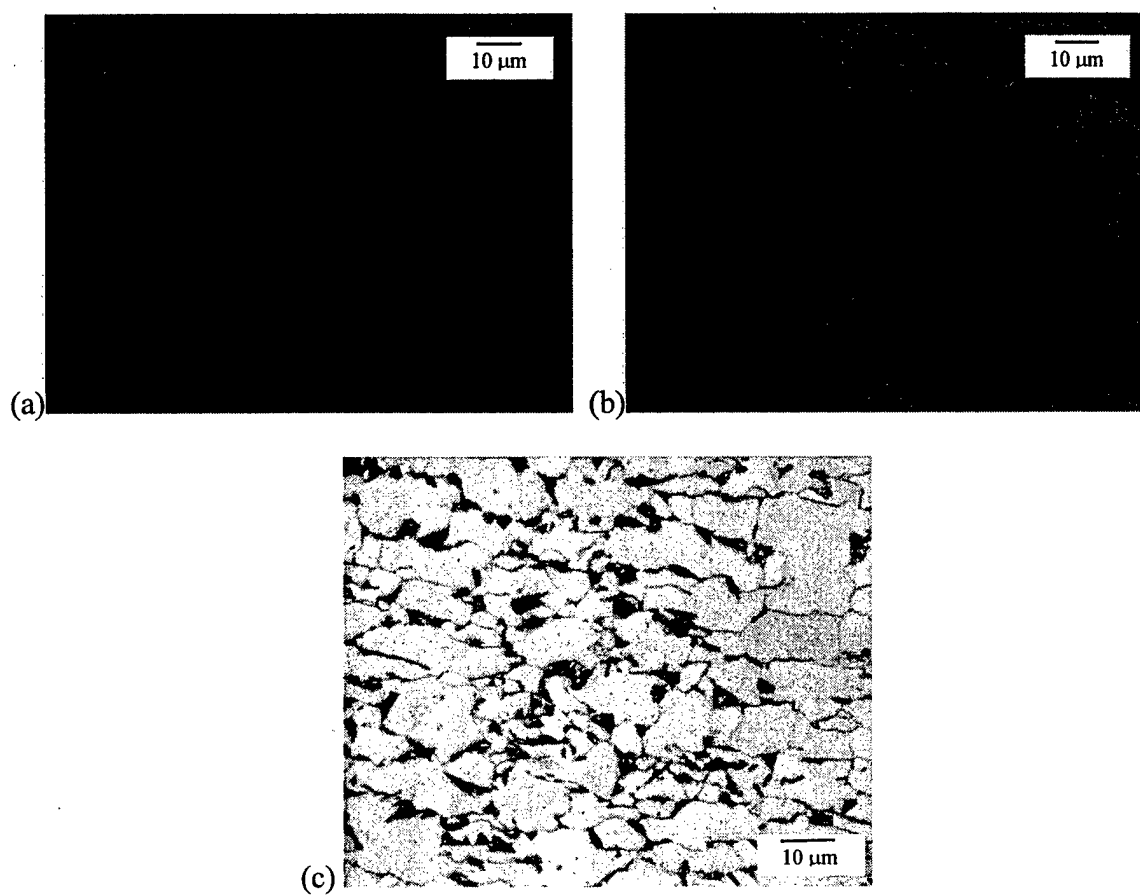


Figure 1.4: Optical micrographs of (a) ULC-C (single phase ferrite), (b) ULC-D (single phase ferrite) and (c) dual phase (light = ferrite, dark = martensite) steel. 2% nital etch.

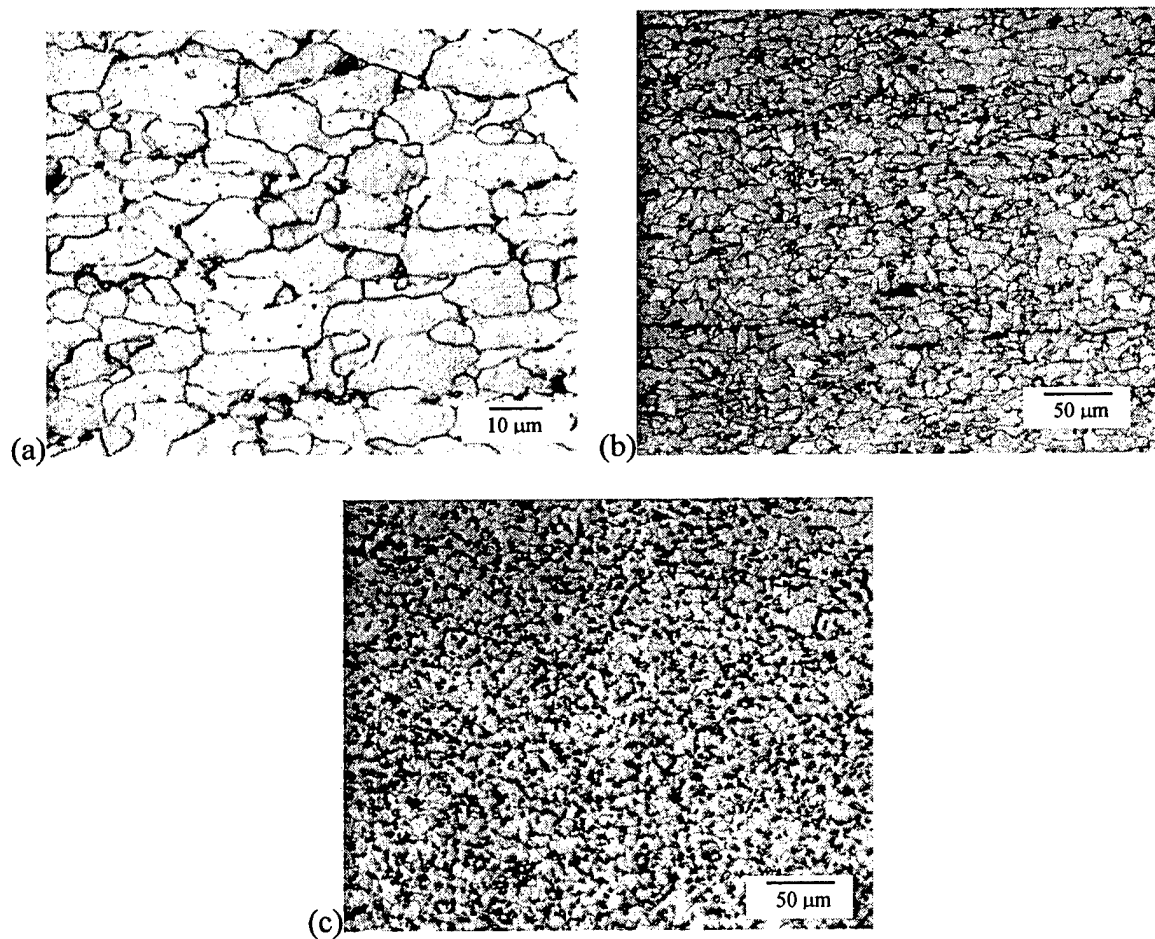


Figure 1.5: Optical micrographs of HSLA steels. Light colored phase is ferrite and dark colored phase in pearlite. (a) HSLA-1, 2% nital etch. (b) HSLA-2, sodium metabisulfite etch. (c) HSLA-3, sodium metabisulfite etch.

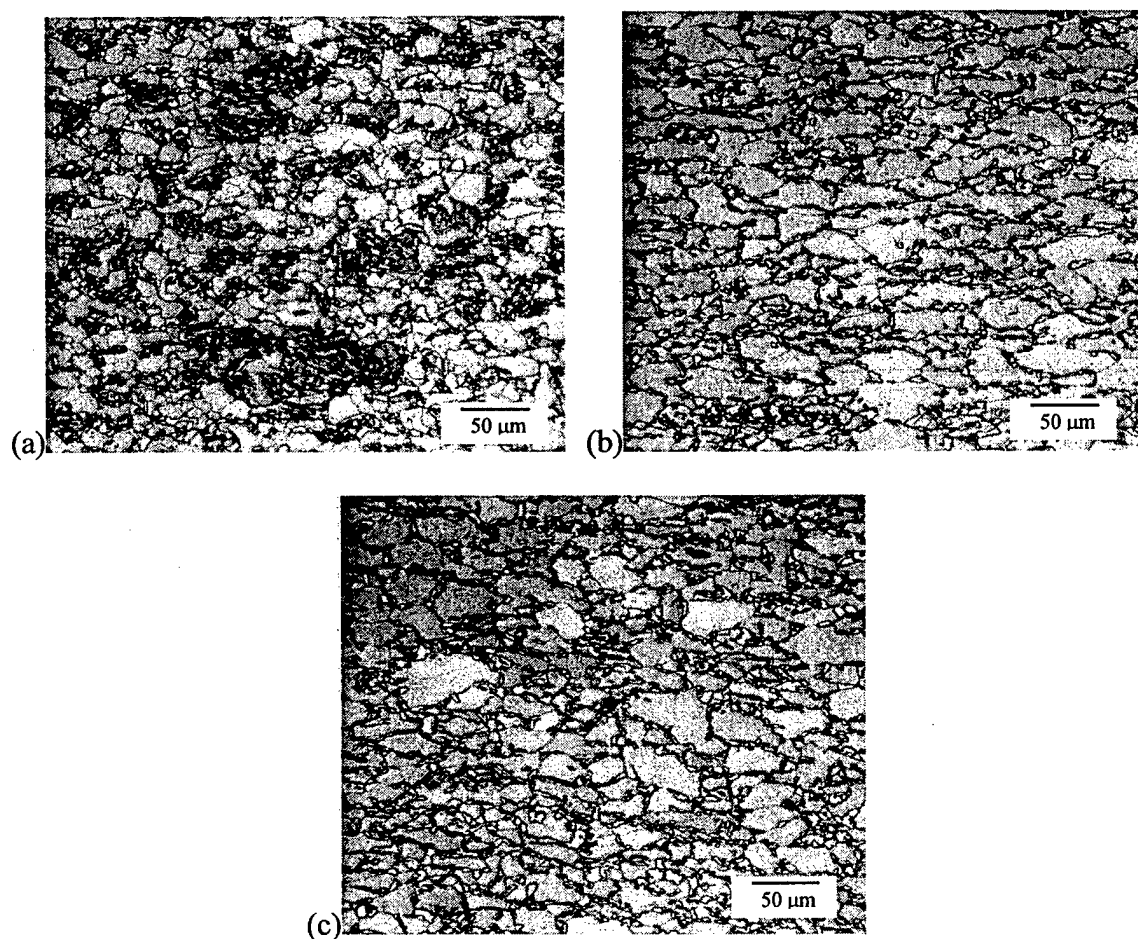


Figure 1.6: Optical micrographs of TRIP steels, sodium metabisulfite etch. White phase is retained austenite, gray phase is ferrite and dark colored phases are bainite and/or martensite. (a) TRIP-1. (b) TRIP-3: LS. (c) TRIP-3: HS.

Table 1.4: Materials used for each test conducted for this thesis.

Thesis Section	Test Conducted	Material(s) Used
4.1	Development of High-Rate Machine Techniques	HSLA-1, HSLA-3 and TRIP-1
4.3	Data Reduction Techniques	DP, IF-1 and TRIP-1
5.1.1	Screw-Driven & High-Rate Machine Comparison	ULC-D and HSLA-1
5.1.2	Tensile Sample Geometry Comparison	HSLA-1, HSLA-2, TRIP-1, ULC-C, IF-1, IF-2 and IF-3
5.1.3	Low-Strain Accuracy of Stress-Strain Curve	11000-H00 Cu, IF-1, HSLA-1 and ULC-D
5.1.4	Repeatability	HSLA-2
5.2.1	Stress-Strain Curve Shapes	HSLA-1, HSLA-2, DP and IF-1
5.2.2	Strain Rate Sensitivity	HSLA-2 and DP
5.2.3	High Rate Application Comparison	IF-1, IF-2, IF-3, DP, HSLA-1 and HSLA-2
6.1	Cold Work Strengthening	IF-2
6.2	Solid Solution Strengthening	IF-3, IF-4, HSLA-1 and HSLA-2
6.3	Grain Size Strengthening	IF-1 and IF-5
6.6	Multiphase Strengthening: TRIP	TRIP-3
6.7	Multiphase Strengthening: DP & TRIP	DP, TRIP-3 and HSLA-2
6.8	IF Steel Constitutive Modeling	IF-1, IF-2, IF-3 and IF-4
6.9	HSLA Steel Constitutive Modeling	HSLA-1 and HSLA-2

CHAPTER 2

BACKGROUND INFORMATION: DYNAMIC TENSILE TESTING

Many authors have attempted to classify behavior of materials as either “static” or “dynamic” with sub-classifications in each realm. An example of such divisions developed by M.A. Meyers is shown in Figure 2.1 [1 (p. 299)]. Meyers has established a strain rate of 5 s^{-1} as a dividing value below which inertial forces are negligible and above which there is an “increasing influence of inertial forces due to wave propagation effects.” Testing done for this thesis covers the range from “Quasi-Static” to “Dynamic-Low” as defined in Figure 2.1. This testing supports using the rate of 5 s^{-1} as a separation point and tests run below this rate will be designated “low-rate” while tests run above 5 s^{-1} will be designated as “high-rate.”

2.1 High-Rate Tensile Testing Apparatus and Procedures

Tensile testing is commonly used to provide mechanical property information for structural design. The capability to conduct tensile tests at strain rates up to 1 s^{-1} has long been available through the use of screw-driven and, more recently, hydraulic-loading machines. Very high strain rate ($> 500 \text{ s}^{-1}$) compression testing has existed for over 50 years through the use of split Hopkinson pressure bar (SHPB) techniques. A great deal of work has been done in recent decades to establish test methods for tensile testing at constant strain rates in the intermediate range between 1 and 500 s^{-1} .

In the 1930s and 1940s, many researchers investigated the influence of strain rate on the mechanical properties of metals using impact tests [2]. However, in the impact test, strain rate varies along the length of the sample as well as changes with time at particular points in the sample. In 1950, Clark and Duwez [2] designed a complicated machine to conduct high rate constant strain rate tensile tests by expansion of thin-walled cylinders. They achieved strain rates of 200 s^{-1} with their device while collecting load

information with an oscilloscope and were able to determine stress values as a function of time to an accuracy of $\pm 10\%$.

STRAIN RATE, s^{-1}	COMMON TESTING METHODS	DYNAMIC CONSIDERATIONS	
10^7	HIGH VELOCITY IMPACT	SHOCK-WAVE PROPAGATION	INERTIAL FORCES IMPORTANT
10^6	-Explosives		
10^5	-Normal plate impact		
10^4	-Pulsed laser		
10^3	-Exploding foil	SHEAR-WAVE PROPAGATION	INERTIAL FORCES IMPORTANT
10^2	-Ind. plate impact (pressure-shear)		
10^1	DYNAMIC-HIGH	PLASTIC-WAVE PROPAGATION	
10^0	-Taylor anvil tests		
10^{-1}	-Hopkinson Bar		INERTIAL FORCES NEGLIGIBLE
10^{-2}	-Expanding ring		
10^{-3}	DYNAMIC-LOW	MECHANICAL RESONANCE IN SPECIMEN AND MACHINE IS IMPORTANT	
10^{-4}	High-velocity hydraulic, or pneumatic machines; cam plastometer		
10^{-5}	QUASI-STATIC	TESTS WITH CONSTANT CROSS-HEAD VELOCITY STRESS THE SAME THROUGHOUT LENGTH OF SPECIMEN	INERTIAL FORCES NEGLIGIBLE
10^{-6}	Hydraulic, servo-hydraulic or screw-driven testing machines		
10^{-7}			
10^{-8}			
10^{-9}	CREEP AND STRESS-RELAXATION	VISCO-PLASTIC RESPONSE OF METALS	INERTIAL FORCES NEGLIGIBLE
10^{-10}	-Conventional testing machines		
10^{-11}	-Creep testers		
10^{-12}			

Figure 2.1: Schematic classification of testing techniques according to strain rate [1 (p. 299)].

In 1959, Hockett [3] described a cam plastometer designed to conduct compression testing at constant true strain rates up to 1 s^{-1} . His machine used an electric motor to drive a logarithmic cam via three transmissions and three flywheels. Samples were compressed at constant true strain rates as long as the cam speed remained constant. The transmissions allowed variation of the cam speed, and therefore the strain rate. Hockett's machine was also equipped with a heater unit to allow testing at elevated temperatures.

By the 1960s, hydraulic "rapid-loading" machines were available. Marsh and Campbell [4] attempted to run constant strain rate tests in compression on such a machine and achieved strain rates up to about 7 s^{-1} . They used an oscilloscope to collect load and deformation information, with the deformation measured by the deflection of steel cantilevers moved by the deforming sample.

In the late 1960's to early 1970's, equipment with hydraulic actuators became common for testing in tension, compression and torsion. These machines used closed loop control at low speeds and open loop control at high speeds, with strain rates up to 100 s^{-1} possible with small samples. Pneumatically driven open loop machines were also used [5].

In 1974, Saxena and Chatfield [6] reported their design of a slack adapter used with a "servo-controlled hydraulic universal tester" to allow the crosshead of the tester to achieve a desired velocity before loading their samples. They achieved strain rates up to 100 s^{-1} using 31.75 mm gage length flat tensile samples. Saxena and Chatfield used a piezoelectric load cell and an optical extensometer to collect load and strain data, respectively, concurrently on a dual beam oscilloscope. Photographs of the oscilloscope traces were used to record their results. Saxena and Chatfield reported problems with extensometer tracking, hydraulic ram vibration due to excessive dither, and yielding outside the extensometer target area. Interestingly, they didn't appear to have issues with load cell ringing (discussed in section 2.2.1) during their high rate tests. However, this may have been due to an overdamped condition in their test machine.

In recent years, most tensile testing for the strain rate range between 1 and 500 s⁻¹ has been conducted using specially designed large servo-hydraulic machines [7-22]. These machines typically operate in open loop control for high rate testing and use a slack adapter to allow the actuator to achieve the desired speed before loading the sample. Piezoelectric load measuring devices are often used, although other methods for load measurement have been used to improve load signal quality, including a titanium grip combined with a load cell [10], load cell in parallel with the sample [14], and strain gages directly mounted on samples [7, 21, 22]. High rate testing generally causes “ringing” in a piezoelectric load cell, which results in large amplitude fluctuations in the load data acquired. This ringing phenomenon is discussed in section 2.2.1. Methods for measurement of sample deformation vary, and include direct actuator displacement measurement with an LVDT, optical extensometry, or direct application of high-elongation strain gages. Many researchers have used a variety of curve-fitting routines to generate “clean” stress-strain curves, although these methods may not accurately reflect the true nature of high rate data, especially in the low strain elastic-to-plastic transition region of the flow curve. These methods include using a 3rd or 4th order polynomial fit [8], a cubic spline fit [10-12], Fourier transforms to eliminate natural frequencies [18, 19], a Voce equation fit [15], Voce equation combined with Fourier analysis [9, 16, 17], and a running average of the load data [22].

2.2 Problems Associated With Dynamic Tensile Testing on Servo-Hydraulic Machines

There are several issues to contend with when performing dynamic tensile testing on servo-hydraulic machines. These issues include load cell ringing, non-uniform loading through stress waves, adiabatic heating and data collection difficulties.

2.2.1 Load Cell Ringing

Piezoelectric load washers are commonly used to measure load during high-rate testing. Conventional strain gaged load cells are not used because of their high mass,

which seriously degrades the load signal quality at high rates due to load cell “ringing,” as discussed below. In a typical high-rate servo-hydraulic tensile test machine, the load measuring device is located between the machine crosshead and the upper grip which holds the test sample. As shown in Figure 2.2, an actuator accelerates downward with a slack adapter. The slack adapter allows the actuator to achieve a desired velocity before loading the test sample. When the slack adapter is fully extended, it pulls on the lower grip which transfers the load to the sample, the upper grip, through the load washer and to the machine crosshead. When the slack adapter engages the grip, an impulse load travels through the load train and causes the load washer to resonate at a specific natural frequency, which can be seen as oscillations in the load versus time data collected. These oscillations are commonly called “ringing” and an example is shown in Figure 2.3.

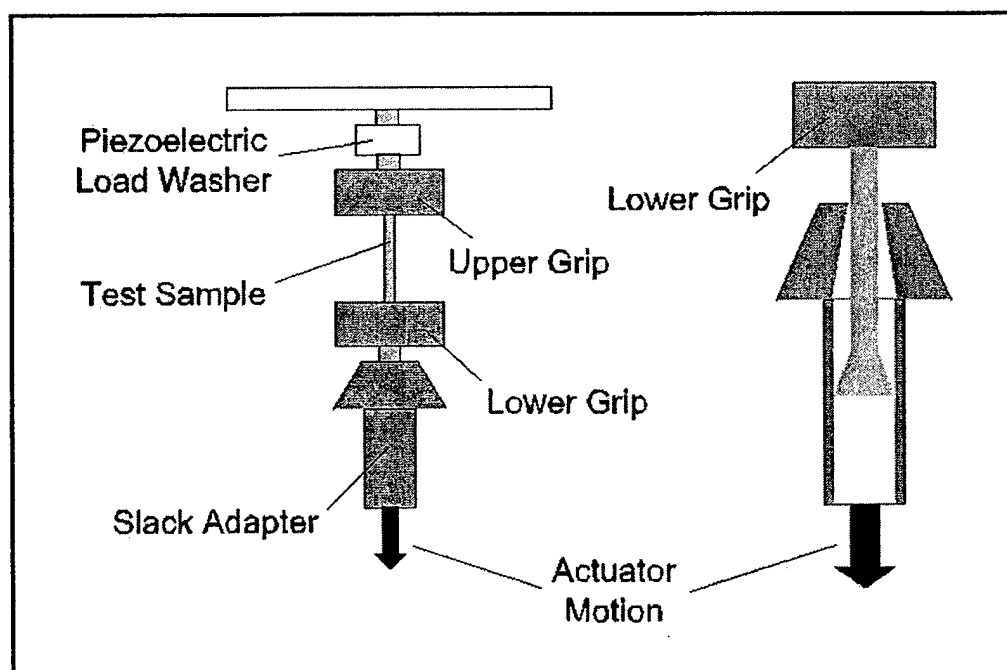


Figure 2.2: Schematic drawing of high-rate servo-hydraulic tensile test machine.

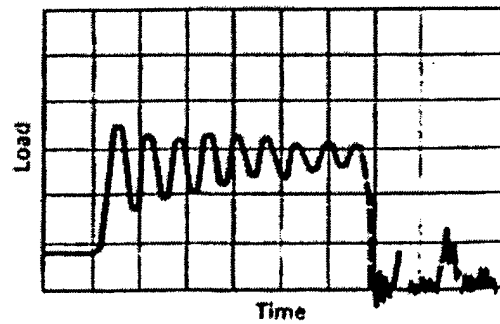


Figure 2.3: Oscilloscope record of load cell force versus time during a dynamic tension test depicting the phenomenon of ringing [23].

The ringing of the load washer can be described by equations of motion due to free damped vibration of a linear system. Free vibration means that the vibration is caused by a single input and not forced to oscillate by a recurring input. Damped vibration means that the oscillation amplitude decreases with time. A high-rate tensile test essentially imparts an impulse excitation to the load train when the slack adapter engages. To understand the equations of motion, it is easiest to start with the basic equations of motion for a free undamped spring-mass system which moves only in the vertical direction as shown in Figure 2.4.

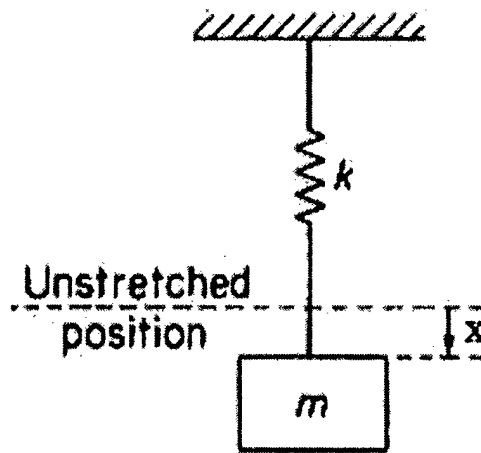


Figure 2.4: Spring and mass vibration system [24 (p. 17)].

The system shown in Figure 2.4 has one degree of freedom (DOF) because its motion can be described by a single coordinate, x [24 (p. 16)]. When the mass is displaced and released, the mass will be acted upon by the restoring force of the spring, kx (where k = spring constant). Summing the forces in the system yields Equation 2.1.

$$\sum F = ma = -kx \quad [2.1]$$

Since acceleration is in the x direction, $a = \frac{d^2x}{dt^2} = \ddot{x}$ which leads to Equation 2.2.

$$m \ddot{x} = -kx \quad [2.2]$$

The solution to Equation 2.2 is Equation 2.3.

$$x(t) = C_1 \sin(\omega_n t) + C_2 \cos(\omega_n t), \quad \omega_n = \sqrt{\frac{k}{m}} \quad [2.3]$$

C_1 and C_2 can be evaluated knowing the initial conditions of the system, $x(0)$ and $\dot{x}(0)$.

For $x(0) = x$ and $\dot{x}(0) = 0$, the solution is Equation 2.4:

$$x(t) = x(0) \cos(\omega_n t) + \frac{\dot{x}(0)}{\omega_n} \sin(\omega_n t) \quad [2.4]$$

ω_n is known as the angular natural frequency of vibration of the system. The linear natural frequency, f_n , can be calculated by Equation 2.5.

$$f_n = \frac{\omega_n}{2\pi} = \frac{1}{2\pi} \sqrt{\frac{k}{m}} \quad [2.5]$$

Now, suppose the system is not made up of a separate mass and spring, but instead a single bar with mass, m , elastic modulus, E , length, L , and cross-sectional area, A , as shown in Figure 2.5.

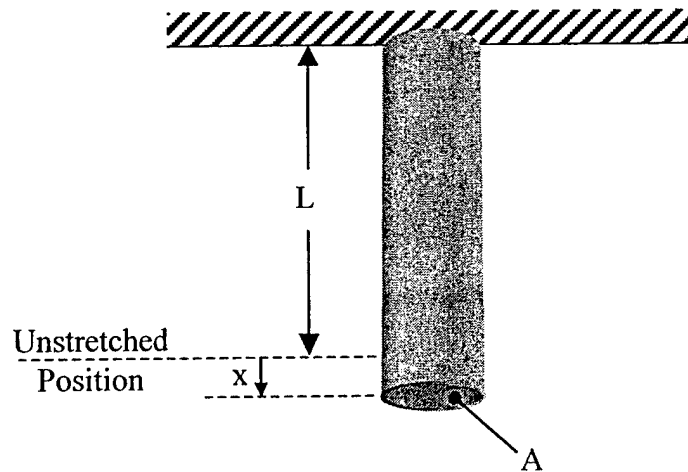


Figure 2.5: Single bar vibration system.

If the bar is displaced a small amount x within the elastic region, the restoring force, F , can be determined using the one-dimensional Hooke's Law, $\sigma = E\varepsilon$, as shown in Equation 2.6, where σ = stress = F/A and ε = strain = x/L .

$$\sigma = E\varepsilon \Rightarrow \frac{F}{A} = E \frac{x}{L} \Rightarrow F = \frac{EA}{L} x \quad [2.6]$$

Equations 2.1 through 2.5 could all be written again substituting EA/L for k . Therefore, the natural frequency of a bar displaced longitudinally will vibrate with a natural frequency, f_n shown in Equation 2.7:

$$f_n = \frac{1}{2\pi} \sqrt{\frac{EA}{Lm}} \quad [2.7]$$

Now, assume the system is initially disturbed by an impulse function, \hat{F} . An impulse acting on a mass results in a sudden change in its velocity with negligible change in displacement [24 (p. 90)]. Therefore, Equation 2.4 simplifies to Equation 2.8:

$$x(t) = \frac{\dot{x}(0)}{\omega_n} \sin(\omega_n t) \text{ where } \dot{x}(0) = \frac{\hat{F}}{m} \quad [2.8]$$

All of the above equations were derived for undamped free vibrations in a single degree of freedom system. For the high-rate system load train, the vibrations are “underdamped” which means that the system still vibrates (for a critically damped or overdamped system, the motion decays to zero after the first disturbance), but each oscillation has a lower amplitude than the previous one. Damping reduces the magnitude

of the natural frequency [24 (p. 30)] according to Equation 2.9 where ω_d = damped natural frequency, and ξ = damping ratio.

$$\omega_d = \omega_n \sqrt{1 - \xi^2} \quad [2.9]$$

Equations 2.1 through 2.9 show that the frequency and amplitude of oscillations in load data are dependent upon a number of variables, including the mass between the test sample and load measuring device. For the best quality load data, it is desired for the oscillation amplitude to be as low as possible and frequency to be as high as possible. This can be accomplished by minimizing the mass between sample and load washer since ringing frequency is inversely proportional to mass, while the amplitude is directly proportional to the mass.

The ringing amplitude is also directly dependent upon the acceleration of the mass in the load train. Therefore, reducing the actuator velocity will decrease the amplitude, since actuator velocity directly affects the impulse generated as the slack adapter engages, and therefore the resulting accelerations in the load train.

2.2.2 Elastic and Plastic Stress Waves

Elastic stress waves travel through solid materials that are dynamically loaded. If the material experiences permanent deformation, plastic stress waves are also generated. The general equation of motion for a disturbance that remains unchanged and propagates through a medium at a velocity V is shown in Equation 2.10 [1 (p.15-16)], where u is the displacement, t is time, and x is the direction in which the disturbance is traveling.

$$\frac{\partial^2 u}{\partial t^2} = V^2 \frac{\partial^2 u}{\partial x^2} \quad [2.10]$$

For an elastic wave propagating longitudinally through a cylindrical bar (and neglecting transverse strains) the wave velocity, V_e , is represented by Equation 2.11, where E is the elastic modulus and ρ is the density.

$$V_e = \sqrt{\frac{E}{\rho}} \quad [2.11]$$

For steel, the longitudinal elastic wave velocity is about 5200 m/s. Once a material deforms into the plastic region, plastic waves propagate at a theoretical velocity, V_p , as shown in Equation 2.12, where $d\sigma/d\varepsilon$ is the slope of the true stress-strain curve.

Therefore, plastic wave velocity varies greatly depending on the work-hardening rate of a particular sample.

$$V_p = \sqrt{\frac{d\sigma/d\varepsilon}{\rho}} \quad [2.12]$$

As with all waves, stress waves traveling through a tensile sample will interact with boundaries by reflection and transmission [25 (p. 29-36), 26 (p. 24-38)]. For a valid tensile test, the sample must be in a state of uniform stress [27]. Davies and Hunter [28] have estimated that three reverberations of stress waves are required for stress equilibrium in compression testing [29]. The number of longitudinal stress wave oscillations can be calculated knowing the test duration, sample length, and stress wave velocity using Equations 2.13 and 2.14, where t is the test duration, t_1 is the wave transit time, L is the sample length, and V is the wave velocity.

$$\# \text{ oscillations} = \frac{t}{t_1} \quad [2.13]$$

$$t_1 = \frac{L}{V} \quad [2.14]$$

If a minimum of three oscillations is required for uniform stress, one can expect valid elastic data after 3 oscillations of elastic waves, and valid plastic region data after 3 oscillations of plastic waves. For steel, it will take approximately 15 μs for 3 elastic wave reverberations in a 25.4 mm gage length sample. For the plastic region, the time required is more difficult to estimate. However, if it is assumed that the initial work-hardening rate is 1% of the elastic modulus [29], then $V_p = 0.10 V_e$ and uniform stress in the plastic region would be achieved after 150 μs . Based on the assumptions above, for a 25.4 mm gage length sample tested at a strain rate of 100s^{-1} , one could expect valid elastic data at 0.0015 strain and valid plastic data at 0.015 strain. As strain rate increases, gage length must decrease to continue to achieve valid stress-strain data.

2.2.3 Adiabatic Heating

During a tensile test, some of the energy of deformation is stored in the material via changes in microstructure, while the rest is converted to heat. The fraction of plastic work converted to heat is designated by β and its generally accepted value is about 0.9 [1 (p. 377), 30 (p. 303)], although recent measurements have indicated that β may be a function of plastic strain and/or imposed strain rate for some materials [31].

The heat generated by plastic deformation must be dissipated to the surrounding environment, and the rate at which that occurs depends on a number of factors, including the thermal diffusivity, α , of the material being tested and the nature of the surrounding environment. The thermal diffusivity is calculated for a specific material from the thermal conductivity, k , density, ρ , and specific heat, c_p , according to Equation 2.15 [32 (p. 51)]. The distance that heat can “travel” during a certain time, t , is called the thermal

diffusion distance, d_t , and is calculated by Equation 2.16 [1 (p. 375)]. The diffusion distance governs whether or not the heat generated can travel far enough through the material being deformed to arrive at the sample's outer surface, where it can be dissipated to the environment. A large diffusion distance (relative to sample dimensions) is expected to produce an isothermal tensile test, which means there is no significant temperature rise during the test, while a short diffusion distance results in adiabatic (no heat dissipated) heating of the sample. When adiabatic heating occurs, the temperature rise in the sample can be calculated by Equation 2.17, where ϵ is true strain and σ is flow stress [1 (p. 377)].

$$\alpha = \frac{k}{\rho c_p} \quad [2.15]$$

$$d_t = 2\sqrt{\alpha t} \quad [2.16]$$

$$\Delta T = \frac{\beta}{\rho c_p} \int_0^{\epsilon} \sigma d\epsilon \quad [2.17]$$

Since the thermal diffusion distance decreases with decreasing time, and increasing strain rate causes decreasing test duration, the likelihood of adiabatic heating occurring increases with increasing strain rate. The strain rate at which adiabatic heating occurs will decrease with increasing test sample dimensions.

For pure iron at 300K, α is 23.1 mm²/s, while for an AISI 1010 steel, the value is 18.8 mm²/s and the values for other steel compositions decrease with increasing alloying [32 (p. A4)]. α values also decrease with increasing temperature due to changes in k and c_p with temperature. For a tensile test at a strain rate of 10⁻³ s⁻¹, with a total elongation of 0.30 strain, the test duration would be 300 seconds, and for a strain rate of 10³ s⁻¹ with the

same elongation, the test duration would be 0.0003 seconds. For AISI 1010 steel, the thermal diffusion distance for the low-rate test would be 150 mm, and for the high-rate test would be 0.15 mm. For these extremes, it is expected that the low-rate test would be isothermal and the high-rate test would be adiabatic when testing sheet steels.

In a recent study of adiabatic heating in stainless steels, K. Clarke determined that tensile samples with thickness of 1.168 mm achieved adiabatic conditions at strain rates above about 1.0 s^{-1} , while for sample thickness of 1.651 mm, adiabatic conditions occurred at strain rates above 0.1 s^{-1} [22]. For stainless steels, room temperature values of α are on the order of $3.5 \text{ mm}^2/\text{s}$ [32 (p. A5)]. Using this value of α , and an average total elongation of 0.20 strain for the stainless steels tested by Clarke, the thermal diffusion distance for a strain rate of 1.0 s^{-1} is 1.67 mm (about 1.4 times the sample thickness), and for a strain rate of 0.1 s^{-1} , the thermal diffusion distance is 5.29 mm, which is about 3 times the sample thickness. Based on these results, perhaps a simple estimate of the strain rate at which adiabatic heating will occur for sheet steels pulled in tension can be made by relating the sheet thickness to thermal diffusion distance. The sheet thickness would be multiplied by a constant (on the order of 2) and, using that value for the diffusion distance, the test duration calculated using Equation 2.16 and then the strain rate determined based upon the expected total elongation. For example, using α equal to $18.8 \text{ mm}^2/\text{s}$, total strain to failure of 0.30 and thermal diffusion distance of two times the sheet thickness, steel samples with sheet thickness of 1.5 mm would experience adiabatic heating at strain rates above 2.5 s^{-1} .

For strain rates at which adiabatic heating is anticipated, Equation 2.17 can be used to calculate the expected temperature rise as a function of strain. As the temperature rises, thermal effects on mechanical behavior is expected.

2.2.4 Data Collection Issues

Tensile tests run at high strain rates have very short test durations, which can be estimated using Equation 2.18.

$$t = \epsilon_f / \dot{\epsilon} \quad [2.18]$$

where t = time, ϵ_f = strain to failure, and $\dot{\epsilon}$ = strain rate of the test. For a sample with 30% strain to failure and a strain rate of 300 s^{-1} , the expected test duration is 1 ms. Such short test durations require very high rate data acquisition capability. In addition, load and strain signal recording will not appear coincident in time due to the finite speed of stress waves.

2.2.4.1 High Rate Data Acquisition

An objective of high rate tensile testing is to create stress-strain curves for the materials tested. In order to capture the important details of the stress-strain curve, a sufficient number of data points is required. If 500 data points are desired, and the test duration is 1 ms (strain rate of 300 s^{-1} with 30% total elongation), then one data point must be collected every 20 μs , which is a data sampling rate of 50 kHz. Higher strain rates require faster sampling rates. To achieve these rates requires adequate response times for the load and strain measurement devices, as well as the electronic conditioning and signal processing and recording devices.

Piezoelectric load cells are commonly used for high rate load information because of their low response times compared to conventional load cells. Unfortunately, they are subject to ringing as discussed in section 2.2.1, but the ringing effects can be reduced by appropriate placement in the load train, and reduction of mass in the load train. Load can also be measured directly from the grip section of each test sample through the use of an electrical resistance strain gage [7, 21, 33]. This method produces better load results, but is quite time consuming for sample preparation and data reduction.

A variety of methods can be used for gathering sample deformation information. Use of conventional contact extensometers is not feasible due to inertia effects. The simplest method is to merely record actuator motion and convert to strain based on the

sample gage length. This method is not particularly accurate, since the test frame is not perfectly rigid. Use of actuator displacement also assumes a constant strain rate throughout the test, which is not possible due to inertial effects during initial loading. Another method is optical extensometry, which requires very careful alignment and sample preparation. A direct and reliable method [29] for strain measurement is the use of a high elongation electrical resistance strain gage directly adhered to each sample gage section. This method was employed in the present study.

2.2.4.2 Time Delays Due to Stress Wave Velocities

At high strain rates, loading of the sample takes place by stress waves that originate at the point where the slack adapter engages and are transmitted through the lower grip into the sample. These stress waves continue through the load train and eventually arrive at the load washer. During high-rate tests, there is a noticeable time difference between the time that the initial stress wave loads the sample and the time it arrives at the load washer. Therefore, for high-rate tests, load data must be shifted in time to coincide with the strain data, which requires estimation or measurement of the time delay.

CHAPTER 3

BACKGROUND INFORMATION: STRENGTHENING MECHANISMS

High strength steels are designed for a range of applications and employ a combination of strengthening mechanisms, which may include cold work, grain size, dispersion, solid solution strengthening, bake hardening and multiphase strengthening. Strengthening mechanisms typically raise the flow stress of a material by providing obstacles to dislocation motion. Cold work employs other dislocations as obstacles, dispersion strengthening uses second phase particles, grain boundaries provide grain size strengthening, and solute atoms supply solid solution strengthening.

The effects of various strengthening mechanisms are well known for quasi-static loading conditions. Some work has been done to establish the effects of strain rate and temperature on strengthening mechanisms. W. Leslie [34 (p. 27)] made the statement, “All strengthening mechanisms reduce both the strain-rate dependence and temperature dependence of the yield stress.” without giving an explanation for the reason. However, there is some conflicting evidence, both theoretical and empirical, to question the generality of this statement for some strengthening mechanisms, including grain size [35-37], second phase [35], and cold work [38].

3.1 Fundamentals of Strengthening in BCC Metals

The flow stress of a material is determined by its resistance to dislocation motion. In all materials, the most fundamental obstacle to dislocation motion is the Peierls-Nabarro frictional stress, which is the theoretical shear stress required to move a dislocation through a crystal lattice, by temporary distortion of that lattice. The frictional stress calculated by Peierls and Nabarro is given by Equation 3.1 [39 (p. 90)], where τ_f is the frictional stress, G is the shear modulus, ν is Poisson’s ratio, a is the separation distance between slip planes, and b is the slip distance (Burger’s vector).

$$\tau_f = G \exp \left[\frac{-2\pi a}{(1-\nu)b} \right] \quad [3.1]$$

In Equation 3.1, the frictional stress is minimized when the distance between slip planes is large and the Burger's vector is small, which is the reason slip occurs most readily in close-packed directions on close-packed planes. For BCC metals, such as iron, the slip direction is the close-packed direction $\langle 111 \rangle$, while the most common slip plane is $\{110\}$. In iron single crystals, different planes containing a $\langle 111 \rangle$ direction can act as a slip plane [34 (p. 3), 40 (p. 145-6)]. Equation 3.1 can also be written in terms of the dislocation width, w , as shown in Equation 3.2 [39 (p. 91)]. As dislocation width decreases, the Peierls-Nabarro stress increases. The temperature dependence of the Peierls-Nabarro stress relates to the temperature sensitivity of the dislocation width. Dislocation width in BCC iron is strongly temperature-dependent, with increasing temperature causing increasing dislocation width. Therefore, the friction stress of BCC iron is also a strong function of temperature [39 (p. 93), 41 (p.161)].

$$\tau_f = G \exp \left[\frac{-2\pi w}{b} \right] \quad [3.2]$$

In addition to overcoming the Peierls-Nabarro stress, dislocations in a lattice must also surmount other obstacles to create plastic flow. These obstacles can be characterized as either "short-range" or "long-range" depending on how much an increase in temperature helps to overcome them. Short-range obstacles are greatly influenced by changes in temperature, while long-range obstacles are not. In general, increasing strain rate may be considered analogous to decreasing temperature, and thus strain rate should also have a significant impact on ability to overcome short-range obstacles and a less significant effect on long-range obstacles.

3.2 Influence of Strain Rate and Temperature on BCC Iron

In BCC metals, at “low” temperatures the primary short-range obstacle to dislocation motion is the Peierls-Nabarro stress [41 (p.243)]. Therefore, the temperature and strain rate sensitivities of the flow stress in BCC iron are quite high as shown in Figures 3.1 through 3.3. In Figure 3.1, the temperature dependence of flow stress for iron is slight at high (above about 375K) temperatures, but increases at lower temperatures. Between 250K and 375K the temperature dependence increases, with the temperature dependence becoming quite pronounced below 250K. With room temperature approximately 300K, and increasing strain rate considered analogous to decreasing temperature, one expects an increasingly strong strain rate dependence of flow stress with increasing strain rate, which is illustrated in Figure 3.3.

In Figure 3.3, flow stress is shown as a function of strain rate for a variety of temperatures and three distinct regions of behavior are indicated. In region I (low strain rates and high temperatures), the flow stress shows little strain rate or temperature dependence. In this region, flow is controlled by long-range (athermal) obstacles. In region II, the rate and temperature dependence of flow stress increases considerably, and flow is now controlled by short-range obstacles that can be overcome with thermal assistance. At very high strain rates in region IV, strain rate dependence continues to increase, and may be due to the addition of another mechanism opposing dislocation motion, such as dislocation drag, where dislocation velocity is controlled by dissipation of energy through interactions with thermal vibrations and electrons as it moves through the lattice [42].

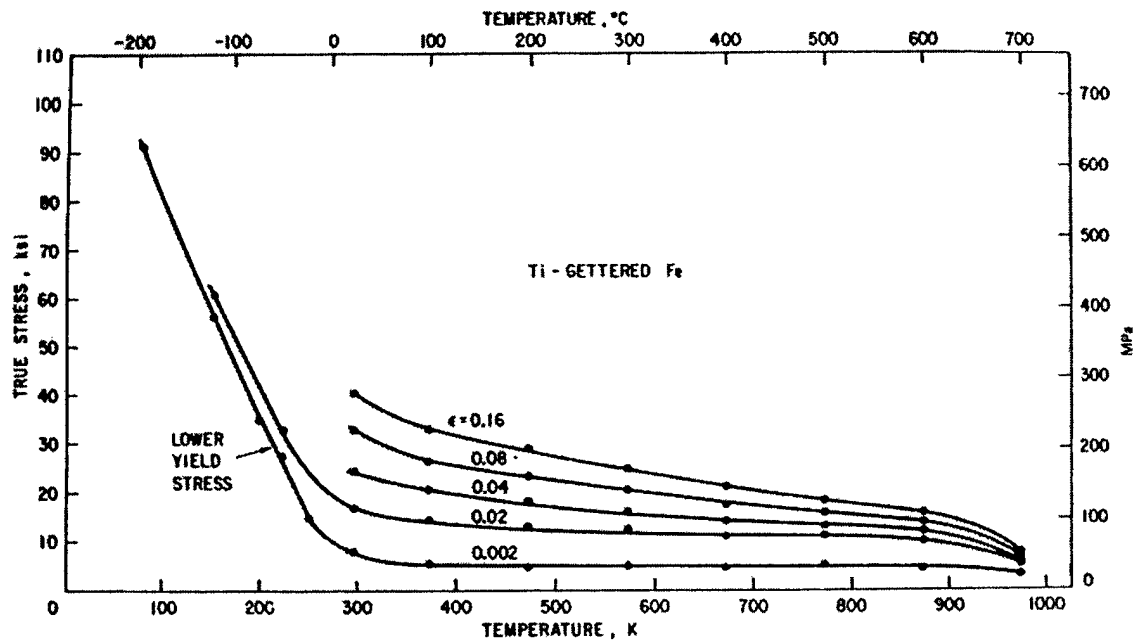


Figure 3.1: Temperature dependence of yield and flow stresses in Fe-0.15%Ti tested at strain rate of $2.5 \times 10^{-4} \text{ s}^{-1}$ [34 (p. 23)].

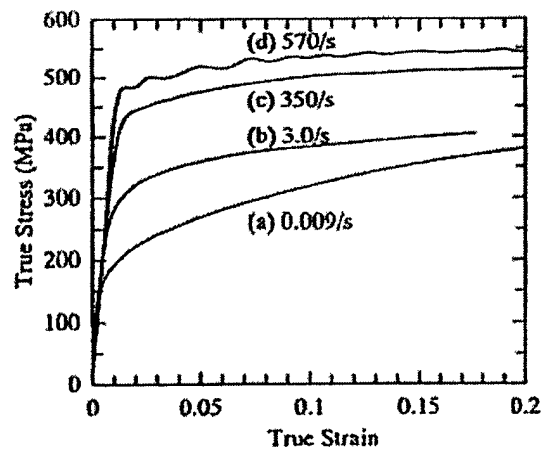


Figure 3.2: True stress-strain curves at four different strain rates for an interstitial free steel tested in compression at room temperature [43].

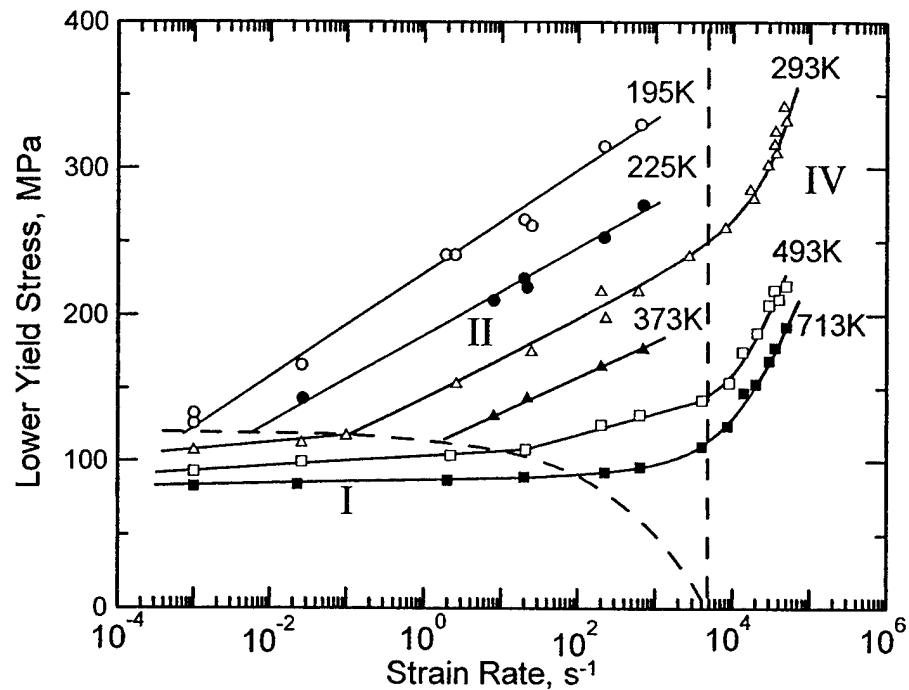


Figure 3.3: Variation of lower yield stress of mild steel with strain rate at different constant temperatures [replotted from 42].

For this thesis, all tests were conducted at room temperature and at strain rates ranging from 10^{-3} to 10^3 s^{-1} , which includes regions I and II in Figure 3.3. Over this strain rate range, the deformation mechanisms in BCC iron are expected to remain constant, with no deformation by twinning or formation of shear bands. This assumption has been verified by TEM analysis for room temperature high-rate ($2.5 \times 10^3 \text{ s}^{-1}$) compression testing of interstitial free steel by Milititsky [38].

In BCC iron, the primary slip planes are $\{110\}$ and $\{112\}$ at temperatures between 143K and 573K [44], with slip by movement of screw dislocations controlled by nucleation and migration of double kink pairs [45, 46]. Below 250K, the predominant slip planes are $\{110\}$ [47], while the $\{112\}$ planes become active above 250K [48]. This change of active slip plane is consistent with the increasing temperature dependence of

flow stress below 250K as seen in Figure 3.1 and the increasing rate sensitivity of flow stress in region II of Figure 3.3.

3.3 Work Hardening

The flow stress curves of metals exhibit work hardening, which is the increase in flow stress with increasing plastic strain. Work hardening is caused by the fact that dislocations are multiplied with increasing plastic strain and these dislocations interact with each other. There are a variety of sources for new dislocations, such as Frank-Read sources and grain boundaries [30 (p. 176), 40 (p. 124-128)]. Equation 3.3 has been observed to relate flow stress to dislocation density for a wide range of metals [39 (p. 179), 40 (p. 159), 41 (p. 308)]. In Equation 3.3, τ is the flow stress, τ_o is the stress required to move a single dislocation in the absence of other dislocations, a is a constant, G is the shear modulus, b is the Burger's vector, and ρ is the dislocation density. For BCC materials, a is on the order of 0.4 [39 (p. 179)].

$$\tau = \tau_o + aGb\sqrt{\rho} \quad [3.3]$$

In BCC materials, dislocation interactions are considered long-range obstacles to dislocation motion because temperature change doesn't significantly affect the stress required to overcome them. This is true because BCC materials have a large number of intersecting slip planes that allow relatively easy cross-slip of dislocations at all temperatures. Therefore, the intrinsic work hardening rate in BCC materials is not a strong function of temperature or strain rate. However, with increasing strain rate, experimental results generally show a decrease in work hardening rate in iron and steel. This may be due to adiabatic heating.

In FCC materials such as copper, dislocation interactions are short-range obstacles because increasing temperature greatly aids cross-slip in materials with low

stacking fault energy, and also assists the formation of jogs to cut across forest dislocations [49 (p. 133, 141)]. Therefore, FCC materials generally show strong temperature dependence of work hardening rate.

There are several theories to explain the occurrence of work hardening, which are complicated by the fact that plastic strain is not a state function, but a path-dependent function [41 (p. 310)]. Amount of plastic strain cannot be determined simply by examining the microstructure. Three of the well-known theories to explain work hardening were developed by Taylor, Seeger and Kuhlmann-Wilsdorf.

The Taylor theory was proposed in 1934 and based upon a parabolic stress-strain curve [40 (p. 160), 41 (p. 310)]. In his model, he assumed a uniform distribution of parallel edge dislocations moving on parallel slip planes. With a uniform dislocation distribution, the average distance between dislocations, L , is equal to $\rho^{-1/2}$ where ρ is the dislocation density. The stress field around an edge dislocation can be shown to be inversely proportional to the distance, r , from the dislocation core, according to Equation 3.4, where τ is the shear stress, G is the shear modulus, and b is the Burger's vector.

$$\tau \approx \frac{Gb}{r} \quad [3.4]$$

As one edge dislocation moves towards another, their stress fields interact and this interaction must be overcome for the first dislocation to move past the second. Assuming that all stress fields add to zero except that due to the nearest dislocation, and if the average distance between the dislocations is L , r in Equation 3.4 can be replaced by L . Since L is equal to $\rho^{-1/2}$, Equation 3.4 can be rewritten as Equation 3.5, where a is a constant.

$$\tau = a G b \rho^{1/2} \quad [3.5]$$

Adding the friction stress term, τ_o (the stress to move the dislocation in the absence of other dislocations), gives Equation 3.3 once again. Problems with the Taylor theory include the fact that dislocations are not uniformly distributed in real materials and screw dislocations and cross-slip are not considered.

In 1957, Seeger proposed mechanisms for each of the three stages observed in single-crystal flow curves [40 (p. 160), 41 (p. 311), 49 (p. 133)]. The third stage of the single-crystal flow curve is applicable to polycrystalline materials. Seeger assumed that the flow stress is composed of two components, τ_G and τ_S , where the τ_G term is temperature independent due to the interactions of parallel dislocations, and the τ_S term is a strong function of temperature due to interactions of dislocations cutting through forest dislocations, forming jogs which interfere with further dislocation movement.

In 1985, Kuhlmann-Wilsdorf presented qualitative explanations for the three work hardening stages in single crystals based upon formation of dislocation cells and their progression to subgrain boundaries [41 (p.312)].

3.4 Influence of Strain Rate and Temperature on Work Hardened BCC Metals

An increase in yield strength is expected as cold work (work hardening) increases [30, (p. 231)], simply based upon the shape of the flow curve for a fully annealed material. Figure 3.4 shows a family of predicted stress-strain curves based on a single flow curve for a fully annealed material.

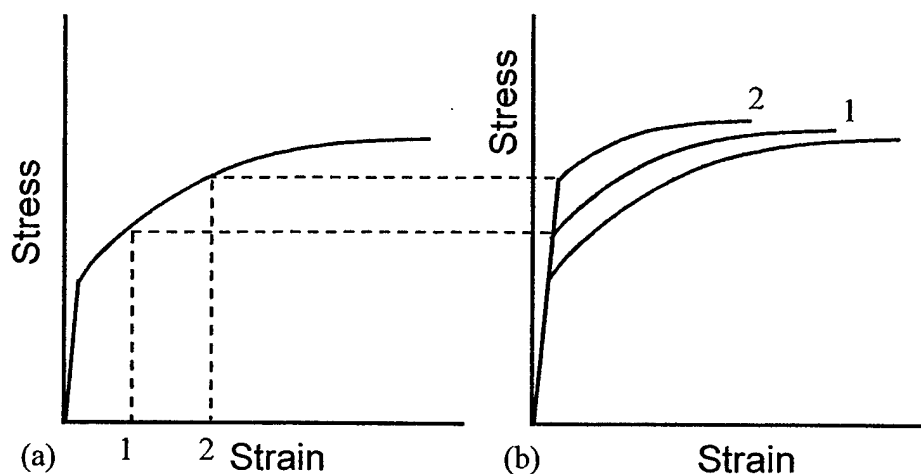


Figure 3.4: (a) Schematic stress-strain curve for a fully annealed material. (b) Predicted stress-strain curves for the same material as in (a) but cold-worked to the strain levels "1" and "2" as shown in (a).

In 1955, Cottrell and Stokes [50] presented a procedure (now known as a "temperature jump test") designed to measure the thermal component of stress at constant dislocation structure. Their procedure involved establishing a known amount of deformation at one temperature, then cooling to a lower temperature and resuming the deformation, and measuring the flow stress increment between the two tests. A similar method was introduced by Basinski and Christian [51] in 1960 which used changes in strain rate (strain rate jump test) instead of changes in temperature. Both methods have established for BCC metals that "the stress increments corresponding to a fixed change of temperature or strain rate generally do not vary systematically with the strain. This implies that, in contrast to the behavior of FCC metals, the 'obstacles' which are being overcome by thermal activation do not increase in density during straining." [50]. Christian believes that the strong temperature and strain rate dependence of the flow stress of BCC metals is an intrinsic property of the BCC structure and probably due to the Peierl's-Nabarro stress and resistance caused by "dispersed impurities."

Several studies [38, 52-54] have confirmed that the flow stress increment for BCC metals with variations in temperature or strain rate is independent of strain or in other words, independent of the dislocation density or amount of cold work. Figure 3.5 shows yield strength as a function of temperature for six different pre-strain levels. For these tests, each sample was pre-strained at room temperature and then tested to failure at a different temperature [54]. The temperature sensitivity at each pre-strain level is approximately the same, as shown by the lines drawn on the figure. Figure 3.6 shows flow stress at 0.02 true strain plotted as a function of strain rate (logarithmic scale) for five different pre-strain amounts. For these tests, each sample was pre-strained in compression at a quasi-static strain rate and then compression tested at a higher strain rate [38]. The strain rate sensitivities for each pre-strain level are shown by the dashed lines and are about the same for each pre-strain level. The increase in strain rate sensitivity at high rates is typical for mild steels.

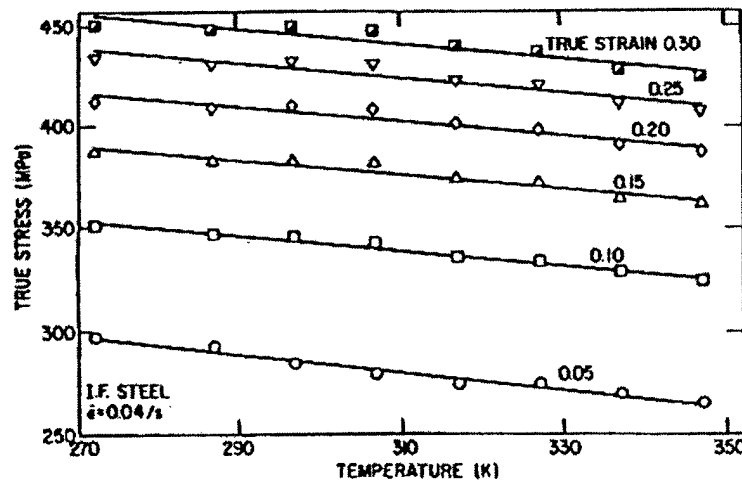


Figure 3.5: True stress at yield versus temperature for an IF steel pre-strained to six different levels at room temperature. All tests conducted at a strain rate of 0.04 s^{-1} [54].

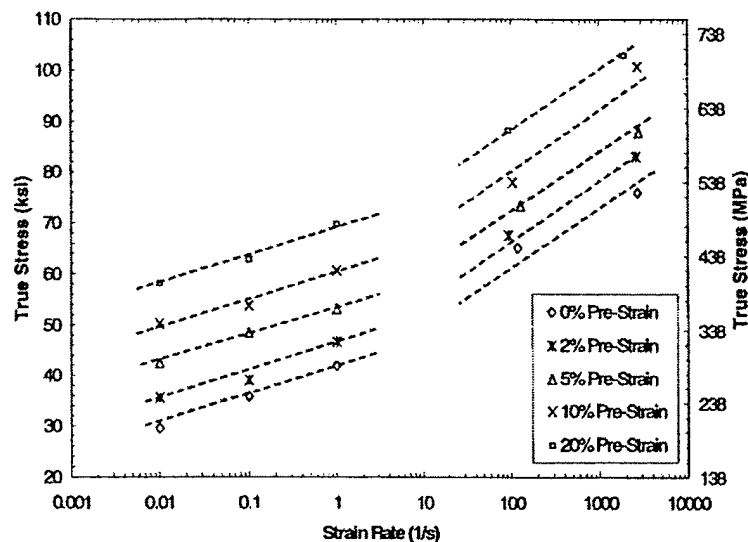


Figure 3.6: True stress at 0.02 true strain versus strain rate for an IF steel quasi-statically pre-strained in compression to five different levels. All tests conducted at room temperature [38].

3.5 Solid Solution Strengthening

Introducing solute atoms into solution with a pure metal generally creates an alloy that is stronger than the pure metal, because the solute atoms interact with dislocations. Typically, the addition of solute raises the yield strength and the level of the entire stress-strain curve [30 (p. 204)]. If solute atoms are of similar size to the solvent atoms, they will occupy lattice sites in the solvent crystal and are called substitutional. Hume-Rothery rules were created to predict whether substitutional solid solutions would form, and are based on size difference, chemical affinity, valence and crystal structure of the two elements. If the solute atoms are small compared to the solvent atoms, they are more likely to occupy interstitial sites.

Substitutional and interstitial atoms have different effects on dislocation interactions because they affect the solvent lattice in different ways. Since a substitutional atom simply replaces a solvent atom, it creates a purely dilatational (or

volume) strain in the lattice, which is either tensile or compressive depending on the size of the solute atom. Therefore, the stress field surrounding a substitutional atom has no shear component and will interact more strongly with edge dislocations than with screw dislocations. However, interstitial atoms create both dilatation (volume change) and distortion (shape change) of the solvent lattice resulting in a stress field with both normal and shear components. Therefore, interstitial atoms will interact with both edge and screw dislocations, and should have a greater impact on strengthening.

Figure 3.7 shows the increase in strength, $\Delta\sigma$, of steel as a function of solute content. The solid lines indicate substitutional atoms in the iron lattice, while the dashed line indicates interstitial atoms. Clearly, interstitial atoms have a greater impact on strengthening in iron. Also, increasing solute content usually increases the strength of the alloy because adding more solute atoms creates more obstacles to dislocation motion through the solvent lattice.

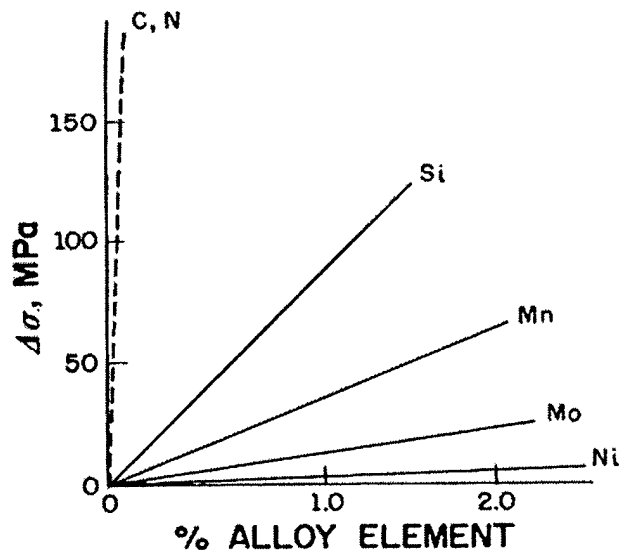


Figure 3.7: Strength increase, $\Delta\sigma$, of steel versus solute content. Solid lines represent substitutional atoms in the iron solvent lattice, while the dashed line represents interstitial atoms. [41 (p. 465)].

The interactions between solute atoms and the solvent matrix create energy barriers to dislocation motion. These interactions include elastic misfit interaction due to the size difference, modulus interaction, electrical and chemical interactions, and short and long range order interactions [30 (p. 205), 41 (p. 466), 49 (p. 145)]. For metals, the elastic interactions (misfit and modulus) are the most important [41 (p. 470), 49 (p. 177), 55].

To calculate the approximate contribution of the elastic misfit interaction to strengthening, first the interaction energy must be derived. The force can then be determined as the first derivative of energy with respect to distance and finally the strength calculated based on the force and appropriate dimensions. The calculations shown here assume an edge dislocation interaction with a substitutional solute atom. The calculations are similar (although more complicated) for interstitial atoms interacting with screw dislocations.

The interaction energy, U_{int} , is calculated by Equation 3.6, where V_{defect} is the volume, and σ_{ij} and ϵ_{ij} are the stress and strain tensors associated with the defect.

$$U_{\text{int}} = V_{\text{defect}} \sum_{ij} \sigma_{ij} \cdot \epsilon_{ij} \quad [3.6]$$

For the substitutional solute atom, σ_{ij} is the hydrostatic stress generated by its presence and ϵ_{ij} is the dilatation strain, which can be written as $\Delta V/V$. Therefore, the misfit interaction energy, U_{misfit} , is given by Equation 3.7, where σ_h is the hydrostatic stress.

$$U_{\text{misfit}} = \sigma_h \cdot \Delta V \quad [3.7]$$

Substituting appropriate values for σ_h and ΔV leads to Equation 3.8 [55], where G is the shear modulus, b is the Burger's vector, η_a is the size misfit parameter, r_o is the radius of the solvent atom, θ is the angle between dislocation and solute atom, and r is the distance from dislocation to solute atom.

$$U_{\text{misfit}} = 4Gb\eta_a r_o^3 \frac{(\sin\theta)}{r} \quad [3.8]$$

Taking the first derivative of Equation 3.8 with respect to distance, r , results in Equation 3.9 for the force, F , exerted on the solute by the dislocation.

$$F = \frac{-\partial U_{\text{misfit}}}{\partial r} = A \frac{\sin\theta}{r^2}, A = 4Gb\eta_a r_o^3 \quad [3.9]$$

Next, if L is the spacing between solute atoms that pin a dislocation and C is the concentration of solute atoms per unit volume, then L is equal to $C^{-1/2}$. Finally, the stress increase can be calculated by equation 3.10 if it is assumed that $r \approx b$ and $\sin \theta \approx 1$.

$$\Delta\tau = \frac{F}{bL} = \frac{A\sqrt{C}}{b^3} \quad [3.10]$$

For binary iron alloys, Leslie [34 (p. 119)] plotted the strength increment for specific substitutional alloying elements as a function of the size misfit parameter (Figure 3.8), and found a strong correlation as expected. However, elements that contract the lattice such as silicon and phosphorus provide much greater strengthening than predicted by the size misfit. Nickel and manganese also strengthen iron more than can be accounted for by size misfit alone. Not surprisingly, these elements are commonly used to strengthen steel.

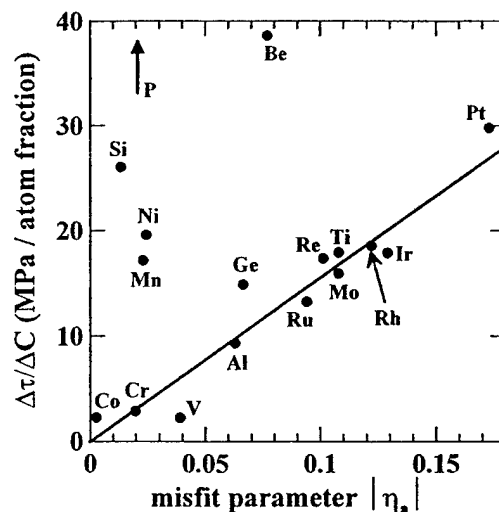


Figure 3.8: Correlation of solid solution strengthening of iron-base binary alloys at 298K with size misfit parameter [replotted from 34 (p. 119)].

There have been a variety of models proposed to explain solid solution strengthening, which can be classified into two categories: dislocation locking or frictional resistance of solute atoms to moving dislocation [55]. The most accepted dislocation locking theories are from Cottrell and Suzuki. Cottrell's theory deals with the formation of Cottrell atmospheres where solute atoms congregate near dislocations. Suzuki's theory is based on solute segregation to stacking faults. Both of the dislocation locking theories support the development of a sharp yield point in solid solution strengthened alloys, but fail to account for the fact that alloying generally raises the level of the entire stress-strain curve. Two well known models associated with moving dislocations are the Mott-Nabarro and Fleischer theories. The Mott-Nabarro theory is based on the stress field surrounding isolated solute atoms due to size misfit between solute and solvent, while the Fleischer theory is based on contributions of both misfit and modulus effects.

3.6 Influence of Strain Rate and Temperature on Solution Strengthened BCC Iron

Since solute atoms are point defects in the solvent lattice, they present short-range obstacles to dislocation motion. Therefore, the strengthening effects of solute additions will be highly temperature and strain rate dependent. One would expect the solid solution strengthening increment to increase with decreasing temperature or increasing strain rate for short range obstacles, since thermal energy can help to overcome the obstacles. This temperature effect is seen for alloying in iron at and above room temperature when tested at quasi-static strain rates. However, for several solute elements, peak strengthening occurs at room temperature and drops dramatically as temperature decreases as shown in Figure 3.9, which plots $\Delta\sigma$ (the yield strength of the alloy minus the yield strength of iron) as a function of temperature for 1.5 atomic percent of various alloying elements [34 (p. 115-116)]. Strengthening reportedly increases again at temperatures below some critical temperature. As shown in Figure 3.9, for a particular temperature range below room temperature (about 100 to 220K), silicon, manganese and nickel additions actually reduce the strength of iron below its unalloyed strength. For solute additions to iron, one might also expect increasing strain rate to decrease the strengthening increment up to some critical strain rate value, above which the strengthening will increase again.

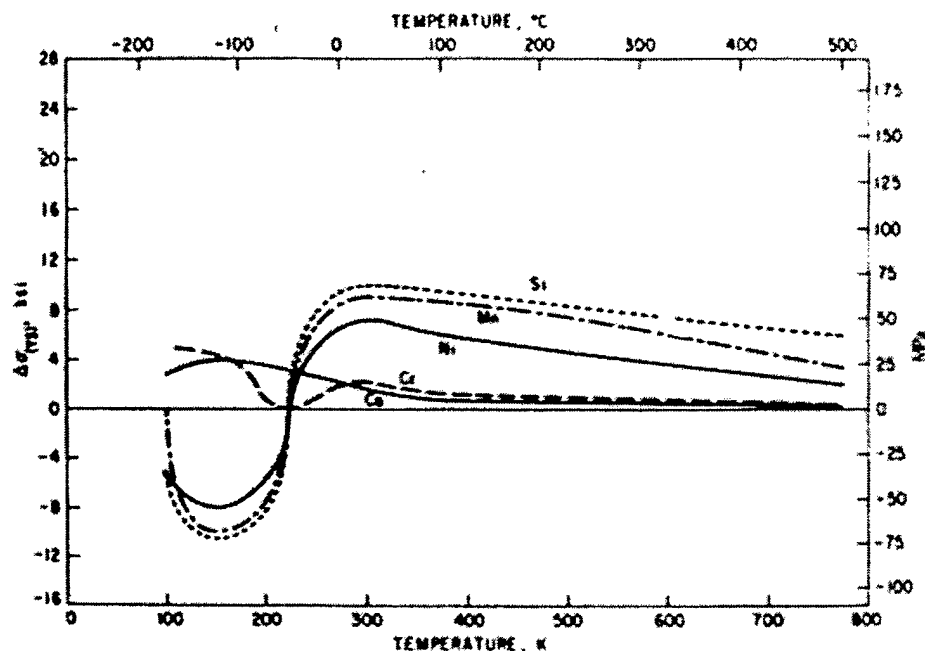


Figure 3.9: Change in yield strength ($\Delta\sigma$) from pure iron to alloy (1.5 atomic %) versus temperature for several solute elements. The curves show both solid solution strengthening and softening. [34 (p. 117)].

There are two different types of theories to explain solid solution softening in BCC metals: extrinsic and intrinsic. The extrinsic theory is based on the solvent material containing residual impurity atoms which strengthen it. When the intended solute atoms are added, they scavenge the residual impurities, resulting in a net softening of the solvent. Several studies support this theory for niobium and tantalum [56, 57]. However, the extrinsic theory does not account for the limited temperature range of the softening effect.

The intrinsic theories are based on solute atoms causing reduction of the lattice friction (or Peierl's) stress on screw dislocations by "enhancement of the thermally-activated nucleation rate of double kinks" [50]. This theory is supported by research on molybdenum- and iron-based alloys [50, 57]. It is thought [58, 59] that the elastic and

other interactions between the solute atoms and dislocations and the effects of solute on interatomic potentials are responsible for the reduced Peierl's stress. The double kink nucleation model predicts from theory what is experimentally observed in curves of stress versus temperature for several BCC metals which show an inflection. An example of this inflection is shown in Figure 3.10, which plots the critical resolved shear stress for pure iron and an iron-carbon (185 atomic ppm) alloy as a function of temperature. Note that the iron-carbon curve does not show the inflection, and therefore its critical resolved shear stress is less than that of pure iron for a specific temperature range.

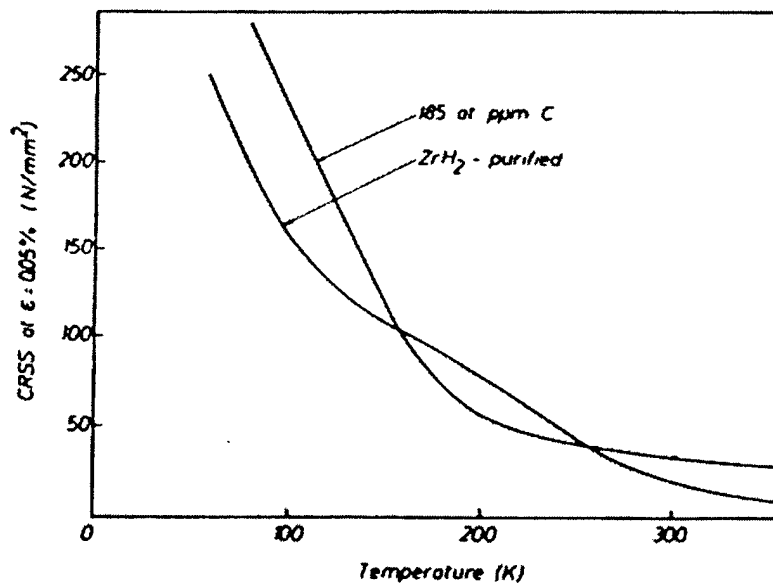


Figure 3.10: Critical resolved shear stress versus temperature for pure iron (designated by "ZrH₂-purified") and an iron-carbon alloy (designated by "185 at ppm C") [50].

3.7 Grain Size Strengthening

Material strength increases with decreasing grain size because the grain boundaries and difference in orientation between adjacent grains provide obstacles to dislocation motion. The Hall-Petch relationship [60, 61, 62 (p. 40)] shown in Equation 3.11 is often used to predict flow behavior, where σ is the flow stress, d is the mean grain diameter and σ_0 and k_y are material constants.

$$\sigma = \sigma_0 + k_y d^{-1/2} \quad [3.11]$$

The Hall-Petch equation was originally derived from empirical observations of the lower yield strength of low-carbon steels as a function of grain size [41 (p. 270)]. Since then, a variety of models have been proposed to explain the relationship from a theoretical standpoint, including the dislocation pile-up model and dislocation density models [63]. These models produce different interpretations for the constant, k_y , in Equation 3.11.

The dislocation pile-up model is based on yielding occurring when the stress at some distance, r , ahead of a dislocation pile-up blocked by a grain boundary, exceeds the required stress for dislocation motion due to the stress concentration caused by the pile-up [64]. Figure 3.11 illustrates this model with the dislocation pile-up originating in grain “1” due to its favorable orientation for slip. In Figure 3.11, d is the grain diameter, and r is the distance from the grain boundary to a dislocation source in grain “2”. As slip in grain “1” proceeds, the dislocations generated from the source at the center of grain “1” pile-up at the grain boundary causing a stress concentration, shown in Equation 3.12. When the stress concentration is large enough, a dislocation source in grain “2” is activated, and slip proceeds in the polycrystalline material, resulting in macroscopic yield. The dislocation source in grain “2” will be activated on its slip plane when the stress at the source exceeds some critical stress, τ^* , according to Equation 3.13 where τ_{app} is the applied shear stress and τ_0 is the resistance to dislocation motion in the deforming

grain "1". Rearrangement of Equation 3.13 to solve for τ_{app} gives Equation 3.14.

Converting from shear stress to normal stress results in Equation 3.15, which resembles the Hall-Petch Equation 3.11, where $k_y = \tau^* r^{1/2}$. To operate the source on a slip plane of arbitrary orientation requires including the Taylor orientation factor, m , which produces Equation 3.16 for k_y [65]. The value of m for cubic materials should be between 2 (infinite number of slip systems) and 3.1 (twelve available slip systems) [65].

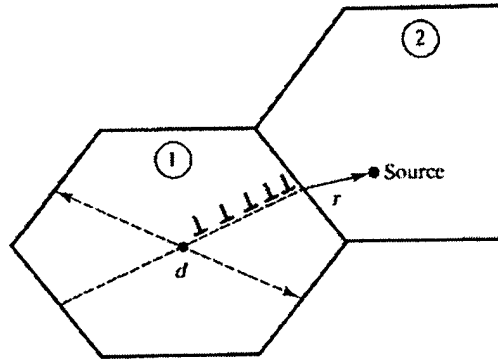


Figure 3.11: Dislocation pile-up model of grain size strengthening [43 (p. 182)]. Slip begins in grain "1". As dislocations pile-up at the grain boundary, the stress concentration eventually activates slip in grain "2".

$$\text{stress conc. factor} = \left(\frac{d}{4r} \right)^{1/2} \quad [3.12]$$

$$\tau^* = (\tau_{app} - \tau_o) \left(\frac{d}{4r} \right)^{1/2} \quad [3.13]$$

$$\tau_{app} = \tau_o + \tau^* \left(\frac{4r}{d} \right)^{1/2} = \tau_o + 2\tau^* r^{1/2} d^{-1/2} \quad [3.14]$$

$$\sigma = \sigma_o + \tau^* r^{1/2} d^{-1/2} \quad [3.15]$$

$$k_y = \frac{m^2 \tau^* r^{1/2}}{2} \quad [3.16]$$

There are two predominant dislocation density models which assume yielding to begin when the applied stress exceeds the back stress of a dislocation array. The two models differ in interpretation of the nature of the dislocation array. The dislocation density model proposed by Li [66] asserts that grain size affects yield strength due to dislocation emission from ledges on grain boundaries. Increasing the number of grain boundary ledges able to emit more dislocations will increase the strength. The ability of a grain boundary to emit dislocations corresponds to the total length of dislocation line emitted per unit area of grain boundary, q . The dislocation density at yielding, ρ , is related to q by Equation 3.17, where d is the grain diameter. Substituting Equation 3.17 into Equation 3.3 (the relationship between flow stress and dislocation density) yields Equation 3.18 where a is a constant, G is the shear modulus, and b is the Burger's vector. Therefore, for Li's dislocation density model based on grain boundary ledges, k_y is given by Equation 3.19.

$$\rho = \frac{8q}{\pi d} \quad [3.17]$$

$$\tau = \tau_o + aGb\sqrt{\frac{8q}{\pi d}} = \tau_o + aGb\sqrt{\frac{8q}{\pi}} d^{-1/2} \quad [3.18]$$

$$k_y = aGb\sqrt{\frac{8q}{\pi}} \quad [3.19]$$

The second dislocation density model is based upon the sum of geometrically necessary and statistically stored dislocations. For small strains, the geometrically necessary dislocation density, ρ_G , is much greater than the statistically stored dislocation density, ρ_s , and therefore the work-hardening strength increment in Equation 3.3 is proportional to ρ_G . The geometrically necessary dislocation density is defined by Equation 3.20, where γ is the shear strain, b in the Burger's vector and d is the grain diameter [39 (p. 168), 67]. Substituting ρ_G for ρ in Equation 3.3 results in Equation 3.21, where a and C are constants and G is the shear modulus, and therefore, k_y is given by Equation 3.22. Note that Equations 3.21 and 3.22 are only valid for small strain values.

$$\rho_G = \frac{\text{strain gradient}}{b} = \frac{\gamma}{4bd} \quad [3.20]$$

$$\tau = \tau_o + aGb\sqrt{\frac{\gamma}{4bd}} = \tau_o + CG\sqrt{\gamma b} d^{-1/2} \quad [3.21]$$

$$k_y = CG\sqrt{\gamma b} \quad [3.22]$$

3.8 Influence of Strain Rate and Temperature on Grain Size Strengthening in BCC Iron

As discussed in section 3.7, there are a variety of models to explain the observed Hall-Petch relationship between grain size and flow stress. The models differ in the variables affecting the k_y constant. It is expected that the σ_o constant in Equation 3.11 is affected by temperature and/or strain rate because it is the stress required to move

dislocations regardless of the grain size and is therefore a function of the other obstacles to dislocation motion in the material, including the Peierls-Nabarro friction stress. Therefore, σ_0 should increase with decreasing temperature or increasing strain rate. However, the theoretical interpretation of k_y determines whether or not it should be affected by temperature and/or strain rate.

The expression for k_y due to the dislocation pile-up model was shown in Equation 3.16 and includes a term, τ^* , the critical stress required for dislocation motion in the second grain, which inherently includes a friction stress. Therefore, if the dislocation pile-up model is correct, k_y should increase for decreasing temperatures or increasing strain rates. Also, if the dislocation pile-up model is correct, pile-ups should be observed in the microstructure of deformed materials. They are not commonly found in steel [39 (p. 182), 68].

Equations 3.19 and 3.22 show the expressions for k_y based on the two dislocation density models discussed in section 3.6. Both equations include the shear modulus, G , which has a very slight temperature dependence. The other variables in both equations (q - related to grain boundary ledge density, γ - shear strain, and b - Burger's vector) are not affected by temperature or strain rate. Therefore, if one of the dislocation density models is correct, k_y should remain nearly constant with changes in temperature and/or strain rate. Furthermore, if the model based upon geometrically necessary dislocations is correct, k_y values should increase with increasing strain for small strains.

There are several examples in the literature of research investigating the effects of temperature or strain rate along with grain size on the yield strength of iron and steel [35-37, 69-72]. Most of these show that k_y is independent of temperature [37, 69] and strain rate [36, 70-72], which suggests that a dislocation density model is accurate for grain size strengthening in iron and steel. Figure 3.12 shows a plot of lower yield stress as a function of grain size ($d^{-1/2}$) for three different strain rates. As strain rate increases, σ_0 (the y-axis intercept) increases, but k_y remains essentially constant. In Figure 3.13, upper and

lower yield stress values are shown as a function of grain size ($d^{-1/2}$) and temperature. For either the upper or lower yield strength, as temperature decreases, σ_0 increases, and k_y remains approximately constant. One study [35] shows k_y increasing with increasing strain rate, which supports the dislocation pile-up model. However, the details of how the different grain sizes were achieved were not specified and may have led to some other changes in the microstructure in addition to grain size. The results of this study are shown in Figure 3.14 as a plot of yield strength versus grain size ($d^{-1/2}$) for three different strain rates. As strain rate increases, σ_0 increases significantly and k_y increases slightly.

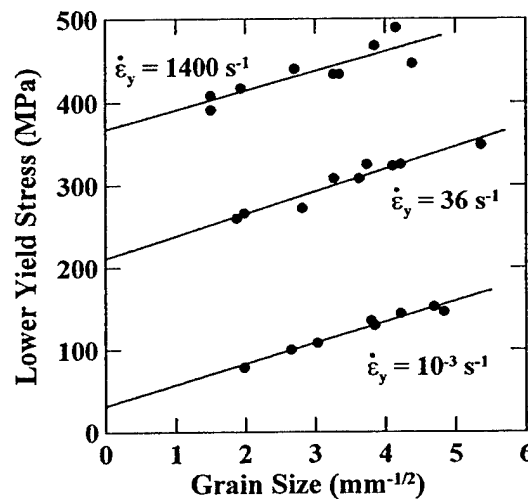


Figure 3.12: Effect of grain size and strain rate on the lower yield stress of pure iron [replotted from 36].

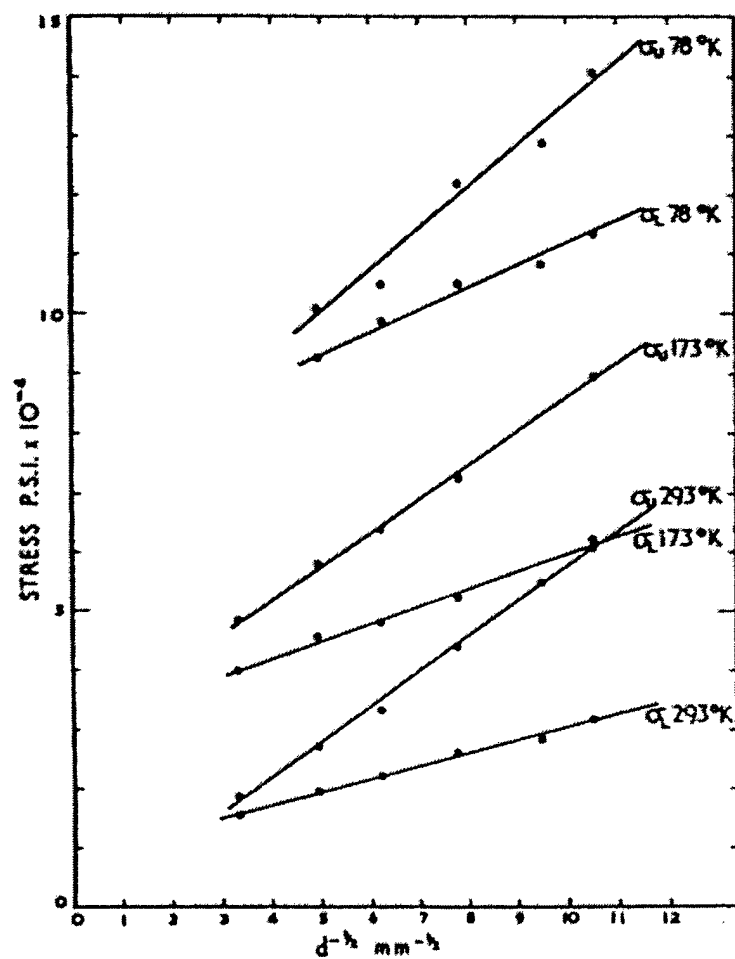


Figure 3.13: Effect of grain size and temperature on the upper (σ_U) and lower (σ_L) yield strengths of Armco iron with composition (wt. pct.) of 0.03C-0.005Si-0.08Mn-0.007P-0.03S-0.03Ni. [69].

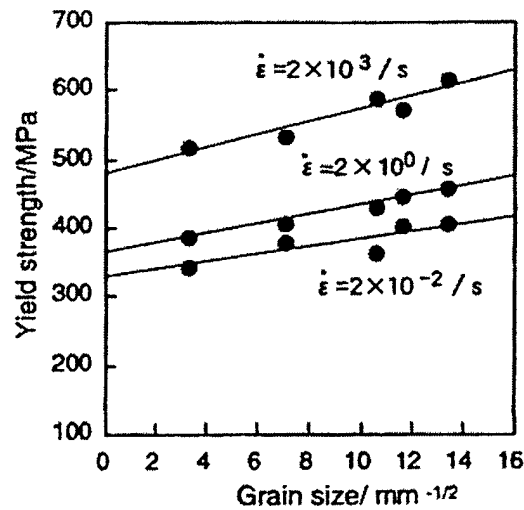


Figure 3.14: Effect of grain size and strain rate on the yield strength of a ferritic single phase steel with composition (wt. pct.) of 0.003C-1.5Si-2.0Mn-0.01P [35].

3.9 Precipitation Strengthening in Steel

The addition of small hard particles to a softer matrix material improves the strength of the material and causes the work hardening rate to increase. The degree of strengthening depends on the volume fraction of particles, particle size and shape, and the nature of the particle/matrix interface. Particles provide obstacles to dislocation motion and these obstacles are overcome either by the dislocations cutting through them or bowing around them. In steel, particles are typically carbides, nitrides and carbonitrides which are very hard. Therefore, the predominant method for dislocations overcoming these particles is to bow around them, rather than cut through them [41 (p. 491)]. According to Orowan [73], for strengthening by bowing, dislocations will bow in between particles under an applied stress, τ , leaving dislocation loops around them as shown in Figure 3.15.

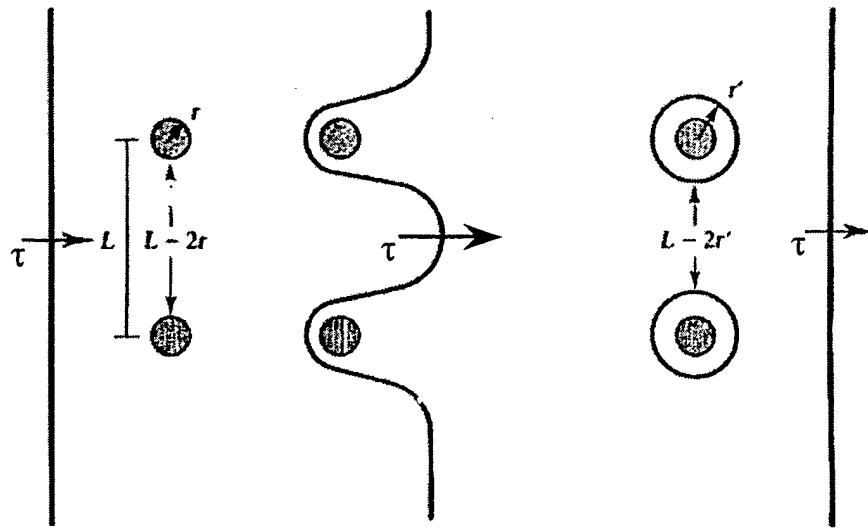


Figure 3.15: Illustration of dislocation bowing around precipitate particles under applied shear stress, τ [adapted from 39 (p. 209)].

The approximate shear stress, τ , required to bend a dislocation to a radius, r , is given by Equation 3.23, where G is the shear modulus, and b is the Burger's vector.

$$\tau \approx \frac{Gb}{2r} \quad [3.23]$$

If $(L - 2r)$ is the distance between the two particles (as shown in Figure 3.15), then the dislocation must be bent to a radius of about $(L - 2r)/2$ to pass between the particles. Therefore, the shear stress required to bow around the particles is estimated by replacing r in Equation 3.23 by $(L - 2r)/2$, resulting in Equation 3.24. The yield strength, τ_y , of the material can then be calculated by including a term, τ_0 , to account for the matrix strength in the absence of precipitates as shown in Equation 3.25, where x is the distance between particles.

$$\tau \approx \frac{Gb}{L - 2r} \quad [3.24]$$

$$\tau_y = \tau_o + \frac{Gb}{x} \quad [3.25]$$

After the first dislocation passes the particles, leaving behind dislocation loops, the distance between the particles is smaller, as shown in Figure 3.15. Therefore, the stress required for subsequent dislocations to bow around the particles will increase, which is the reason why the work hardening rate of a material increases with precipitation strengthening.

Precipitates are long-range obstacles and thermal assistance is not useful in overcoming them. Therefore, changes in temperature and/or strain rate are not expected to influence the strengthening increment due to precipitation strengthening.

3.10 Multiphase Strengthening in Dual Phase and Transformation Induced Plasticity (TRIP) Steels

Dual phase and TRIP steels make use of other phases in the microstructure to enhance their properties. Dual phase steel is made up of ferrite and martensite, generally with “a dispersion of about 20% of hard martensite particles in a soft, ductile ferrite matrix” [74]. These steels are typically continuous-yielding, have low yield/tensile strength ratios, high work hardening rate, and high uniform and total elongations, which gives them good formability. Multiphase TRIP steels are normally comprised of three microconstituents: ferrite, bainite and retained austenite. They may also contain a small amount of martensite. When a TRIP steel is deformed, some of the retained austenite will transform to martensite. The work hardening associated with this phenomenon is responsible for transformation induced plasticity, or TRIP. Like dual phase steels,

multiphase TRIP steels may also exhibit low yield/tensile strength ratios, high work hardening rates and high ductility, although they often display discontinuous yielding. Although dual phase and TRIP steels have many similar properties, the mechanisms responsible are different.

3.10.1 Strengthening in Dual Phase Steels

Dual phase steels are created by an intercritical anneal (in the ferrite plus austenite portion of the phase diagram) followed by quenching to transform the austenite to martensite. Variations in annealing temperature and/or time and cooling rate govern the amount and type of martensite created. During quenching, as austenite is transformed to martensite, dislocations are formed in the ferrite phase to accommodate the shear deformation and volume expansion associated with the martensite transformation [75]. These highly mobile dislocations are responsible for the low yield strengths and continuous yielding behavior typical of dual phase steels [76 (p. 276)]. The work hardening behavior may be explained due to the dispersion of martensite particles having a similar effect as precipitation strengthening [34 (p. 163), 62 (p. 328)]. This explanation is supported by the fact that martensite island refinement correlates with increasing work hardening rate [62 (p. 331)]. Some authors [74] have divided the work hardening process in dual phase steels into three stages. In the first stage (up to 0.5% strain) rapid work hardening is caused by the elimination of residual stresses and buildup of back stresses in the ferrite due to its plastic incompatibility with martensite. The second stage (0.5 to 4% strain) is due to dispersion strengthening, and the third stage (past 4% strain) is governed by dislocation cell structure formation in ferrite and eventual yielding of the martensite phase.

3.10.2 Strengthening in TRIP Steels

TRIP steels are created by an intercritical anneal step to obtain the desired amount of equiaxed ferrite, followed by quenching to an isothermal hold temperature that allows bainite to form. As bainitic ferrite forms, it rejects carbon into the austenite. Normally, Fe_3C would also form during the bainite transformation, but the high silicon content typically found in TRIP steels inhibits carbide formation [77] allowing the austenite to become enriched with carbon. The high carbon content stabilizes austenite, causing the martensite-start temperature (M_s) to drop below room temperature. After holding at the bainite transformation temperature for the desired amount of time, the steel is quenched to room temperature. Since the M_s temperature is below room temperature, the remaining austenite does not transform to martensite, but remains in the microstructure as retained austenite. The particular properties of a TRIP steel are highly dependent upon the nature of the retained austenite, including its grain size, morphology, carbon content, and volume fraction, all of which are influenced by processing [78-81].

TRIP steels often display yield point elongation behavior, which is due to the low dislocation densities introduced into ferrite during bainite formation [78]. During deformation, strain energy causes retained austenite to transform to martensite. This transformation leads to high work hardening and delays the onset of plastic instability (necking) during deformation, which results in high uniform elongation [82, 83]. The driving force available determines when the transformation from retained austenite to martensite will occur.

For any phase transformation to proceed, the change in total Gibbs free energy, ΔG_{total} , from the “parent” phase to the product phase must be negative. The contributions to ΔG_{total} for nucleation of the product phase are shown in Equation 3.26, where A is the surface area of the nucleus, γ is the interfacial free energy between the two phases, V is the volume of the nucleus, ΔG_s is the strain energy change, and ΔG_v is the volume free energy change [84 (p. 398)].

$$\Delta G_{\text{total}} = A\gamma + V\Delta G_S + V\Delta G_V \quad [3.26]$$

For the nucleation process of martensite, the interfacial free energy term is positive since an interface is being created and the strain energy term is positive since the parent (austenite) and product (martensite) phases have different crystal structures. The sign and magnitude of the volume free energy term will therefore determine whether or not the transformation can proceed. Schematic plots of free energy versus composition as shown in Figure 3.16 can be used to find the value of ΔG_V as the difference in free energy from austenite to martensite at a particular temperature and composition of interest.

In Figure 3.16, at composition C_X and temperature T_1 , $\Delta G_{V(A \rightarrow M)} > 0$, at T_2 , $\Delta G_{V(A \rightarrow M)} = 0$, and at T_3 , $\Delta G_{V(A \rightarrow M)} < 0$. When austenite and martensite are in equilibrium, their free energies are equal (T_2 in Figure 3.16), and this temperature is called T_O [85]. For a particular composition of steel, Figure 3.17 schematically shows free energy versus temperature. In Figure 3.17, the M_S temperature indicates where ΔG_V (labeled $\Delta G_{V(\text{crit})}$) is just large enough to allow the transformation from austenite to martensite to proceed. This temperature will vary greatly for different compositions of steel. TRIP steels take advantage of this by processing and alloying appropriately to cause the M_S temperature to fall below room temperature, thereby allowing austenite to be retained in the microstructure.

The martensite start temperature is directly related to the stability of the austenite in the TRIP steel microstructure. The more stable the austenite, the lower the M_S temperature. One of the mechanisms for austenite stabilization is to increase the amount of carbon in the austenite. In general, as carbon content increases, M_S temperature decreases because greater carbon content both increases the elastic energy of the transformation and decreases the available chemical driving force [86].

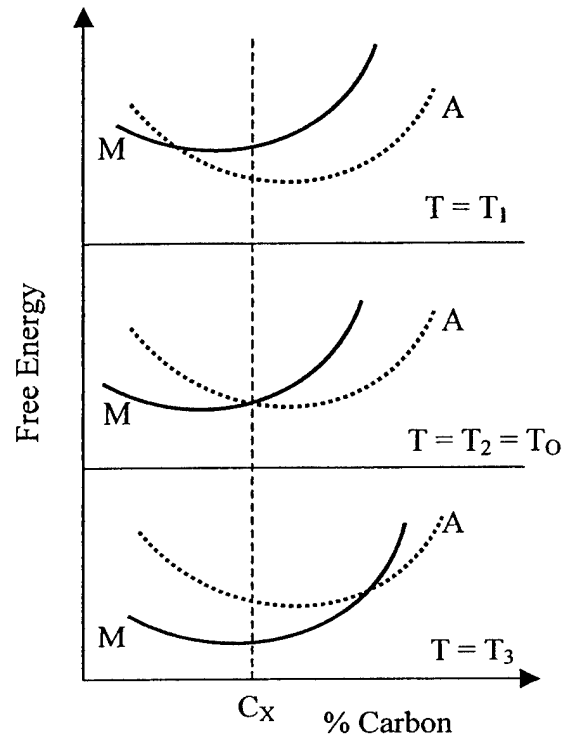


Figure 3.16: Schematic free energy versus composition curves for austenite (A) and martensite (M) at different temperatures, where $T_1 > T_2 > T_3$.

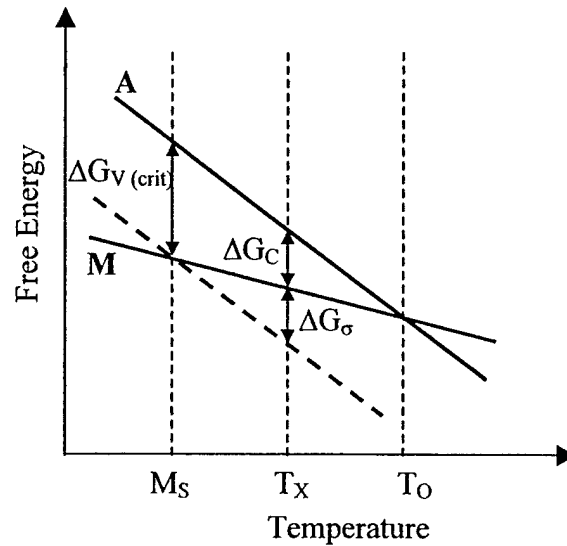


Figure 3.17: Schematic free energy versus temperature curves for austenite (A) and martensite (M) at a fixed composition.

In TRIP steel, the chemical free energy difference at room temperature between austenite and martensite is insufficient to cause a transformation because the M_S temperature is below room temperature. During deformation, the total ΔG_V in TRIP steels is made up of a chemical driving force, ΔG_C , and a mechanical driving force, ΔG_σ , as shown in Equation 3.27. ΔG_σ is due to strain energy added to the austenite during deformation. When the total value of ΔG_V is equal to $\Delta G_{V(crit)}$, martensite nucleation is possible at temperatures greater than M_S . Figure 3.17 illustrates this at temperature T_X .

$$\Delta G_V = \Delta G_C + \Delta G_\sigma \quad [3.27]$$

3.11 Influence of Strain Rate and Temperature on Dual Phase Steels

In dual phase steel tensile tested at quasi-static strain rates, the martensite islands remain largely undeformed until necking begins [87]. If tests were run at elevated

temperatures, martensite strength would decrease and would likely reduce the strength of the steel. However, tests run at lower temperatures should influence the steel tensile properties primarily through the change in properties of the ferrite phase. Increasing strain rate would be expected to have the same effect. Therefore, it is expected that changes in the volume fraction of martensite in dual phase steel should not affect the strengthening increment due to temperature reduction or strain rate increase. A study by Miura, *et al.* [35] confirms this hypothesis for tensile strength as shown in Figure 3.18, which plots tensile strength as a function of volume fraction of martensite for two different strain rates. However, Miura's work also showed an increase in the rate sensitivity of yield strength (difference between quasi-static yield strength and dynamic yield strength) with increasing volume fraction of martensite, as shown in Figure 3.19 which plots yield strength versus martensite volume fraction for two different strain rates. In Figure 3.19, the static yield strength does not change appreciably with volume fraction of martensite. Other studies [88] have shown a decrease in quasi-static yield strength with increasing martensite volume percent up to about 10%, which was attributed to the transition from discontinuous to continuous yielding behavior. Beyond 10% volume percent martensite, the yield strength increased with increasing martensite amounts. Perhaps the increase in yield strengthening increment seen by Miura, *et al.* is actually related to the change in yield behavior between static and dynamic tests. This theory is supported by their static and dynamic stress-strain curves shown in Figure 3.20, where the curve labeled "b" is for dual phase steel. In Figure 3.20, the quasi-static curve is continuous-yielding, while the dynamic curve shows a yield point.

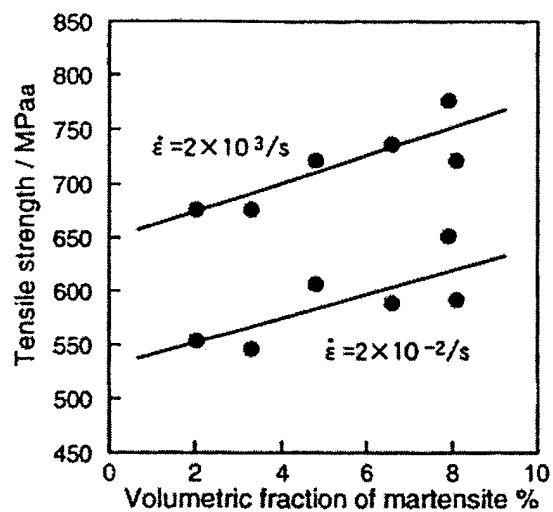


Figure 3.18: Influence of strain rate and volumetric fraction of martensite on tensile strength of dual phase steel [35].

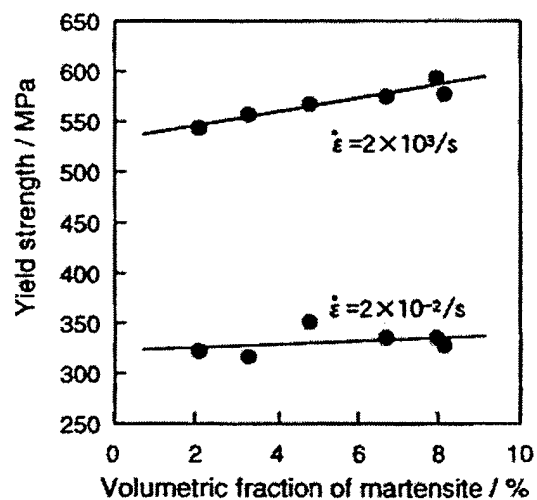


Figure 3.19: Influence of strain rate and volumetric fraction of martensite on yield strength of dual phase steel [35].

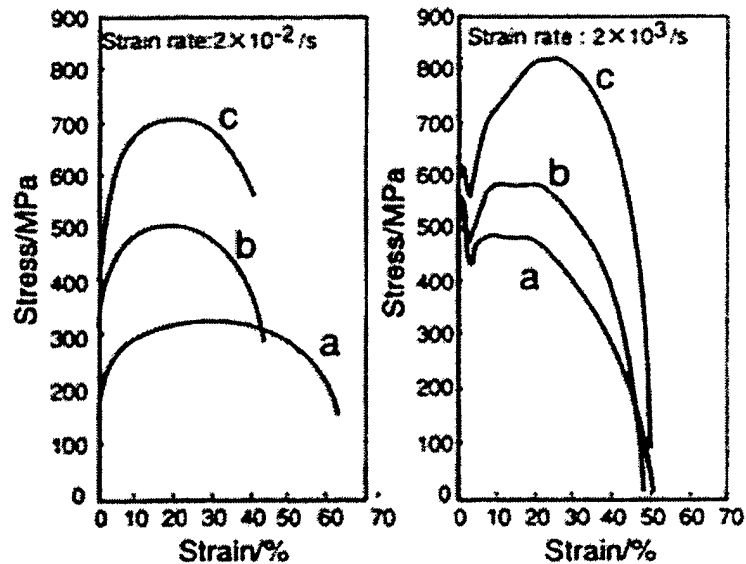


Figure 3.20: Nominal stress-strain curves at two different strain rates for (a) mild steel, (b) solution-hardened steel, and (c) dual phase steel. [35]

3.12 Influence of Strain Rate and Temperature on TRIP Steels

In TRIP steels, the nature of the retained austenite phase and its transformation to martensite with strain greatly influences tensile properties. The transformation of retained austenite to martensite is highly temperature dependent. It will transform to martensite at or below its martensite start, M_s , temperature without any mechanical assistance. With the addition of a mechanical driving force (strain energy of deformation), austenite may transform to martensite above its M_s temperature, with the required amount of strain energy increasing as the temperature increases. The nucleation of martensite above the M_s temperature may be promoted through either a stress-assisted or strain-induced mechanism, as shown in Figure 3.21 [89-92].

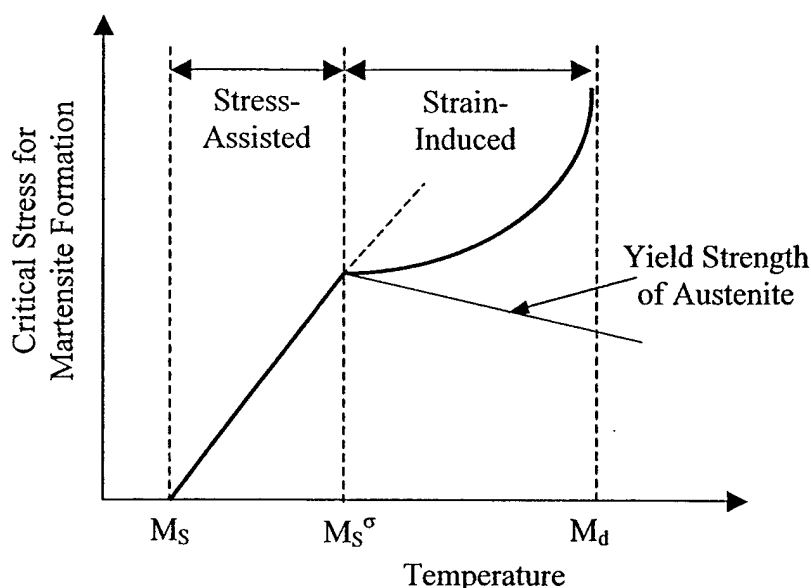


Figure 3.21: Schematic drawing of critical stress for martensite formation versus temperature for a TRIP steel.

At stresses below the yield strength of austenite, martensite will nucleate by the stress-assisted mechanism, which provides the needed mechanical driving force through the work generated by an applied stress. This occurs at temperatures between M_s and M_s^σ as shown in Figure 3.21. At temperatures above M_s^σ , the retained austenite will plastically deform before martensite nucleation occurs and the critical stress required for martensite transformation drops below the extended line from the stress-assisted region (see Figure 3.21). There are two prominent theories to explain this phenomenon. The first holds that plastic deformation creates dislocations and shear bands in the retained austenite which provide more nucleation sites for martensite [90, 93]. The second theory proposes that stress concentrations are created at obstacles such as grain boundaries and twins during deformation, and that the increased stress at these obstacles is responsible for the further martensite transformation [89, 94]. At temperatures above M_d , transformation from austenite to martensite is found to cease.

With increasing temperature, more strain energy is required to cause retained austenite to transform to martensite, which delays the transformation to higher strain values and may prevent some of the austenite from transforming. Therefore, with increasing temperature, work hardening rate and tensile strength might decrease more than the amount expected due to simple thermal softening of the steel. This result has been verified by Bleck, *et al.* [95]. If the temperature is high enough (above M_d), retained austenite transformation will not occur at all, and the work hardening rate, tensile strength and uniform elongation values will greatly decrease.

Decreasing temperature or increasing strain rate may cause competing processes to take place which may hinder or promote austenite transformation to martensite. With decreasing temperature or increasing strain rate, the yield strength of ferrite (BCC structure) increases substantially, while the yield strength of austenite (FCC structure) does not change as much [30 (p.301)], although the work hardening rate in austenite will increase. Typically, ferrite is the matrix phase surrounding islands of retained austenite in TRIP steel. Since the austenite-to-martensite transformation involves a volume expansion, it may be inhibited by increasing the strength of the surrounding ferrite. However, a lower temperature will also provide more chemical driving force to the transformation, and as the temperature decreases, the rate of transformation is expected to increase.

As strain rate increases, the yield strength of FCC austenite does not change as much as that of the BCC ferrite. As the yield strength of ferrite increases, a higher stress is imposed on the austenite phase, which may cause stress-assisted transformation to martensite. Therefore, increasing strain rate may promote austenite transformation to martensite. Once the austenite phase begins to work harden, higher strain rate will provide more mechanical driving force which may increase the transformation rate through the strain-induced mechanism. However, as plastic strain in the steel increases during high rate testing, adiabatic heating causes the temperature to rise, which inhibits the transformation by reducing the chemical driving force. Figure 3.22 shows the volume

fraction of martensite versus effective strain for a 304 stainless steel (austenitic single phase) tensile tested at low and high strain rates [96]. At high strain rate, the transformation begins immediately and increases linearly with increasing strain. At low strain rate, the transformation begins later (after some plastic strain has accumulated) but the rate of transformation increases rapidly to a much higher rate than in the high-rate test. In Figure 3.22, the point where the two curves cross is designated ϵ^* . For strains less than ϵ^* , the austenite to martensite transformation is accelerated by higher stress due to higher strain rate. However, as strain increases, temperature increases due to adiabatic heating, so that for strains greater than ϵ^* the transformation is retarded in high rate tests. Therefore, the total amount of austenite transformed during a high-rate test is much less than during a low-rate test.

The strain rate dependence of austenite transformation in TRIP steel is expected to be complicated. Based on the relationships described above, increasing strain rate should initially accelerate transformation, resulting in increased yield strength and initial work hardening rate. As the steel work hardens, the high work hardening rate should persist until adiabatic heating impedes the transformation, causing a drop in strain hardening.

Several researchers have measured the amount of austenite remaining in the necked region of TRIP steels after tensile testing and all have found that the amount increases with increasing strain rate, which they attribute to adiabatic heating [97-100]. This explanation seems reasonable because the highest strain rates and therefore highest temperatures occur in the necked region and the transformation should be suppressed. There are conflicting results comparing the amount of austenite transformed as a function of strain for low-rate and high-rate tensile tests. A study by Wei, *et al.* [98] showed less transformed austenite at all strains for the higher rate test, while another by Pychmintsev [97] showed more transformed austenite at low strains for the higher rate test, but less at higher strain values, similar to the 304 stainless steel results. The TRIP steels used in

these two studies were quite different, with Wei's material having only about 0.07 volume fraction retained austenite, while Pychmintsev's had about 0.20 volume fraction retained austenite. Another study by Wei, *et al.* [99] showed waves in some high-rate stress-strain curves for TRIP steels, which they attributed to alternant softening and hardening as transformation from austenite to martensite occurred during the tests.

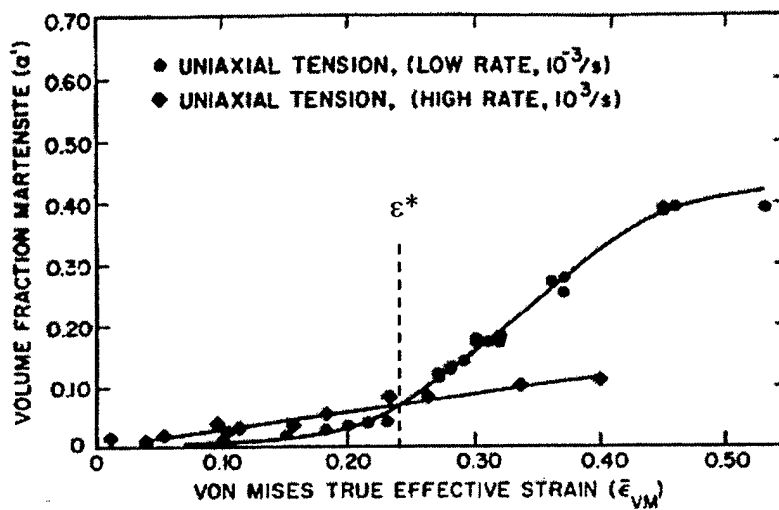


Figure 3.22: Volume fraction of martensite formed during straining of 304 stainless steel at room temperature in uniaxial tension at high (10^3 s^{-1}) and low (10^{-3} s^{-1}) strain rates [adapted from 96].

3.13 Modeling of Flow Behavior with Strain Rate and Temperature

There are a great many constitutive relationships in the literature used to attempt prediction of material properties for different combinations of temperature, strain rate and strain. Some models predict only the yield strength, while others attempt to model the entire flow curve. Models used to predict the entire flow curve are generally not very accurate for low ($< 2\%$) strains, as they do not account for subtle yielding effects [101]. Modeling of the entire flow curve is also complicated at high rates by adiabatic heating,

since the amount of heating is dependent upon sample dimensions.

Constitutive relationships can also be divided into two categories: empirical and physically-based. Empirical relationships have various numbers of constants that are determined from analysis of experimental data. Physically-based relationships use theoretical analysis of fundamental processes that contribute to flow stress in materials together with empirical data to account for specific material behavior.

3.13.1 Empirical Relationships

At low strain rates, many metals exhibit parabolic hardening, which leads to Equation 3.28, where σ is the flow stress, σ_0 is the yield strength, k is a constant, ϵ is the true strain, and n is the work-hardening exponent.

$$\sigma = \sigma_0 + k\epsilon^n \quad [3.28]$$

For mild steel, the effects of temperature and strain rate can be estimated by Equations 3.29 and 3.30, which were determined by simple curve fitting [41 (p. 325)]. In Equation 3.29, T_m is the melting point, T_r is a reference temperature at which σ_r (a reference stress) is measured, T is the temperature for which σ is calculated and m is an experimentally determined constant.

$$\sigma = \sigma_r \left[1 - \left(\frac{T - T_r}{T_m - T_r} \right)^m \right] \quad [3.29]$$

$$\sigma \propto \ln \dot{\epsilon} \quad [3.30]$$

3.13.2 Dislocation Mechanics

The force, F , on a dislocation per unit length is given by Equation 3.31, where τ is the applied shear stress and b is the Burger's vector.

$$F = \tau b \quad [3.31]$$

An array of N dislocations per unit area that do not interact with each other produce a shear strain, $\gamma = \tan \theta$, as shown in Figure 3.23. Since each step in Figure 3.23 moves a distance b , the total deformation is Nb and therefore $\gamma = \tan \theta = Nb/L$. Since the mobile dislocation density, ρ_m , can be written as N/L^2 , the shear strain can also be written as Equation 3.32. Taking the time derivative of Equation 3.32 yields Equation 3.33. Assuming the dislocation density does not change with time gives Equation 3.34, which is known as the Orowan equation [41 (p. 236)]. In Equation 3.34, \bar{v} is the average dislocation velocity (dL/dt). The shear strain can be converted to longitudinal strain, ϵ , by adding the Taylor orientation factor, m , as shown in Equation 3.35.

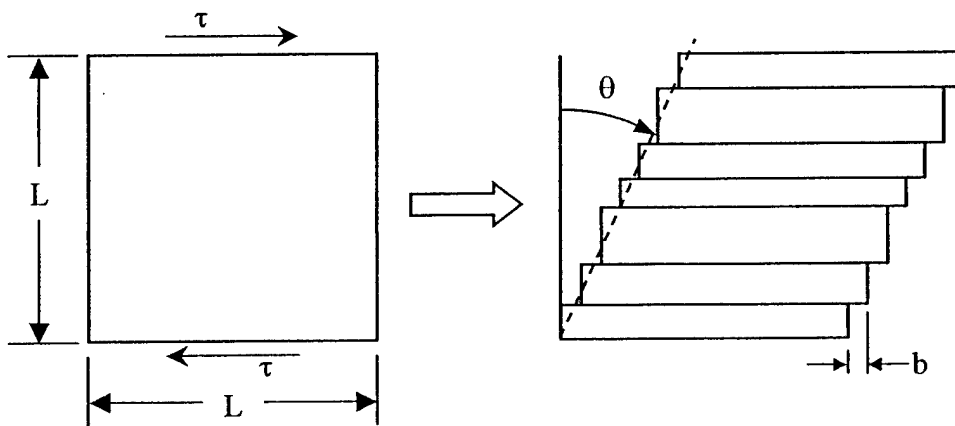


Figure 3.23: Movement of an array of dislocations causing shear strain $\gamma = \tan \theta$ [adapted from 1 (p. 331)].

$$\gamma = \rho_m b L \quad [3.32]$$

$$\frac{d\gamma}{dt} = \frac{d\rho_m}{dt} b L + \rho_m b \frac{dL}{dt} \quad [3.33]$$

$$\dot{\gamma} = b \rho_m \bar{v} \quad [3.34]$$

$$\dot{\epsilon} = \frac{1}{m} b \rho_m \bar{v} \quad [3.35]$$

The mobile dislocation density is some fraction of the total dislocation density and may be dependent upon applied stress [102 (p. 14)]. The dislocation velocity is dependent upon applied stress, with velocity increasing with increasing stress up to a theoretical limit of the shear wave velocity in the material [1 (p. 332)]. An equation relating average dislocation velocity, \bar{v} , to stress for a Fe-3%Si alloy is shown in Equation 3.36, where τ is the resolved shear stress, τ_o is the shear stress at unit velocity, and m is a constant (not the Taylor orientation factor) [103]. There are three generally accepted regimes for dislocation velocities which govern plastic deformation mechanisms: thermally-activated, dislocation drag, and relativistic [1 (p. 336)]. Dislocation drag effects become significant at strain rates above 10^3 s^{-1} , and relativistic effects above 10^5 s^{-1} [102]. Therefore, for the strain-rate range examined in this thesis, it is assumed that all deformation occurs in the thermally-activated dislocation motion regime.

$$\bar{v} = \left(\frac{\tau}{\tau_o} \right)^m \quad [3.36]$$

As discussed in previous sections in this chapter dealing with the influence of strain rate and temperature, dislocations encounter various obstacles as they move through a material. These obstacles have been classified as long-range (athermal) or short-range (thermally activated) depending on whether or not they can be overcome by thermal energy. For BCC ferrite, it has been determined that the Peierls-Nabarro stress is the primary short-range barrier [1 (p. 341)]. Dislocation interactions, grain boundaries, and precipitates are assumed to be long-range obstructions, while solute atoms may be short-range obstacles. The flow stress of a material, σ , can be expressed by a combination of stresses due to long-range (σ_L) and short-range (σ_S) barriers to dislocation motion as shown in Equation 3.37.

$$\sigma = \sigma_L + \sigma_S, \quad \sigma_S = f(T, \dot{\epsilon}) \quad [3.37]$$

Figure 3.24 shows a schematic drawing of the effect of temperature on the applied energy required to overcome short-range barriers. Increasing temperature provides increasing amounts of thermal activation energy, indicated by the cross-hatched areas in Figure 3.24 labeled ΔG . At temperature T_3 , ΔG_3 provides enough energy to overcome the barrier with no applied stress. At temperature, T_0 ($= 0K$), there is no thermal energy available and the barrier must be overcome with a high stress, τ_0 .

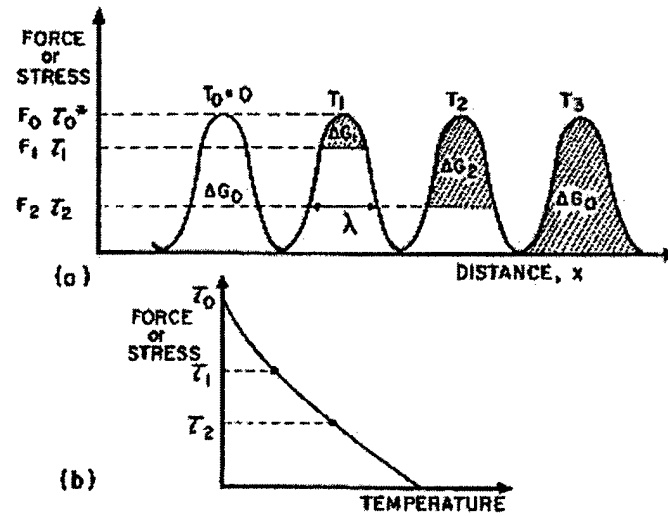


Figure 3.24: (a) Schematic drawing of thermal energy used to overcome short-range obstacles. $T_3 > T_2 > T_1 > T_0$. Cross-hatched areas show thermal energy contributions. (b) Stress required to overcome a short-range obstacle as a function of temperature. [1 (p. 341)]

The frequency, ν , with which a dislocation will overcome an obstacle is given by Equation 3.38, where ν_0 is the vibration frequency of the dislocation, ΔG is the activation energy, T is absolute temperature, and k is Boltzmann's constant [1 (p. 342)].

$$\nu = \nu_0 \exp\left(-\frac{\Delta G}{kT}\right) \quad [3.38]$$

Once a dislocation overcomes one obstacle, there is a period of time, Δt , before it overcomes the next obstacle. This time can be divided into the time required for the dislocation to move between obstacles, called the running time, t_r , and the time it waits, t_w , for a large enough thermal fluctuation to overcome the obstacle, such that $\Delta t = t_r + t_w$. The average waiting time is $1/\nu$ and is much longer than t_r and therefore, $\Delta t \approx t_w$.

Returning to Equation 3.35, for short times Δt , the strain rate can be approximated by $\Delta\epsilon/\Delta t$ as shown in Equation 3.39, where ΔL is the distance between obstacles.

$$\frac{d\epsilon}{dt} \approx \frac{\Delta\epsilon}{\Delta t} = \frac{1}{m} \rho b \frac{\Delta L}{\Delta t} \quad [3.39]$$

Substituting $1/v$ for Δt in Equation 3.39 and rearranging to solve for ΔG results in Equation 3.40, which shows that increasing temperature or decreasing strain rate increases the activation energy available to help overcome short-range obstacles. The necessary activation energy can be calculated as the hatched area under the barrier in Figure 3.24a using Equation 3.41 if the shape of the barrier is known. In Equation 3.41 ΔG_0 is the activation barrier at 0K and the integral is the non-hatched area in Figure 3.24a. Combining Equations 3.40 and 3.41 gives Equation 3.42. Since the shape of the activation barrier determines the solution to the integral in Equation 3.42, the shape must be known (or assumed) in order for Equation 3.42 to be written in terms of stress.

$$\Delta G = kT \ln \frac{\dot{\epsilon}_0}{\dot{\epsilon}}, \quad \dot{\epsilon}_0 = \frac{v_0 \rho b \Delta L}{m} \quad [3.40]$$

$$\Delta G = \Delta G_0 - \int_0^{F^*} \lambda(F) dF \quad [3.41]$$

$$kT \ln \frac{\dot{\epsilon}_0}{\dot{\epsilon}} = \Delta G_0 - \int_0^{F^*} \lambda(F) dF \quad [3.42]$$

3.13.3 Yield Strength Models

Several models have been proposed to predict the yield strength of materials as a function of microstructure, temperature, and/or strain rate. Two of these models are discussed in this section, including the Brunner-Diehl model and the Hahn model.

3.13.3.1 Brunner-Diehl BCC Model

The Brunner-Diehl model [45, 48] uses fundamentals of dislocation movement in BCC metals to predict yield strength as a function of temperature and strain rate. The analyses were dependent on temperature, and the only one discussed here will be for temperatures between 250 and 340K. In this temperature range, the primary deformation mechanism for BCC metals is thermally activated motion of screw dislocations, which move by the formation of double kink pairs [48].

Similar to Equation 3.37, Brunner and Diehl divide the flow stress, τ , into two components, thermal (τ^*) and athermal (τ_G), as shown in Equation 3.43. The thermal component is dependent upon strain rate and temperature, while the athermal component is independent of strain rate and weakly dependent upon temperature through the shear modulus, G . According to the Orowan equation (Equation 3.35), the strain rate is dependent upon dislocation velocity. The stress and temperature dependence of the dislocation velocity can be written with an Arrhenius-type formula with activation enthalpy, H , which transforms Equation 3.35 into Equation 3.44, where k is Boltzmann's constant, T is absolute temperature, and $\dot{\epsilon}_0$ contains geometrical factors, an attempt frequency and entropy terms [45].

$$\tau = \tau^* + \tau_G \quad [3.43]$$

$$\dot{\epsilon} = \dot{\epsilon}_0 \exp\left(\frac{-H(\tau^*)}{kT}\right) \quad [3.44]$$

For temperatures between 250 and 340K, $H(\tau^*)$ is replaced with H_{kp} , the enthalpy of kink pair formation, given by Equation 3.45, where H_k is the enthalpy of an isolated kink, a is the kink height, b is the Burger's vector, and γ_o is "the pre-logarithmic factor of the elastic part of the line tension of the dislocations" [48]. Combining Equations 3.44 and 3.45 and rearranging yields Equation 3.46.

$$H_{kp} = 2H_k - 2\alpha\sqrt{\tau^*}, \quad \alpha \equiv \frac{a^3 b \gamma_o}{2} \quad [3.45]$$

$$\tau^* = \left[\frac{2H_k + kT \ln\left(\frac{\dot{\epsilon}}{\dot{\epsilon}_o}\right)}{2\alpha} \right] \quad [3.46]$$

Published values are used to determine the parameters and then H_k , α and τ_G are adjusted to fit experimental data [22]. For pure α -iron, Brunner & Diehl determined the constants shown in Table 3.1.

Table 3.1: Constants for the Brunner-Diehl model for pure α -iron [48].

Material	$2H_k$ (eV)	α ($N^{1/2}m^2$)	$\dot{\epsilon}_o$ (s^{-1})	τ_G (MPa)
Pure α -Iron	0.92	3.24×10^{-24}	30,000	0

3.13.3.2 Hahn Yield Drop Model

The Hahn model [104] is based upon dislocation multiplication and velocity and specifically addresses the nature of the yield drop observed in some BCC materials including iron. The derivation of Hahn's model starts with the Orowan equation (Equation 3.35) and Equation 3.36 which relates dislocation velocity to applied stress. The mobile dislocation density, ρ_m , in Equation 3.35 is assumed to be a function of the initial dislocation density, ρ_o , and plastic strain, ϵ , according to Equation 3.47, where f is the fraction of mobile dislocations, and C and β are constants.

$$\rho_m = f(\rho_o + C\epsilon^\beta) \quad [3.47]$$

Equation 3.36 is modified to use normal stress (where $\sigma = 2\tau$) and incorporate a strain hardening term ($q\epsilon$) as shown in Equation 3.48. Combining Equations 3.35, 3.47 and 3.48 and using a Taylor orientation factor of 2 results in Equation 3.49, which relates strain rate and stress. Rearranging to solve Equation 3.49 for stress gives Equation 3.50.

The Hahn model predicts a yield drop (upper and lower yield points) in materials which have a low initial dislocation density, ρ_o , and/or low values of m (the exponent in the dislocation velocity equation). Furthermore, if the strain rate sensitivity of a material is calculated as the exponent, r , in Equation 3.51, where σ is flow stress, $\dot{\epsilon}$ is the strain rate, and B is a constant, Hahn found that $m \approx r^{-1}$. Therefore, for materials (such as steel) where the strain rate sensitivity increases at high strain rates, a corresponding decrease in m is expected, which increases the magnitude of the yield drop. Values for the parameters in Equation 3.50 are shown in Table 3.2 for 1020 steel.

$$\bar{v} = \left(\frac{\frac{\sigma}{2} - q\epsilon}{\tau_o} \right)^m \quad [3.48]$$

$$\dot{\epsilon} = \frac{b}{2} f(\rho_o + C\epsilon^\beta) \left(\frac{\sigma/2 - q\epsilon}{\tau_o} \right)^m \quad [3.49]$$

$$\sigma = 2q\epsilon + 2\tau_o \left[\frac{2\dot{\epsilon}}{bf(\rho_o + C\epsilon^\beta)} \right]^{1/m} \quad [3.50]$$

$$\sigma = B\dot{\epsilon}^r \quad [3.51]$$

Table 3.2: Constants for the Hahn model for 1020 steel [104]. m_L is for strain rates less than 1 s^{-1} , while m_H is used for strain rates between 1 and 1000 s^{-1} .

Material	f	ρ_o (cm^{-2})	C (cm^{-2})	β	b (nm)	m_L	m_H	τ_o (MPa)	q (GPa)
1020 Steel	0.1	10^4	1.6×10^9	0.8	0.248	33	13	100	3.44

3.13.4 Flow Curve Models

Many models have been developed to predict the shape of the entire stress-strain curve for changes in temperature and/or strain rate. This discussion includes descriptions of the empirically-based Johnson-Cook model and the physically-based Zerilli-Armstrong and MTS (Mechanical Threshold Stress) models.

3.13.4.1 Johnson-Cook Model

The most widely-used empirical relationship [1 (p. 329)] to predict stress-strain curves was developed by Johnson and Cook [105]. The Johnson-Cook equation is shown

in Equation 3.52, where A , B , C , n and m are experimentally determined parameters, T_r is the reference temperature at which A is measured, ϵ is the equivalent plastic strain and $\dot{\epsilon}_0$ is a reference strain rate. The basic elements of Equations 3.28 - 3.30 are seen in Equation 3.52. In the first set of brackets, A is proportional to yield stress and B and n represent the effects of strain hardening. The term in the second set of brackets accounts for strain rate, where $\dot{\epsilon}^*$ is the dimensionless plastic strain rate for which Johnson and Cook used $\dot{\epsilon}_0 = 1.0 \text{ s}^{-1}$. The third set of brackets gives the effects of temperature.

$$\sigma = [A + B \epsilon^n] [1 + C \ln \dot{\epsilon}^*] [1 - (T^*)^m] \quad [3.52]$$

$$\dot{\epsilon}^* = \frac{\dot{\epsilon}}{\dot{\epsilon}_0}, \quad T^* = \left(\frac{T - T_r}{T_m - T_r} \right)$$

Johnson and Cook conducted tests at various temperatures and strain rates for a wide variety of materials and determined constants for Equation 3.52. Some of these constants for iron alloys are listed in Table 3.3. It should be noted that the Johnson-Cook equation was developed primarily for use at high strain rates and tends to underpredict strength for $\dot{\epsilon} < 1.0 \text{ s}^{-1}$ [106]. Also, moderate rate (quasi-static up to 400 s^{-1}) experimental data were obtained from torsion tests. Johnson and Cook calculated equivalent uniaxial tensile flow stress and strain from torsion data using the von Mises flow rule ($\sigma = \sqrt{3}\tau$, $\epsilon = \gamma/\sqrt{3}$).

Table 3.3: Material and constitutive constants for the Johnson-Cook equation (Equation 3.52) for Armco iron and 1006 steel [105].

Material	Density (kg/m ³)	Specific Heat (J/kg·K)	T _m (K)	A (MPa)	B (MPa)	n	C	m
Armco Iron	7890	452	1811	175	380	0.32	0.060	0.55
1006 Steel	7890	452	1811	350	275	0.36	0.022	1.00

Xu, *et al.* [101] modified the Johnson-Cook equation to better describe the high strain rate behavior of several high strength steels for automotive body structure applications at room temperature. They contend that if the Johnson-Cook model is used for an isothermal test (where T remains constant), it can only predict divergent stress-strain curves as shown in Figure 3.25. Since only room temperature results were of interest to Xu, *et al.*, their modified Johnson-Cook model neglects temperature and is shown in Equation 3.53, where B , C , n and n' are constants and the other terms are identical to those in Equation 3.52. By leaving out the temperature-dependent term, the modified Johnson-Cook model does not allow strain-dependent temperature change due to adiabatic heating. Xu, *et al.* found better correlation between their model and experimental results on several high strength steels than for the original Johnson-Cook model. Furthermore, they found that the constant, C , in Equation 3.53 could be approximately predicted based on only the quasi-static tensile strength for several steels. This relationship is shown in Equation 3.54, where TS is the quasi-static tensile strength.

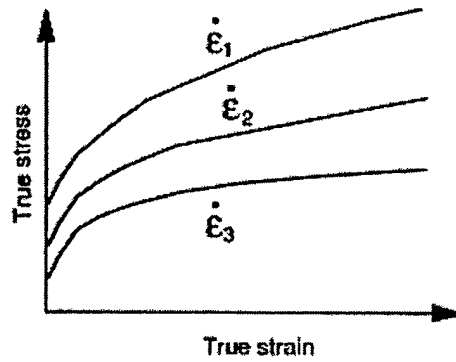


Figure 3.25: Divergent stress-strain curves predicted by isothermal use of the Johnson-Cook equation (Equation 3.52). $\dot{\epsilon}_1 > \dot{\epsilon}_2 > \dot{\epsilon}_3$

$$\sigma = B\epsilon^n \left[1 + C\epsilon^{n'} \ln \left(\frac{\dot{\epsilon}}{\dot{\epsilon}_0} \right) \right] \quad [3.53]$$

$$C = -0.00003(TS) + 0.0402 \quad [3.54]$$

3.13.4.2 Zerilli-Armstrong Model

Zerilli and Armstrong [107] proposed two constitutive equations based upon dislocation mechanics. One equation was established for copper and is applicable to FCC materials and the other was developed for iron and is appropriate for BCC materials. Using the dislocation dynamics concepts discussed in Section 3.13.2, they developed an expression for the thermal portion of the stress, σ_s , as Equation 3.55, where m is the Taylor orientation factor, ΔG_0 is the activation energy at 0K, A_0 is the dislocation activation area at 0K, b is the Burger's vector, $\dot{\epsilon}$ is the strain rate, and C_3 and C_4 are constants. The β term in Equation 3.55 is a function of the activation area, and thus the short-range barrier shape. Since for BCC metals, the primary short-range barrier is the Peierls-Nabarro stress, the barrier shape does not change with increasing plastic strain,

and therefore the thermal portion of the stress is independent of strain as shown in Equation 3.56. Adding terms to account for the athermal component of stress (σ_L), work hardening ($C_5 \epsilon^n$) and grain size ($kd^{-1/2}$) gives the final Zerilli-Armstrong equation for BCC materials shown in Equation 3.57, where C_5 , n and k are constants, and d is the grain diameter. The simple addition of the work hardening term ($C_5 \epsilon^n$) in Equation 3.57 means that changing temperature or strain rate will simply shift the stress-strain curve up or down, which has been shown correct for iron alloys tested under isothermal conditions [108]. Use of Equation 3.57 assumes no change in deformation mechanism, such as deformation twinning at very low temperatures or very high strain rates in iron. Although the form of Equation 3.57 is governed by physical processes, the constants are determined with empirical data. Zerilli and Armstrong determined constants for Equation 3.57 for iron as shown in Table 3.4.

$$\sigma_s = \frac{m \Delta G_o}{A_o b} e^{-\beta T}, \quad \beta = C_3 - C_4 \ln(\dot{\epsilon}) \quad [3.55]$$

$$\sigma_s = C_1 \exp[-C_3 T + C_4 T \ln(\dot{\epsilon})] \quad [3.56]$$

$$\sigma = \sigma_L + C_1 \exp[-C_3 T + C_4 T \ln(\dot{\epsilon})] + C_5 \epsilon^n + kd^{-1/2} \quad [3.57]$$

Table 3.4: Constants for the Zerilli-Armstrong equation (Equation 3.57) for iron [107].

Material	σ_L (MPa)	C_1 (MPa)	C_3 (K^{-1})	C_4 (K^{-1})	C_5 (MPa)	n	k ($N/mm^{3/2}$)
Iron	0	1033	0.00698	0.000415	266	0.289	22

Goldthorpe, *et al.* [108] have proposed a variation to the Zerilli-Armstrong model to account for a “transition from the domination of thermally activated processes to those controlled by the temperature dependence of the shear modulus” as the strength of iron-based alloys increases. Their equation is shown in Equation 3.58, where μ_T is the shear modulus at temperature, T , μ_{293} is the shear modulus at 293K, the grain size dependence is included in σ_L , and all other terms are identical to those in Equation 3.57. The temperature dependence of μ_T is given by Equation 3.59. For a carbon-chromium-molybdenum steel with quasi-static yield strength of 800 MPa, Goldthorpe, *et al.* determined the constant for Equation 3.58 shown in Table 3.5. They also suggest that long-range obstacles to dislocation motion, such as precipitates, have their effect through the shear modulus and that adiabatic shear may control instability in strong materials.

$$\sigma = \left(\sigma_L + C_5 \epsilon^n \right) \frac{\mu_T}{\mu_{293}} + C_1 \exp \left[-C_3 T + C_4 T \ln(\dot{\epsilon}) \right] \quad [3.57]$$

$$\mu_T = \mu_{293} (1.13 - 0.000445T) \quad [3.58]$$

Table 3.5: Constants for the modified Zerilli-Armstrong equation (Equation 3.58) for carbon-chromium-molybdenum steel with quasi-static yield strength of 800 MPa [108].

Material	σ_L	C_1 (MPa)	C_3 (K ⁻¹)	C_4 (K ⁻¹)	C_5 (MPa)	n
Iron	710	575	0.0048	0.00032	567	0.41

3.13.4.3 Mechanical Threshold Stress (MTS) Model

Like the Zerilli-Armstrong mode, the MTS model was developed using the basic concepts of dislocation mechanics to determine an expression for the thermal portion of stress, σ_s . However, the MTS model is based upon the use of state variables and their evolution with plastic deformation. It uses a single set of equations for all materials, incorporating the shape of the activation barrier into two parameters, p and q as shown in Equation 3.60 [109], which gives the activation energy, ΔG , as a function of stress, σ . In Equation 3.60, σ_o is the threshold stress, which can be described as the height of the barrier in Figure 3.24, or the flow stress of a particular microstructure at 0K (no thermal assistance). ΔG_o is given by Equation 3.61 [110], where μ is the temperature-dependent shear modulus, b is the Burger's vector and g_o is a normalized total activation energy.

$$\Delta G = \Delta G_o \left[1 - \left(\frac{\sigma}{\sigma_o} \right)^p \right]^q \quad [3.60]$$

$$\Delta G_o = g_o \mu b^3 \quad [3.61]$$

The fundamental aspects of the MTS model include a yield criterion, a stress evolution equation, and a flow rule. The yield criterion determines when yielding occurs, the flow rule gives the direction of the next increment of plastic strain, and the evolution equation describes the strain hardening behavior of the material. The MTS model requires the determination of a “mechanical threshold stress”, $\hat{\sigma}$, which is the flow stress of the material at absolute zero temperature. Goto, *et al.* [111] further break down the mechanical threshold stress into an intrinsic part, $\hat{\sigma}_i$, and an evolving part, $\hat{\sigma}_e$. The intrinsic part includes barriers to thermally activated dislocation motion, such as the Peierls barrier, and dislocation interactions with other defects. The evolving part includes

microstructural evolution with increasing deformation, or strain-hardening behavior. In addition to the contribution of the mechanical threshold stress, the model also includes the athermal contribution, σ_a , to flow behavior.

The yield criterion for the MTS model is given by Equation 3.62, where σ is the flow stress, μ is the temperature-dependent shear modulus, μ_0 is shear modulus at 0K, and S_i and S_ϵ are temperature and strain rate dependent scaling factors, respectively. The scaling factors, S_j , are derived from Equation 3.63, where k is the Boltzmann constant, T is absolute temperature, $\dot{\epsilon}$ is the strain rate, and $\dot{\epsilon}_0$ is a reference strain rate which is set to a high value.

$$\frac{\sigma}{\mu} = \frac{\sigma_a}{\mu} + S_i \frac{\hat{\sigma}_i}{\mu_0} + S_\epsilon \frac{\hat{\sigma}_\epsilon}{\mu_0} \quad [3.62]$$

$$S_j = \left[1 - \left(\frac{kT}{g_{oj}\mu b^3} \ln \frac{\dot{\epsilon}_{oj}}{\dot{\epsilon}} \right)^{1/q_j} \right]^{1/p_j} \quad [3.63]$$

The evolution equation for the MTS model is based on a modified Voce hardening rule given by Equation 3.64, where θ_0 is a temperature and strain rate dependent experimentally determined strain hardening rate, α is an empirical constant and $\hat{\sigma}_{es}$ is a temperature and strain rate dependent saturation stress. The saturation stress values are derived from the saturation threshold stress, $\hat{\sigma}_{eso}$, using Equation 3.65, where $\dot{\epsilon}_{oe\epsilon}$ is a large (saturation) value of strain rate, and g_{oes} is a normalized activation energy.

$$\theta = \frac{d\hat{\sigma}_\varepsilon}{d\varepsilon} = \theta_o(\dot{\varepsilon}, T) \left[1 - \frac{\tanh\left(\alpha \frac{\hat{\sigma}_\varepsilon}{\hat{\sigma}_{\varepsilon s}(\dot{\varepsilon}, T)}\right)}{\tanh(\alpha)} \right] \quad [3.64]$$

$$\ln\left(\frac{\dot{\varepsilon}_{oEE}}{\dot{\varepsilon}}\right) = -\frac{\mu b^3 g_{oEE}}{kT} \ln\left(\frac{\hat{\sigma}_{\varepsilon s}}{\hat{\sigma}_{\varepsilon so}}\right) \quad [3.65]$$

3.13.4.4 Comparison of Flow Curve Models

For copper and iron Taylor impact tests, Zerilli and Armstrong [107] found their predictions to fit the experimental results better than those using the Johnson-Cook model. Johnson and Holmquist [106] also compared the Zerilli-Armstrong and Johnson-Cook equations and determined that the Johnson-Cook model has a more simple form with constants easier to determine, but the Zerilli-Armstrong model can be extrapolated to extended strain, strain rates and temperatures with greater confidence due to its physically-based origins. An advantage of the Zerilli-Armstrong model over the MTS model is that the testing methodology for the Zerilli-Armstrong model is simpler with no requirement for low temperature testing [1 (p. 375)].

CHAPTER 4

EXPERIMENTAL PROCEDURES

4.1 MTS High Rate Testing System

All tensile testing was conducted at room temperature using a servo-hydraulic high strain rate testing system manufactured by the MTS Systems Corporation. The system consists of a 50 kN (11,000 lb) capacity actuator (model 244.21S, #100-030-675) mounted in a 500 kN (110,000 lb) capacity frame (model 318.50S, #100-030-983). All tests were run in displacement control, with the actuator moving at a constant speed and resulting strain rate measured using methods described in Section 4.1.1. Conventional actuator speeds are attained through a 10 gpm servo valve supplied by a 10 gpm hydraulic pump. High rates are achieved through a 400 gpm servo valve supplied by a 5 gallon capacity oil accumulator. System control is provided through a MTS TestStarTM digital controller with associated computer system. The specified peak velocity for the system was 13.5 m/s at zero load and 10 m/s at 50% of the peak load capacity. The system was verified to meet or exceed these performance specifications. The system is equipped with tensile grips capable of testing flat tensile samples with grip width up to 25.4 mm (1.0 in) and thickness up to 6.35 mm (0.25 in). A slack-adaptor is installed between the lower grip and the moving actuator to accommodate the required displacement to accelerate the actuator. Photographs of the entire system, the loading assembly, and installed test sample are shown in Figure 4.1.

Data were acquired at conventional rates (up to 5 kHz) with the MTS TestWareTM program and at high rates (up to 5 MHz) with a National Instruments data acquisition board and VirtualBench ScopeTM software.

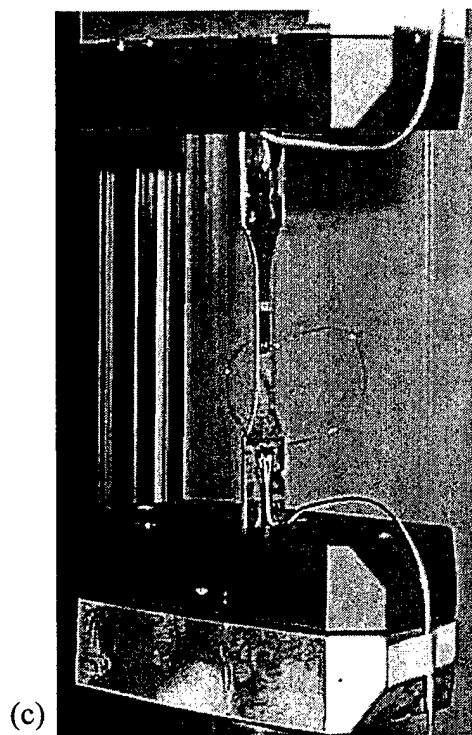
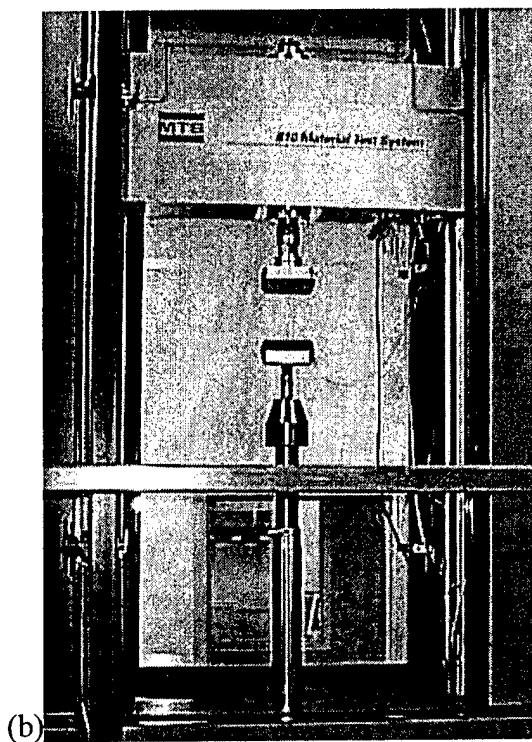
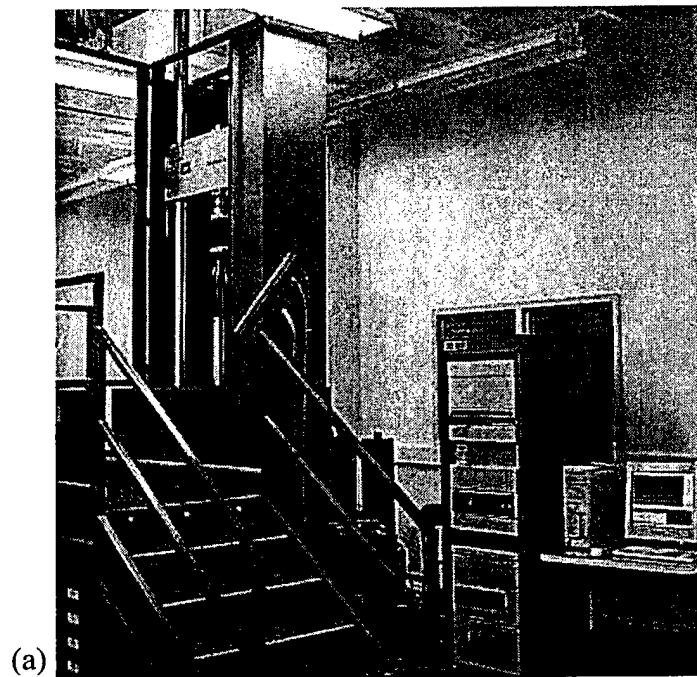


Figure 4.1: Photographs of the MTS servo-hydraulic high rate testing system. (a) Entire system. (b) Loading assembly. (c) Test sample.

4.1.1 Strain Measurement

Several different methods for strain measurement were initially considered. An optical non-contacting extensometry system was investigated, but was eliminated from consideration due to expense and complex data acquisition methods. Standard contact extensometers cannot be used at high rates due to response time limitations. High-elongation strain gages were chosen for simplicity of measurement and excellent high-rate response. The particular strain gages chosen (Vishay Measurements Group EP-08-250BG-120) accurately measure strain up to about 25% when used with an appropriate high-elongation adhesive (Vishay Measurements Group Epoxy Resin and Hardener #A-12) and correct application methods [112, 113]. Figure 4.2 shows a photograph of two copper tensile samples with high-elongation strain gages attached to the gage lengths. In the photograph, each sample also has a strain gage attached to the grip section. The grip section strain gages will be discussed in Section 4.1.2. In Figure 4.2, the upper sample is shown prior to testing, and the lower sample is shown after testing to fracture with approximately 50% elongation. As evident in the deformed sample, the high-elongation strain gage stretched with the sample and remained attached throughout the test.

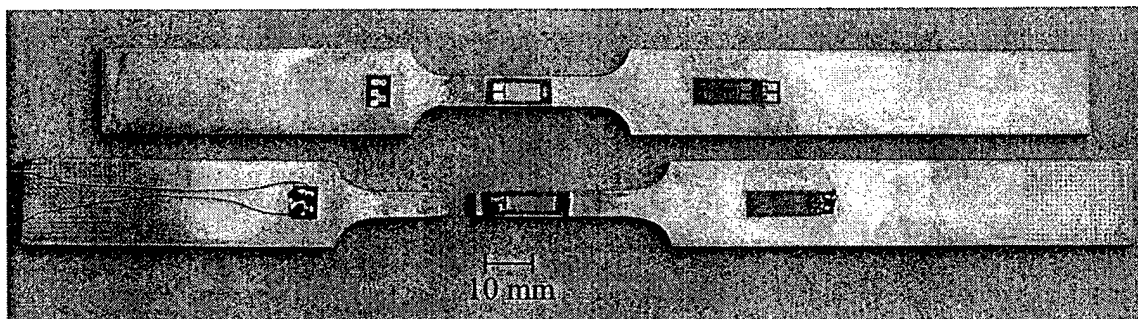


Figure 4.2: Photograph of two copper tensile samples. The upper sample is shown prior to testing and the lower sample is shown after testing to fracture with approximately 50% elongation.

Strain data were acquired through the use of a standard quarter-bridge Wheatstone Bridge circuit. Calibration of an MTS DC conditioner (model 490.21, serial #1150330) to convert Wheatstone Bridge output voltage to strain provides direct strain indication through the TestWareTM program for all tests and also through the National Instruments data acquisition system for high rate tests. At large strains, output from a Wheatstone Bridge becomes significantly non-linear. Therefore, this non-linearity is mathematically corrected using Equations 4.1 and 4.2 [114] to determine actual strain values. The correction has been verified as accurate (within 2% error) by comparing the mathematically corrected final strain values to final strain values calculated directly from the resistance of the strain gage after tensile testing.

$$\epsilon = \tilde{\epsilon} + n \quad [4.1]$$

$$n = \frac{F(\tilde{\epsilon})^2}{2 - F\tilde{\epsilon}} \quad [4.2]$$

ϵ = actual strain

$\tilde{\epsilon}$ = indicated strain

n = incremental error in indicated strain

F = gage factor

Quoted strain rates were obtained directly from measured strain-time data of the high-elongation strain gage mounted on each tensile sample gage section. Figure 4.3 shows engineering strain versus time data for TRIP-1 steel tested at low and high strain rates. In Figure 4.3, the strain data are nearly linear with time throughout the tests. At high strain values the curves turn sharply upward as a result of strain gage failure. Engineering strain rates were determined by fitting a line to the linear portion of the strain versus time plots.

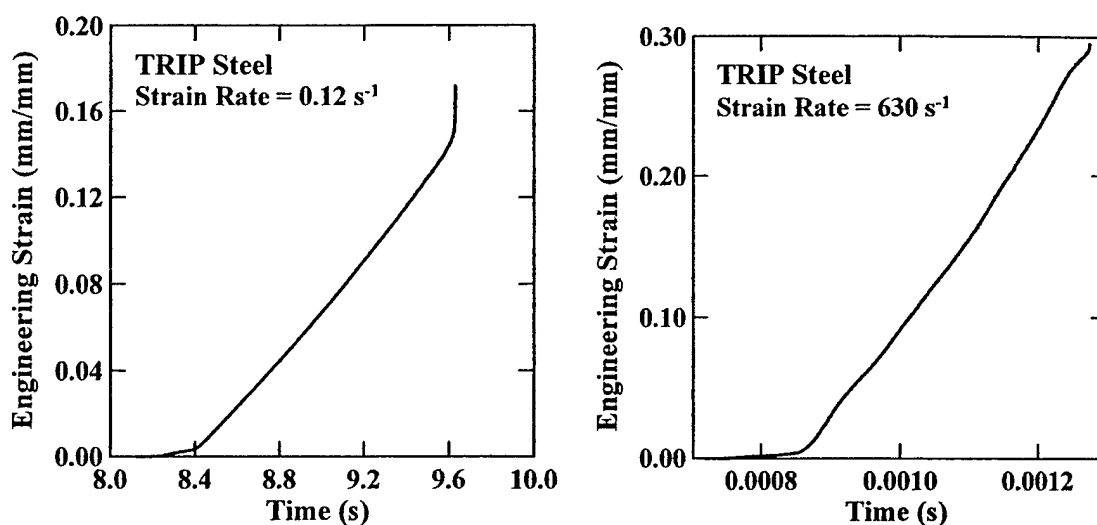


Figure 4.3: Engineering strain versus time plots for TRIP-1 steel. a) Low-rate test: gage length = 50.8 mm, actuator velocity = 6 mm/s, strain rate = 0.12 s^{-1} b) High-rate test: gage length = 12.7 mm, actuator velocity = 8 m/s, strain rate = 630 s^{-1} .

4.1.2 Load Measurement

The MTS high-rate system was supplied with a piezoelectric load washer (Kistler type 9361B, serial #1022938) for load measurement. The signal from the load washer is transmitted to the TestWareTM computer program and National Instruments data acquisition system through a Kistler amplifier (model 5010B, serial #C93013). The load washer exhibited some noise (about $\pm 20 \text{ N}$) when used during low-rate tensile tests. Load washer data were satisfactory for strain rates at or below approximately 10 s^{-1} , but for higher rates the load washer data exhibited increasingly large fluctuations, commonly referred to as “ringing,” as shown in Figure 4.4. Figure 4.4 shows engineering stress (calculated from the piezoelectric load washer) versus engineering strain for HSLA-1 steel tested at four different strain rates. The curve for a strain rate of 10^{-3} exhibits very small amplitude noise, but no noticeable fluctuations. The 10 s^{-1} curve shows small

amplitude fluctuations, while the curves at strain rates of 100 and 530 s^{-1} exhibit very large amplitude fluctuations. The oscillation frequency is constant at a value of about 2500 Hz regardless of strain rate, which is the reason a lesser number of oscillations is present for tests at higher strain rates. Load washer ringing is an expected phenomenon and was discussed in detail in section 2.2.1 dealing with vibration during high-rate testing.

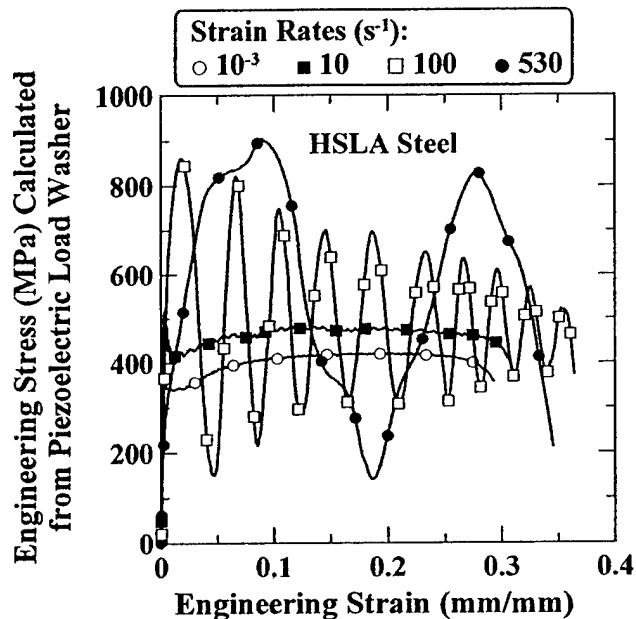


Figure 4.4: Engineering stress-strain curves for HSLA-1 steel calculated using load data from the piezoelectric load washer at four strain rates. Increasing strain rate increases ringing amplitude while ringing frequency remains approximately constant. All tests run using 25.4 mm gage length samples with actuator velocities of 0.025 mm/s, 250 mm/s, 2.5 m/s and 13.5 m/s used to achieve strain rates of 10^{-3} , 10, 100 and 530 s^{-1} , respectively.

In Section 2.2.1, load cell ringing was discussed along with methods to reduce the effects of ringing. One such method was to reduce the mass between test sample and

load washer, which should increase the frequency and reduce the amplitude of ringing. The effect of reducing the mass on oscillation amplitude and frequency is illustrated in Figure 4.5. To create Figure 4.5, two frequency response tests were conducted by tapping the MTS high-rate system load train with a hammer and recording the output of the load washer. The first test (“High Mass”) was conducted with the load train set up for a normal test with the upper grip installed as usual. A hammer was used to tap the center of the upper grip to impose a load. For the second test (“Low Mass”), the upper grip and its attachment post were removed and the hammer used to tap the bottom of the load washer assembly directly. Figure 4.5 shows that the lower mass situation results in lower amplitude oscillations at a higher frequency, as expected.

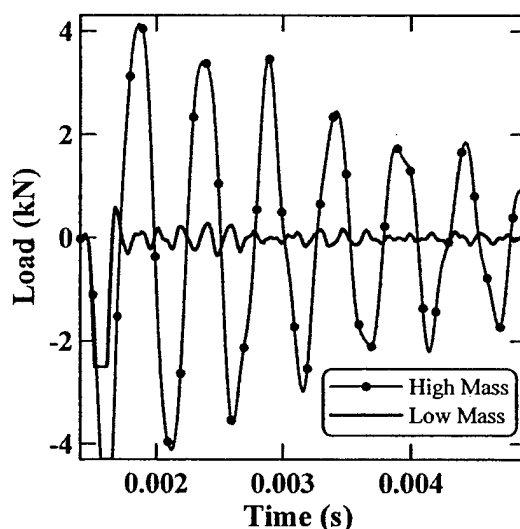


Figure 4.5: Load versus time plot for two frequency response tests. One test (“High Mass”) was conducted with the upper grip installed, while the other (“Low Mass”) was conducted without the upper grip installed. The plot shows the higher mass test resulted in larger amplitude, lower frequency oscillations.

Clearly, reducing the mass between test sample and load washer is important for producing the highest quality load data. This can be accomplished by minimizing the mass of the upper grip and further reduced by incorporating the load measuring device directly into the upper grip.

Another method to minimize the amplitude of load washer ringing is to reduce the actuator velocity and use a shorter gage length sample to achieve the same desired strain rate. The effect of reduced actuator velocity is shown in Figure 4.6. To create Figure 4.6, two tensile tests were run on HSLA-1 steel samples with identical properties and dimensions except that one sample had a reduced section length of 25.4 mm while the other had a reduced section length of 12.7 mm. The 25.4 mm sample was tested with an actuator velocity of 2.65 m/s, which resulted in a true strain rate of about 100 s^{-1} . The 12.7 mm sample was tested with an actuator velocity of 1.27 m/s, which resulted in a true strain rate of about 150 s^{-1} . As seen in Figure 4.6, the ringing frequencies for both tests are approximately the same, while the amplitude is lower for the lower velocity test. Although this method effectively reduces ringing amplitude, decreasing the gage length reduces the portion of the tensile sample that can achieve a state of uniform stress during testing. For this reason, no tensile tests were run using gage lengths smaller than 12.7 mm, and most tests were run using samples with 25.4 mm gage lengths.

A method for acquiring accurate load data at high strain rates by greatly reducing the mass between test sample and load measuring device was developed. An elastic strain gage (Vishay Measurements Group EA-06-250BG-120 or EA-06-125BT-120) was installed on the grip section of each tensile sample and strain data acquired through a second Wheatstone Bridge circuit and appropriate MTS conditioner (model 490.21, serial #1295723H). A schematic drawing of the tensile sample is shown in Figure 4.7. This method essentially uses the grip section strain gage as a load cell and significantly improves the quality of high-rate load data as demonstrated in Figure 4.8.

Figure 4.8 shows load washer data versus time for HSLA-3 steel along with load data collected from a grip section strain gage. The grip section strain gage data still

exhibited some oscillation, but of significantly lower amplitude and higher frequency than the load washer data. The grip section strain gage load curve shown in Figure 4.8 has an oscillation frequency of about 22 kHz, which is very close to the expected natural frequency of 23 kHz for the tensile sample used in this particular test. The details of how the theoretical natural frequency of the tensile sample was calculated are contained in Appendix A.

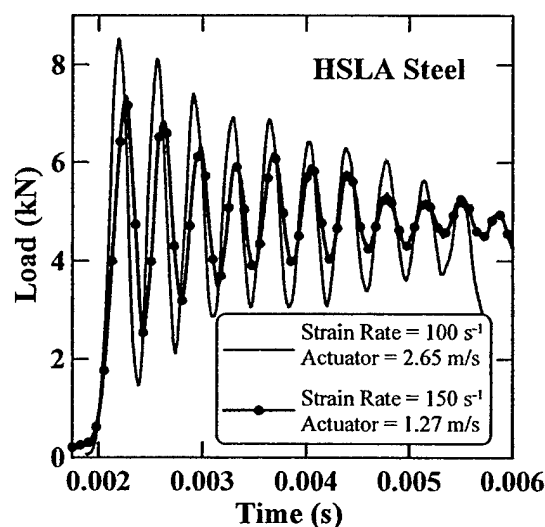


Figure 4.6: Load versus time plot for two HSLA-1 steel tensile samples with different gage lengths. One sample (solid line) had a gage length of 25.4 mm and the other sample had a gage length of 12.7 mm. The smaller gage length sample provided a higher strain rate even with a lower actuator velocity. The lower actuator velocity resulted in lower amplitude oscillations in the load washer data.

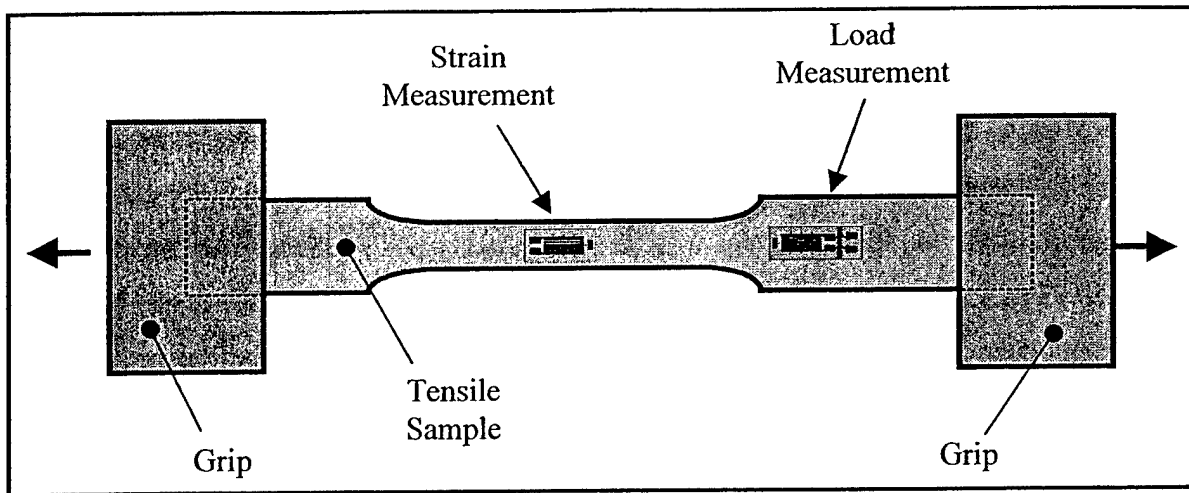


Figure 4.7: Schematic drawing of tensile sample with strain and load measurement strain gages attached.

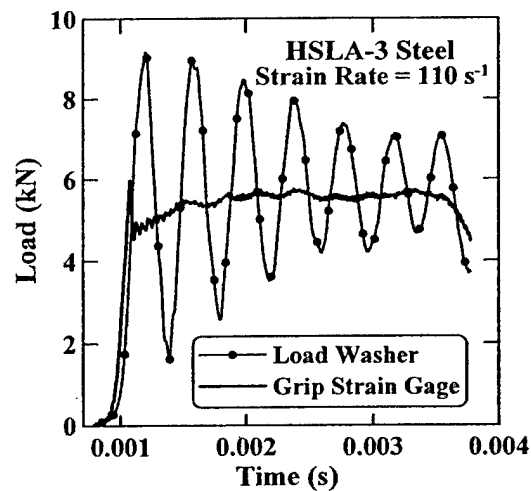


Figure 4.8: Load versus time plot for HSLA-3 steel tensile test at an engineering strain rate of 110 s^{-1} . Load data from a piezoelectric load washer are compared with load data gathered using a grip section strain gage. Sample gage length was 25.4 mm and actuator velocity was 2.8 m/s.

The use of a grip section strain gage for acquiring load data requires that the grip section of the tensile sample remain in the elastic deformation region during the entire

tensile test. Therefore, tensile samples were designed with appropriate grip-section/gage-section width ratios to ensure the grip sections did not plastically deform during testing. Details of tensile sample geometry are discussed in Section 4.2.

In addition to the ringing problems associated with using the piezoelectric load washer, loading by stress waves traveling through the load train causes a time delay between strain measurement on the sample and load measurement at the load washer. In samples instrumented with a grip section strain gage, this time lag can be measured by plotting the grip section strain gage data and the load washer data versus time as shown in Figure 4.9, and simply reading the time delay between the two signals. In Figure 4.9, the time delay is approximately 50 μ s. During the test shown in Figure 4.9, there was a distance of about 150 mm between the grip section strain gage and the load washer, which corresponds to a stress wave velocity of 3000 m/s.

Since the grip section strain gage is also located a finite distance away from the gage section strain gage, the load data obtained from the grip section strain gage should be shifted in time to make them coincident with the strain data. In this case, an elastic stress wave velocity of 5200 m/s [25 (p. 78)] can be used to calculate the time shift for steel tensile samples.

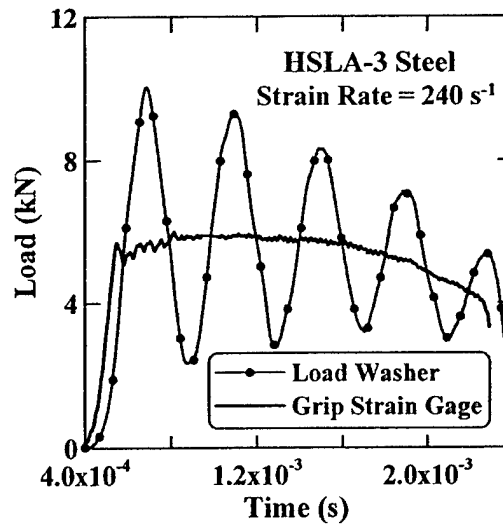


Figure 4.9: Load versus time plot for HSLA-3 steel tensile test at an engineering strain rate of 240s^{-1} . Load data from a piezoelectric load washer lags load data gathered using a grip section strain gage by about $50\text{ }\mu\text{s}$. Tensile sample gage length = 25.4 mm and actuator velocity = 6.1 m/s.

4.2 Test Sample Details

Initial samples made for testing in the high-rate system were machined according to the standard ASTM E-8 specifications. However, the long (50.8 mm, 2 in) gage length of these samples, limited the maximum achievable strain rate to about 200 s^{-1} . Therefore, samples were also created according to the subsize ASTM E-8 specifications, which stipulate a 25.4 mm (1 in) gage length, and other samples made with 12.7 mm (0.5 in) gage lengths. After it was decided to use the grip section of each sample as the load cell for high-rate testing, further changes to the sample geometry were made to preclude plastic deformation in the grip sections of the samples. Details of ASTM E-8 and other tensile sample dimensions are contained in Appendix B.

4.3 Data Collection & Reduction Methods

The MTS high-rate system used for all tensile testing is capable of running displacement-control tests over a wide range of actuator speeds. The lowest possible speed has not been determined, but the lowest speed used was about 0.05 mm/s which was used to achieve strain rates of about 10^{-3} s^{-1} in tensile samples with 50.4 mm gage lengths. For low rate testing, the MTS TestWareTM program was used to collect data. At the TestWareTM maximum acquisition rate of 5000 Hz, if a minimum of 500 data points are desired for a particular test, the test duration must be at least 100 ms. If a maximum total strain of 30% under constant strain rate is assumed, a 100 ms duration test translates to a strain rate of 3 s^{-1} , which is then the maximum strain rate at which the minimum number of data points can be collected using the TestWareTM program.

For strain rates greater than 3 s^{-1} , a commercially available software program, National Instruments (NI) VirtualBench ScopeTM, was used to collect data in conjunction with a National Instruments high-rate data acquisition circuit board (model PCI-6110E). The NI system allows data collection at speeds up to 5 MHz. Using 30% total strain and constant strain rate assumptions along with 500 data points desired, the NI system is sufficient to gather data at strain rates up to 3000 s^{-1} .

Both the MTS TestWareTM and NI data collection systems provide time, actuator displacement, load from the load washer, strain from the gage section strain gage, and strain from the grip section strain gage for each data point. Each set of raw data was imported to an ExcelTM file where further calculations could be performed.

As mentioned in Section 4.1.2, load data gathered from the piezoelectric load washer were adequate for tests run at strain rates at and below about 10 s^{-1} . Above that strain rate, load washer ringing was significant and grip section strain gages were used to acquire reasonable load information.

Analyses of stress-strain curve shapes, and how those shapes change with strain rate, are very important to understanding material behavior. Therefore, standard methods

were developed to convert raw data gathered either from the TestWareTM or NI system into engineering and true stress-strain curves.

4.3.1 Conversion of Raw Data Into Stress-Strain Curves

In this section, two typical sets of tensile test data are used to show how both low-rate and high-rate raw data were converted into stress-strain curves. The example tensile tests were run on dual phase (DP) steel, with dimensions shown in Table 4.1, at engineering strain rates of approximately 1 s^{-1} and 100 s^{-1} . Ten steps described below were followed to create stress-strain curves.

Table 4.1: Nominal dimensions of dual phase (DP) steel tensile samples.

Overall Length	200 mm
Thickness	1.4 mm
Gage length of reduced section	25.4 mm
Width of reduced section	6.4 mm
Width of grip section	19.1 mm

1. Correct both gage section and grip section strain data for Wheatstone Bridge non-linearity using Equations 4.1 and 4.2 as described in Section 4.1.1.

2. Plot engineering strain versus time as shown in Figure 4.10. Gage section strain gages for these dual phase steel examples remained attached for a large portion of each test. For the low rate test, the arrow in Figure 4.10a indicates where the strain gage completely detached from the sample at slightly more than 0.18 engineering strain. For the high-rate test shown in Figure 4.10b, the strain gage remained attached up to about 0.3 engineering strain. However the apparent reduction in strain rate between about 0.17 and 0.22 strain (shown by the arrow in Figure 4.10b) is most likely due to a partial

debonding of the gage before its complete failure around 0.3 strain. Therefore, the strain rate for the high rate test will be calculated using the strains below 0.17.

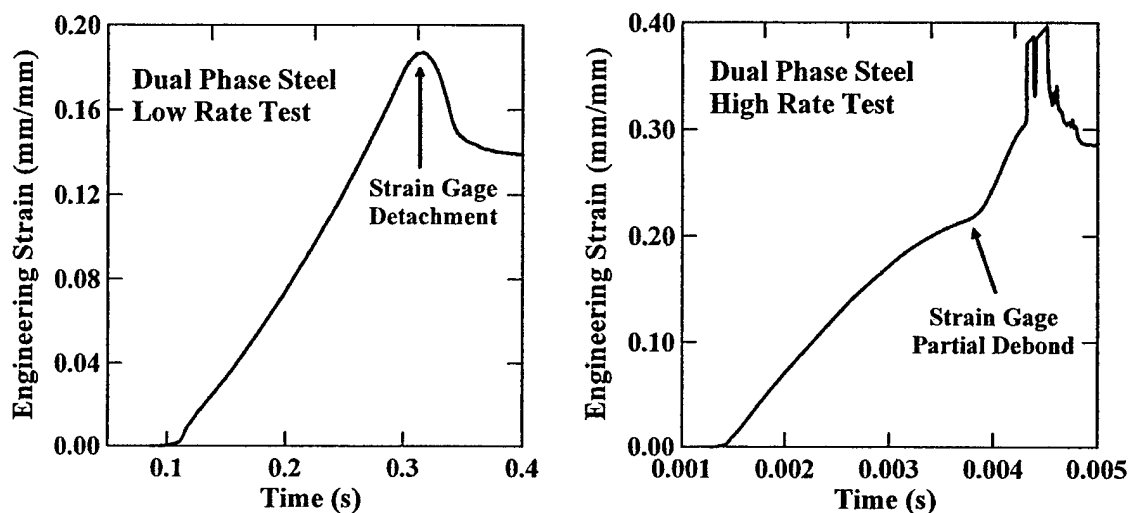


Figure 4.10: Engineering strain versus time for two dual phase steel tensile tests.

a) Low rate test with gage length = 25.4 mm and actuator velocity = 25 mm/s. b) High rate test with gage length = 25.4 mm and actuator velocity = 2.7 m/s.

3. Determine engineering strain rate by fitting a straight line through the linear part of the engineering strain versus time plot as shown in Figure 4.11. For these examples, the engineering strain rate for the low rate test was calculated to be 0.94 s^{-1} and for the high rate test to be 110 s^{-1} .

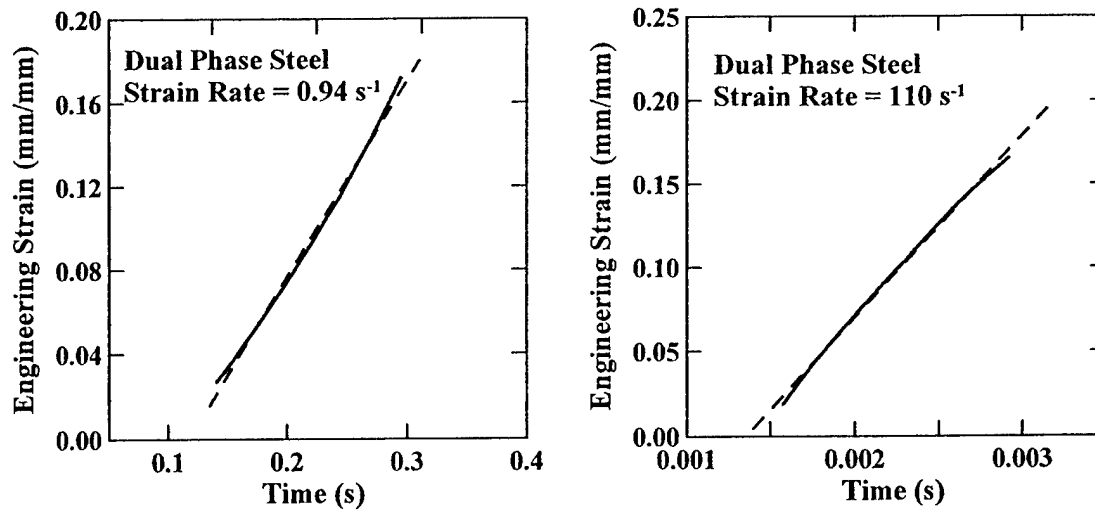


Figure 4.11: Linear portion of the engineering strain versus time plots from Figure 4.10 for two dual phase steel tensile tests. In each figure, the dashed line is the linear curve fit. a) Low rate test with gage length = 25.4 mm and actuator velocity = 25 mm/s. b) High rate test with gage length = 25.4 mm and actuator velocity = 2.7 m/s.

4. Since actuator velocity is constant, engineering strain rate can be assumed constant through the uniform strain portion of the tensile test. Therefore, strain data can be extrapolated past the last good strain data point using the strain rate and time. The calculation is shown in Equation 4.3.

$$e_x = e_{x-1} + \dot{e}(t_x - t_{x-1}) \quad [4.3]$$

e_x = engineering strain at data point x

e_{x-1} = engineering strain at data point (x-1)

\dot{e} = engineering strain rate

t_x = time at data point x

t_{x-1} = time at data point (x-1)

5. Calculate engineering stress. This calculation is straightforward for low rate tests, as shown in step 5A, but is more complicated for high rate tests, as shown in steps 5B-1 through 5B-4.

5A. For low rate tests, calculate engineering stress using Equation 4.4.

$$s = \frac{F}{w \cdot t} \quad [4.4]$$

s = engineering stress

F = load (from the piezoelectric load washer)

w = tensile sample gage section width

t = tensile sample thickness

5B. For high rate tests, the calculation of engineering stress required several steps, since the grip section strain gage data were used for load information. The following steps were used to determine engineering stress for high rate tests:

5B-1. Determine the elastic modulus of the material. For steel, the elastic modulus is about 200 GPa. A more accurate value for the particular material tested can be determined by plotting engineering stress versus engineering strain for the grip section of a tensile sample during a low rate test on the same material. The grip section engineering stress was calculated using Equation 4.4 with the tensile sample grip section width instead of the gage section width. As long as the grip section of the tensile sample remained in the elastic region, the plot of grip section engineering stress versus strain was a straight line with the elastic modulus of the material being the slope of that line as shown in Figure 4.12. Figure 4.12 is a plot of engineering stress versus engineering strain for the grip section of the dual phase steel low rate tensile test. The approximate

value of the elastic modulus for this particular material was 192 GPa. The value is approximate because it may vary slightly depending on the placement of the strain gage on the tensile sample grip section due to stress concentrations caused by the gripping of the sample and the fillets used to transition to the reduced section of the sample.

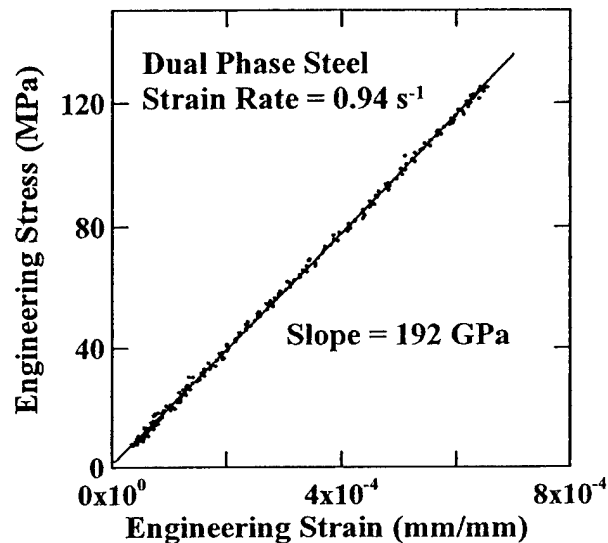


Figure 4.12: Engineering stress versus engineering strain for the grip section of a dual phase steel low rate test. The slope of the plot gives the material's elastic modulus. Sample gage length = 25.4 mm and actuator velocity = 25 mm/s.

5B-2. Convert grip section strain data to load data. Assuming the grip section remained in the elastic region, the load was calculated using the elastic modulus and grip section dimensions as shown in Equation 4.5.

$$F_{\text{grip}} = t \cdot w_{\text{grip}} \cdot E \cdot e_{\text{grip}} \quad [4.5]$$

F_{grip} = load calculated from the grip section strain gage

t = tensile sample thickness

w_{grip} = tensile sample grip section width

E = tensile sample elastic modulus

e_{grip} = grip section engineering strain

5B-3. Compare grip section load data to piezoelectric load washer load data.

Ringings associated with load data from the load washer is caused by oscillations around a mean value which is the actual load signal. Therefore, if there were sufficient oscillations in the load washer data, a simple data averaging routine yielded the actual load values. The data-averaging technique required calculating a running average of the load data, which worked well for post-yield load information when there were several oscillations during the test, but did not provide details of the elastic to plastic transition (which is why the grip section strain gages were used). The data-averaged load values from the load washer at large strains were used to verify the amplitude of the grip section strain gage load values. As mentioned previously, location of the grip section strain gage may cause slight differences in the load information it provides, and may require slight adjustment of the elastic modulus value used in Equation 4.5. Therefore, comparing the grip section strain gage load data to the load washer load data provided more accurate load information. An example of this procedure is shown in Figure 4.13, where load versus time data are plotted for the load washer, the grip section strain gage, and the data averaged load washer information. In Figure 4.13a, the elastic modulus calculated in step 5B-1 (192 GPa) was used to determine the load values from the grip section strain gage. Since those values were higher than the data-averaged load washer curve, the elastic modulus was modified to 189 GPa and plotted again in Figure 4.13b.

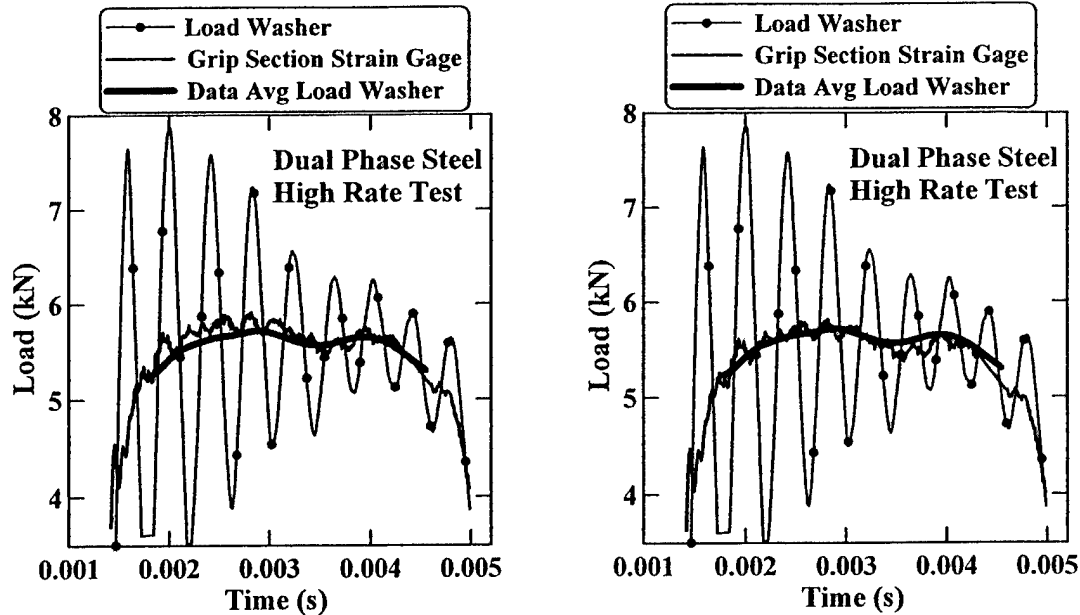


Figure 4.13: Load versus time plots comparing piezoelectric load washer, grip section strain gage and data-averaged load washer data for a dual phase steel high rate test. Tensile sample gage length = 25.4 mm and actuator velocity = 2.7 m/s. (a) Elastic modulus of 192 GPa used to calculate grip section strain gage loads. (b) Elastic modulus of 189 GPa used to calculate grip section strain gage loads.

5B-4. Calculate engineering stress using the grip section load. The same procedure as used for the low rate tests was used to calculate engineering stress from Equation 4.6.

$$s = \frac{F_{\text{grip}}}{w \cdot t} \quad [4.6]$$

s = engineering stress

F_{grip} = load calculated from the grip section strain gage

w = tensile sample gage section width

t = tensile sample thickness

6. Calculate true strain and true stress values. True strain and true stress are calculated from the engineering strain and stress values using Equations 4.7 and 4.8, which may only be used up to the uniform strain limit (before the onset of necking) of the material.

$$\epsilon = \ln (1 + e) \quad [4.7]$$

$$\sigma = s (1 + e) \quad [4.8]$$

ϵ = true strain

e = engineering strain

σ = true stress

s = engineering stress

7. Determine the uniform strain limit. There are a variety of different ways to do this. If the material exhibits a high degree of strain hardening, the simplest method was to plot the engineering stress-strain curve and visually find the ultimate tensile strength (UTS) value which corresponded to the point of maximum uniform strain. This method was used whenever possible. One could also simply find the maximum load value in the data set and then choose the corresponding strain value. Another, and more accurate, method was to plot the true stress-strain curve and on the same graph also plot $d\sigma/de$ versus true strain. The point at which the curves cross is the uniform strain limit [30 (p. 289-290)]. A graphical method called Considère's construction [30 (p. 290)] can also be used where true stress is plotted versus engineering strain and a line drawn from a point where engineering strain is equal to -1, to the tangent of the curve. The tangent point corresponds to the uniform strain limit. Finally, if the tensile sample exhibits a localized region of necking (versus a diffuse neck) and sufficient length of the reduced section

existed outside of the necked region, measurements of the width and thickness of the uniformly strained portion gave an estimate of the uniform strain limit according to Equation 4.9 [30 (p. 286)]. Note that the error in this calculation is greatly increased if the sample dimensions (especially thickness) are small.

$$\epsilon_u = \ln \left(\frac{w_o \cdot t_o}{w_u \cdot t_u} \right) \quad [4.9]$$

ϵ_u = true uniform strain

w_o = gage section width before testing

t_o = gage section thickness before testing

w_u = gage section width in the uniform strain region after testing

t_u = gage section thickness in the uniform strain region after testing

For the example dual phase steel samples, several different methods were used to determine the uniform strain limits with the results listed in Table 4.2. From Table 4.2, it is clear that methods 1 through 4 give very similar results for each sample, while method 5 gave similar results to methods 1 through 4 for the low rate sample and gave a significantly higher result for the high rate sample. For these examples, both the low rate and high rate samples exhibited fairly diffuse necked regions, with the high rate sample being more diffuse than the low rate sample. A diffuse necked region made the measurement of the uniform strain area difficult and therefore was not a reliable measure of uniform strain for these samples. For materials (such as dual phase steel) that exhibited a high degree of strain hardening, method 1 was used to determine the uniform strain limit. Methods 1 and 4 become more difficult with a material that has a low degree of strain hardening, and method 3 may be required. As strain rate increases, the stress-strain curve becomes more noisy, which makes methods 2 and 3 unreliable. In the case

of a noisy stress-strain curve, method 1 was used if practical (high degree of strain hardening). If the stress-strain curve was noisy and had little strain hardening, method 5 was used to find the uniform strain limit, or method 3 was used after a smooth stress-strain plot was created by performing a curve fit of the data.

Table 4.2: True uniform strain limits based on different calculation methods for two different rate tensile tests on dual phase steel.

Calculation Method	True Uniform Strain Limit (mm/mm)	
	Low Rate Test	High Rate Test
1. Visual plot of engineering stress-strain	0.158	0.141
2. True strain corresponding to maximum load	0.161	0.146
3. Intersection of true stress-strain & $d\sigma/d\varepsilon$ vs. ε	0.161	0.142
4. Considère's construction	0.157	0.141
5. Measurement of sample dimensions	0.162	0.185

8. Estimate engineering strain values beyond the uniform strain limit up to tensile sample fracture. Before each tensile test was run, gage length marks were placed on the sample so that the total elongation could be measured after sample fracture. This total elongation was used to calculate the engineering strain value at fracture using Equation 4.10.

$$e_f = \frac{L_f - L_o}{L_o} \quad [4.10]$$

e_f = engineering fracture strain

L_f = length between gage marks after fracture

L_o = length between gage marks before testing

The engineering strain rate could only be assumed constant up to the uniform strain limit because the strain was concentrated in the necked region after that point. To plot the entire engineering stress-strain curve, the post-uniform strain values had to be estimated. To accomplish this, the strain rate after necking was assumed to be a constant value different from the strain rate before necking. The strain rate value was chosen so that the predicted fracture strain would match the actual measured fracture strain.

9. Plot engineering stress-strain curves. Engineering stress-strain curves for the dual phase steel examples are shown in Figure 4.14.

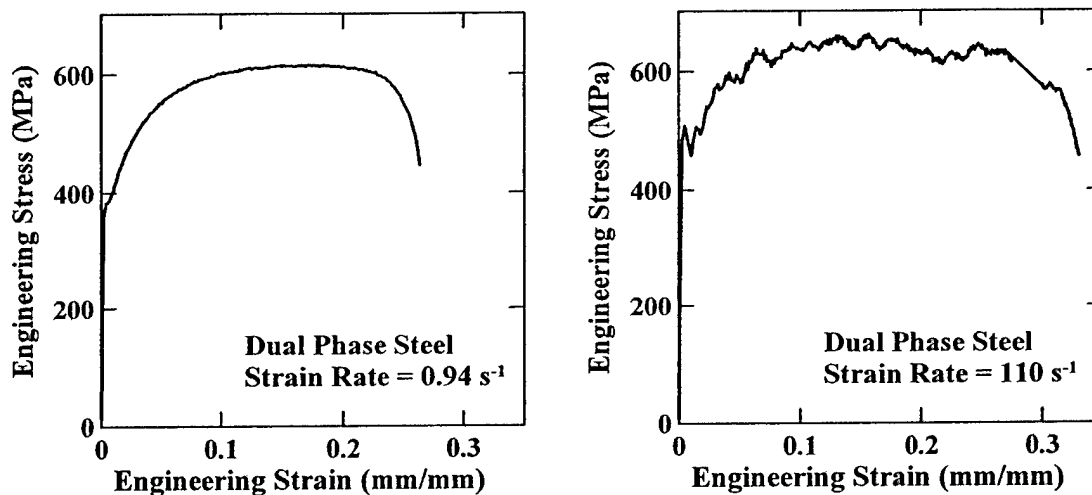


Figure 4.14: Engineering stress-strain curves for dual phase steel tensile tests at two different strain rates. a) Low rate test with gage length = 25.4 mm and actuator velocity = 25 mm/s. b) High rate test with gage length = 25.4 mm and actuator velocity = 2.7 m/s.

10. Plot true stress-strain curves. True stress-strain curves plotted up to the uniform strain limit for the dual phase steel examples are shown in Figure 4.15.

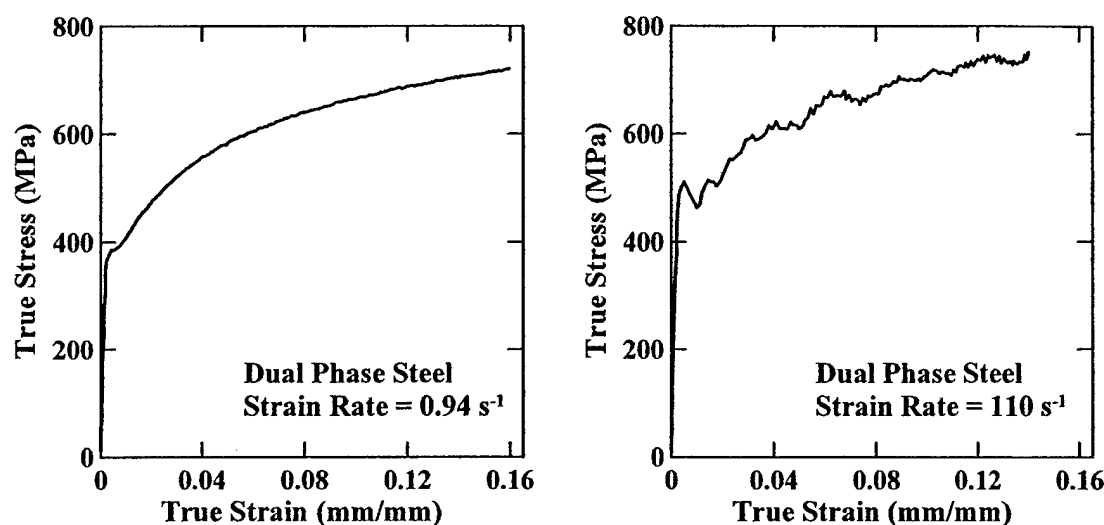


Figure 4.15: True stress-strain curves for dual phase steel tensile tests at two different strain rates. a) Low rate test with gage length = 25.4 mm and actuator velocity = 25 mm/s. b) High rate test with gage length = 25.4 mm and actuator velocity = 2.7 m/s.

4.3.2 Interpreting Anomalous Strain and Load Data

The strain versus time curves (Figure 4.10) presented in Section 4.3.1 were typical for samples that did not exhibit a high amount of yield point elongation (YPE), while the grip section strain gage load data shown in Figure 4.13 were typical for grip section strain gages that remained perfectly bonded during the entire test and for tensile samples that did not experience plastic deformation in the grip section. However, some materials did exhibit significant YPE, grip section strain gages did not always stay completely attached to the sample, and some tensile samples experienced plastic deformation in the grip section. Therefore, interpretation of strain and load information was not always straightforward.

Conducting tensile tests using constant actuator velocity on materials with significant YPE caused an increase in local strain rate during the YPE, followed by a lower strain rate afterwards. A low-rate engineering stress-strain curve for IF-1 steel exhibiting YPE extending to almost 0.07 strain is shown in Figure 4.16a. Figure 4.16b

shows the engineering strain versus time plot for the same tensile test. In Figure 4.16b, the strain rate below 0.07 strain is about double the strain rate later in the test. For materials exhibiting YPE, quoted strain rates were those calculated using strain values beyond the YPE.

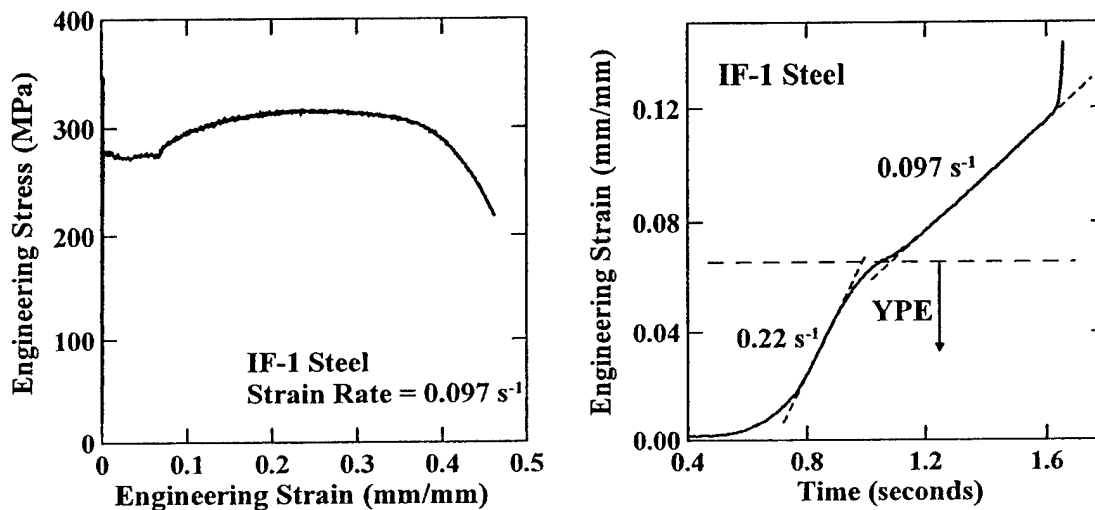


Figure 4.16: Tensile test results for IF-1 steel sample with gage length of 25.4 mm run using an actuator velocity of 27 mm/s. a) Engineering stress-strain curve showing yield point elongation (YPE) up to nearly 0.07 strain. b) Engineering strain versus time plot showing difference in strain rates for YPE region and the rest of the test.

Occasionally, the grip section strain gage partially debonded during the tensile test. This was noticeable by a drop in the load data calculated using the grip section strain gage compared to the load washer information as demonstrated in Figure 4.17a, where the grip section strain gage experienced partial debonding at the location shown by the arrow. For some tests, the grip section of a tensile sample did not remain in the elastic region during the entire tensile test, causing the correlation between the actual load and grip section strain gage data to become nonlinear. This was evidenced by a rapid

increase in load data calculated using the grip section strain gage compared to the load washer information as shown in Figure 4.17b. If there were sufficient oscillations in the load washer data, the test information was still useable. For both cases, the solution was to use load data calculated from the grip section strain gage up to the point where it became unreliable either due to gage debonding or plastic deformation. After that point, the data-averaged load washer data were used to complete the load time curve as shown in Figure 4.18.

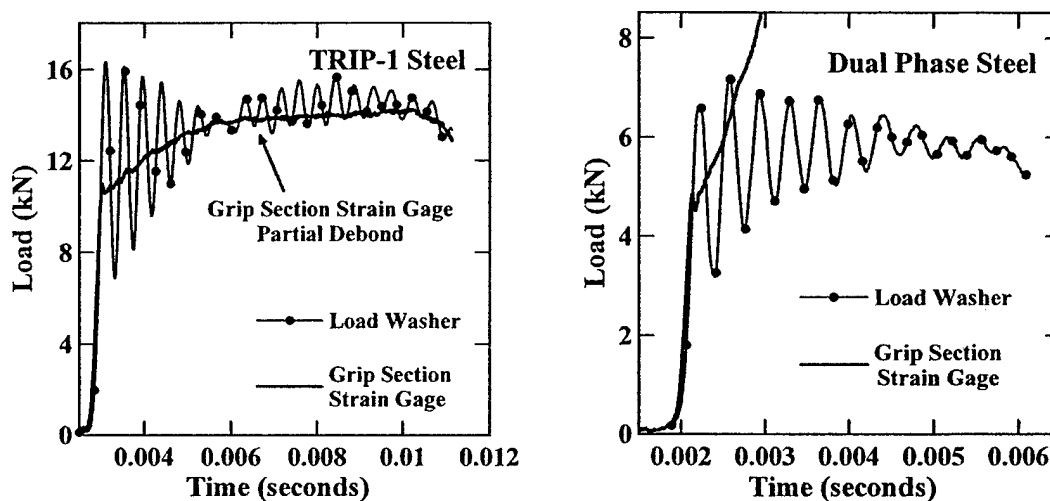


Figure 4.17: Load versus time plots comparing piezoelectric load washer and grip section strain gage data. a) Grip section strain gage partial debond location shown by arrow. TRIP-1 steel with tensile sample gage length = 12.7 mm and actuator velocity = 350 mm/s. b) Tensile sample grip section experiences plastic deformation. Dual phase steel with tensile sample gage length = 25.4 mm and actuator velocity = 2.7 m/s.

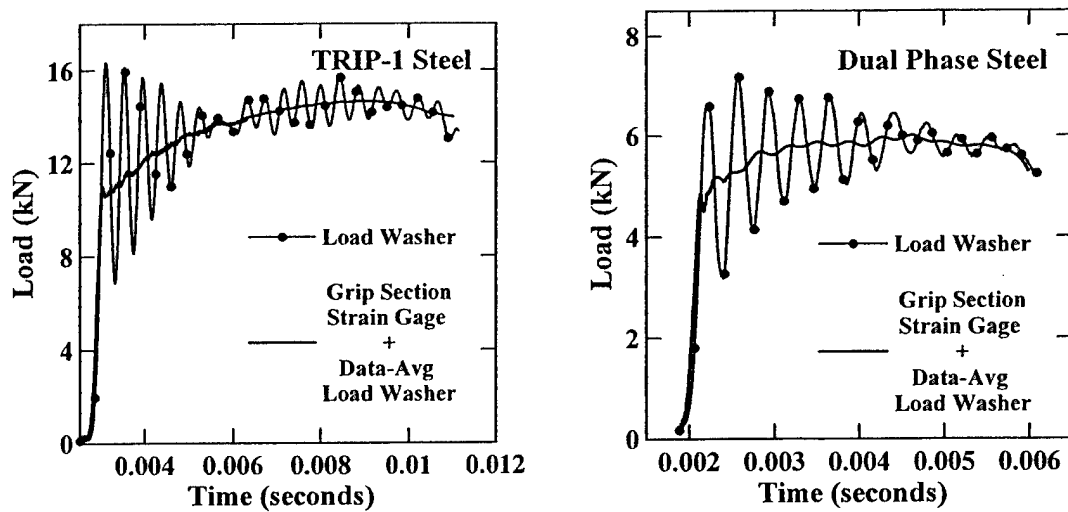


Figure 4.18: Figure 4.17 data re-plotted using data-averaged load washer signal after the grip section strain gage data becomes unreliable. a) TRIP-1 steel with tensile sample gage length = 12.7 mm and actuator velocity = 350 mm/s. b) Dual phase steel with tensile sample gage length = 25.4 mm and actuator velocity = 2.7 m/s.

4.3.3 Determination of Mechanical Properties

In addition to knowing the shapes of stress-strain curves, often it is desirable to identify the yield strength, ultimate tensile strength (UTS) and strain hardening exponent for each tensile test. In general, the UTS value was the easiest mechanical property to determine. If the data collected were not “noisy”, the UTS was simply calculated as the engineering stress at the maximum load value. If the data were noisy, an engineering stress-strain curve was plotted and the UTS value determined visually. A definition of the term “yield strength” was required before that value could be determined. In keeping with standard practice, the 0.2% offset method was used for continuous-yielding materials, while the lower yield point was used for materials exhibiting yield point elongation behavior. Both of these methods required a visual inspection of the stress-strain curve.

The strain hardening exponent is “n” in Equation 4.11, which assumes that the flow curve of a material can be expressed as a simple power curve relation [30 (p. 287)]. If families of stress-strain curves were plotted on the same chart, a qualitative determination of degree of strain hardening was made by visual comparison of the curves. An example of this is shown in Figure 4.19 for the dual phase steel example tests. From Figure 4.19, it appears that the low rate test had a higher degree of strain hardening than the high rate test, which is typical for steel. To obtain a numerical value for the strain hardening exponent, a plot of log (stress) versus log (strain) was made, with “n” being the average slope of that plot. Such plots are shown in Figure 4.20 for the dual phase steel example tensile tests. In Figure 4.20, only one value was calculated for “n” for each test. However, if the plots were broken into two regions (low strain and high strain), two values for “n” could have been calculated, where the low strain values would be larger.

$$\sigma = K\epsilon^n \quad [4.11]$$

σ = true (flow) stress

K = strength coefficient

ϵ = true strain

n = strain hardening exponent

For the dual phase steel examples, the mechanical properties (yield strength, UTS and strain hardening exponent) are summarized in Table 4.3.

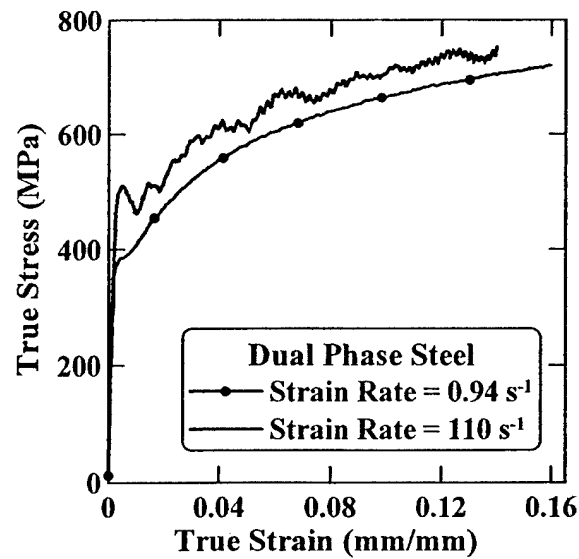


Figure 4.19: True stress-strain curves for dual phase steel tensile tests at two different strain rates. Low rate test used sample gage length = 25.4 mm and actuator velocity = 25 mm/s. High rate test used sample gage length = 25.4 mm and actuator velocity = 2.7 m/s.

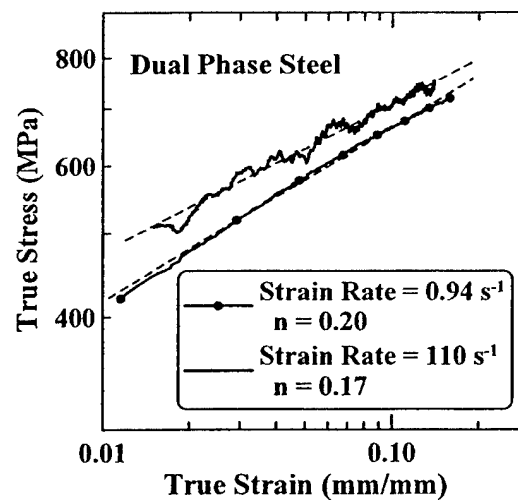


Figure 4.20: True stress-strain plots on a log-log scale for dual phase steel tensile tests at two different strain rates. The slope of each plot is the strain hardening exponent. Low rate test used sample gage length = 25.4 mm and actuator velocity = 25 mm/s. High rate test used sample gage length = 25.4 mm and actuator velocity = 2.7 m/s.

Table 4.3: Mechanical properties of dual phase steel for two different strain rates.

	Low Rate (0.94 s^{-1})	High Rate (110 s^{-1})
Yield Strength (MPa)	385	480
Ultimate Tensile Strength (MPa)	615	650
Strain Hardening Exponent	0.203	0.172

4.4 Validation of High-Rate Test Methods

Several experiments were conducted to verify the accuracy of results obtained using the MTS high-rate tensile test system. These experiments included a comparison between stress-strain curves obtained using a screw-driven tensile test machine with low-rate test run on the MTS high-rate machine, an investigation of the effects of using samples with different geometries, determination of the low-strain region accuracy of stress-strain curves at high rates, and evaluation of the repeatability of results.

4.4.1 Comparison of Screw-Driven and High-Rate Tensile Test Machine Results

Ultra-low carbon (ULC) and HSLA-1 steel tensile samples, with dimensions shown in Table 4.4, were initially used to develop experimental procedures. Low-rate tensile tests using HSLA-1 and ULC-D samples were run on an MTS screw-driven tensile test machine with a conventional load cell and contact extensometer. These results were compared with the MTS high-rate machine data to ensure accuracy of the high-rate machine results at low strain rates. For these tests, crosshead speed on the screw-driven machine and actuator speed on the high-rate machine were set to the same value.

Table 4.4: Nominal dimensions of ULC-D and HSLA-1 steels used for low-rate tensile test comparison between screw-driven and high-rate machines.

Dimension	ULC-D	HSLA-1
Overall Length	240 mm	200 mm
Gage length of reduced section	76 mm	50.8 mm
Width of reduced section	12.7 mm	12.7 mm
Width of grip section	25 mm	19 mm

4.4.2 Geometry Change Effects

Tensile samples with different geometries were machined to achieve increased strain rates and to evaluate the effects of geometry on dynamic material properties. The specific gage lengths chosen were 50.8 mm, 25.4 mm, and 12.7 mm, which allowed maximum strain rates of about 250, 500, and 1000 s⁻¹, respectively, using the highest possible actuator velocity. To evaluate the potential effects of geometry on stress-strain behavior, tests were run on HSLA-1, HSLA-2 and TRIP-1 steels using different gage length samples, while setting actuator speeds to attain approximately the same strain rates. Tensile sample nominal dimensions are shown in Table 4.5. During testing, it was noticed that thinner samples produced “noisier” stress-strain curves than thicker samples. An investigation of the cause of the noisiness was conducted using ULC-C, IF-1, IF-2 and IF-3 steels with different sheet thicknesses ranging from 0.72 mm to 4.1 mm.

Table 4.5: Nominal dimensions of steel samples used for geometry comparison tensile tests.

Material Designation	Gage Section Length (mm)	Gage Section Width (mm)	Grip Section Width (mm)
HSLA - 1	50.8	12.7	19
	25.4	6.35	10
HSLA - 2	50.8	12.7	25
	25.4	6.4	16
	12.7	6.4	16
TRIP-1	50.8	12.7	25
	25.4	6.4	16
	12.7	6.4	16

4.4.3 Accuracy of Low-Strain Region of the Stress-Strain Curve

Many types of steel exhibit yield point elongation behavior which may change with strain rate. To accurately record this information, it is important to gather stress-strain data that reflect true material behavior and are not corrupted by artifacts of the testing techniques. To make sure that the test techniques described in Section 4 reveal actual material behavior, it was decided to test a pure FCC material known to exhibit continuous-yielding at all strain rates. The material selected was 11000-H00 commercially pure copper (99.9% Cu) with thickness chosen so that the loads imposed during testing would be similar to those experienced by steel samples. This material was machined into tensile samples with nominal dimensions shown in Table 4.6 and tested over a range of strain rates from quasi-static up to about 400 s^{-1} .

Table 4.6: Nominal dimensions of 11000-H00 Cu used for tensile tests.

Overall Length	200 mm
Gage length of reduced section	25.4 mm
Width of reduced section	6.35 mm
Width of grip section	18 mm

4.4.4 Repeatability of Tests

Whenever tensile testing was conducted, typically two or three samples were tested at the same strain rate to check consistency of the results and to reveal statistical scatter in the properties of the material. It is important that the testing technique not contribute to the scatter and thus mask actual material behavior. Therefore, several tests were run at a variety of strain rates on a commercially-produced material believed to have consistent properties. The material chosen was HSLA-2 steel.

4.5 Presentation of Results

There are a wide variety of options to choose from when presenting tensile test data, and the choice of which one(s) to use depends on the information important to the user of the data. Much information about how material behavior changes with strain rate can be gathered from simply plotting families of stress strain curves. Often, strain rate sensitivity plots are made to show the effect of strain rate on either the yield strength or UTS values. Strain rate sensitivity is commonly defined as the slope of a plot of $\log(\sigma)$ versus $\log(\dot{\epsilon})$, where “m” is the strain rate sensitivity in Equation 4.12. However, for steels [30 (p. 297), 38, 115-119], a semilogarithmic relationship may be used, where the strain rate sensitivity, “ β ” in Equation 4.13, is the slope of a plot of σ (on a linear scale) versus $\log(\dot{\epsilon})$. Both definitions of strain rate sensitivity assume that the test temperature and plastic strain value are held constant. Other properties can also be plotted as a function of strain rate to easily show their strain rate dependence. When comparing

various materials to each other for a high-rate application, it is often desired to plot a particular value, such as strain rate sensitivity, dynamic/static strength ratio, or ($\sigma_{\text{dynamic}} - \sigma_{\text{static}}$), for each material versus the material's quasi-static yield or tensile strength.

$$\sigma = C(\dot{\epsilon})^m \quad [4.12]$$

σ = flow stress

C = material constant

$\dot{\epsilon}$ = strain rate

m = strain rate sensitivity

$$\sigma = \beta \log (\dot{\epsilon}) + K \quad [4.13]$$

σ = flow stress

K = material constant

$\dot{\epsilon}$ = strain rate

β = strain rate sensitivity

4.6 Strengthening Mechanisms: Cold Work

Tensile samples with dimensions shown in Table 4.7 were machined from IF-2 steel. Samples were divided into five groups for different amounts of pre-straining: 0%, 2%, 5%, 10% and 18%. An MTS screw-driven machine (Alliance RT/100) was used with an Instron 25.4 mm gage length 50% extensometer (model # G51-12, serial # 2065) and MTS TestWorks 4TM software to perform tensile pre-straining using a crosshead speed of 0.01 mm/s resulting in engineering strain rates of about $4 \times 10^{-4} \text{ s}^{-1}$ for all pre-

strain procedures. Gage marks were placed on the reduced section of each sample at an initial distance of 25.4 mm. The distance between gage marks was accurately measured before and after pre-straining using a traveling microscope to verify the actual amount of pre-strain imparted to each sample. For each group of 21 samples, the minimum, maximum, mean and standard deviation values for the amount of pre-strain accomplished are shown in Table 4.8. After completion of pre-strain, samples were placed in a freezer at -20°C to prevent strain aging. Samples were prepared for tensile testing and tested as quickly as possible following removal from the freezer. Since the adhesive used to attach the high elongation strain gages required an overnight curing time, total time between removal from the freezer and actual testing was at least 24 hours but not more than 48 hours.

Table 4.7: Nominal dimensions of IF-2 steel tensile samples (before pre-strain).

Dimension	IF-2
Overall Length	215 mm
Gage length of reduced section	25.4 mm
Width of reduced section	5.75 mm
Width of grip section	24 mm

Table 4.8: Statistical analysis of pre-strain data for IF-2 tensile samples.

Pre-Strain	Minimum	Maximum	Mean	Std. Dev.
2%	2.04%	2.34%	2.20%	0.09%
5%	4.79%	5.27%	5.07%	0.14%
10%	9.77%	10.12%	9.96%	0.12%
18%	17.65%	18.05%	17.81%	0.14%

Each of the five pre-strain groups of IF-2 steel samples were tensile tested at strain rates ranging from about 0.001 to 500 s⁻¹, according to the test matrix shown in

Table 4.9. Since the initial gage length of the tensile samples increased with increasing amount of pre-strain, actuator speeds were adjusted appropriately to attain the target strain rates for each pre-strain group.

Table 4.9: Test matrix for IF-2 steel tensile tests.

Target Strain Rate (s^{-1})	0.001	0.1	1	10	30	60	100	500
# of Samples	2	2	2	2	2	2	2	2

4.7 Strengthening Mechanisms: Solid Solution Strengthening

Experiments to determine the effects of strain rate on solid solution strengthening were conducted on two IF steels with different compositions and two HSLA steels with different compositions as discussed in the following sections.

4.7.1 IF Steel

Tensile samples were prepared from IF-3 and IF-4 steel. IF-4 steel has a greater degree of solid solution strengthening than IF-3 steel due to greater amounts of Mn and P. Three different gage section geometry samples with nominal dimensions shown in Table 4.10 were tested at strain rates ranging from 0.01 to 800 s^{-1} according to the test matrix shown in Table 4.11.

Table 4.10: Nominal dimensions of IF-3 and IF-4 steel tensile samples.

Dimension	IF-3A	IF-3B	IF-3C
Overall Length (mm)	192	175	164
Gage length of reduced section (mm)	50.8	25.4	12.7
Width of reduced section (mm)	12.7	6.4	6.4
Width of grip section (mm)	25	16	16
Dimension	IF-4A	IF-4B	IF-4C
Overall Length (mm)	192	175	164
Gage length of reduced section (mm)	50.8	25.4	12.7
Width of reduced section (mm)	12.7	6.3	6.4
Width of grip section (mm)	25	16	16

Table 4.11: Test matrix for IF-3 and IF 4 steel tensile samples used for solid solution strengthening study.

Target Strain Rate (s^{-1})	0.01	1	10	100	300	600	800
Designation & # of Samples Tested	A - 2 B - 1 C - 1	A - 3	A - 3	B - 3	B - 3	C - 3	C - 3

4.7.2 HSLA Steel

Tensile samples were prepared from HSLA-1 and HSLA-2 steel. HSLA-2 steel has a greater degree of solid solution strengthening than HSLA-1 steel due to greater amounts of Mn, P and Si. Three different gage section geometry samples with nominal dimensions shown in Table 4.12 were tested at strain rates ranging from 0.01 to 500 s^{-1} according to the test matrix shown in Table 4.13.

Table 4.12: Nominal dimensions of HSLA-1 and HSLA-2 steel tensile samples.

Material Designation		Gage Section Length (mm)	Gage Section Width (mm)	Grip Section Width (mm)
HSLA - 1	A	50.8	12.7	19
	B	25.4	6.35	10
	C	12.7	6.35	10
HSLA - 2	A	50.8	12.7	25
	B	25.4	6.4	16
	C	12.7	6.4	16

Table 4.13: Test matrix for HSLA-1 and HSLA-2 steel tensile samples used for solid solution strengthening study.

Target Strain Rate (s^{-1})	0.01	1	10	100	500
Designation & # of Samples Tested	A - 2 B - 1	A - 3	A - 3	B - 3	C - 3

4.8 Strengthening Mechanisms: Grain Size

Two separate studies were conducted to investigate the effects of strain rate on interstitial free steel with different grain sizes. In the first study, samples were prepared with four different grain sizes, ranging from 10 to 250 μm . Unfortunately, the tensile properties of samples produced with a grain size of 65 μm did not conform (at any strain rate) to the expected Hall-Petch relationship of decreasing strength with increasing grain size. This anomalous behavior is likely due to a change in some other microstructural parameter besides grain size during heat treating. However, the other three sets of grain size samples did follow a Hall-Petch relationship and their tensile data were analyzed. Due to the anomaly in the first grain size study, a second grain size study was initiated with samples created with grain sizes ranging from 15 to 200 μm . Unfortunately, again

only three of the four grain size sample sets created followed the Hall-Petch relationship and again it was speculated to be due to other microstructural differences created by variations in heat treating to achieve the desired grain sizes. In both grain size studies, the anomalous behavior of one set of grain size samples was most likely due to variations in precipitation strengthening, since both studies used interstitial free steels.

4.8.1 First Grain Size Study

IF-1 steel was heat treated to prepare samples with different grain sizes using the procedures listed in Table 4.14.

Tensile samples were prepared from each of the four grain-size materials with nominal dimensions shown in Table 4.15. The 10 μm and 25 μm samples maintained the as-received material thickness. The 65 μm and 135 μm samples were surface ground, resulting in thinner samples, because heat treating for these two grain sizes produced extremely uneven surfaces. Tensile tests were conducted at strain rates ranging from 0.001 to 500 s^{-1} according to the test matrix shown in Table 4.16.

Table 4.14: Heat treat procedures used on the IF-1 steel for the first grain size study.

Mean Grain Size Achieved (μm)	Heat Treatment
10	None (As Received Material)
25	Unknown
65	Heat as-received to 950°C, hold for 1 hour and air cool
135	Heat as-received to 1290°C, hold for 30 min and furnace cool at 0.75°C/min

Table 4.15: Nominal dimensions of IF-1 steel tensile samples used for the first grain size study.

Dimension	10 & 25 μm	65 μm	135 μm
Overall Length (mm)	143	143	143
Thickness (mm)	4.1	2.7 - 2.8	2.0 - 2.6
Gage length of reduced section (mm)	25.4	25.4	25.4
Width of reduced section (mm)	6.4	6.4	6.4
Width of grip section (mm)	10	10	10

Table 4.16: Test matrix for IF-1 steel tensile samples used for first grain size study.

Target Strain Rate (s^{-1})	0.001	0.1	1	10	30	60	100	500
# of Samples Tested	2	2	2	2	2	2	3	2

4.8.2 Second Grain Size Study

A second grain size study was initiated to verify results due to problems with the 65 μm grain size samples from the first grain size study. A fully-stabilized IF steel (IF-5) available at CSM as hot rolled 4.69 mm thick sheet was chosen for this grain size study. The as-received material was cut into 300 x 75 mm strips, pickled in 10% H_2SO_4 at 75°C for 3 minutes to remove oxide layers, and cold-rolled approximately 58% to final thickness of 1.99 mm. The cold-rolling was performed at the US Air Force Academy Department of Engineering Mechanics laboratory on a Stanat Model TA-215 rolling mill with 102 mm roller diameter and roller speed of 84 rpm.

Multiple heat treat processes were evaluated to determine the optimum heat treatment processes to achieve desired grain sizes. The heat treatment processes chosen along with the resulting average grain sizes are listed in Table 4.17. Tensile samples were prepared from each of the four grain-size materials with nominal dimensions shown

in Table 4.18. Tensile tests were conducted at strain rates ranging from 0.001 to 400 s⁻¹ according to the test matrix shown in Table 4.19.

Table 4.17: Heat treat procedures used on IF-5 steel for the second grain size study.

Mean Grain Size Achieved (μm)	Heat Treatment
10 μm	Recrystallization treatment: Hold at 700°C 3 hrs & air cool.
14 μm	Recrystallize. Hold at 900°C 240 hrs, furnace cool.
36 μm	Recrystallize. Hold at 1200°C 150 min, cool to 900°C, hold 150 min, furnace cool.
130 μm	Recrystallize. Hold at 1200°C 180 min, cool to 900°C, hold 240 min, furnace cool.

Table 4.18: Nominal dimensions of IF-5 steel tensile samples used for the second grain size study.

Dimension	
Overall Length (mm)	159
Gage length of reduced section (mm)	25.4
Width of reduced section (mm)	6.4
Width of grip section (mm)	16

Table 4.19: Test matrix for IF-5 steel tensile samples used for second grain size study.

Target Strain Rate (s ⁻¹)	0.001	0.1	1	10	40	80	150	400
# of Samples Tested of Each Grain Size	2	2	2	2	2	2	2	2

4.9 Strengthening Mechanisms: Multiphase TRIP Steel

TRIP-3 steel was processed to obtain differing degrees of stability in the retained austenite phase. Two different heat treatment processes along with resulting volume percentage of retained austenite and retained austenite carbon contents are shown in Table 4.20. The heat treatment designed for high stability retained austenite is designated “HS” and low stability by “LS”.

Tensile samples were prepared from the HS and LS materials with nominal dimensions shown in Table 4.21. Tensile tests were conducted at strain rates ranging from 0.01 to 600 s⁻¹ according to the test matrix shown in Table 4.22.

Table 4.20: Heat treatment details for TRIP-3 steel processed to achieve two different retained austenite stabilities.

	Intercritical Annealing Temp	Isothermal Treatment Temperature & Time	Retained Austenite (Volume Percent)	Retained Austenite (wt. pct. carbon)
HS	810 °C	450 °C, 3 minutes	9.8%	1.26
LS	810 °C	470 °C, 3 minutes	9.0%	1.17

Table 4.21: Nominal dimensions of TRIP-3 steel tensile samples used for the TRIP austenite stability study.

Dimension	TRIP-3A	TRIP-3B	TRIP-3C
Overall Length (mm)	192	175	164
Gage length of reduced section (mm)	50.8	25.4	12.7
Width of reduced section (mm)	12.7	6.4	6.4
Width of grip section (mm)	25	16	16

Table 4.22: Test matrix for TRIP-3 steel tensile samples used for the TRIP austenite stability study.

Target Strain Rate (s^{-1})	0.01	1	10	100	250	600
Designation & # of Samples Tested	A - 2 B - 1	A - 3	A - 3	B - 3	B - 3	C - 3

4.10 Multiphase Strengthening Mechanisms: Comparison of Dual Phase to TRIP Steel

Tensile samples were prepared from dual phase steel with nominal dimensions shown in Table 4.23. Tensile tests were conducted at strain rates ranging from 0.001 to 500 s^{-1} according to the test matrix shown in Table 4.24. These results were compared with those obtained for the TRIP-3 steels discussed in Section 4.9.

Table 4.23: Nominal dimensions of dual phase (DP) steel tensile samples.

Overall Length	200 mm
Thickness	1.4 mm
Gage length of reduced section	25.4 mm
Width of reduced section	6.4 mm
Width of grip section	19.1 mm

Table 4.24: Test matrix for dual phase steel tensile samples used for comparison to TRIP-3 steels.

Target Strain Rate (s^{-1})	0.001	0.1	1	10	30	60	100	300	500
# of Samples Tested	2	2	3	3	2	2	3	2	3

CHAPTER 5

RESULTS & DISCUSSION: DYNAMIC TENSILE TESTING

5.1 Validation of High-Rate Test Methods

Several experiments were conducted to verify the accuracy of results obtained using the MTS high-rate tensile test system. These experiments included a comparison between stress-strain curves obtained using a screw-driven tensile test machine with low-rate tests run on the MTS high-rate machine, an investigation of the effects of using samples with different geometries, determination of the accuracy of the low-strain region of stress-strain curves at high rates, and evaluation of the repeatability of results.

5.1.1 Comparison of Screw-Driven and High-Rate Tensile Test Machine Results

Several methods for conducting high-rate tensile testing were discussed in Section 2.1. Since the MTS high-rate system is a unique servo-hydraulic test machine, it was necessary to verify the accuracy of both load and strain measuring methods. This was accomplished by performing identical low-rate tensile tests on the high-rate system and on an MTS screw-driven tensile test machine which used a conventional load cell and contact extensometer. HSLA-1 and ULC-D samples were used for these tensile tests which used identical crosshead and actuator speeds for the screw-driven and high-rate machines, respectively. The resulting true stress-strain curves are shown in Figure 5.1, where it is clear that both the screw-driven and high-rate tensile test machines produced similar results, with less than two percent difference at any point in the curves. For each material shown in Figure 5.1, both the screw-driven and high-rate machine results show approximately the same shape and magnitude of the yield point elongation behavior. Therefore, the accuracy of the high-rate system is verified for low-rate tensile tests.

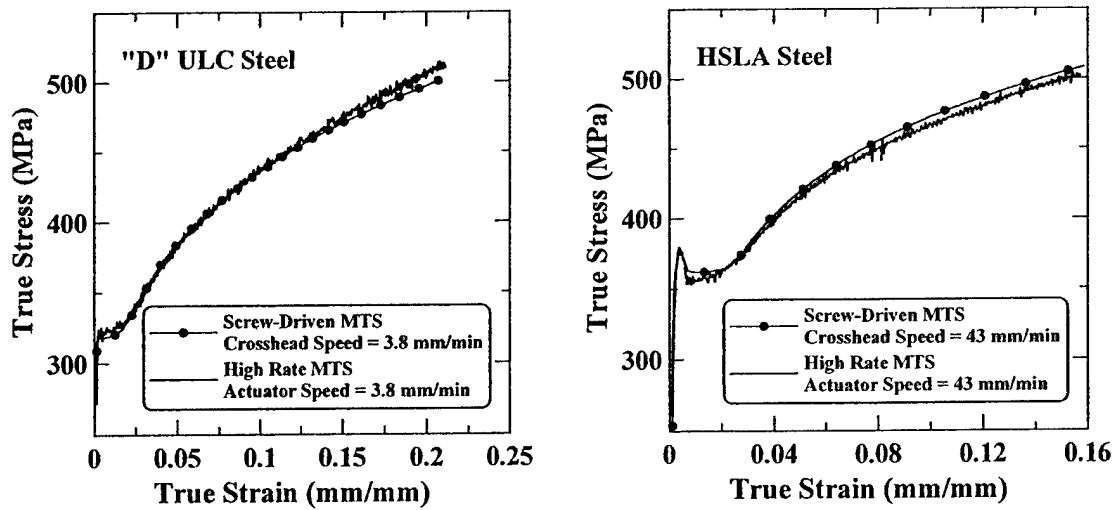


Figure 5.1: Comparison of low-rate true stress-strain curves for tensile tests run on screw-driven MTS and high-rate MTS tensile test machines at identical crosshead/actuator speeds for a) ULC-D steel with gage length of 76 mm and b) HSLA-1 steel with gage length of 50.8 mm. Results in both cases are similar.

5.1.2 Geometry Change Effects

The engineering strain rate, $\dot{\epsilon}$, of a tensile test may be calculated using Equation 5.1, where L is the tensile sample gage length and v is the displacement speed (actuator velocity).

$$\dot{\epsilon} = \frac{v}{L} \quad [5.1]$$

In Equation 5.1, if the velocity is constant and increased strain rate is desired, the gage length must be reduced. The maximum velocity attainable (under load) with the MTS high-rate system was about 10 m/s, which gives a maximum engineering strain rate of about 200 s^{-1} with a standard ASTM E-8 tensile sample which has a gage length of 50.8 mm. Reducing the sample gage length increases the maximum attainable strain rate.

Also, as discussed in Section 4.1.2, high-rate load measurement using a grip-section strain gage may require increasing the grip-section widths of tensile samples to avoid plastic deformation. The desire for higher strain rates and grip-section load measurement required various tensile sample geometries which differed from the ASTM E-8 standard. Therefore, it was necessary to determine whether these geometry changes changed the resulting stress-strain curves.

Tensile samples with different geometries were tested at similar strain rates to determine the effects of sample geometry on stress-strain curve results. Sample dimensions for each material were given in Table 4.5 in Section 4.4.2. True stress-strain curves for these tests on HSLA-1, HSLA-2, and TRIP-1 steels are shown in Figures 5.2 through 5.4 and engineering stress-strain curves for the HSLA-2 and TRIP materials are shown in Figures 5.5 and 5.6. Figures 5.2 - 5.4 suggest that sample geometry does not substantially affect true stress-strain behavior, which is in agreement with a similar study carried out by Clark and Wood [120]. Figures 5.5 and 5.6 show that decreasing gage length causes an apparent increase in engineering strain to failure, which is a well-known and expected result [30 (p. 280)] since the necked region is a larger portion of the gage length as gage length decreases.

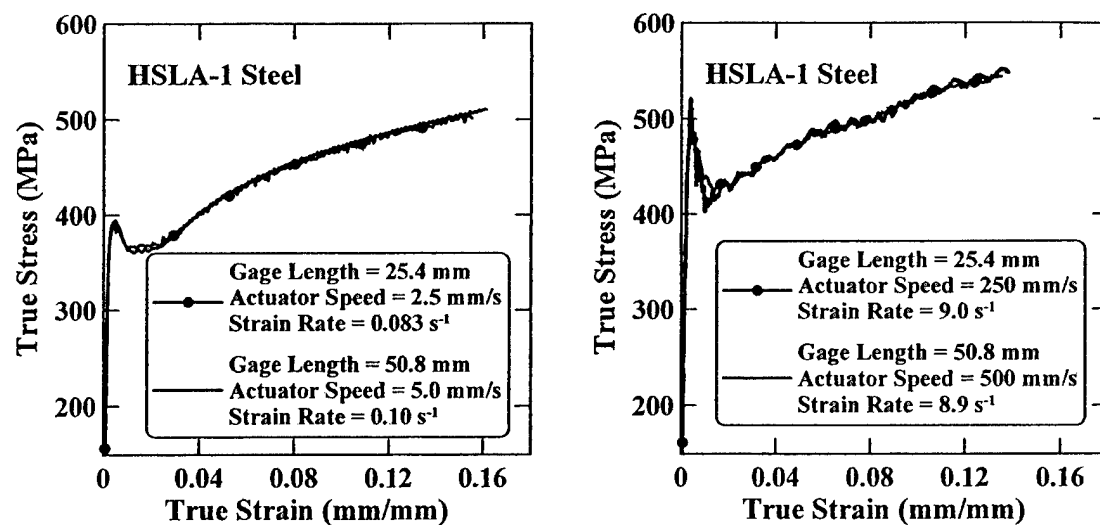


Figure 5.2: True stress-strain curves for HSLA-1 steel. Each plot shows two different gage lengths tested at similar strain rates.

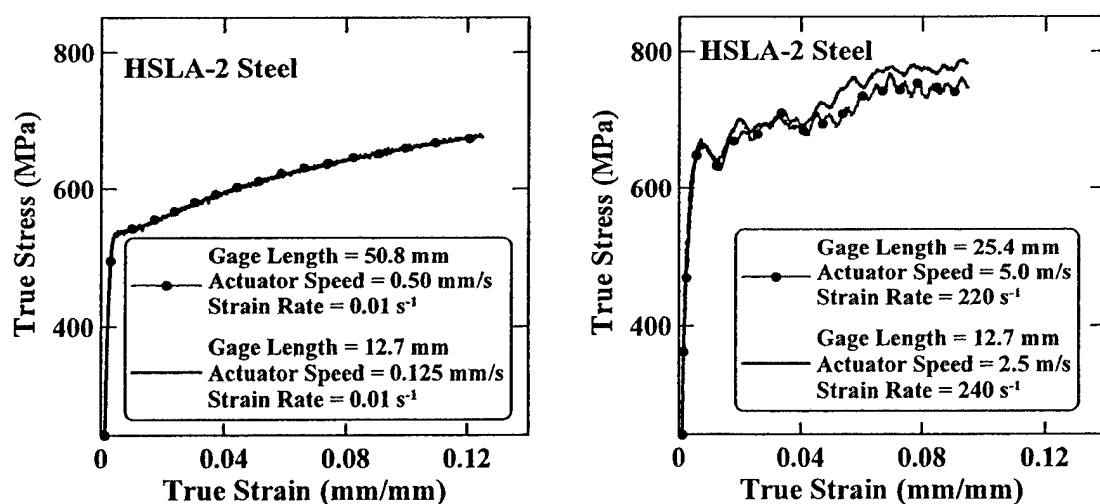


Figure 5.3: True stress-strain curves for HSLA-2 steel. Each plot shows two different gage lengths tested at similar strain rates.

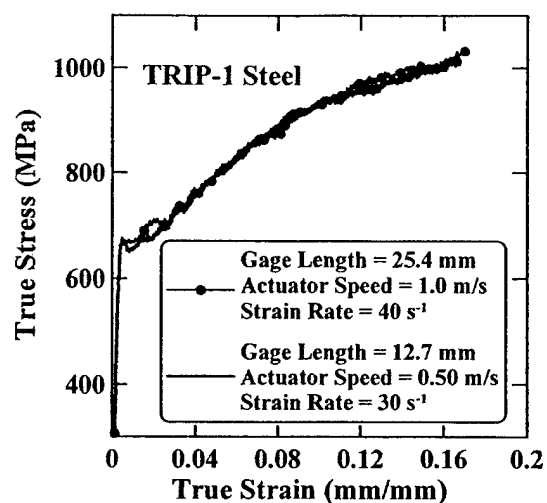


Figure 5.4: True stress-strain curves for TRIP-1 steel tested with two different gage lengths at similar strain rates.

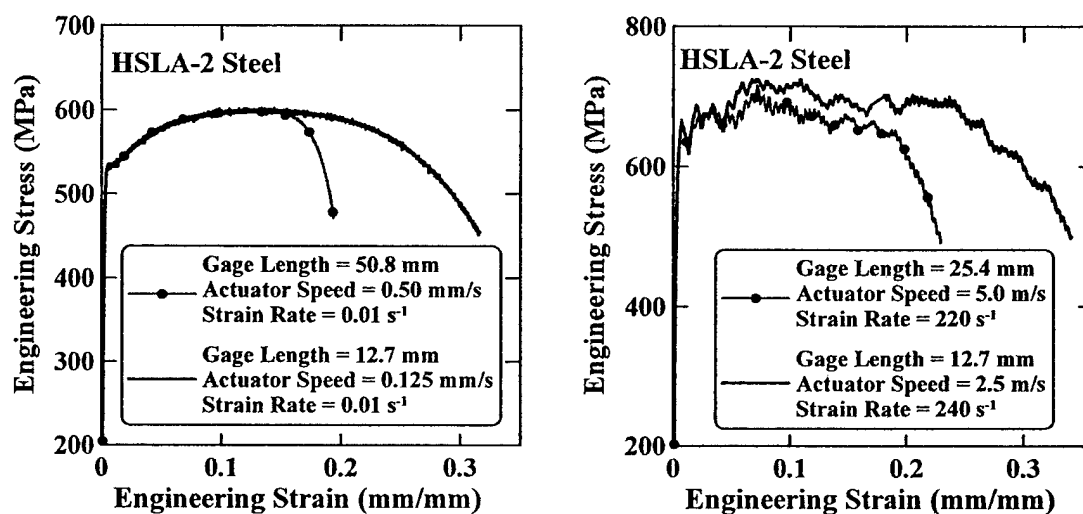


Figure 5.5: Engineering stress-strain curves for HSLA-2 steel. Each plot shows two different gage lengths tested at similar strain rates.

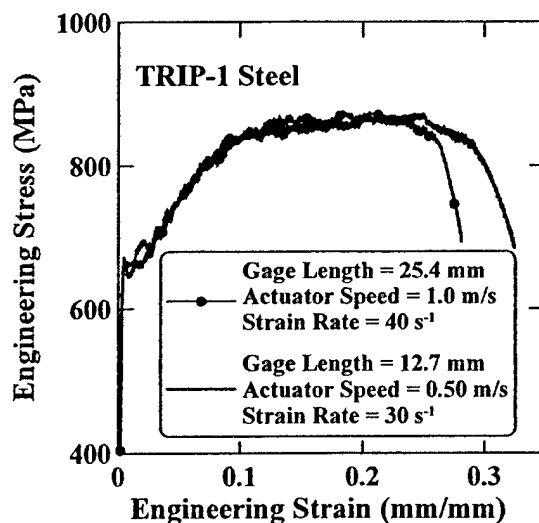


Figure 5.6: Engineering stress-strain curves for TRIP-1 steel tested with two different gage lengths at similar strain rates.

Although gage section width and length variations do not appear to cause significant changes in the data collected, changes in sample thickness seem to affect the “noisiness” of stress-strain curves, with reduced sample thickness resulting in noisier curves. “Noisiness” means the relative amplitude of fluctuations in the stress-strain curve. Examples of this effect are shown in Figure 5.7 which compares stress-strain curves at strain rates of approximately $100\text{--}200 \text{ s}^{-1}$ for various interstitial free and ultra-low-carbon steels which had different sheet thicknesses. Note that each steel also had different composition so the mechanical properties are expected to be different. Table 5.1 summarizes the sheet thickness, gage length, strain rate, actuator speed, yield strength, and load at yield for each of the materials compared.

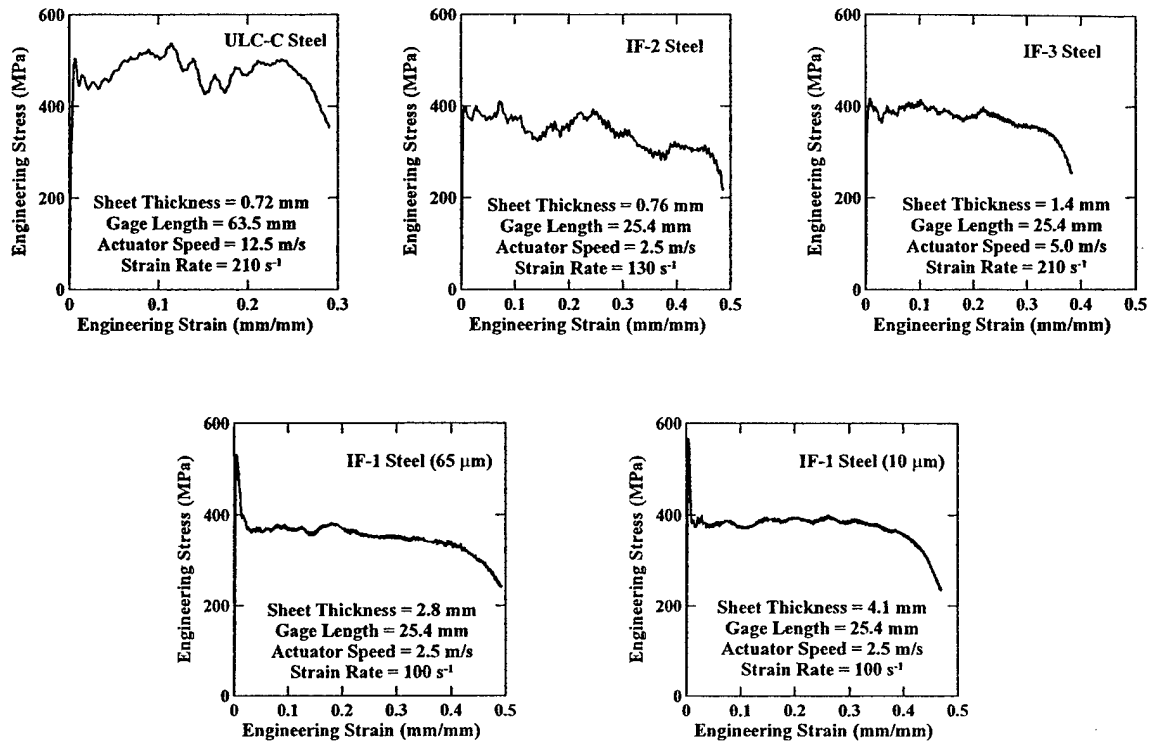


Figure 5.7: Engineering stress-strain curves for five different steels with different sheet thicknesses.

Table 5.1: Sheet thickness, gage length, strain rate, actuator speed, yield strength, and load at yield for each of five materials used to compare “noisiness” of stress-strain curves in Figures 5.7 and 5.8.

Material	Sheet Thickness (mm)	Gage Length (mm)	Strain Rate (s ⁻¹)	Actuator Speed (m/s)	Yield Strength (MPa)	Load at Yield (kN)
ULC-C	0.72	63.5	210	12.5	450	4.1
IF-2	0.76	25.4	130	2.5	380	1.9
IF-3	1.4	25.4	210	5.0	380	3.6
IF-1 (65 μm grains)	2.8	25.4	100	2.5	370	6.5
IF-1 (10 μm grains)	4.1	25.4	100	2.5	385	10.0

In Figure 5.7, a qualitative assessment of the stress-strain curves reveals that the ULC-C steel has the noisiest stress-strain curves, followed by IF-2, then IF-3, then IF-1 (65 μm) and finally the IF-1 (10 μm) curve is the least noisy. The sheet thicknesses of these materials follow the trend of thicker samples giving less noisy stress-strain curves. From Table 5.1, the four IF steels each have comparable yield strengths, but due to sheet thickness, the loads at yield are different. Plotting load versus engineering strain for each of the six materials in Figure 5.8 reveals the explanation for variations in noisiness. In Figure 5.8, the noisiness (oscillation amplitude, ΔLoad) of the load data is smallest for IF-2 and IF-3 steels, slightly greater for the two IF-1 steels and greatest for the ULC-C steel. The ULC-C steel required a much higher actuator speed to achieve the desired strain rate than those used for the IF steels due to the longer gage length of the ULC-C steel. The higher actuator speed accounts for the large fluctuations in load data. The medium-amplitude load fluctuations in the two IF-1 steel curves is probably due to the larger overall loads experienced compared to the IF-2 and IF-3 steels. The noisiness of the stress-strain curves for the four IF steels is a result of the calculation to convert load to engineering stress, as shown in Equation 5.1, where s is the engineering stress, F is the load, and A is the cross-sectional area.

$$s = \frac{F}{A} \quad [5.1]$$

Rewriting Equation 5.1 in terms of the load oscillation, ΔF , gives Equation 5.2.

$$\Delta s = \frac{\Delta F}{A} \quad [5.2]$$

In Equation 5.2, if ΔF remains approximately constant (as it does for the four IF steels) and the cross-sectional area decreases, Δs will increase, resulting in a noisier

stress-strain curve. The very noisy stress-strain curve of the ULC-C steel is due to a combination of small cross-sectional area and fast actuator speed.

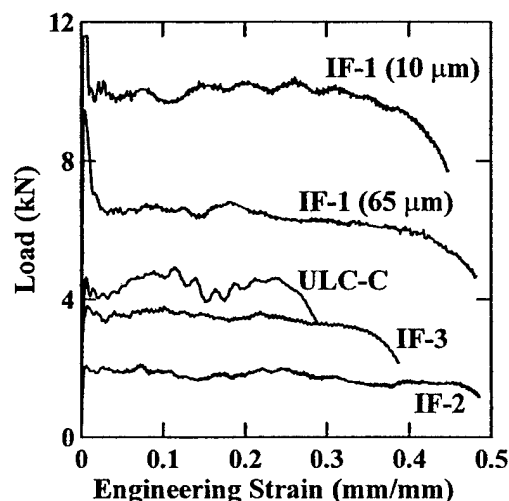


Figure 5.8: Load versus engineering strain curves for the five different steels with different sheet thicknesses shown in Figure 5.7.

5.1.3 Accuracy of Low-Strain Region of the Stress-Strain Curve

To make sure that the test techniques described in Section 4 reveal actual material behavior in the elastic-to-plastic transition region of the stress-strain curve, a 11000-H00 copper material known to exhibit continuous-yielding at all strain rates was tensile tested over a range of strain rates from quasi-static up to about 400 s^{-1} .

The results of the copper tensile tests are shown in Figure 5.9 as true stress-strain curves plotted up to 0.05 true strain. Each strain rate is plotted on a separate graph so that the details of each curve can easily be seen. As expected [121], the strain rate sensitivity of the yield strength is negligible over the strain rates tested, and none of the curves shows a yield point elongation or upper and lower yield points, although at higher strain rates, the curves become more noisy. For comparison, Figures 5.10 through 5.12 show

the low strain regions of true stress-strain curves for IF-1 (10 μm grain size), HSLA-1 and ULC-D steels which all exhibit clear upper and lower yield points.

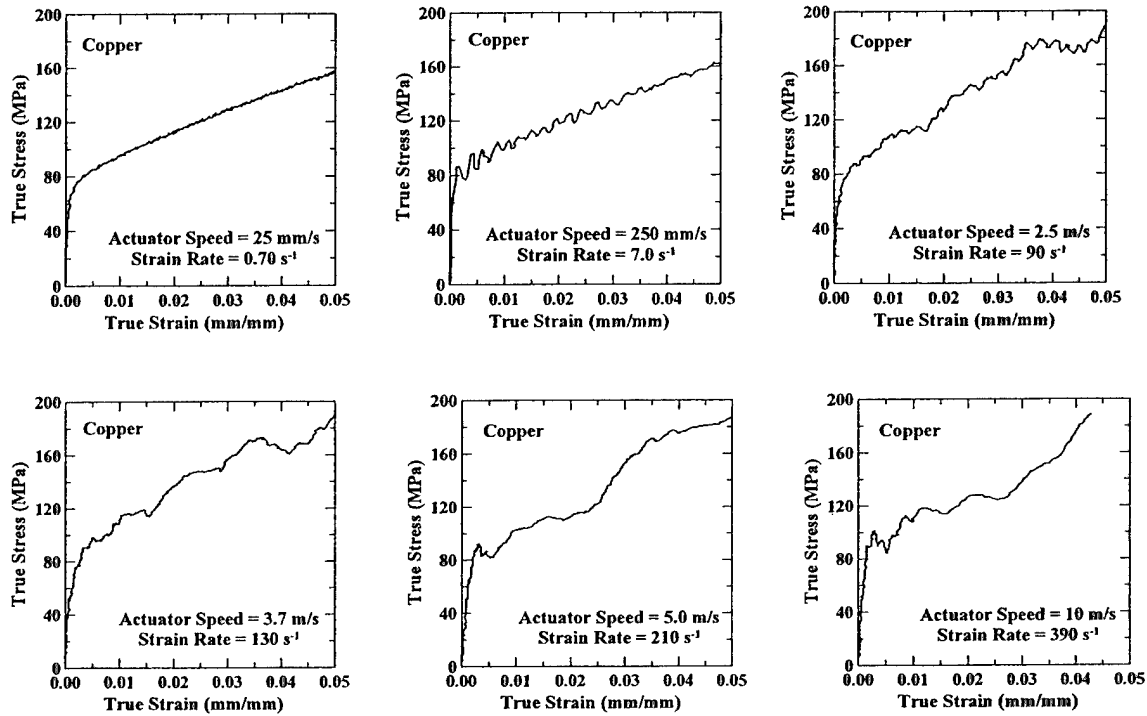


Figure 5.9: True stress-strain curves up to 0.05 true strain for copper samples tensile tested at six different strain rates. All curves show continuous-yielding behavior. All samples had 25.4 mm gage lengths.

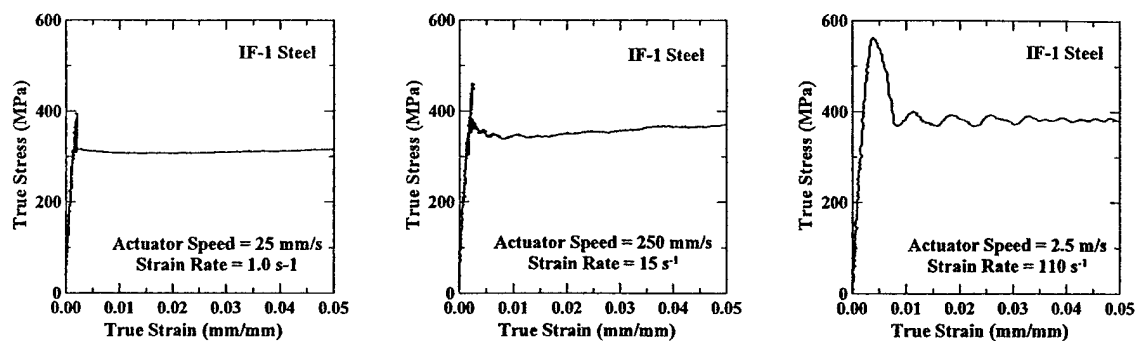


Figure 5.10: True stress-strain curves up to 0.05 true strain for IF-1 steel samples tensile tested at three different strain rates. All curves show upper and lower yield points. All samples had 25.4 mm gage lengths.

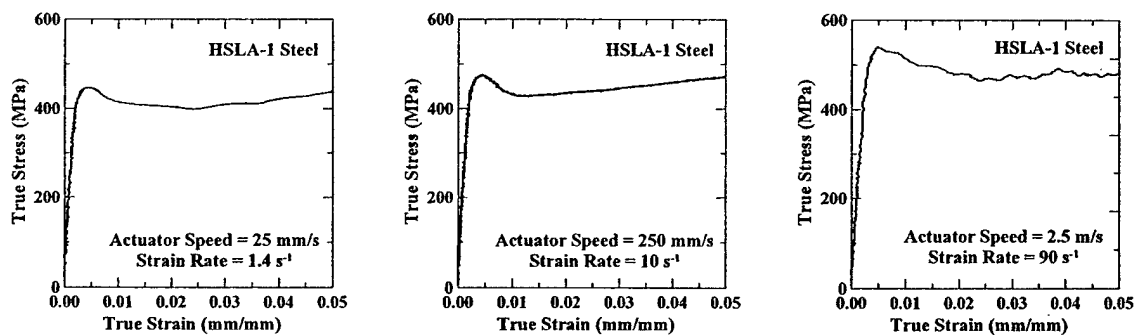


Figure 5.11: True stress-strain curves up to 0.05 true strain for HSLA-1 steel samples tensile tested at three different strain rates. All curves show upper and lower yield points. All samples had 25.4 mm gage lengths.

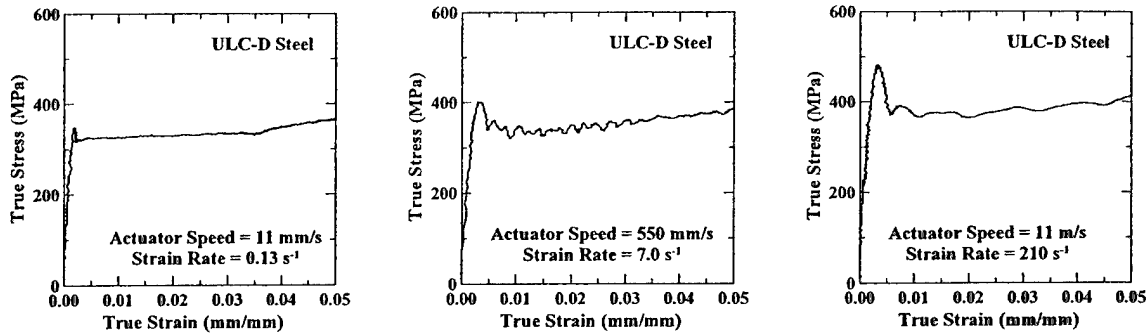


Figure 5.12: True stress-strain curves up to 0.05 true strain for ULC-D steel samples tensile tested at three different strain rates. All curves show upper and lower yield points. All samples had 76 mm gage lengths.

5.1.4 Repeatability of Tests

To obtain reliable data from tensile tests run on the MTS high-rate machine, test results must be repeatable, such that tests run with identical samples at the same strain rate should produce the same stress-strain curve. This is important to distinguish true differences in material behavior without superposition of variability in test results. To determine whether the test methods used gave repeatable results, several tensile tests were run at a variety of strain rates on a commercially-produced material (HSLA-2) believed to have consistent properties.

Engineering stress-strain curves are shown in Figure 5.13 for strain rates ranging from 0.014 to 420 s^{-1} . In each plot, two or three tests are shown for the same strain rate. For the tests at strain rates below 10 s^{-1} , load data were taken using the piezoelectric load washer. For strain rates above 10 s^{-1} , load data were calculated from the grip section strain gage. Figure 5.13 clearly shows that the tensile tests run using different samples at the same strain rates are nearly identical, with the exception of total elongation, which is a property that often has quite a bit of scatter.

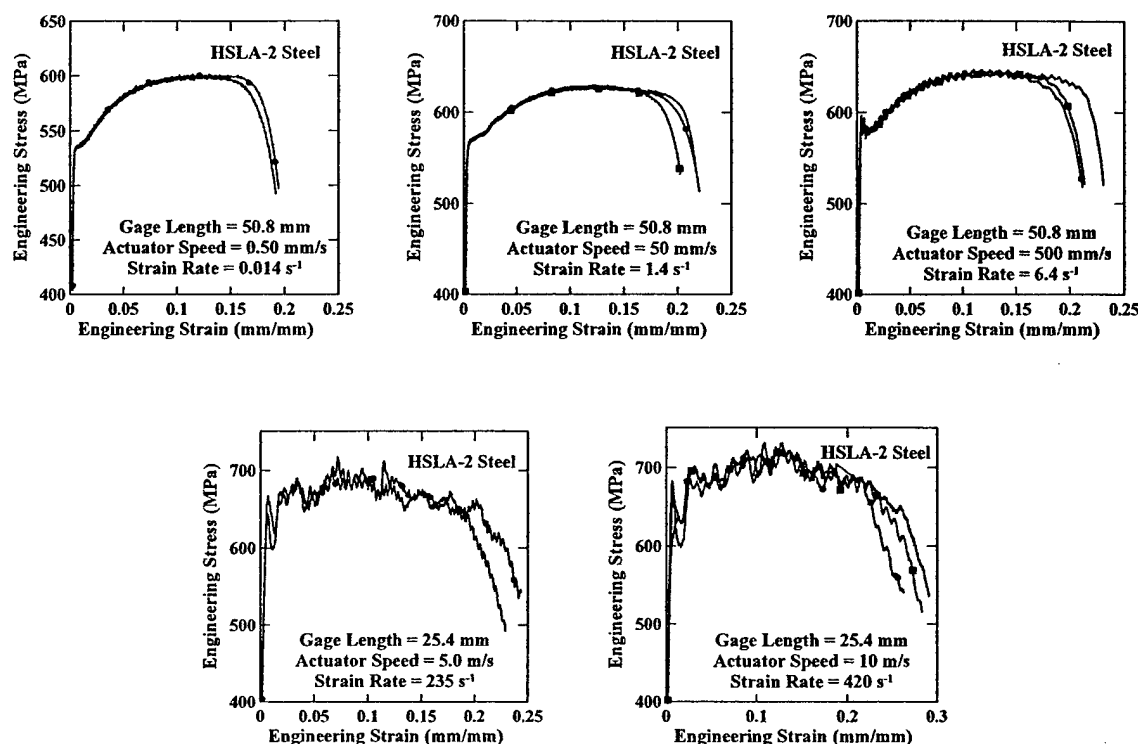


Figure 5.13: Repeatability study of engineering stress-strain curves for HSLA-2 steel samples tensile tested at five different strain rates. Two tests were run at each of the strain rates 0.014 s^{-1} and 235 s^{-1} , while three tests were run for each of the other strain rates.

5.1.5 Discussion of High Rate Test Validation Results

Accuracy of the MTS high-rate tensile test system was verified through a series of experiments. Low-rate stress-strain curves from the high-rate system were compared with those from a conventional screw-driven tensile test machine using the same displacement rates and same geometry test samples, with similar results. This comparison confirmed the accuracy of the load and strain measurement techniques used on the high-rate system.

Since ASTM E-8 standard tensile samples had gage lengths too long to achieve desired strain rates and grip widths too narrow to prevent plastic deformation for some

materials, alternate tensile sample geometries were developed. Samples with different geometries were tested at similar strain rates for a variety of materials to establish whether the geometry changes affected resulting stress-strain curves. It was determined that grip section width, gage section width and gage length did not significantly affect results, except for the expected changes in total elongation. However, decreasing sample thickness increased the noisiness of stress-strain curves due to the calculation to convert load to stress.

Many of the steel materials tested exhibited upper and lower yield points. Typically, the difference between upper and lower yield point values increases with increasing strain rate. The Hahn model for predicting yield point behavior (discussed in Section 3.13.3.2) predicts increasing difference between upper and lower yield points with increasing strain rate if the exponent in Equation 3.48 decreases with increasing strain rate sensitivity.

5.2 Mechanical Properties as a Function of Strain Rate

A goal of high-rate tensile testing is to provide accurate data for computer models used for high-rate applications, such as crash scenarios. These models may require specific data points such as yield or tensile strength, or the entire stress-strain curve for a variety of strain rates. Another goal is to compare materials for suitability in high-rate applications. These comparisons typically include plotting a particular material parameter, such as flow stress or energy absorbed, as a function of strain rate. Materials may also be compared by visual evaluation of differences in stress-strain curves with strain rate. These differences may include yield behavior (continuous or discontinuous), relative strength values, and strain hardening. Experimental data over a range of strain rates are also required to develop or verify constitutive equations which predict material behavior. In this section, several different approaches to displaying high strain rate tensile data are presented and analyzed.

5.2.1 Stress-Strain Curves

Much information can be surmised from families of stress-strain curves plotted over a wide range of strain rates. Qualitative evaluations can be made of how strength, strain hardening rate, yield point elongation behavior, uniform and total elongation, and energy absorption change with strain rate. Figures 5.14 through 5.17 show families of engineering and true stress-strain curves for HSLA-1, HSLA-2, dual phase, and IF-1 steels. All data shown in Figures 5.14 - 5.17 were gathered using 25.4 mm gage length tensile samples, except for the low rate data (below 10s^{-1}) for the HSLA-2 steel shown in Figure 5.15 where 50.8 mm gage length samples were used.

The HSLA-1 steel shown in Figure 5.14 exhibits yield point elongation behavior which becomes more pronounced with increasing strain rate. The yield and tensile strengths both increase with increasing strain rate. The strain hardening rate appears to decrease (beyond the yield point elongation region) with increasing strain rate. The total elongation increases slightly with increasing strain rate while the uniform elongation decreases slightly.

In contrast to HSLA-1, the HSLA-2 steel in Figure 5.15 is nearly continuous-yielding at all strain rates. Its yield and tensile strengths increase with increasing strain rate and the rate of strain hardening appears unchanged. The total elongation increases with increasing strain rate, however the magnitudes of the differences between low and high rate tests can not be determined due to the use of longer gage length samples for the low rate tests. The uniform elongation values remain relatively constant except for the test run at 235 s^{-1} .

The dual phase steel shown in Figure 5.16 is nearly continuous-yielding at all strain rates. Its yield and tensile strengths increase with increasing strain rate and the rate of strain hardening appears unchanged. The total elongation increases with increasing strain rate, except that the highest rate (490 s^{-1}) test has a lower value than the test run at 110 s^{-1} . The uniform elongation values decrease with increasing strain rate above 1 s^{-1} .

The IF-1 steel shown in Figure 5.17 exhibits yield point elongation behavior which becomes more pronounced with increasing strain rate. Its yield and tensile strengths increase while the rate of strain hardening decreases with increasing strain rate. The total elongation decreases with increasing strain rate up to a strain rate of 15 s^{-1} and then increases for the higher rates. The uniform elongation values decrease with increasing strain rate except for the test run at 100 s^{-1} , however the uniform elongation values were difficult to determine at high rates due to the limited strain hardening in those tests.

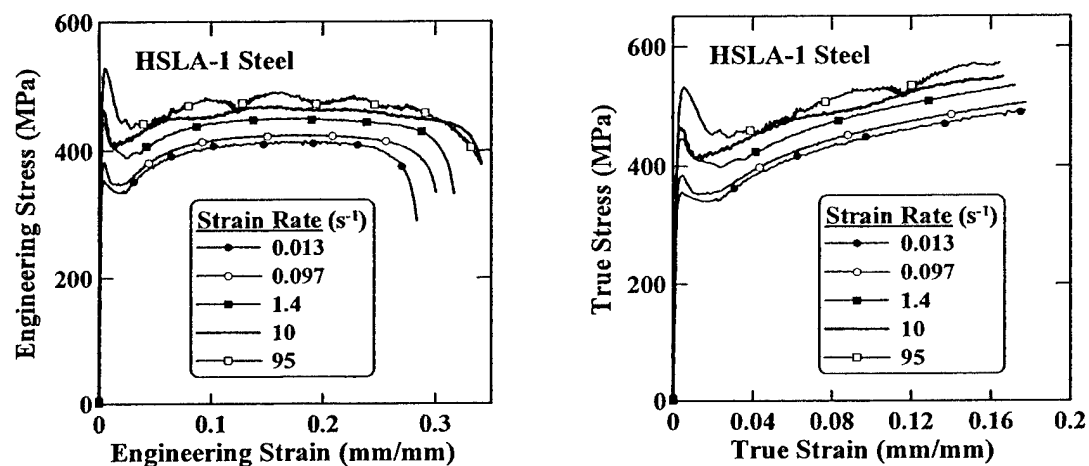


Figure 5.14: Engineering and true stress-strain curves for HSLA-1 steel samples tensile tested at five different strain rates. All sample gage lengths were 50.8 mm, except for the 95 s^{-1} test which used 12.7 mm gage length. Actuator speeds were 0.50 mm/s, 5.0 mm/s, 50 mm/s, 500 mm/s and 2.5 m/s, respectively, to achieve the indicated strain rates of 0.013, 0.097, 1.4, 10 and 95 s^{-1} .

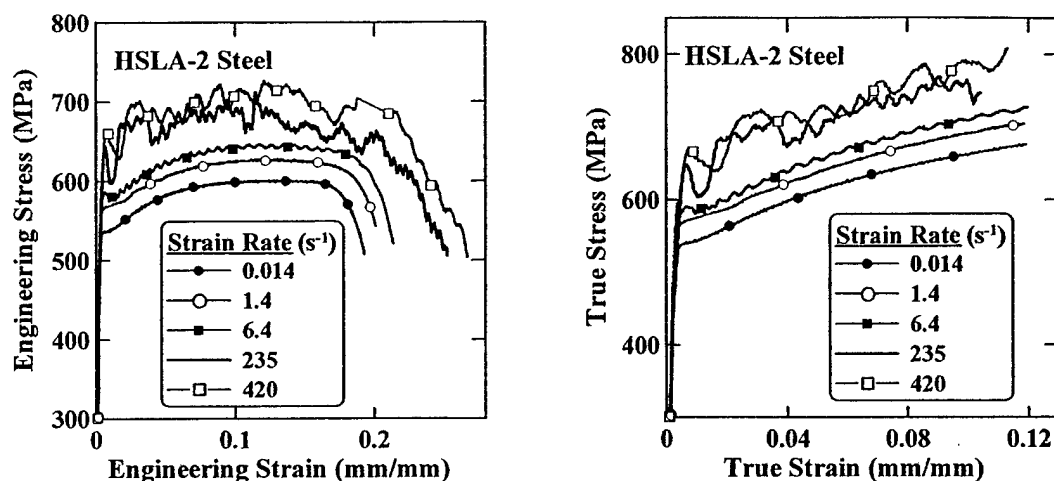


Figure 5.15: Engineering and true stress-strain curves for HSLA-2 steel samples tensile tested at five different strain rates. Sample gage lengths were 50.8 mm for the three lowest rate tests and 25.4 mm for the two highest rate tests. Actuator speeds were 0.5 mm/s, 50 mm/s, 375 mm/s, 5.0 m/s and 10 m/s, respectively, to achieve the indicated strain rates of 0.014, 1.4, 6.4, 235 and 420 s⁻¹.

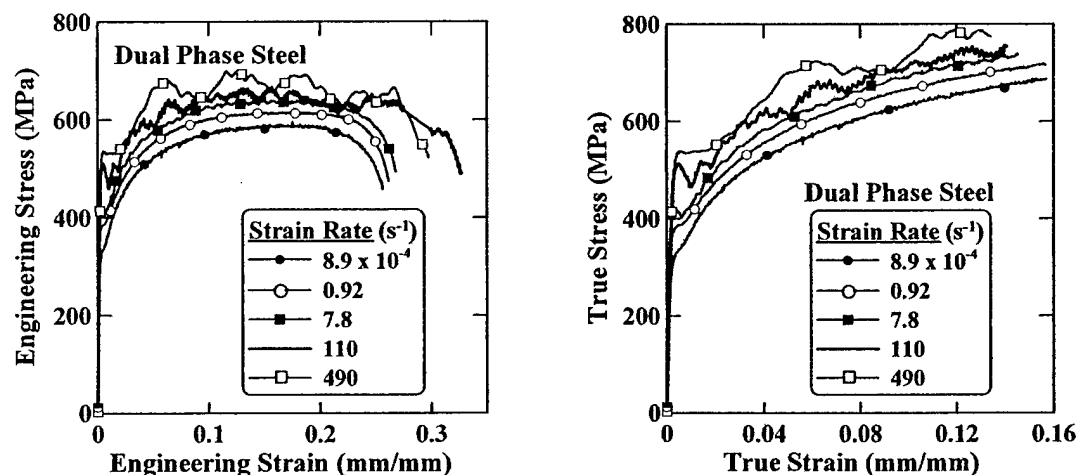


Figure 5.16: Engineering and true stress-strain curves for dual phase steel samples tensile tested at five different strain rates. All sample gage lengths were 25.4 mm. Actuator speeds were 0.025 mm/s, 25 mm/s, 250 mm/s, 2.5 m/s and 12.5 m/s, respectively, to achieve the indicated strain rates of 8.9×10^{-4} , 0.92, 7.8, 110 and 490 s⁻¹.

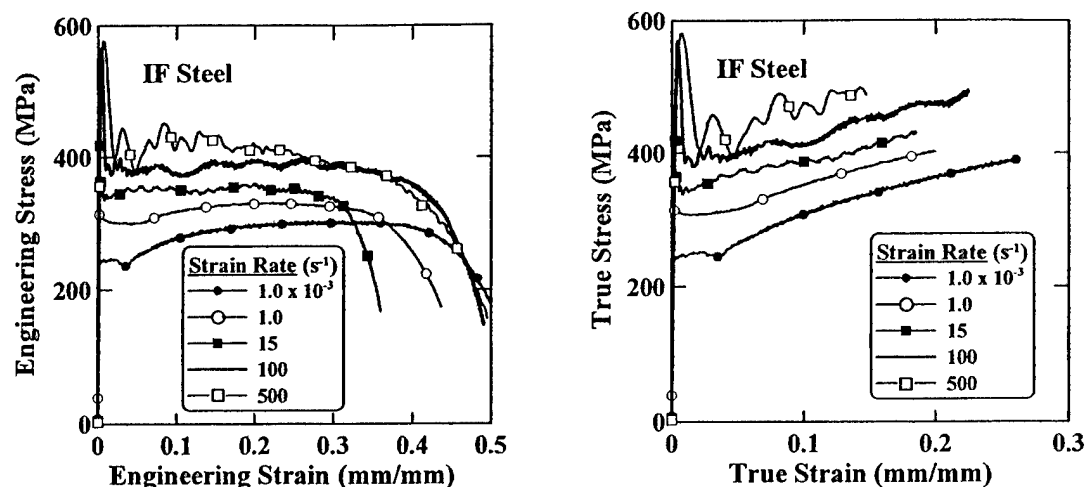


Figure 5.17: Engineering and true stress-strain curves for IF-1 steel samples tensile tested at five different strain rates. All sample gage lengths were 25.4 mm. Actuator speeds were 0.025 mm/s, 25 mm/s, 250 mm/s, 2.5 m/s and 12.5 m/s, respectively, to achieve the indicated strain rates of 1.0×10^{-3} , 1.0, 15, 100 and 500 s^{-1} .

5.2.2 Strain Rate Sensitivity of Material Properties

While families of stress-strain curves provide general information about material behavior with changing strain rate, strain rate sensitivity plots (material property versus strain rate) allow property trends to be more easily evaluated because they present a large amount of data in a compact form. Strain rate sensitivity (SRS) plots are also useful for verifying the accuracy of constitutive equations, since an effective constitutive equation will predict each point in a SRS plot with a single equation.

In section 5.2.1, families of stress-strain curves were plotted for a variety of steels. In Figures 5.15 and 5.16, it appeared that the HSLA-2 and dual phase materials had very similar responses to increasing strain rate. A series of SRS plots for yield and tensile strengths, work hardening exponents, and energy absorbed to a fixed strain further clarify the effects of strain rate.

In Figure 5.18, the yield and tensile strengths for both HSLA-2 and the dual phase steel are plotted versus the logarithm of strain rate. For both materials, both the yield and tensile strengths increase with increasing strain rate, and the rate at which they increase (the strain rate sensitivity) increases for strain rates above about 1 s^{-1} . The logarithmic strain rate sensitivity, β , was calculated as described in Section 4.5 for each material at low (up to 1 s^{-1}) and high (above 1 s^{-1}) strain rates and are listed in Table 5.2. The yield and tensile strengths of the HSLA-2 steel increase at about the same rate with increasing strain rate. However, the yield strength of the dual phase steel increases much more rapidly with strain rate than its tensile strength. As shown in Table 5.2, the strain rate sensitivity of yield strength for the dual phase steel is greater than that of HSLA-2 steel, especially at high strain rates, while the strain rate sensitivity of tensile strength for the dual phase steel is less than that of HSLA-2 steel at all strain rates.

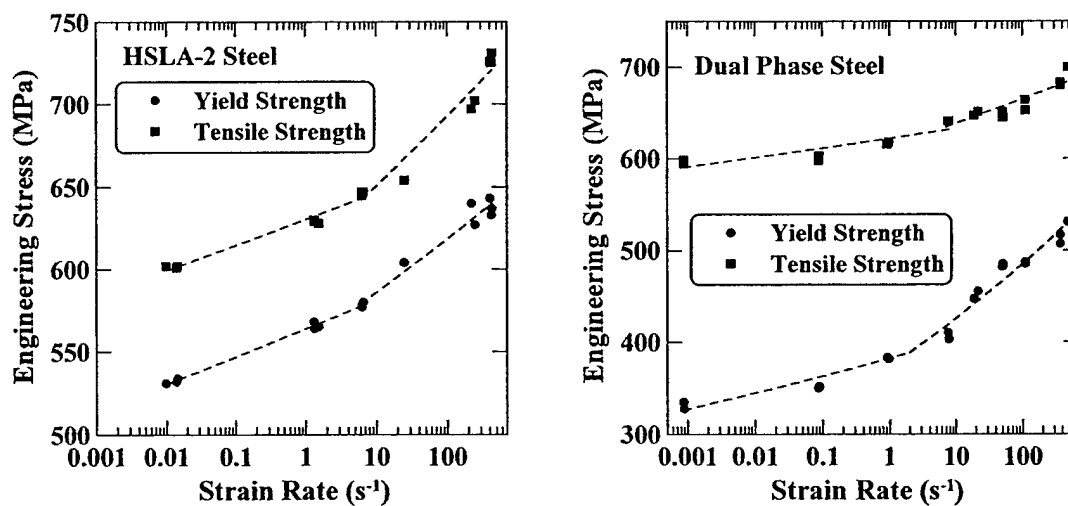


Figure 5.18: Strain rate sensitivities of yield and tensile strengths for (a) HSLA-2 steel, and (b) dual phase steel.

Table 5.2: Logarithmic strain rate sensitivities (β) for the HSLA-2 and dual phase steel data in Figure 5.18.

		β	
		Low Strain Rates	High Strain Rates
HSLA-2	Yield Strength	16.8	32.9
	Tensile Strength	15.7	42.9
Dual Phase	Yield Strength	18.9	60.7
	Tensile Strength	10.4	27.1

To further compare the HSLA-2 and dual phase steels, work hardening exponents were calculated using the entire flow curve between 0.02 true strain and the uniform strain limit. The results are plotted as a function of strain rate in Figure 5.19, which shows that the dual phase steel has a greater degree of strain hardening than HSLA-2 at all strain rates. The work hardening exponent for HSLA-2 slightly increases with increasing strain rate, whereas for dual phase steel it decreases somewhat with increasing strain rate up to 10 s^{-1} and decreases more rapidly at higher strain rates.

The slight increase in strain hardening exponent with increasing strain rate in HSLA-2 steel is unusual and may be a consequence of solid solution softening, which was discussed in Section 3.6. Most steels exhibit decreasing work hardening rates with increasing strain rate due to softening associated with adiabatic heating. However, in materials exhibiting solid solution softening, strength decreases with decreasing temperature or increasing strain rate. For the HSLA-2 steel, the combination of increasing strain rate and increasing temperature may create a balance between solid solution softening due to increasing strain rate and strengthening due to increasing temperature, resulting in little change in work hardening exponent with strain rate.

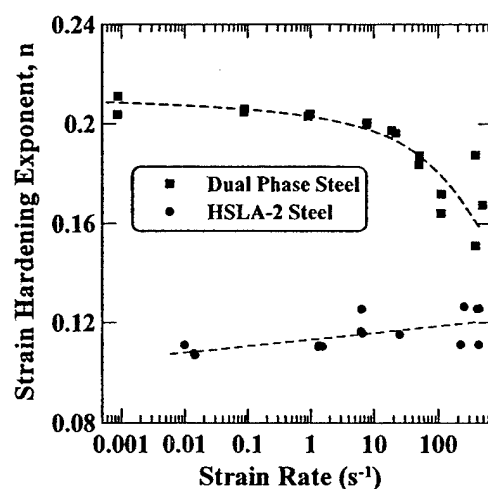


Figure 5.19: Strain hardening exponent versus logarithm of strain rate for HSLA-2 and dual phase steels. Strain hardening exponents calculated from 0.002 true strain up to the uniform strain limit.

Energy absorption capability over a range of strain rates is very important for comparing crash-worthiness of materials. There are several possible ways to determine absorbed energy, including crush tests [122-125] and calculating areas under stress-strain curves [8, 12, 21]. When using the area under the stress-strain curve, one must decide how much of the curve to use because this decision may affect the results of the comparison [12, 21]. If the material is expected to approach fracture strains as part of the crash scenario, then the area under the entire stress-strain curve would be appropriate. However, for a typical automobile crash, steel parts experience an amount of plastic deformation that is less than the total possible. To estimate the energy absorbed for automobile crash scenarios, the area under the stress-strain curve up to 10% strain is often used [8, 21]. Therefore, areas under the engineering stress-strain curves up to 10% strain were calculated for both HSLA-2 and dual phase steels at all strain rates. The results of the energy calculations are plotted versus strain rate in Figure 5.20. In Figure 5.20, the HSLA-2 steel has greater energy absorption capability at all strain rates,

although it appears that the difference between the two steels diminishes slightly with increasing strain rate. The greater energy absorption of HSLA-2 steel is due to its much higher yield strength. Quasi-static and dynamic engineering stress-strain curves are shown in Figure 5.21 for both materials. Visual inspection of the stress-strain curves verifies that the area under the HSLA-2 curve is always greater due to its higher yield strength. Figure 5.21 also shows that the difference in absorbed energy between the two steels changes depending upon the upper strain limit chosen for the calculation of area. As strain increases, the differences between energy absorbed decreases because of the higher degree of strain hardening in the dual phase steel.

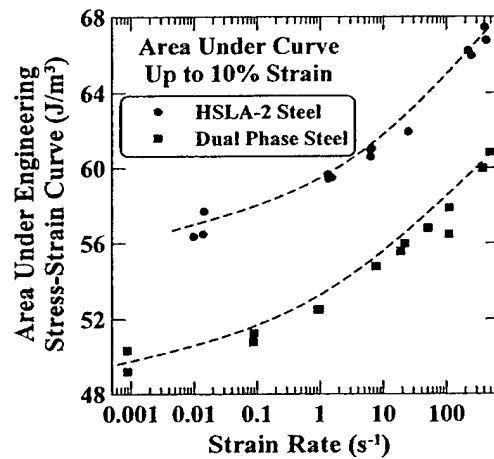


Figure 5.20: Comparison of area under the engineering stress-strain curve up to 10% strain versus logarithm of strain rate for HSLA-2 and dual phase steels.

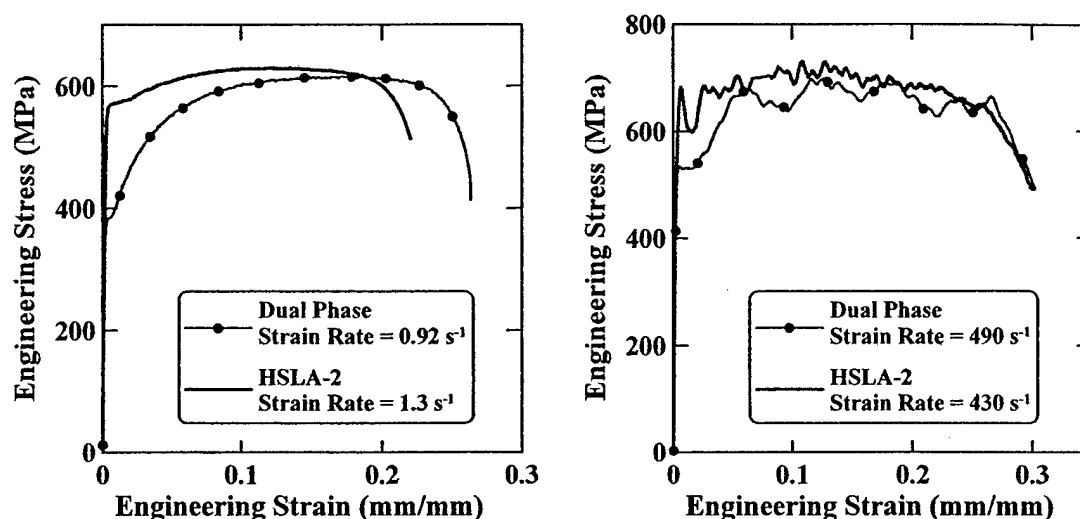


Figure 5.21: Engineering stress-strain curves for HSLA-2 and dual phase (DP) steels. (a) Low-rate tests. Sample gage lengths: HSLA-2 = 50.8 mm, DP = 25.4 mm. Actuator speeds: HSLA-2 = 50 mm/s, DP = 25 mm/s. (b) High-rate tests. Sample gage lengths: HSLA-2 = 25.4 mm, DP = 25.4 mm. Actuator speeds: HSLA-2 = 11.2 m/s, DP = 11.2 m/s.

5.2.3 Material Comparison for High Rate Applications

There are a variety of methods to compare materials for suitability in high rate applications. One such measure is the increase in either yield or tensile strength of a material when loaded at a high rate (dynamic test) compared to a low rate (static test). It is desirable for a structural material to have both high static strength and high increase in strength at high rates for crash-worthiness applications. To find the most suitable material, the strength increase between dynamic and static tests ($\Delta\sigma$) is plotted for several materials versus those materials' static strength (either yield or tensile). Such plots are shown in Figure 5.22 for six materials, which include three different interstitial free steels (IF-1, IF-2 and IF-3), two different high strength low alloy steels (HSLA-1 and HSLA-2) and a dual phase steel. In Figure 5.22, the static tests were run at strain rates of approximately 0.01 s^{-1} , while the dynamic tests were run at strain rates of about 100 s^{-1} .

The benefit of making plots like those shown in Figure 5.22 is the ability to compare many materials in a single chart.

The general trend in Figure 5.22 shows that increasing static strength results in decreasing static-to-dynamic strength increase ($\Delta\sigma$). Materials can best be compared in Figure 5.22 if they have similar static strength values, where the best material for the high rate application will have a higher $\Delta\sigma$ value. In Figure 5.22, all three IF steels have similar static values of yield and tensile strength. Of the three IF steels, IF-1 has the lowest $\Delta\sigma$ for both yield and tensile strengths. The best IF steel for yield strength increase is IF-2, whereas the best IF steel for tensile strength increase is IF-3.

In Figure 5.22, dual phase and HSLA-1 steels have comparable static yield strengths, while the static tensile strength of dual phase is similar to that of HSLA-2 steel. Dual phase steels are specifically designed for this large difference in yield and tensile strength as discussed in Section 3.10.1. Dual phase steel has greater $\Delta\sigma$ for yield strength than HSLA-1 steel, but lower $\Delta\sigma$ for tensile strength than HSLA-2 steel.

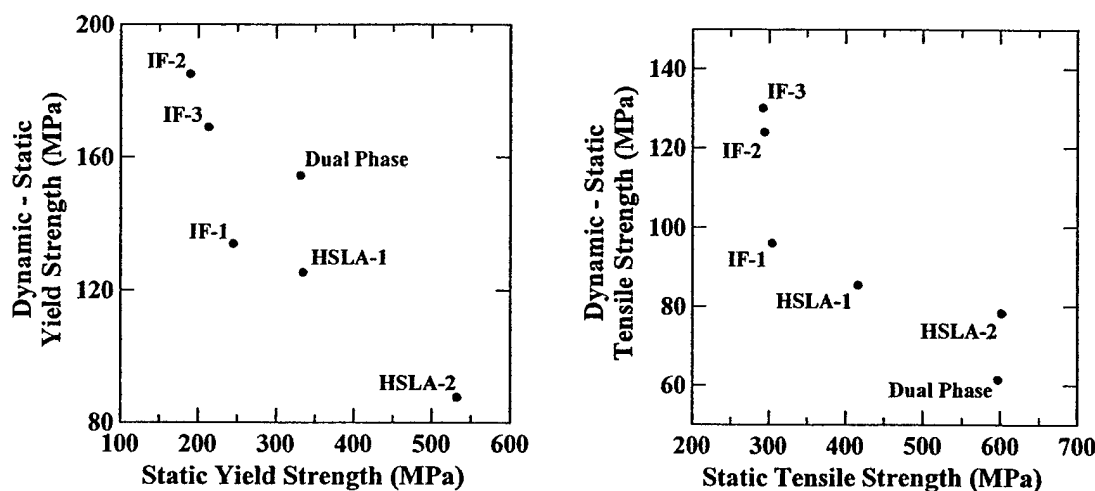


Figure 5.22: Dynamic strength minus static strength versus static strength plots for (a) yield strength and (b) tensile strength. Dynamic strength values determined at strain rate of about 100 s^{-1} and static values determined at strain rate of about 0.01 s^{-1} . In both (a) and (b), the IF-1 steel has $10 \mu\text{m}$ grain size.

Dual phase and HSLA-2 steels were compared in the previous section (Section 5.2.2), and Figure 5.19 (comparison of work hardening exponents) explains the reason for greater $\Delta\sigma$ of tensile strength of HSLA-2 for high rates, since the work hardening rate of HSLA-2 steel remains fairly constant with strain rate, while it decreases at high strain rates for dual phase steel.

Since dual phase and HSLA-1 steels have similar yield strengths, they will be compared in the same manner as dual phase and HSLA-2 steels were compared in Section 5.2.2. Strain rate sensitivity, work hardening exponents and energy absorption comparisons are shown in Figures 5.23 through 5.25. Logarithmic strain rate sensitivity values are listed in Table 5.3.

In Figure 5.23a, the yield strength and UTS values for HSLA-1 steel converge with increasing strain rate, which indicates decreasing strain hardening rate with increasing strain rate, as confirmed in Figure 5.24. The decreasing strain hardening

exponent seen in Figure 5.24 for HSLA-1 steel is opposite that found in HSLA-2 steel, and may be due to the fact that HSLA-1 steel is a less-alloyed, lower strength HSLA steel and is not as affected by solid solution softening. Therefore, adiabatic heating causes a decrease in work hardening rate.

The data in Table 5.3 show that the strain rate sensitivity of tensile strength in HSLA-1 steel is higher at all strain rates than for dual phase steel. For yield strength, the low-rate strain rate sensitivity of HSLA-1 steel is higher than that of dual phase steel. However, for high strain rates, the yield strength strain rate sensitivity of dual phase steel is higher than that of HSLA-1 steel.

In Figure 5.24, dual phase steel has higher strain-hardening exponents than HSLA-1 steel at all strain rates. Since the two steels have comparable yield strengths, but dual phase work hardens faster, dual phase steel also has better energy absorption capability at all strain rates, as shown in Figure 5.25. These differences can also be identified by direct comparison of stress-strain curves as shown in Figure 5.26.

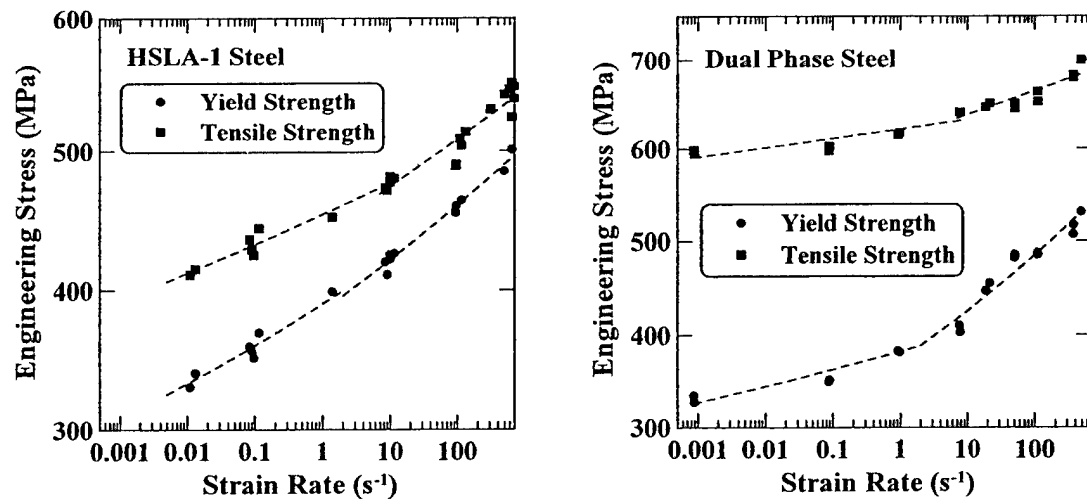


Figure 5.23: Strain rate sensitivities of yield and tensile strengths for (a) HSLA-1 steel, and (b) dual phase steel.

Table 5.3: Logarithmic strain rate sensitivities (β) for the HSLA-1 and dual phase steel data in Figure 5.23.

	β	Low Strain Rates	High Strain Rates
HSLA-1	Yield Strength	30.0	40.1
	Tensile Strength	21.7	35.9
Dual Phase	Yield Strength	18.9	60.7
	Tensile Strength	10.4	27.1

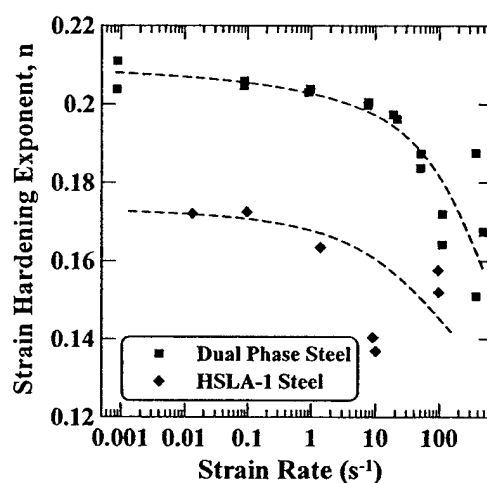


Figure 5.24: Strain hardening exponent versus logarithm of strain rate for HSLA-1 and dual phase steels. Strain hardening exponents were calculated for entire flow curve between 0.02 true strain and uniform strain limit for dual phase and beyond the yield point elongation up to the uniform strain limit for HSLA-1 steel.

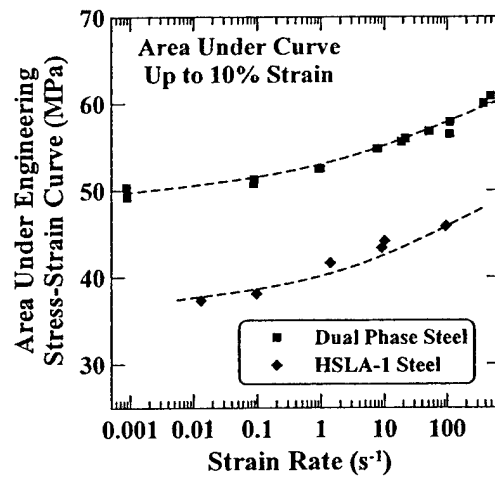


Figure 5.25: Comparison of area under the engineering stress-strain curve up to 10% strain versus logarithm of strain rate for HSLA-1 and dual phase steels.

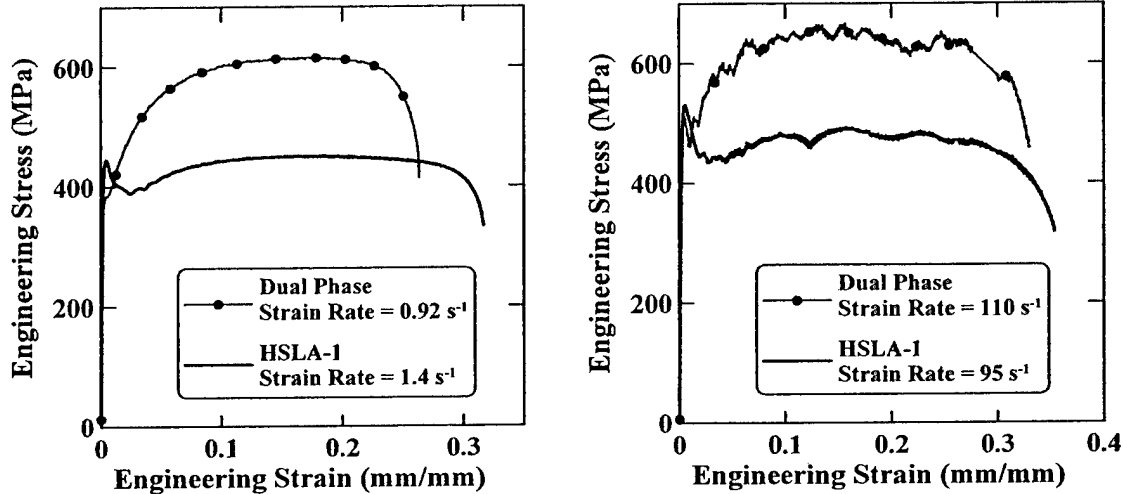


Figure 5.26: Engineering stress-strain curves for HSLA-1 and dual phase (DP) steels. (a) Low-rate test. Sample gage lengths: HSLA-1 = 50.8 mm, DP = 25.4 mm. Actuator speeds: HSLA-1 = 50 mm/s, DP = 25 mm/s. (b) High-rate test. Sample gage lengths: HSLA-1 = 12.7 mm, DP = 25.4 mm. Actuator speeds: HSLA-1 = 1.25 m/s, DP = 2.5 m/s.

The comparison between IF steels in Figure 5.22a is somewhat misleading. In Figure 5.22a, the yield strength $\Delta\sigma$ difference between IF-1 and IF-2 steels is about 50 MPa. True stress-strain curves are shown in Figure 5.27 for IF-1 and IF-2 steels at the quasi-static and dynamic rates at which the data points in Figure 5.22 were determined. In Figure 5.27a, IF-1 steel exhibits yield point elongation while IF-2 steel is continuous-yielding. Beyond about 0.05 true strain, the curves are similar with the flow stress of IF-1 steel about 20 MPa greater than IF-2 steel. In Figure 5.27b, both steels have similar dynamic yield strength values. Therefore, the IF-2 steel does have greater yield strength $\Delta\sigma$, but the difference is primarily due to the different static yield behaviors. The stress-strain curves in Figure 5.27 also show that IF-1 steel has greater uniform strain at both strain rates may be advantageous for some applications.

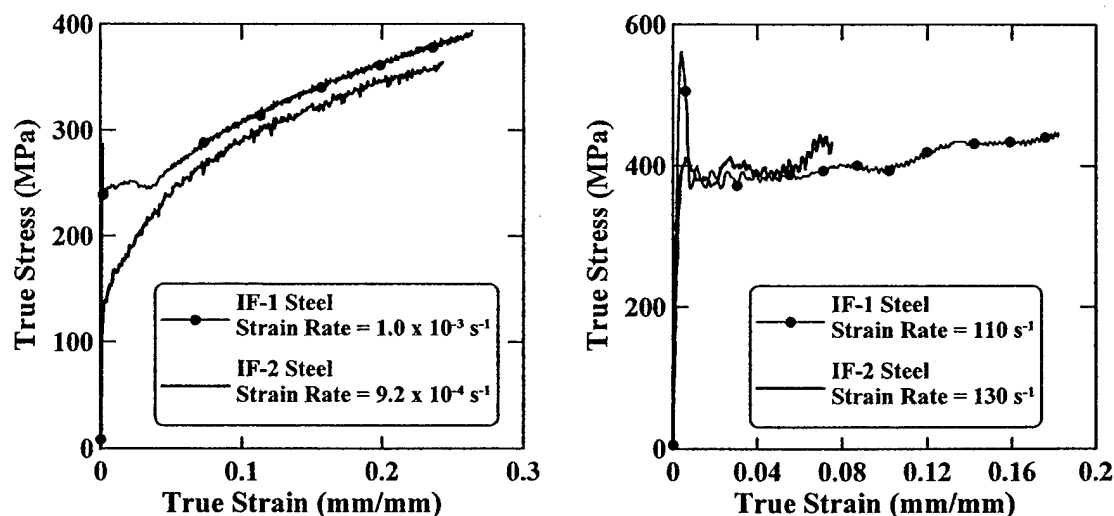


Figure 5.27: True stress-strain curves for IF-1 and IF-2 steels. All sample gage lengths were 25.4 mm. (a) Quasi-static tests. Actuator speed = 0.025 mm/s. (b) Dynamic tests. Actuator speed = 2.5 m/s.

5.2.4 Discussion of Mechanical Property Results

As shown in Section 5.2.1, families of stress-strain curves are useful for determining general trends in material behavior with changes in strain rate. For materials exhibiting yield point elongation, such as HSLA-1 and IF-1 steels, the difference between upper and lower yield point stress values increases with increasing strain rate. In addition, the shape of the yield drop changes, with the strain between upper and lower yield points increasing with increasing strain rate. Both of these trends are predicted by the Hahn yield drop model discussed in Section 3.13.3.2 if strain rate sensitivity increases with increasing strain rate. Contrary to some published results [6], materials that did not show yield point elongation at quasi-static rates (HSLA-2 and dual phase steels) did not develop them at higher rates.

For the dual phase and IF-1 steel engineering stress-strain curves shown in Figures 5.16 and 5.17, all tensile samples had the same gage length (25.4 mm) and therefore, the changes in total elongations with strain rate can be compared. For both dual phase and IF-1 steel, there is a significant increase in total elongation between strain rates of about 10 and 100 s⁻¹. This increase may be due to a local change in strain rate sensitivity of the necked region at high rates causing a more diffuse neck. In the case of the IF-1 steel, the total elongation (ductility) decreases with increasing strain rate up to 15 s⁻¹. The increase in total elongation at a strain rate of 100 s⁻¹ brings its value nearly back to that of the quasi-static test.

In Section 5.2.2 and 5.2.3, dual phase steel was compared to HSLA-2 and HSLA-1 steels. The quasi-static yield strengths of HSLA-1 and dual phase steels were similar while the static tensile strengths of HSLA-2 and dual phase steels were comparable. Various measures of energy absorption were discussed in Section 5.2.2 and the areas under stress-strain curves up to 10% engineering strain were calculated to compare the energy absorption capabilities of dual phase steel compared to HSLA-2 (Section 5.2.2) and HSLA-1 (Section 5.2.3) steels. It was found that dual phase steel had better energy absorption than HSLA-1 steel at all strain rates due to the higher work

hardening rates in dual phase steel. However, HSLA-2 steel had higher energy absorption than dual phase steel at all strain rates because of its higher yield strength values. These differences were readily apparent from the stress-strain curves shown in Figures 5.21 and 5.26.

In Section 5.2.3, static-to-dynamic changes in strength ($\Delta\sigma$) values were plotted as functions of static properties in Figure 5.22. While these charts are useful for convenient comparison of several different materials, it was noted that the differences observed in Figure 5.22 may not convey the differences distinguished by plots of stress-strain curves, as illustrated for IF steels in Figure 5.27.

CHAPTER 6

RESULTS & DISCUSSION: STRENGTHENING MECHANISMS

6.1 Strengthening by Cold Work

IF-2 steel tensile samples were pre-strained at a strain rate of $4 \times 10^{-4} \text{ s}^{-1}$ to various strains ranging from 0.02 to 0.18 as described in Section 4.6. Each of the five pre-strain groups of IF-2 steel samples was tensile tested at strain rates ranging from 0.001 to 500 s^{-1} . Engineering stress-strain curves are shown in Figure 6.1 for tests run at a strain rate of 0.001 s^{-1} . Figure 6.1a shows the expected result of increasing yield and tensile strengths with increasing yield/tensile strength ratios as pre-strain increases. True stress-strain curves for the same data are plotted in Figure 6.1b, but the curves are offset by the corresponding amount of pre-strain. The nearly overlapping curves in Figure 6.1b show that the pre-strain procedures were successful.

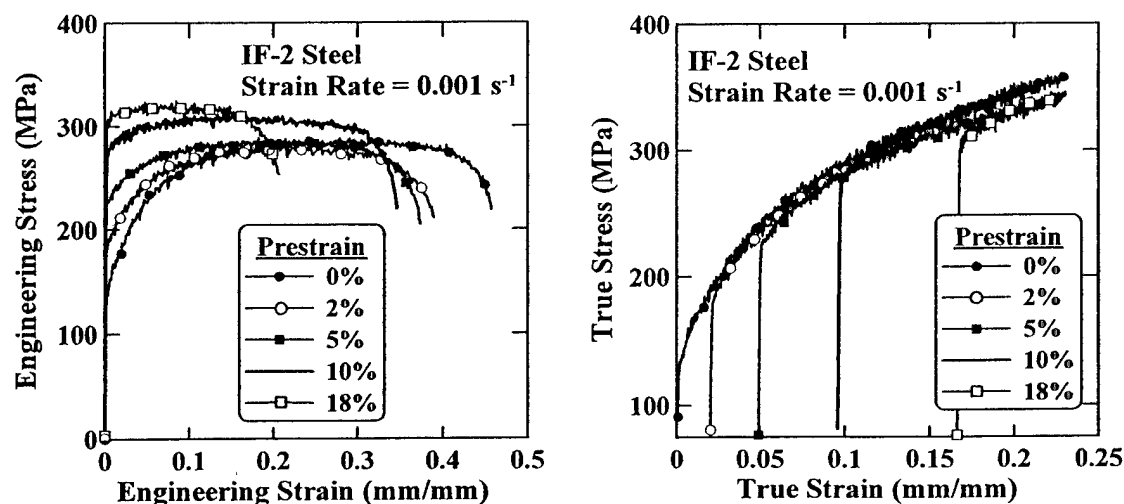


Figure 6.1: Stress-strain curves at a strain rate of about 0.001 s^{-1} for IF-2 steel with five different pre-strain levels. a) Engineering stress-strain curves. b) True stress-strain curves with pre-strained results offset by the appropriate amount.

To determine the effect of strain rate on the strengthening mechanism of cold work, IF-2 samples that were pre-strained at a quasi-static strain rate were then tensile tested to failure at strain rates ranging from 0.1 to 500 s⁻¹. The results of these tests for strain rates of 9 and 150 s⁻¹ are shown in Figures 6.2 and 6.3, respectively. In each figure, the (a) plot shows a family of engineering stress-strain curves for each pre-strain sample tested at the same strain rate. Figure 6.2a shows the expected results of increasing yield and tensile strengths, along with increasing yield/tensile strength ratios and decreasing total elongations. It is difficult to distinguish the effects in Figure 6.3a due to the noise in the high rate curves and the fact that these high-rate samples have very little uniform strain before onset of necking, causing the stress-strain curves to drop rapidly. This is typical high rate behavior for IF steels [129].

Figures 6.2b and 6.3b show the results of pre-strain on true stress-strain curves for tests run at 9 s⁻¹ and 150 s⁻¹, respectively. In both plots, the lower curve is the quasi-static flow curve for the unstrained (0% cold work) condition, while the upper curve (designated "0%" on the chart) is the dynamic curve at the desired strain rate for the unstrained (0% cold work) condition. True stress-strain curves for each pre-strain level are also shown with an appropriate offset to account for the quasi-static pre-strain. In both Figure 6.2b and Figure 6.3b, the pre-strained flow curves follow the same trend as the unstrained sample's dynamic flow curve. In other words, the pre-strained samples yield at the same point one would expect if they had been pre-strained by interruption of the dynamic tensile test. This is an expected result if the degree of quasi-static cold work does not influence the behavior at higher strain rates used in this work. Therefore, Figures 6.2b and 6.3b suggest that cold work does not affect the strain rate sensitivity of IF steel, and that dislocations and dislocation substructures created by cold work are long-range (athermal) obstacles to dislocation motion in IF steel.

Figure 6.4a summarizes strain rate sensitivity for the IF-2 steel by plotting flow stress at 0.02 true strain as a function of strain rate for all five pre-strain levels. For all pre-strain levels, Figure 6.4a shows two distinct regions of strain rate sensitivity, with an

increase at strain rates above 10 s^{-1} . At low strain rates β is about 25, and increases to approximately 83 for high strain rates. Figure 6.4a further supports the result that strain rate sensitivity does not vary significantly with different amounts of pre-strain. Figure 6.4b is a different presentation of some of the data contained in Figure 6.4a. This figure plots flow stress at 0.02 true strain versus the pre-strain level for three different strain rates. Figure 6.4b makes it easy to see that the strength increment from a low strain rate to a high strain rate is approximately constant regardless of the amount of quasi-static pre-strain and does not change even when the strain rate sensitivity increases discontinuously.

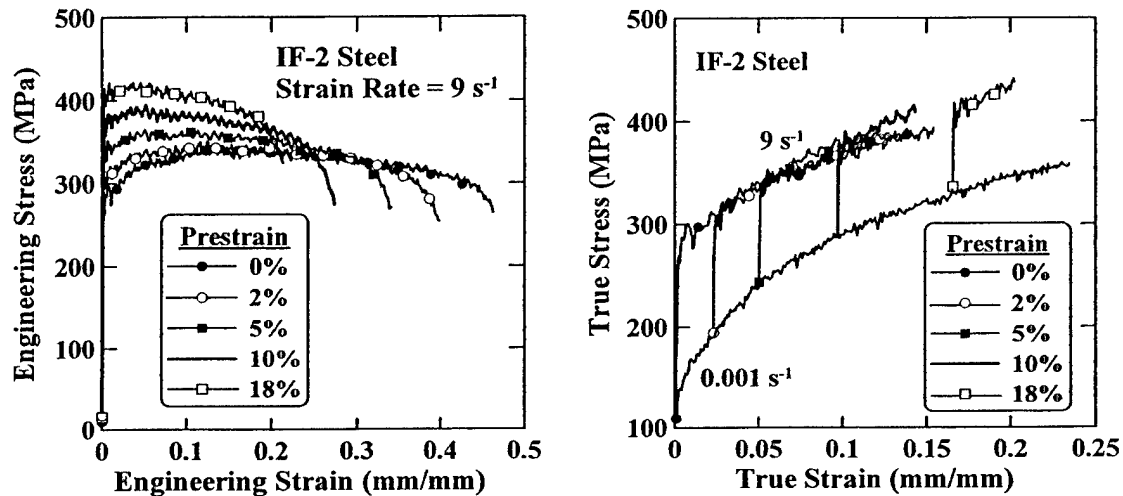


Figure 6.2: Stress-strain curves at a strain rate of about 9 s^{-1} for IF-2 steel with five different pre-strain levels. a) Engineering stress-strain curves. b) True stress-strain curves with pre-strained results offset by the appropriate amount.

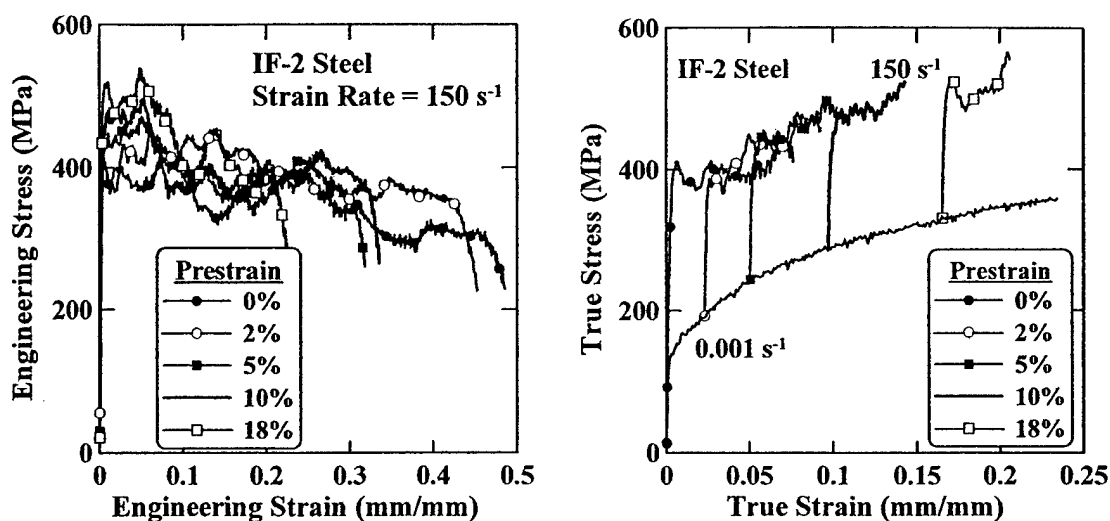


Figure 6.3: Stress-strain curves at a strain rate of about 150 s^{-1} for IF-2 steel with five different pre-strain levels. a) Engineering stress-strain curves. b) True stress-strain curves with pre-strained results offset by the appropriate amount.

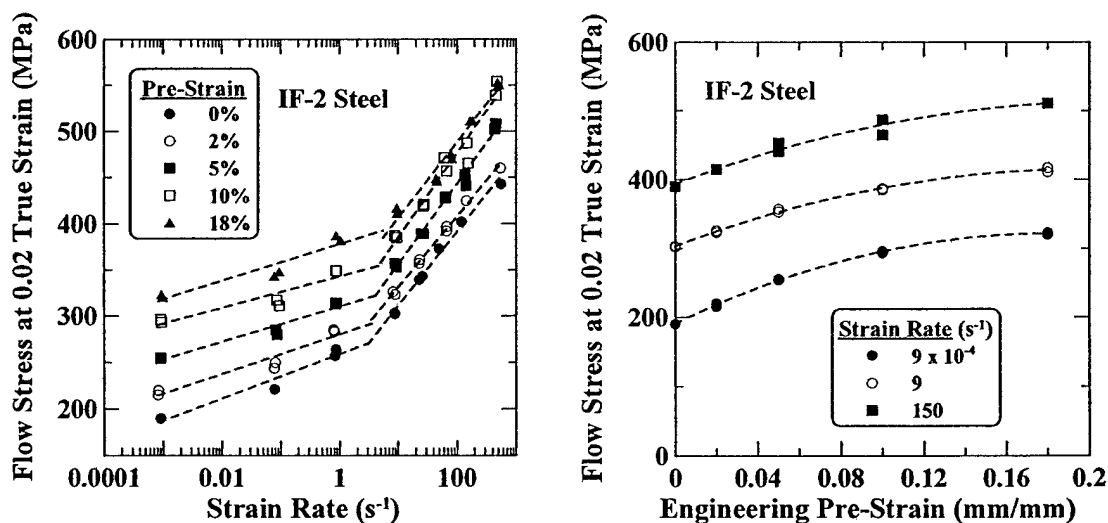


Figure 6.4: a) Flow stress at 0.02 true strain versus strain rate for an IF steel with five different amounts of pre-strain. b) Flow stress at 0.02 true strain versus pre-strain amount for an IF steel at three different strain rates.

6.2 Solid Solution Strengthening

The effects of solid solution strengthening were investigated for two different steel types: IF and HSLA. Both had significant differences in Mn and P content, while the HSLA steels also had differences in Si content.

6.2.1 IF Steel

Tensile tests were conducted at strain rates ranging from 0.01 to about 900 s^{-1} on samples prepared from IF-3 and IF-4 steels. IF-4 steel (0.9 Mn, 0.09 P) had a greater degree of solid solution strengthening than IF-3 steel (0.2 Mn, 0.01 P) due to the greater amounts of Mn and P. Engineering stress-strain curves for each steel are shown in Figure 6.5. For both IF-3 and IF-4 steels, the yield and tensile strengths increase with increasing strain rate, while the yield/tensile strength ratio appears to increase. Comparing the two plots in Figure 6.5 reveals that the IF-4 steel is stronger than the IF-3 steel at the lowest strain rate, but the strength improvement decreases with increasing strain rate.

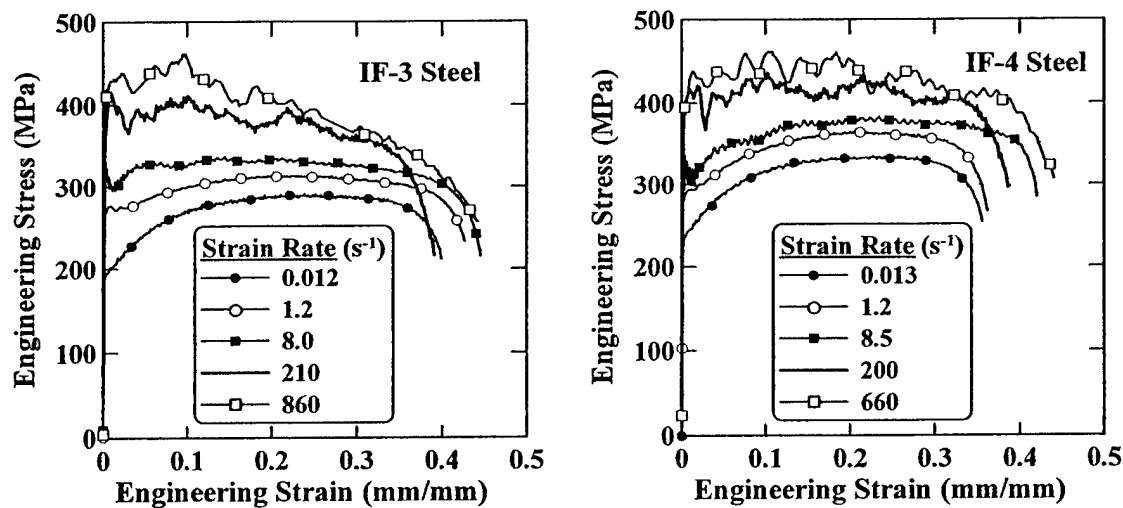


Figure 6.5: Engineering stress-strain curves for IF steels tested at five different strain rates. a) IF-3 steel (0.2 Mn, 0.01 P). b) IF-4 steel (0.9 Mn, 0.09 P).

If it is assumed that the quasi-static strength increase due to solute additions of Mn and P are additive, then the expected strength increase could be predicted based on Figure 6.6, which plots yield and tensile strengths for an IF steel versus solute additions [127]. The difference between the quasi-static yield strengths of IF-3 and IF-4 predicted using Figure 6.6a is 45 MPa. The actual difference in quasi-static yield strengths is about 51 MPa. The grain size of IF-4 steel is about 33 μm , while that of IF-3 steel is about 40 μm , which may account for the remainder of the yield strength difference. However, the predicted tensile strength difference of 85 MPa (21 MPa due to Mn and 64 MPa due to P) exceeds the actual tensile strength difference of about 45 MPa.

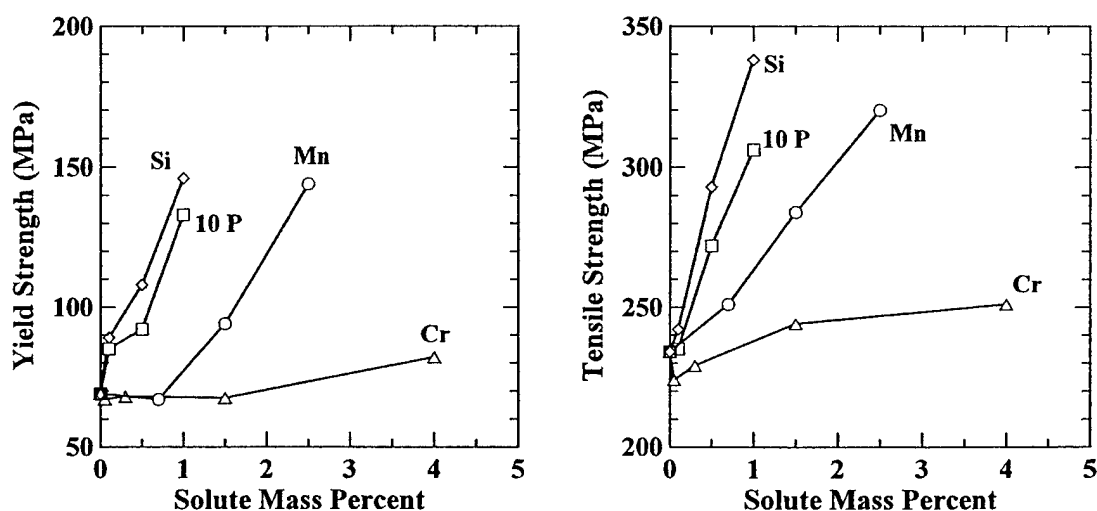


Figure 6.6: (a) Yield strength and (b) tensile strength as functions of alloying additions to an IF steel [replotted from 127].

Figure 6.7a shows strain rate sensitivity by plotting flow stress at 0.02 true strain as a function of strain rate for both IF-3 and IF-4 steels. For both steels, Figure 6.7a shows two distinct regions of strain rate sensitivity, with an increase at strain rates above 10 s^{-1} . For both low and high strain rates, IF-3 steel has higher logarithmic strain rate

sensitivity (β) than IF-4 steel, and the values are shown in Table 6.1. Some of the same data from Figure 6.7a are plotted in Figure 6.7b as flow stress at 0.02 true strain versus the IF steel designation for four different strain rates, where “3” is the IF-3 steel and “4” is the IF-4 steel. It is clear from Figures 6.7a and 6.7b that the increment of strengthening from low strain rate to higher strain rate diminishes with increasing alloying. In fact, at the highest strain rates tested, the flow stress of IF-3 steel is approximately equal to that of IF-4 steel, which suggests that the benefits of increased solute content for strengthening have completely disappeared.

These results for the IF-3 and IF-4 steels indicate that solid solution strengthening diminishes the strain rate sensitivity of IF steel, similar to the solid solution softening at low temperatures discussed in Section 3.6.

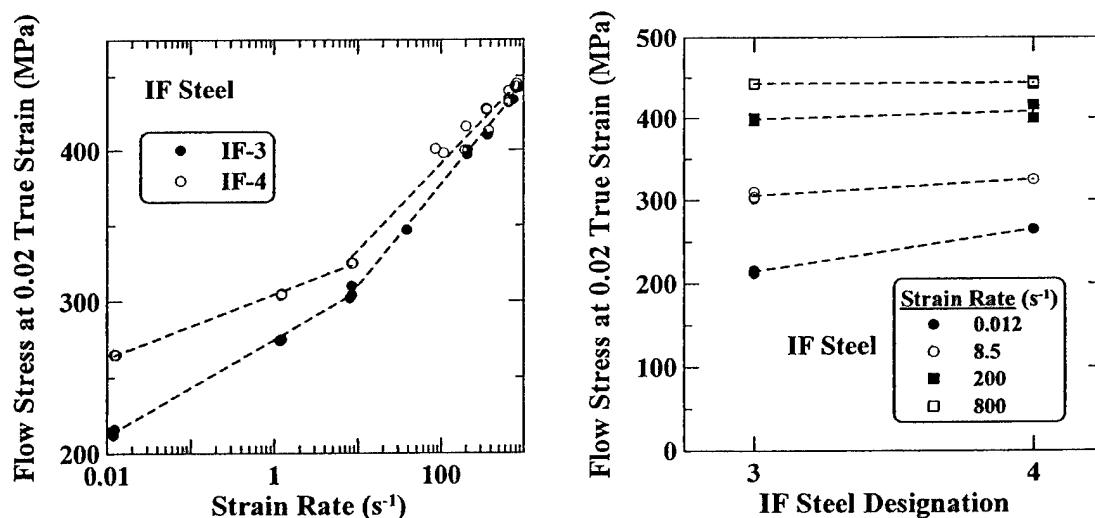


Figure 6.7: a) Flow stress at 0.02 true strain versus strain rate for two IF steels with different solute content. b) Flow stress at 0.02 true strain versus IF steel designation at four different strain rates. “3” is the IF-3 steel composition (0.2 Mn, 0.01 P) and “4” is the IF-4 steel composition (0.9 Mn, 0.09 P).

Table 6.1: Logarithmic strain rate sensitivities (β) for the IF-3 and IF-4 steel data shown in Figure 6.7a.

	β for IF-3	β for IF-4
Low Strain Rates	31.7	20.4
High Strain Rates	69.2	61.1

6.2.2 HSLA Steel

HSLA steels are strengthened by a variety of mechanisms, including grain refinement, precipitation, cold work and solid solution strengthening. They typically have ferrite-pearlite microstructures, whereas IF steels have single phase ferrite microstructures. Since solid solution strengthening is expected to be the only short-range (thermally-assisted) mechanism, differences in solid solution strengthening should show the same trend with increasing strain rate as that seen in IF steel. Since HSLA-1 (0.050C-0.390Mn-0.011P-0.016Si) and HSLA-2 (0.09C-1.46Mn-0.020P-0.08Si) have significantly different compositions, their respective strain rate sensitivities can be compared to see if the higher alloyed (HSLA-2) steel has lower strain rate sensitivity than the lower alloyed (HSLA-1) steel.

Figure 6.8 shows strain rate sensitivity for both HSLA-1 and HSLA-2 steels by plotting yield strength as a function of strain rate. For both low and high strain rates, HSLA-1 steel has higher logarithmic strain rate sensitivity (β) than HSLA-2 steel, and the values are shown in Table 6.2.

To make it easier to compare just the solid solution strengthening differences between the two HSLA steels, the expected difference in quasi-static yield strengths due to solid solution strengthening was calculated using Figure 6.6 and determined to be 39 MPa. The quasi-static yield strength of HSLA-2 steel is actually about 196 MPa higher than that of HSLA-1 steel. Therefore, 157 MPa is assumed due to other strengthening mechanisms, such as grain refinement and precipitation strengthening. HSLA-2 steel

also has slightly more pearlite than HSLA-1 steel due to its higher carbon content. However, for low carbon (below 0.3 wt. pct.) steels, the yield strength is not significantly affected by the volume fraction of pearlite [128]. To compare HSLA-2 to HSLA-1 based only upon solid solution strengthening, 157 MPa was subtracted from all HSLA-2 yield strength values shown in Figure 6.8. These modified yield strength values for HSLA-2 steel are plotted versus strain rate in Figure 6.9a along with the original yield strength values for HSLA-1 steel. Some of the same data from Figure 6.9a are plotted in Figure 6.9b as yield strength versus HSLA steel designation for three different strain rates, where “1” is the low solute content steel and “2” is the high solute steel. Similar to the IF steel results, Figures 6.9a and 6.9b show that the increment of strengthening from low strain rate to higher strain rate diminishes with increasing alloying.

These results for HSLA-1 and HSLA-2 steels indicate that solid solution strengthening diminishes the strain rate sensitivity of HSLA steel, similar to that seen in IF steel and is indicative of solid solution softening as discussed in Section 3.6.

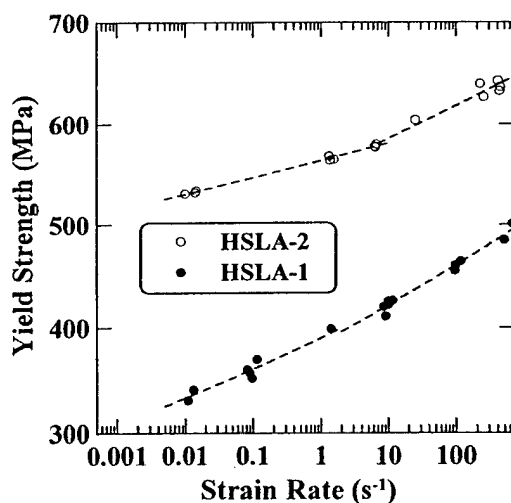


Figure 6.8: Yield strength versus strain rate for two HSLA steels with different solute content.

Table 6.2: Logarithmic strain rate sensitivities (β) for HSLA-1 and HSLA-2 steel data shown in Figure 6.8.

	β for HSLA-1	β for HSLA-2
Low Strain Rates	30.0	16.8
High Strain Rates	40.1	32.9

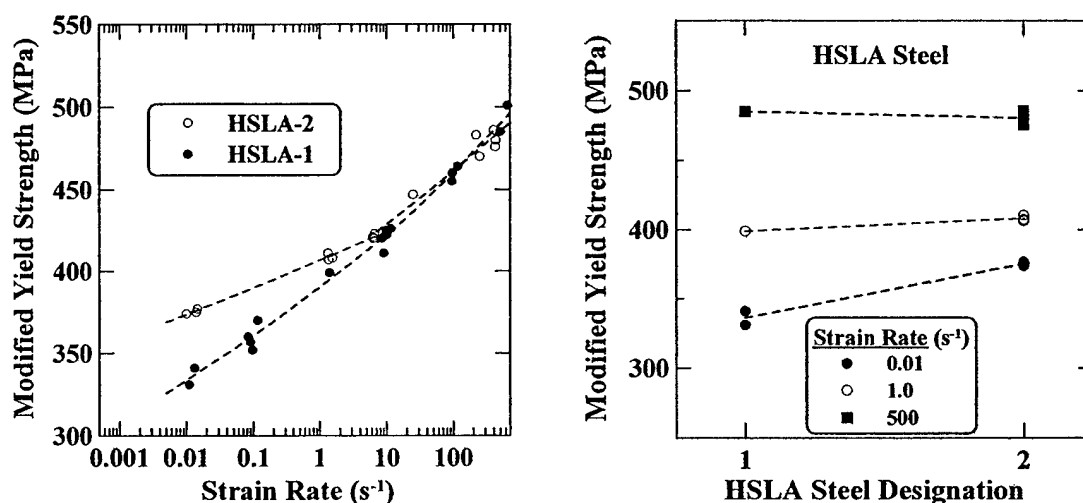


Figure 6.9: a) Yield strength (modified for HSLA-2) versus strain rate for two HSLA steels with different solute content. b) Yield strength (modified for HSLA-2) versus IF steel designation at four different strain rates. “1” is the HSLA-1 steel composition (lower solute content) and “2” is the HSLA-2 steel composition (higher solute content).

6.3 First Grain Size Study

As mentioned in Section 4.8, two grain size studies were conducted to evaluate the effect of strain rate on grain size strengthening in IF steels. The first study used four different grain sizes of IF-1 steel achieved by various heat treating processes, which were described in Section 4.8.1. The samples were all machined with ASTM-E8 subsize dimensions before the need was realized for using a grip section strain gage for load data

collection at high rates. The grip sections were not wide enough to prevent plastic deformation in the 65 and 135 μm grain size samples. Therefore, results for this study are only reported up to strain rates of 35 s^{-1} . The load washer raw data were used for strain rates at and below 10 s^{-1} , while the data-averaging procedure described in Section 4.3.1 was used to curve-fit the load washer data for strain rates of 35 s^{-1} . Example true stress-strain curves are shown in Figure 6.10 for each grain size at strain rates of 0.001 and 35 s^{-1} . All of the samples exhibited yield point elongation except for the largest grain size. The amount of Lüders strain increased with decreasing grain size, which is expected [34 (p. 17), 129].

In Figure 6.11, the flow stress at 0.05 true strain is plotted versus grain diameter, $d^{-1/2}$, for all tensile tests run between strain rates of 0.001 and 35 s^{-1} . Flow stress values for the 65 μm grain size samples do not follow the trend of decreasing strength with increasing grain size, which may be due to precipitation strengthening or solute segregation to grain boundaries during the heat treating process. Since the 65 μm data did not follow the expected trend, further analyses were conducted using only the 10, 25 and 135 μm data.

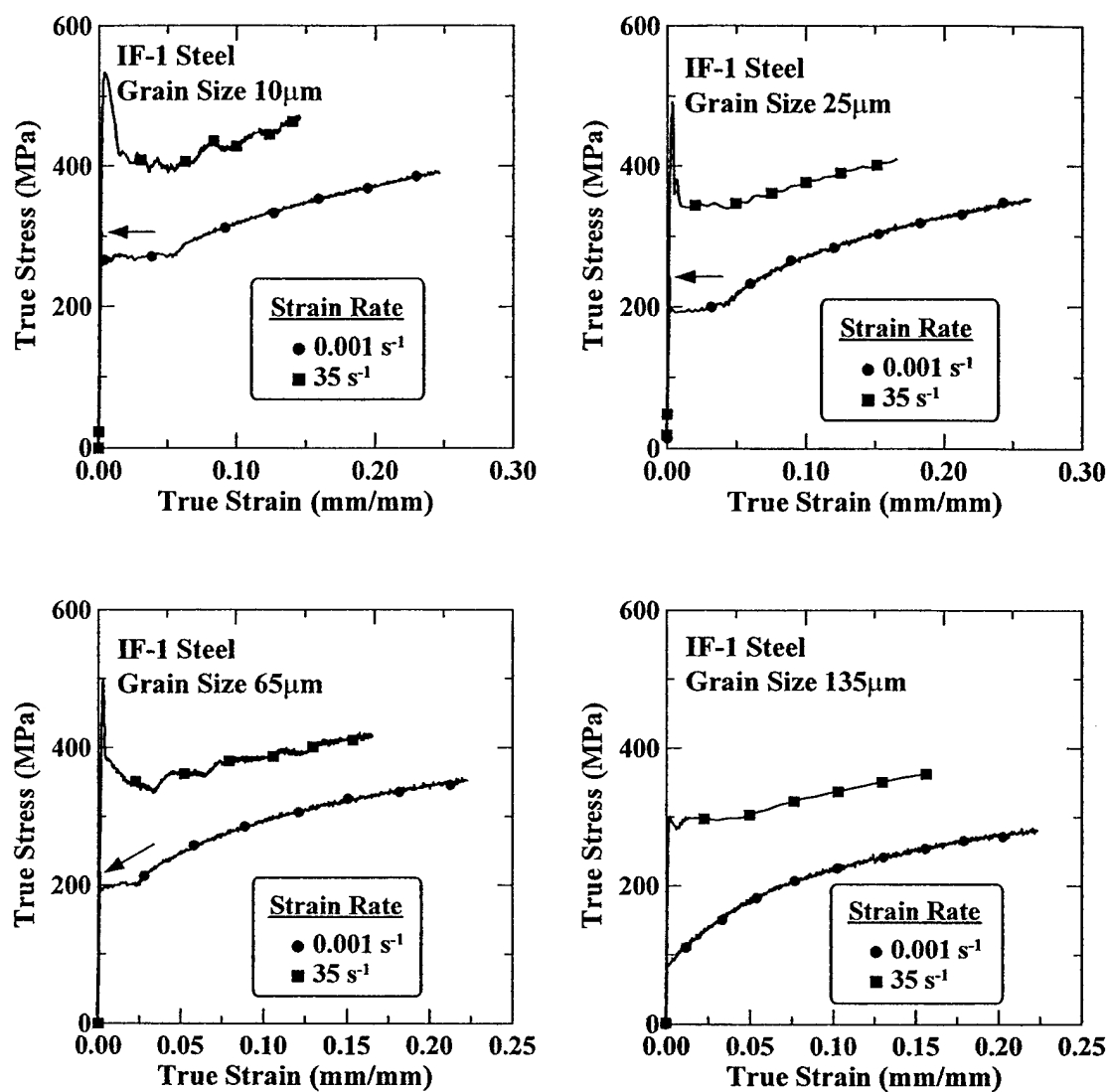


Figure 6.10: True stress-strain curves at two strain rates for IF-1 steel with four different grain sizes. All sample gage lengths were 25.4 mm. Actuator speed for low strain rate was 0.025 mm/s and was 1.0 m/s for high strain rate. Arrows indicate heights of upper yield points for low-rate stress-strain curves.

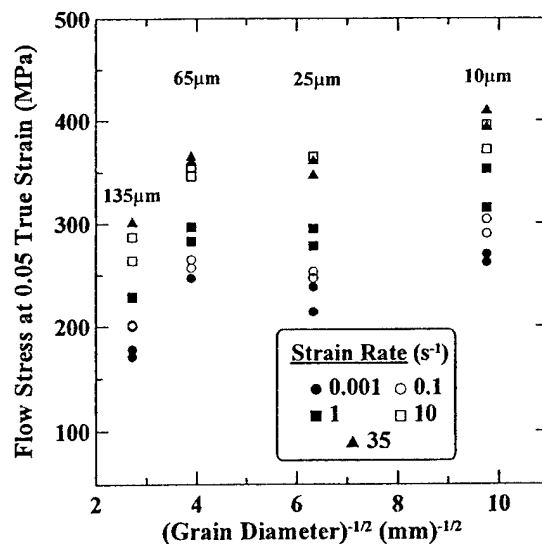


Figure 6.11: Flow stress at 0.05 true strain as a function of $(\text{grain diameter})^{-1/2}$ for IF-1 steel tensile tested at five different strain rates. All sample gage lengths were 25.4 mm. Actuator speeds were 0.025, 2.5, 25, 250 and 1000 mm/s for strain rates of 0.001, 0.1, 1, 10 and 35 s⁻¹, respectively.

Four Hall-Petch plots (flow stress versus $d^{-1/2}$) are shown in Figure 6.12 for yield strength, and for flow stress at values of 0.05, 0.10 and 0.15 true strain. Yield strength was determined as the lower yield stress for discontinuous yielding materials and the 0.002 strain offset value for continuous yielding materials. Each plot contains data for five different strain rates. Hall-Petch parameters, σ_0 and k , were calculated for each strain rate in each graph and are tabulated in Table 6.3. Figure 6.13 shows plots of σ_0 and k for each true strain level as functions of strain rate for the data in Table 6.3.

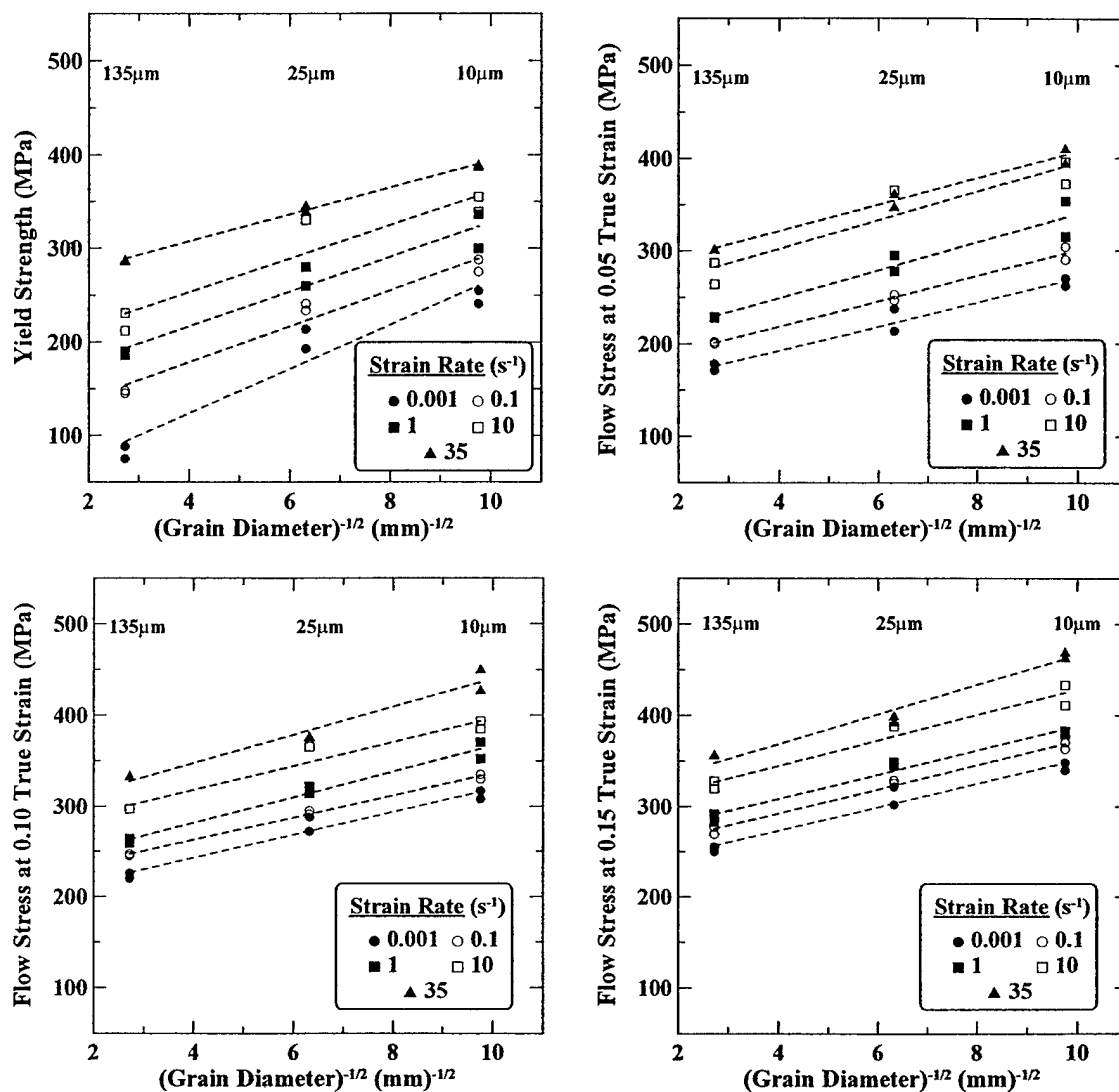


Figure 6.12: Flow stress versus $(\text{grain diameter})^{-1/2}$ for IF-1 steel tested at five different strain rates. a) Yield stress, b) Flow stress at 0.05 true strain, c) Flow stress at 0.10 true strain, and d) Flow stress at 0.15 true strain. All sample gage lengths were 25.4 mm. Actuator speeds were 0.025, 2.5, 25, 250 and 1000 mm/s for strain rates of 0.001, 0.1, 1, 10 and 35 s^{-1} , respectively.

Table 6.3: Hall-Petch parameters, σ_o (MPa) and k (MPa $\sqrt{\text{mm}}$), for each flow stress and strain rate shown in Figure 6.12.

Strain Rate	Flow Stress Measured At:							
	Yield		0.05 true strain		0.10 true strain		0.15 true strain	
	σ_o	k	σ_o	k	σ_o	k	σ_o	k
0.001	29	23.7	141	13.0	192	12.7	221	13.0
0.1	101	19.2	164	13.6	213	12.3	239	13.3
1	143	18.5	189	15.0	225	14.2	255	13.3
10	181	17.9	240	15.5	265	13.1	289	13.9
35	249	14.4	264	14.3	286	15.4	303	16.3

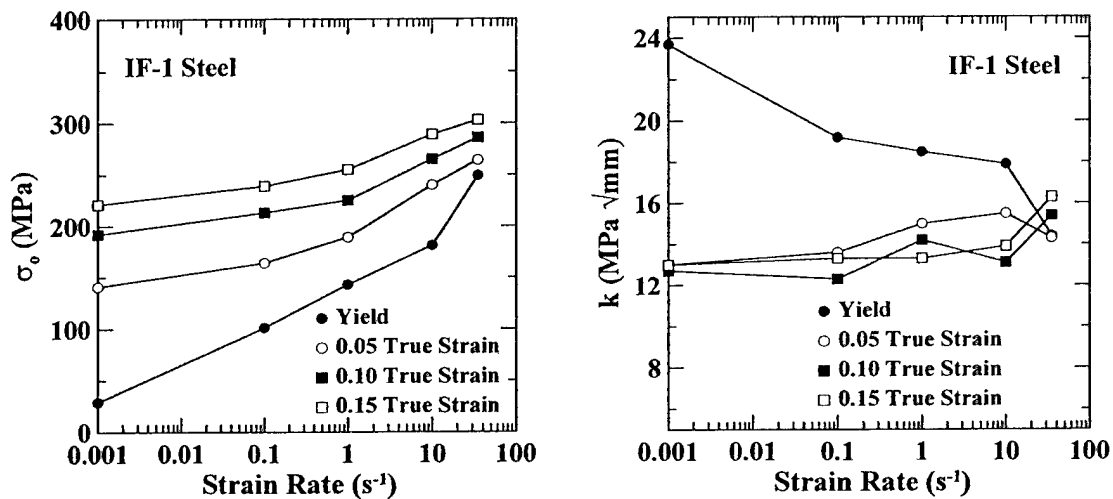


Figure 6.13: Strain rate sensitivities of (a) σ_o and (b) k for the data presented in Table 6.3.

In Figure 6.12, σ_o (the y-axis intercept) increases with increasing strain rate for each plot. It appears that the Hall-Petch slope in each plot remains nearly constant with strain rate, with the exception of the quasi-static rate data in the yield strength plot (Figure 6.12a). Figure 6.13 gives quantitative analyses of the effects of strain rate and

true strain value on σ_0 and k . Figure 6.13a clearly shows increasing σ_0 with increasing true strain and strain rate, as expected due to its strain-rate dependence with the lattice friction stress. In Figure 6.13b, k values for yield strength decrease with increasing strain rate, while k values for the other true strain levels remain fairly constant or increase slightly with increasing strain rate.

The fact that σ_0 and k values for yield strength do not follow the same trends as σ_0 and k values for flow stresses measured at true strains of 0.05, 0.10 and 0.15 are interpreted to reflect the difference in yielding behavior between different grain size samples. The 10 μm and 25 μm grain size samples exhibited yield point elongation at all strain rates, while the 135 μm grain size samples exhibited continuous-yielding at the lowest strain rate, but displayed an increasing tendency towards yield point elongation with increasing strain rate as shown in Figure 6.14. Yield strength was determined as the lower yield point for discontinuous-yielding samples and as the 0.2% offset stress for continuous-yielding samples. For two samples of the same material having identical plastic flow behavior, but different yield behavior, the continuous-yielding sample will have lower yield strength than the discontinuous-yielding sample [76 (p. 129-130)]. For example, temper rolling of a discontinuous-yielding steel produces a continuous-yielding material with lower yield strength [34 (p. 148-149)]. Therefore, the changes in yield behavior of the 135 μm grain size samples may account for the trends seen in σ_0 and k values for yield strength. For example, as shown in Figure 6.12a, the yield strength of the continuous-yielding 135 μm grain size sample at the lowest strain rate is quite low which causes σ_0 (the intercept of the fitted line) to be relatively low and k (the slope of the fitted line) to be relatively high. Flow stresses measured at true strains greater than 0.05 were beyond the yield point elongation portion of the flow curves for all samples and therefore σ_0 and k values followed expected trends.

If the yield strength values are ignored, k values are essentially independent of strain rate, which is consistent with several other studies [36, 70-72]. The magnitudes of

k values in Figure 6.13b fall within the range of k values expected for low carbon steels [63, 68] with a mean value of about $15 \text{ MPa}\sqrt{\text{mm}}$.

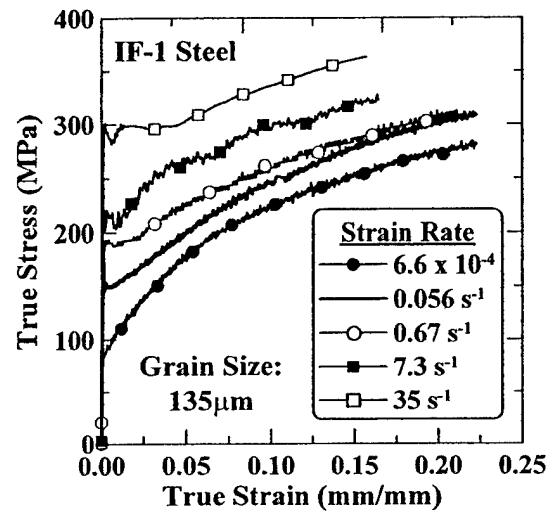


Figure 6.14: True stress-strain curves at five different strain rates for IF-1 steel with 135 μm grain size. All sample gage lengths were 25.4 mm.

In Sections 3.7 and 3.8, several different models for grain size strengthening were described. For each model, the expected temperature or strain rate dependence of k was discussed. The dislocation pile-up model predicted increasing k values with decreasing temperature or increasing strain rate [64], while the dislocation density models predicted the temperature dependence of k to be only related to the temperature dependence of the shear modulus [66, 67]. Since k values did not show a significant increase with increasing strain rate in this experiment, the dislocation pile-up model does not fit these results. This is expected since dislocation pile-ups are not generally found in steels [68]. The nearly constant value of k with changing strain rate for the 0.05, 0.10 and 0.15 true strain flow stress values, supports the use of one of the dislocation density models, which predict this behavior due to the rate independence of k. The true strain values used in

these analyses do not allow a determination of the influence of small strains on k values, and therefore the suitability of the dislocation density model based upon geometrically necessary dislocations can not be adequately determined.

Similar to the strengthening mechanism of cold work, these results show that changes in grain size do not significantly affect the increment of strengthening achieved with increase in strain rate, which implies that grain boundaries are long-range (athermal) obstacles to dislocation motion.

6.4 Second grain size study

The second grain size study was conducted on IF-5 steel heat treated to achieve four different grain sizes as described in Section 4.8.2. However, there was quite a bit of scatter in actual grain sizes achieved for the samples designed to have grain sizes of 36 μm . Also, some samples designed to have the same grain sizes were continuous-yielding while others exhibited yield point elongation. Heat treating of the IF-5 steel to achieve uniform grain growth was complicated by the relatively high alloy content (0.008C-1.42Mn-0.009P-0.006S-0.220Si-0.016Al-0.0030N-0.128Ti) which most likely resulted in more carbide precipitates than the IF-1 steel (0.0038C-0.17Mn-0.003P-0.0074S-0.002Si-0.06Al-0.0042N-0.072Ti) used in the first grain size study. Precipitates tend to pin grain boundaries, thus making uniform grain growth difficult [34 (p. 169)]. Figure 6.15 shows quasi-static engineering stress-strain curves for IF-1 and IF-5 steel samples with the same grain size of 135 μm . The higher strength and strain hardening of IF-5 steel is presumably a result of both solution and precipitation strengthening.

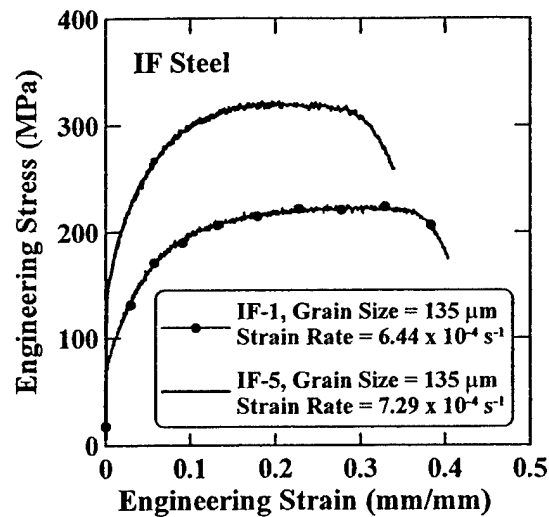


Figure 6.15: Quasi-static engineering stress-strain curves for IF-1 and IF-5 steels with grain size of about 135 μm .

In spite of the difficulties in producing uniform grain sizes in the IF-5 steel, tensile samples were machined and tested over the strain rate range from 0.001 s^{-1} to about 400 s^{-1} . In Figure 6.16a, yield strength is plotted versus grain diameter, $d^{-1/2}$, for all quasi-static tensile tests. Yield strength values for the $10 \mu\text{m}$ grain size samples did not follow the trend of increasing strength with decreasing grain size, which may be due to precipitation strengthening and solute segregation to grain boundaries occurring during heat treating of the other (14 , 36 and $130 \mu\text{m}$) samples. Since the $10 \mu\text{m}$ data did not follow the expected trend, further analyses were conducted using only the other samples. In Figure 6.16b, yield strength is plotted versus grain diameter, $d^{-1/2}$, for the quasi-static tests used in the first grain size study with IF-1 steel, and the 14 , 36 and $130 \mu\text{m}$ quasi-static tests run in this study with IF-5 steel. k_y (k at yield) values were calculated for both sets of results and found to be similar, as shown in Figure 6.16b.

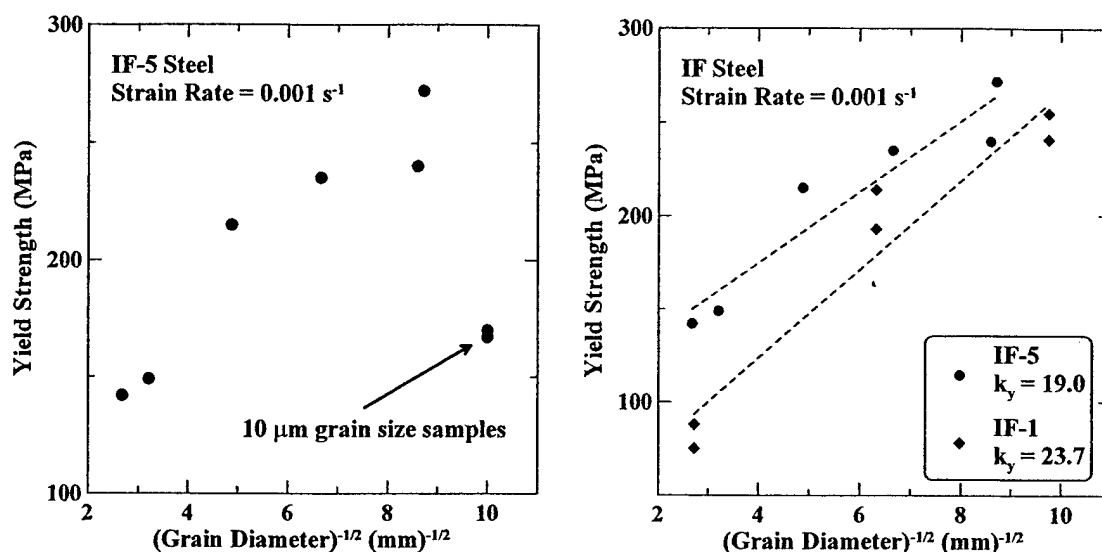


Figure 6.16: Yield strength as a function of $(\text{grain diameter})^{-1/2}$. All sample gage lengths were 25.4 mm. Actuator speed was 0.025 mm/s. (a) All quasi-static IF-5 steel sample results. 10 μm grain size samples do not follow the expected Hall-Petch trend. (b) IF-5 steel results (without 10 μm data) compared to IF-1 steel results. The k_y values are similar.

Four Hall-Petch plots (flow stress versus $d^{-1/2}$) are shown in Figure 6.17 for yield strength and flow stress at values of 0.05, 0.075 and 0.10 true strain. Yield strength was determined as the lower yield stress for discontinuous yielding materials and the 0.002 strain offset value for continuous yielding materials. Figures 6.17a and 6.17b contain data for five different strain rates. Figures 6.17c and 6.17d do not contain data for the strain rate of 400 s^{-1} because the uniform strain was not sufficient at this strain rate. Data for strain rates of 0.080 and 8.5 s^{-1} were omitted from Figure 6.17 to reduce clutter. In Figure 6.17, the Hall-Petch slope does not remain constant with strain rate, but there is also no discernable trend.

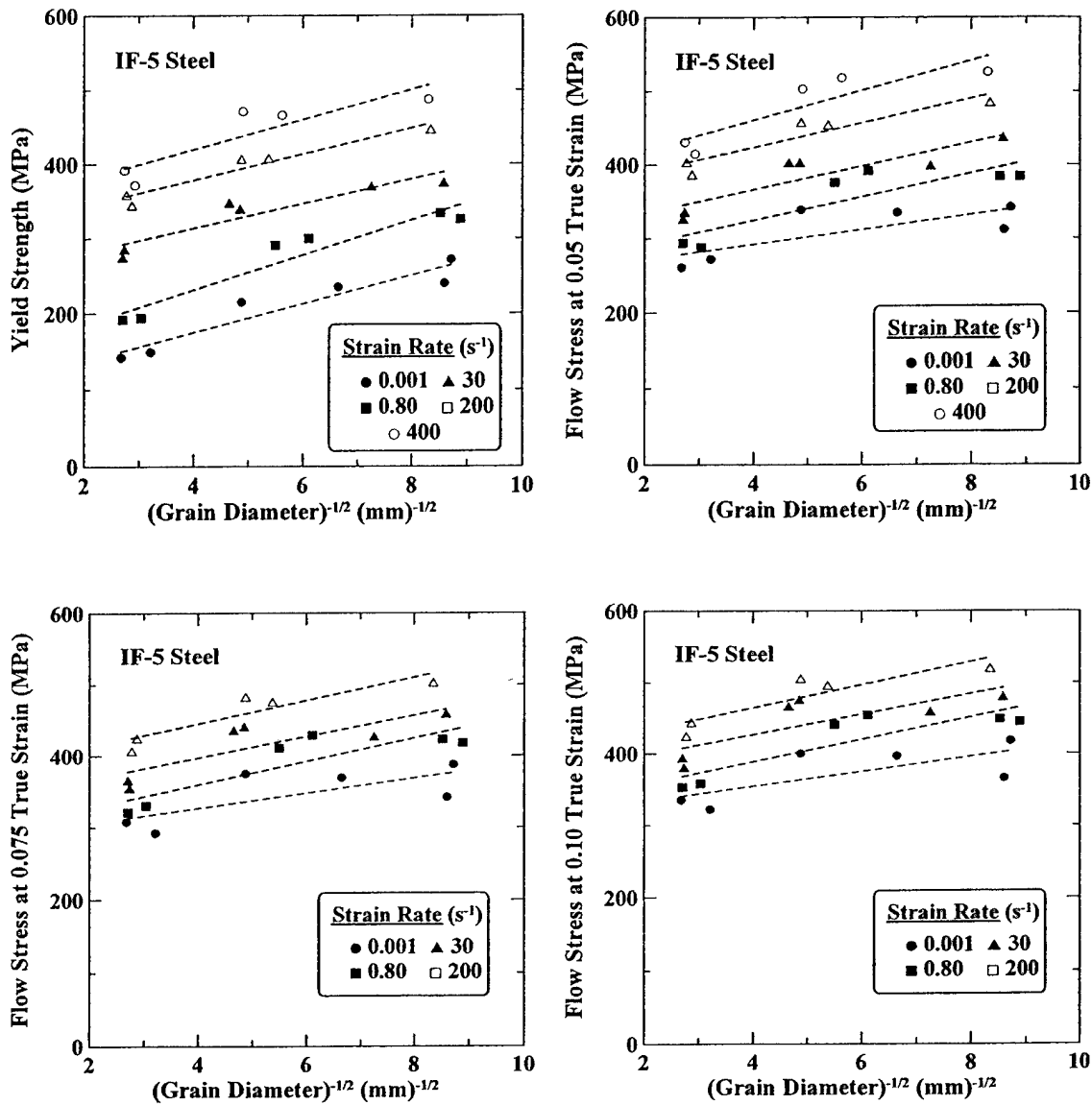


Figure 6.17: Flow stress versus $(\text{grain diameter})^{-1/2}$ for IF-5 steel tested at five different strain rates. a) Yield stress, b) Flow stress at 0.05 true strain, c) Flow stress at 0.075 true strain, and d) Flow stress at 0.10 true strain. All sample gage lengths were 25.4 mm. Actuator speeds were 0.025 mm/s, 25 mm/s, 750 mm/s, 5.0 m/s and 10.0 m/s for strain rates of 0.001, 1, 30, 200 and 400 s^{-1} , respectively.

Hall-Petch parameters, σ_0 and k , were calculated for each strain rate in each graph of Figure 6.17 and are tabulated in Table 6.4. Figure 6.18 shows plots of σ_0 and k for each true strain level as functions of strain rate for the data in Table 6.4. Figure 6.18a shows generally increasing σ_0 with increasing true strain and strain rate, as expected since σ_0 includes both long-range (athermal) contributions to flow stress such as cold work, and short-range (thermal) contributions such as the strain-rate dependence of the lattice friction stress. In Figure 6.18b, there is quite a bit of scatter in the k values, however they still fall within the range of k values expected for low carbon steels [63, 68]. The mean k value for IF-5 steel was about 14 MPa $\sqrt{\text{mm}}$, while it was slightly higher at about 15 MPa $\sqrt{\text{mm}}$ for IF-1 steel.

Table 6.4: Hall-Petch parameters, σ_0 (MPa) and k (MPa $\sqrt{\text{mm}}$), for each flow stress and strain rate shown in Figure 6.17.

Strain Rate	Flow Stress Measured At:							
	Yield		0.05 true strain		0.10 true strain		0.15 true strain	
	σ_0	k	σ_0	k	σ_0	k	σ_0	k
0.001	99	19.0	252	10.0	285	10.6	313	10.4
0.070	144	16.4	282	8.2	315	8.7	348	7.9
0.80	138	23.4	261	15.9	294	16.4	326	15.7
8.5	197	19.8	318	9.5	355	8.6	381	9.0
30	248	16.5	302	16.0	337	14.9	369	14.4
200	308	17.5	357	16.6	380	16.3	400	16.1
400	339	20.2	379	20.2	-	-	-	-

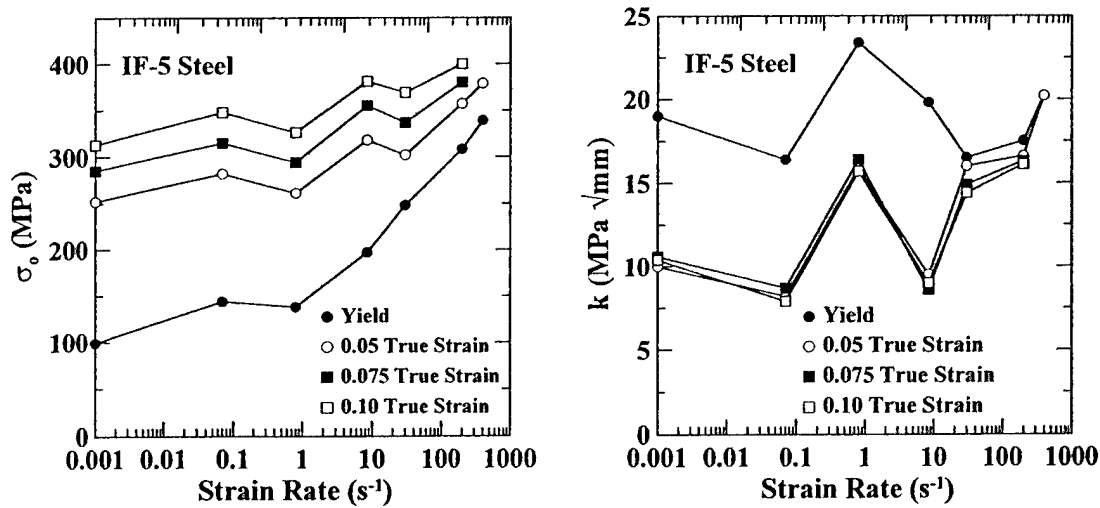


Figure 6.18: Strain rate sensitivities of (a) σ_0 and (b) k for the data presented in Table 6.4.

To compare σ_0 and k value results between the two grain size studies, Figure 6.19 shows plots of σ_0 and k at 0.05 true strain as functions of strain rate for both IF-1 and IF-5 steels. In Figure 6.19a, σ_0 values are higher for IF-5 as expected due to its higher strength, although the trends with increasing strain rates are similar. In Figure 6.19b, there is no trend in k values with strain rate for either steel. Although the k values for IF-5 steel exhibit more scatter in the data, the mean values for both steels are approximately the same.

As in the first grain size study, the lack of a trend in k values with strain rate supports the use of a dislocation density model to describe grain size strengthening. This second study also further supports the assumption that grain boundaries are long-range (athermal) obstacles to dislocation motion.

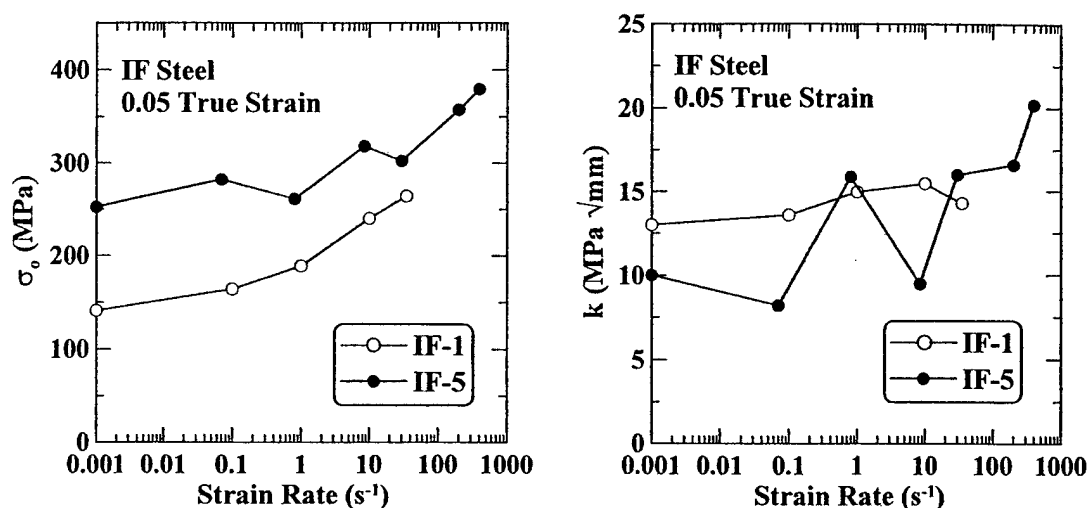


Figure 6.19: Comparison of the strain rate sensitivities of (a) σ_0 and (b) k for IF-1 and IF-5 steels at 0.05 true strain.

6.5 Discussion of Cold Work, Solid Solution and Grain Size Strengthening Results

In the preceding sections, it was established that in the range of strain rates tested, strengthening of BCC ferrite by means of cold work or grain refinement is not greatly affected by increasing strain rate, but strengthening by solute addition decreases with increasing strain rate. Therefore, dislocation interactions and grain boundaries were found to be long-range (athermal) obstacles to dislocation motion, while solid solution softening was a short-range (thermally activated) mechanism. If this is true, then increasing the static strength of ferrite through cold work or grain refinement should not change the strengthening increment from static to dynamic loading. However, if the strengthening increment ($\sigma_{\text{dynamic}} - \sigma_{\text{static}}$) is plotted versus static strength values, the strengthening increment typically decreases with increasing static strength as shown in Figure 6.20.

The three IF steels shown in Figure 6.20 all have similar yield strengths, but the IF-1 (10 μm grain size) strengthening increment is significantly less than those of IF-2 or

IF-3. However, in Section 5.2.3 it was determined that the difference is primarily due to the discontinuous-yielding behavior of IF-1 steel at low rates compared to the continuous-yielding behavior of IF-2 and IF-3 steels. The compositions of the two HSLA steels are significantly different (HSLA-1: 0.050C-0.390Mn-0.011P-0.008S-0.016Si-0.029Cr-0.039Al-0.006Ti-0.001V-0.029Nb, HSLA-2: 0.09C-1.46Mn-0.020P-0.001S-0.08Si-0.045Nb), which contributes to the greater static yield strength in HSLA-2 steel and accounts for its lower strengthening increment due to solid solution softening as discussed in Section 6.2.2.

For the controlled experiments carried out for this thesis on cold work, grain size, and solid solution strengthening changes in IF steels, static-to-dynamic strengthening increments are plotted as a function of static strength in Figure 6.21. Table 6.5 lists the static and dynamic strain rates used, along with the true strain value at which flow stress was measured for each steel. Yield strength values were not used because of differences in yield point elongation behavior between samples.

In Figure 6.21, static-to-dynamic strengthening increments for the cold work experiment (IF-2) and grain size experiments (IF-1 and IF-5) remain approximately constant regardless of static strength, while the strengthening increments for the solid solution experiment (IF-3 and IF-4) decrease significantly with increasing static strength. These results support the conclusions made in Sections 6.1 through 6.4 that cold work and grain size refinement add long-range (athermal) obstacles to dislocation motion and these strengthening mechanisms are therefore independent of strain rate, while substitutional solute atoms are short-range barriers to dislocation motion which cause strength to be dependent upon strain rate.

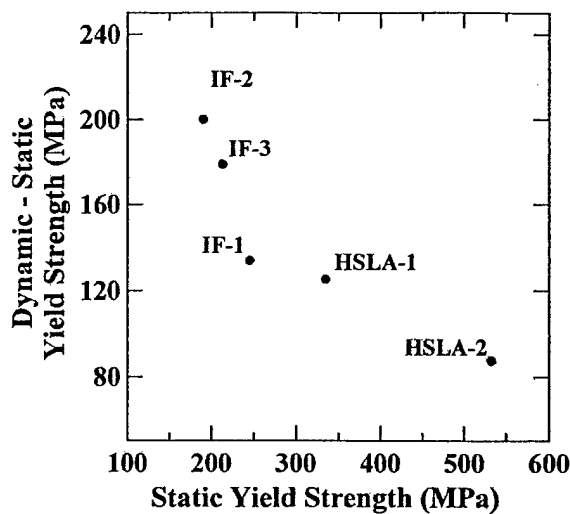


Figure 6.20: Static-to-dynamic strength increment versus static strength for six different steels. Dynamic yield strength measured at strain rate of approximately 100 s^{-1} . IF-2 data point based on 0% pre-strain. IF-1 data point based on $10 \mu\text{m}$ grain size.

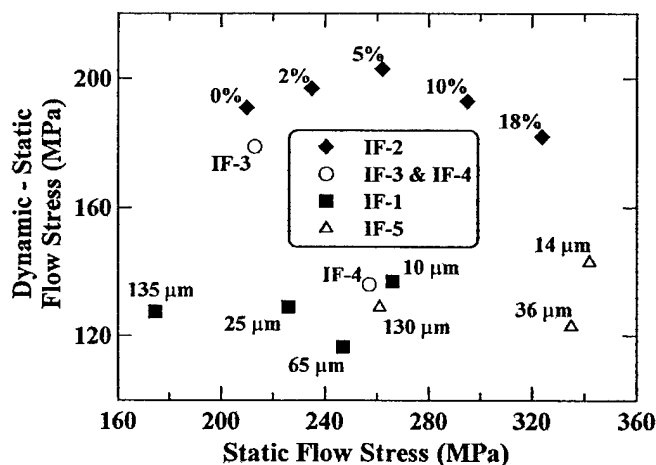


Figure 6.21: Static-to-dynamic strength increment versus static strength for four different IF steels. IF-1 steel data points for different amounts of tensile pre-strain (cold work). IF-2 and IF-5 steel data points for different grain sizes. IF-3 and IF-4 steel data points are from the solid solution strengthening experiment. Strain rates and true strain values used for data points are given in Table 6.5.

Table 6.5: Strain rates and true strain values used for flow stress measurements in Figure 6.21.

Steel	Strain Rate (s^{-1})		True Strain
	Static	Dynamic	
IF-1	0.001	35	0.05
IF-2	0.001	150	0.03
IF-3	0.01	200	0.02
IF-4	0.01	200	0.02
IF-5	0.001	200	0.05

6.6 Multiphase Strengthening: Effect of Retained Austenite Stability in a TRIP Steel

Tensile tests were conducted over the strain rate range from 0.01 to 250 s^{-1} for each of the two TRIP-3 steels (HS and LS). True stress-strain curves for each steel at two strain rates are shown in Figure 6.22. The LS steel shows higher initial strain hardening rate and lower elongation compared to the HS steel, although the strain hardening rate difference appears to diminish with increasing strain rate. These differences are seen in Figure 6.23 where both steels are compared at three different strain rates.

The isothermal treatment temperature used to create the low stability retained austenite (LS) steel was higher than that used for the high stability retained austenite (HS) steel, while the hold times were the same. At the higher temperature, diffusion occurs more rapidly which increases the transformation rate of austenite to bainite. For equal times, the higher isothermal transformation temperature resulted in lower amounts of austenite. LS had 9.0% retained austenite, while HS had 9.8%. Also carbides may form more easily at higher temperature [130], and the austenite remaining after the higher temperature transformation had a lower carbon content, resulting in lower stability because its martensite-start temperature is higher. The carbon content of retained austenite was 1.17 wt. pct. in LS and 1.26 wt. pct. in HS. Therefore, the low stability (LS) retained austenite should need less addition of mechanical driving force than high stability (HS) retained austenite in order to transform to martensite, which means the

retained austenite in the LS steel should transform earlier (with less strain) in the deformation process. If this occurs, the LS stress-strain curve should show higher initial strain hardening rate and lower elongation compared to the HS heat treatment, which is the case in Figure 6.23a.

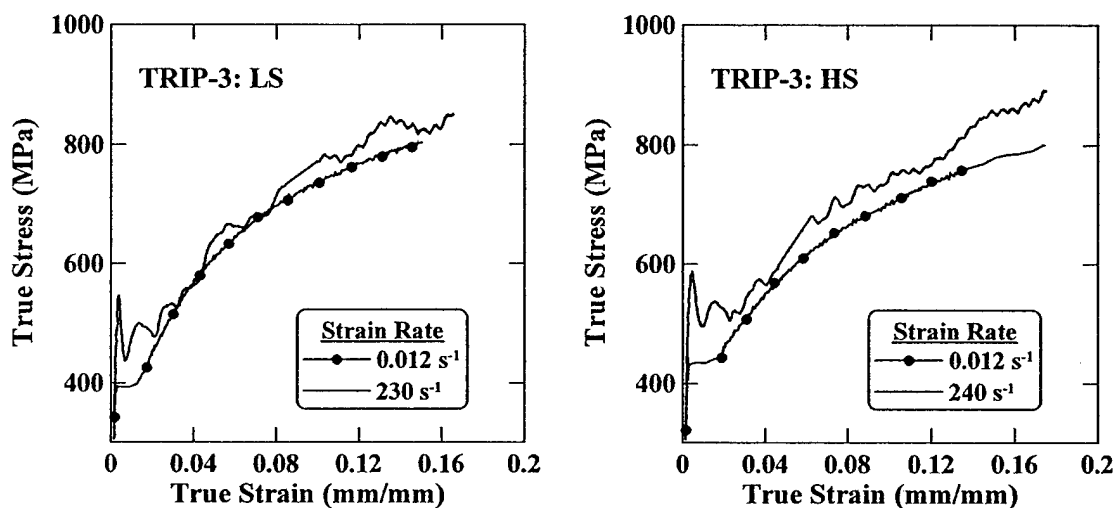


Figure 6.22: True stress-strain curves at two different strain rates for (a) LS and (b) HS TRIP-3 steel. Sample gage length was 50.8 mm and actuator speed was 0.25 mm/s for both low-rate tests. Gage length was 25.4 mm and actuator speed was 6.0 m/s for the high-rate tests.

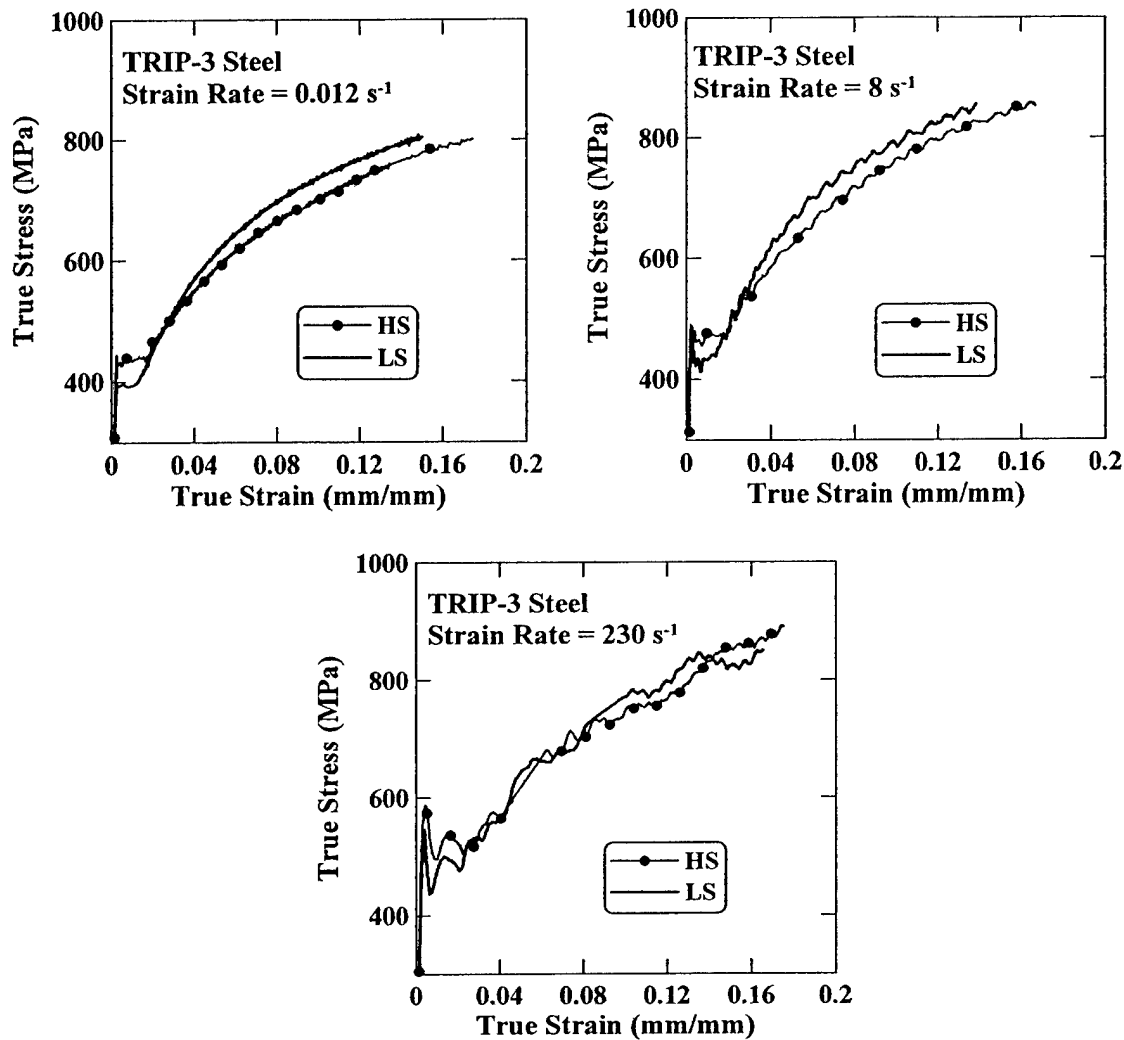


Figure 6.23: True stress-strain curves comparing LS and HS heat treatments for TRIP-3 steel at three different strain rates. a) Sample gage length = 50.8 mm and actuator speed = 0.50 mm/s. b) Sample gage length = 50.8 mm and actuator speed = 500 mm/s. c) Sample gage length = 25.4 mm and actuator speed = 6.0 m/s.

With increasing strain rate, it is expected that the low-strain work hardening rate of a TRIP steel may increase as the increased mechanical driving force (due to higher overall flow stress) causes more retained austenite to transform earlier in the test.

However, at high strain values during high-rate tests, the work hardening rate is expected to decrease due to adiabatic heating, which inhibits the transformation. Work hardening exponents, n , were calculated for low strain (0.02 to 0.05) and high strain (0.08 to uniform strain limit) values for each test shown in Figure 6.23a and 6.23b and the results are listed in Table 6.6. The data from Figure 6.23c at 230 s^{-1} were too noisy to calculate work hardening exponents. As expected, n at low strain values increases with increasing strain rate for both materials, and increases more for the HS steel. The work hardening exponents at high strain values were lower than those at low strain values and the difference was much more pronounced in the LS steel. This result might be expected since the lower stability retained austenite in LS steel should transform quickly (with little strain energy) during deformation, while the higher stability retained austenite in HS steel should require more strain energy and therefore more deformation for transformation to martensite to occur.

Table 6.6: Work hardening exponents, n , for low and high strain values for each tensile test shown in Figures 6.23a and 6.23b.

Strain Rate (s^{-1})	Low Stability TRIP-3		High Stability TRIP-3	
	Low Strain (0.02 - 0.05)	High Strain (0.08 - ϵ_u)	Low Strain (0.02 - 0.05)	High Strain (0.08 - ϵ_u)
0.012	0.337	0.223	0.264	0.248
8	0.353	0.225	0.294	0.243
$n(8) - n(0.012)$	+ 0.017	+ 0.002	+ 0.030	- 0.005

At the highest strain rate of about 230 s^{-1} , the behavior of LS and HS materials in Figure 6.23c appears similar. This behavior may be explained by the “saturation” of martensite transformation in both steels. The mechanical driving force might be high enough to cause all of the retained austenite in both steels (LS and HS) to transform early

in the test, causing equivalent hardening behavior in both. In a study by Choi, *et al.* [21] of a TRIP steel with identical composition and processing as TRIP-3 HS steel, it was found that all of the retained austenite transformed to martensite during tensile tests at all strain rates ranging from quasi-static to 250 s^{-1} .

6.7 Multiphase Strengthening: Comparison of Dual Phase to TRIP Steel

Although a systematic study was not conducted to compare dual phase and TRIP steels, data collected on a dual phase steel used to develop a dynamic tensile test capability will be compared with the TRIP steels discussed in Section 6.6. Figure 6.24 shows quasi-static true stress-strain curves for both TRIP-3 steels (low stability “LS” and high stability “HS”) and the dual phase steel. The dual phase steel is continuous-yielding while both TRIP-3 steels have yield point elongation. The uniform strain is about equal for the TRIP-3 LS and dual phase steels, while the uniform strain for TRIP-3 HS is greater, due to the more gradual transformation of retained austenite to martensite. The strain hardening rate throughout the flow curve in the dual phase steel is lower than for the TRIP-3 steels. Work hardening exponents at low strains (0.02 to 0.05) and high strains (0.08 to the uniform strain limit) were calculated for all three steels and are shown in Table 6.7. The work hardening exponents in TRIP steels compared to dual phase are higher because of the retained austenite transformation to martensite.

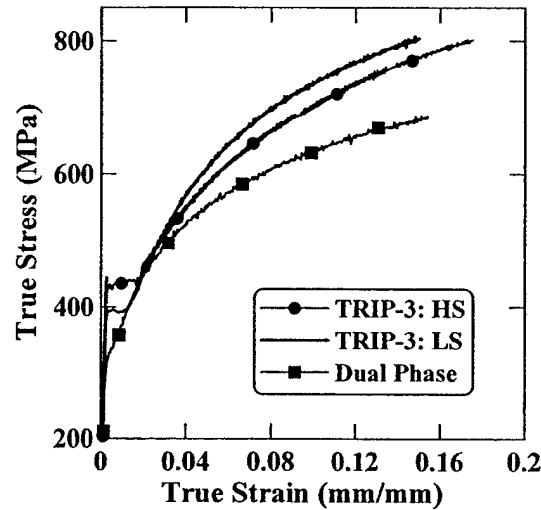


Figure 6.24: True stress-strain curves comparing TRIP-3 LS and HS with dual phase steel at quasi-static strain rates. For both TRIP-3 steels, sample gage length = 50.8 mm, actuator speed = 0.50 mm/s and strain rate = 0.012 s^{-1} . For the dual phase steel, sample gage length = 25.4 mm, actuator speed = 0.025 mm/s and strain rate = $8.9 \times 10^{-4} \text{ s}^{-1}$.

Table 6.7: Work hardening exponents, n , for low and high strain values for the quasi-static tensile tests shown in Figure 6.24.

Material	Work Hardening Exponent, n	
	Low Strain (0.02 - 0.05)	High Strain (0.08 - ϵ_u)
TRIP-3 LS	0.337	0.223
TRIP-3 HS	0.264	0.248
Dual Phase	0.230	0.183

Figure 6.25 shows logarithmic strain rate sensitivity plots for both yield and UTS values for all three multiphase steels. Logarithmic strain rate sensitivity values, β , for Figure 6.25 are tabulated in Table 6.8. There are dramatic differences in strain rate sensitivity between the three steels. For yield strength, the TRIP-3 HS steel β value is constant at 18.9 for all strain rates, while the β value for TRIP-LS increases from 10.9 at

low rates to 20.0 for high rates. However, for dual phase steel, the yield strength β value at low rates is 18.9 and increases to 60.7 for high rates. Consequently, even though dual phase has significantly lower quasi-static yield strength than either TRIP-3 steel (330 MPa versus about 400 MPa for TRIP-3), its dynamic yield strength of 530 MPa at a strain rate of 500 s^{-1} surpasses that of the TRIP-3 steels (about 500 MPa at 600 s^{-1}).

For tensile strength, both TRIP-3 steels have higher β values at low strain rates than dual phase steel, probably because the retained austenite to martensite transformation is enhanced by increasing strain rate for strain rates below 1 s^{-1} . However, at high strain rates, the β value for tensile strength is higher for dual phase than for either TRIP-3 steel. In fact, both TRIP-3 steels have lower high-rate β values than low-rate β values for tensile strength, which is opposite the trend seen in other low carbon steels. This is most likely due to adiabatic heating at high rates which suppresses the retained austenite transformation to martensite.

To summarize the differences between dual phase and TRIP-3 steel, the advantages of dual phase steel include its low quasi-static yield strength and continuous yielding behavior, which make it better for forming operations, and its high strain rate sensitivity values, which may make it favorable for certain high-rate applications. The advantage of the TRIP-3 steels is its higher strain hardening behavior which may improve energy absorption for crash-worthiness applications.

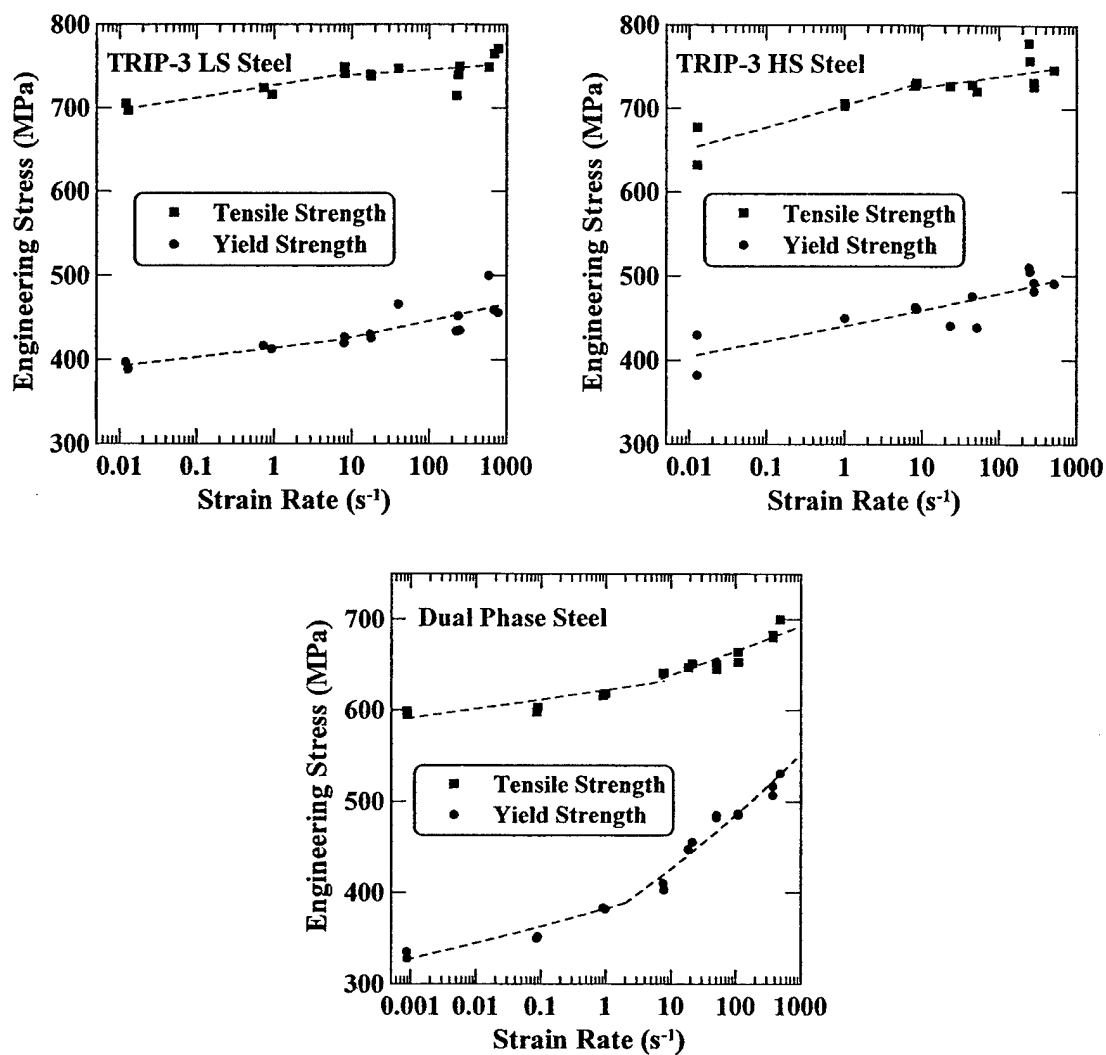


Figure 6.25: Strain rate sensitivity plots for both yield and tensile strengths for (a) TRIP-3 LS steel, (b) TRIP-3 HS steel and (c) dual phase steel.

Table 6.8: Logarithmic strain rate sensitivities (β) for the TRIP-3 and dual phase steel data in Figure 6.25.

	β	Low Strain Rates	High Strain Rates
TRIP-3 LS	Yield Strength	10.9	20.0
	Tensile Strength	14.9	6.7
TRIP-3 HS	Yield Strength	18.9	18.9
	Tensile Strength	26.5	13.8
Dual Phase	Yield Strength	18.9	60.7
	Tensile Strength	10.4	27.1

In Table 6.8, at high strain rates (above 1 s^{-1}) the strain rate sensitivities (β) of both yield and tensile strengths for TRIP-3 steels are significantly lower than those of the dual phase steel. The TRIP-3 high-rate β values are also lower than any of those calculated in Chapters 5 and 6 for all of the IF and HSLA steels investigated. Since β is a measure of strength increase with increasing strain rate, TRIP-3 steels have the lowest strength improvements at high strain rates compared to all other low carbon steels tested in this thesis. This is an important observation for energy absorption applications, such as automobile crash-worthiness, because it means that a material which has equal or greater energy absorption than TRIP-3 steel at low strain rates (most likely due to higher yield strength) may have better energy absorption capability at high strain rates. In addition, some materials with less low-rate energy absorption, but high β values, may surpass TRIP-3 energy absorption capability at high rates. Testing of pre-strained dual phase and TRIP steels may be worthwhile to assess this behavior in conditions that would apply to formed parts.

To illustrate the energy absorption comparison, TRIP-3 HS steel was compared to HSLA-2 steel. β values for both steels are shown in Table 6.9. At low rates, TRIP-3 HS steel has higher β values, especially for tensile strength, but the opposite is true at high rates. Therefore, for low strain rates, the energy absorption of TRIP-3 HS steel

should increase with increasing strain rates more than HSLA-2 steel. At high strain rates, the energy absorbed by HSLA-2 steel will increase with increasing strain rate more than the energy absorbed by TRIP-3 HS steel. Engineering stress-strain curves at three strain rates are shown in Figure 6.26 for TRIP-3 HS and HSLA-2 steels.

Table 6.9: Logarithmic strain rate sensitivities (β) for TRIP-3 HS and HSLA-2 steels.

	β	Low Strain Rates	High Strain Rates
HSLA-2	Yield Strength	16.8	32.9
	Tensile Strength	15.7	42.9
TRIP-3 HS	Yield Strength	18.9	18.9
	Tensile Strength	26.5	13.8

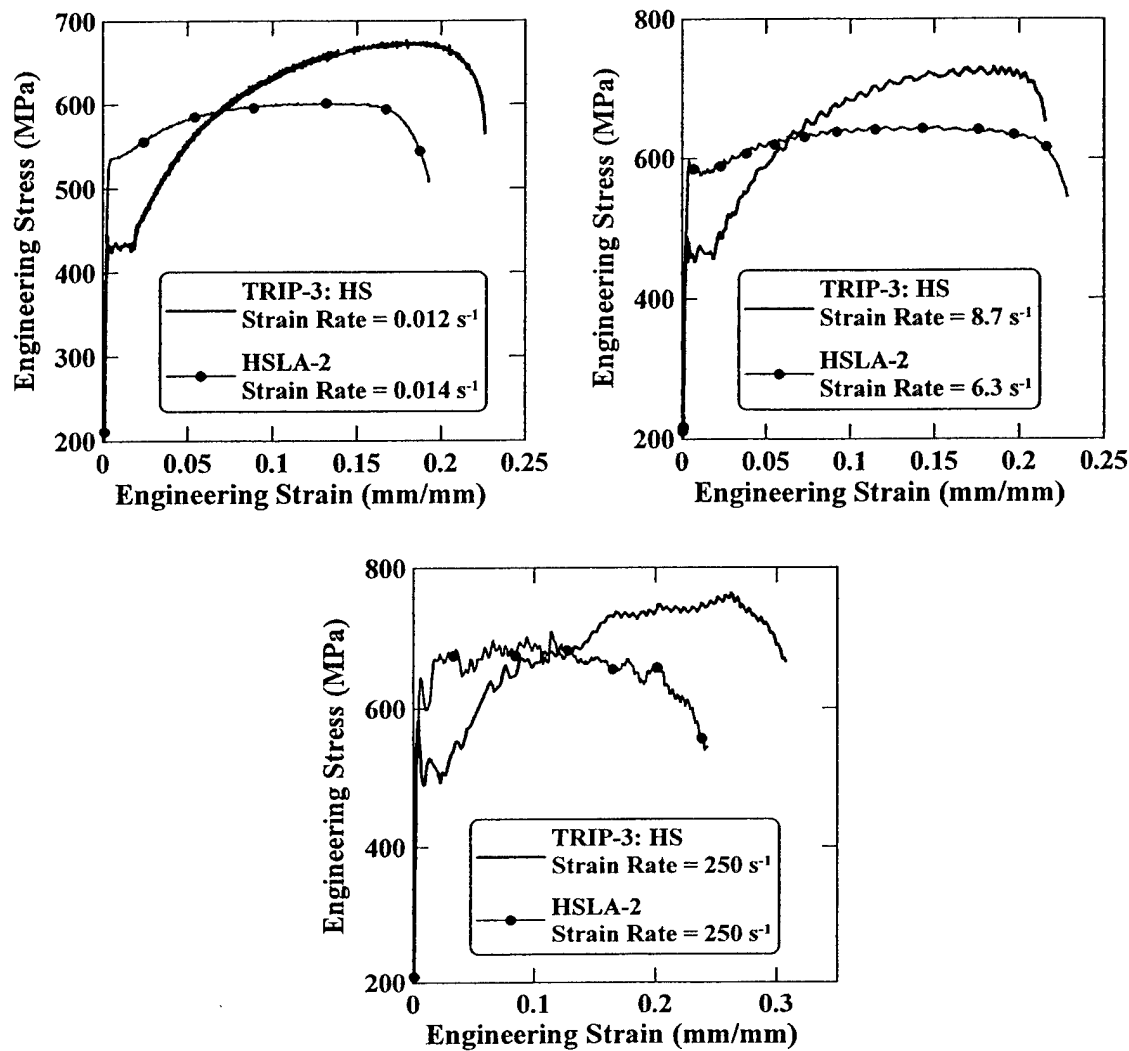


Figure 6.26: Engineering stress-strain curves for HSLA-2 and TRIP-3 HS steels at three different strain rates. (a) Gage length = 50.8 mm and actuator speed = 0.50 mm/s. (b) Gage length = 25.4 mm and actuator speed = 250 mm/s. (c) Gage length = 25.4 mm and actuator speed = 6.2 m/s.

At all strain rates in Figure 6.26, the yield strength of HSLA-2 steel exceeds that of TRIP-3 HS steel, but the TRIP steel strain hardens considerably more. The areas under each stress-strain curve in Figure 6.26 were calculated and plotted in Figure 6.27 as

functions of engineering strain. At the lowest strain rate in Figure 6.27a, the area curves for HSLA-2 steel and TRIP-3 HS steel cross at about 0.16 strain, while they cross at about 0.15 strain in Figure 6.27b for the moderate rate. At the high strain rate in Figure 6.27b, the area curves cross at about 0.24 strain. Therefore, the steel with greater energy absorption capability depends on the strain rate and strain limit chosen for the area calculation. Table 6.10 shows the area under each engineering stress-strain curve up to 10% strain since this strain level is often used for automobile crash-worthiness calculations [8, 21]. In Table 6.10, the energy absorption of HSLA-2 steel exceeds that of TRIP-3 HS steel at all strain rates, but the amount changes. At low strain rate, the difference is 6.6 J/m^3 , while for moderate rate the difference is only 3.0 J/m^3 due to the higher low-rate strain rate sensitivities of TRIP-3 HS steel. At the highest rate, the difference in energy absorbed increases to 8.6 J/m^3 due to the greater high-rate strain rate sensitivities of HSLA-2 steel.

It should be noted that these analyses of TRIP steel were conducted on a laboratory-melted and heat treated TRIP steel and results for other TRIP steels will be greatly affected by the type and amount of retained austenite. Furthermore, it should be recognized that the comparison here between HSLA and TRIP steels is made for materials with different as-received yield strengths, and higher strength TRIP steels are certain to absorb more energy.

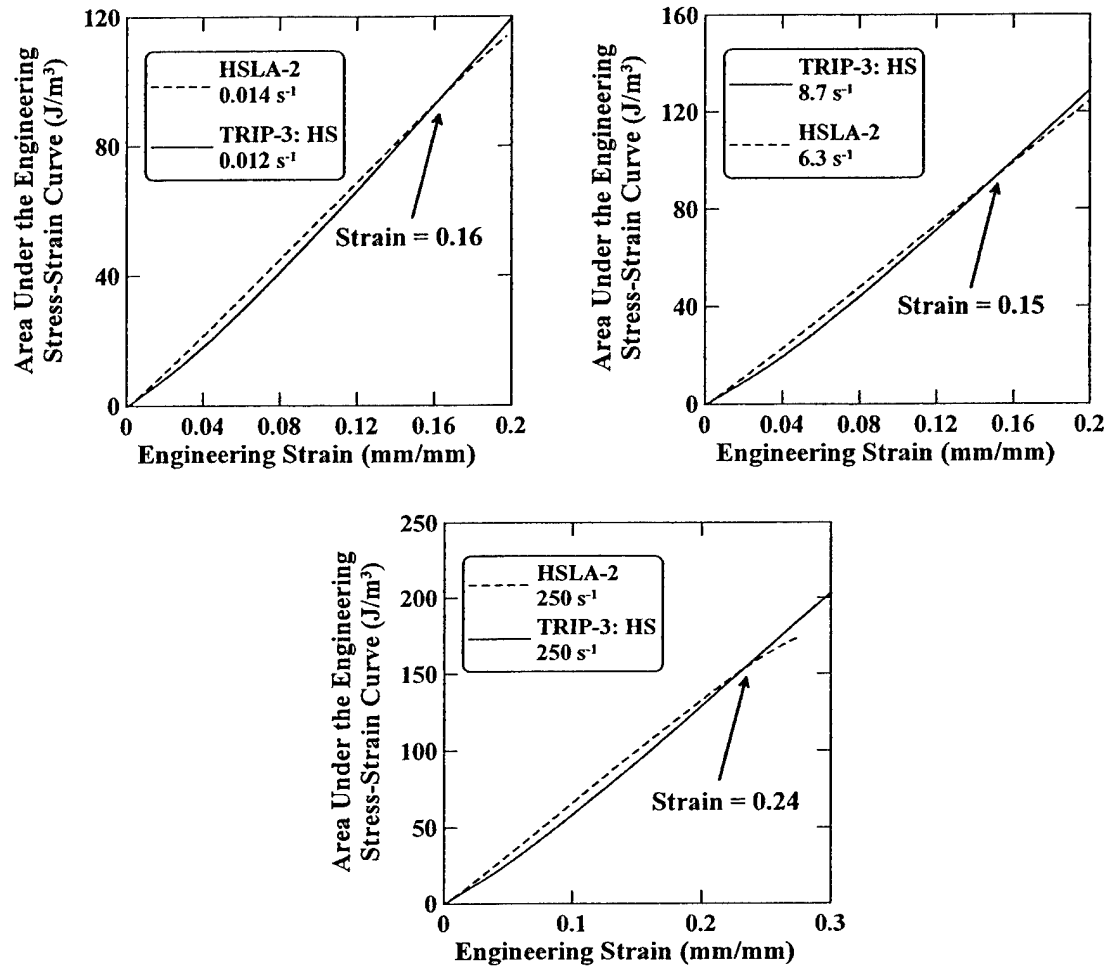


Figure 6.27: Area under the engineering stress-strain curve versus engineering strain for HSLA-2 and TRIP-3 HS steels at two different strain rates. (a) Gage length = 50.8 mm and actuator speed = 0.50 mm/s. (b) Gage length = 25.4 mm and actuator speed = 250 mm/s. (c) Gage length = 25.4 mm and actuator speed = 6.2 m/s.

Table 6.10: Area under the engineering stress-strain curve up to 10% engineering strain for TRIP-3 HS and HSLA-2 steels at three different strain rates as shown in Figures 6.26 and 6.27.

	Low Strain Rate (0.01 s^{-1})	Moderate Strain Rate (HSLA-2: 6.3 s^{-1} TRIP-3 HS: 9 s^{-1})	High Strain Rate (250 s^{-1})
HSLA-2	59.9 J/m^3	60.2 J/m^3	69.4 J/m^3
TRIP-3 HS	53.3 J/m^3	57.2 J/m^3	60.8 J/m^3
Difference	6.6 J/m^3	3.0 J/m^3	8.6 J/m^3

6.8 Constitutive Equation for IF Steels Strengthened by Cold Work, Solid Solution Strengthening and Grain Refinement

An attempt was made to develop a constitutive equation for the flow stress of low carbon steel as a function of strain, strain rate and temperature, which includes variables of cold work, grain refinement, and solid solution strengthening. This analysis is based on the BCC version of the Zerilli-Armstrong equation (Equation 3.57) [107] that was obtained from a model based on physical principles of dislocation mechanics and has been shown to accurately predict flow behavior in iron alloys [1 (p.375), 106, 107]. It also includes grain size as a variable.

The Zerilli-Armstrong model was discussed in Section 3.13.4.2 with the constitutive equation given by Equation 3.57, which is shown again here as Equation 6.1. In Equation 6.1, σ is the flow stress, σ_L is the athermal (long-range) component of stress, ϵ is the plastic strain, $\dot{\epsilon}$ is the strain rate, T is the absolute temperature, d is the grain diameter, and C_1 , C_3 , C_4 , C_5 , n and k are constants.

$$\sigma = \sigma_L + C_1 \exp[-C_3 T + C_4 T \ln(\dot{\epsilon})] + C_5 \epsilon^n + k d^{-1/2} \quad [6.1]$$

In Equation 6.1, the grain size component of strengthening is included in the $k d^{-1/2}$ term. Since cold work effects have been shown to be independent of strain rate, the amount of pre-strain, ϵ_{CW} , can simply be added to the plastic strain in the $C_5 \epsilon^n$ term as $C_5 (\epsilon + \epsilon_{CW})^n$. Solid solution strengthening at quasi-static rates can be calculated using Figure 6.6, but since solute additions are short-range (thermally-assisted) obstacles to dislocation motion, the effect of solute addition must also be included in the temperature and strain-rate sensitivity terms. Therefore, it was necessary to add two terms to Equation 6.1 to account for solute additions, one for the quasi-static, room temperature strengthening increment, σ_{SS} , and one to account for the change in strain rate (and temperature) sensitivity, C_{SS} . These changes are shown in Equation 6.2, where C_{SS} was used to modify the constant, C_1 . For solid solution strengthening with increasing strain rate or decreasing temperature, C_{SS} will be greater than 1, and for softening it will be less than 1. In Equation 6.2, σ_L includes other strengthening mechanisms such as precipitation and second phase strengthening. The modified Zerilli-Armstrong model in Equation 6.2 will be referred to as the "MZA model." Adiabatic heating was included in the MZA model for strain rates greater than 1 s^{-1} by using Equation 2.17 to predict temperature rise during deformation and updating the temperature as plastic strain is updated in the MZA equation. Equation 2.17 is shown again here as Equation 6.3, where β is the fraction of plastic work converted to heat, ρ is density, C_p is specific heat, ϵ is true strain and σ is flow stress.

$$\sigma = \sigma_L + \sigma_{SS} + C_{SS} C_1 \exp[-C_3 T + C_4 T \ln(\dot{\epsilon})] + C_5 (\epsilon + \epsilon_{CW})^n + k d^{-1/2} \quad [6.2]$$

$$\Delta T = \frac{\beta}{\rho C_p} \int_0^{\epsilon} \sigma d\epsilon \quad [6.3]$$

The IF steels to be modeled included IF-1 steel with 10, 25 and 135 mm grain sizes, IF-2 steels with 0%, 2%, 5%, 10% and 18% pre-strain, IF-3, and IF-4 steels. Since solute strengthening was to be included in Equation 6.2 as σ_{ss} , the amount of strengthening due to solute atoms was calculated for each of the four IF steel compositions. In Figure 6.6, the yield strength without any solute additions is about 69 MPa. The increase in yield strength due to additions of silicon, phosphorus, and manganese was calculated for each of the four steel compositions by determining the yield strength shown in Figure 6.6 for each solute amount, subtracting 69 MPa (the yield strength with no solute), and adding the contributions from each element. The results of these calculations are shown in Table 6.11.

Table 6.11: Quasi-static solid solution strengthening increment for several IF steels.

	IF-1	IF-2	IF-3	IF-4
Quasi-Static Solid Solution Strengthening Increment (MPa)	4	10	15	60

Ideally, the flow curve behavior of all IF steels can be defined using a single MZA equation, with the only variables between specific materials being used to account for differences in precipitation or second phase strengthening (σ_L), solid solution strengthening (σ_{ss} and C_{ss}), cold work (ϵ_{cw}), and grain size (d). If differences in precipitation strengthening are small, a single MZA model is possible. However, large changes in precipitation or second phase strengthening will probably also require a

change to the constant C_5 , to account for different strain hardening behavior. MZA model constants were determined for all four IF steels and they are shown in Table 6.12. The value for k was set equal to the mean value found for IF steels in Sections 6.3 and 6.4. The details of how other model constants were determined are contained in Appendix C.

In Table 6.12, the C_{SS} values for IF-2 and IF-3 steels are equal to 1, indicating that small amounts of solute additions do not significantly change the dynamic properties of IF steel. However, the C_{SS} value for IF-4 steel is significantly lower than 1, which illustrates the solute softening effect for larger solute additions.

Table 6.12: Constants for the modified Zerilli-Armstrong (MZA) equation (Equation 6.2) for IF steels.

Material	C_1 (MPa)	C_3 (K^{-1})	C_4 (K^{-1})	C_5 (MPa)	n	k (MPa $\sqrt{\text{mm}}$)
IF Steel	825	0.00698	0.000415	415	0.475	14
		β	ρ (kg/m^3)	C_p (J/kg \cdot K)		
		0.9	7870	445		

Material		σ_L (MPa)	σ_{SS} (MPa)	C_{SS}	ϵ_{CW} (mm/mm)	d (mm)
IF-1	10 μm	1	4	1.00	0	0.010
	25 μm					0.025
	135 μm					0.135
IF-2	0%	10	10	1.00	0	0.030
	2%				0.022	
	5%				0.051	
	10%				0.100	
	18%				0.178	
IF-3		15	15	1.00	0	0.040
IF-4		25	60	0.85	0	0.033

Figures 6.28 through 6.31 show true stress-strain curves for each IF steel at several different strain rates along with the curves predicted by the MZA model. In the MZA model, adiabatic heating was included for strain rates above 1 s^{-1} . This rate was chosen based upon adiabatic heating analysis done by Clarke [22] for ferritic stainless steels. In Figure 6.28, the highest strain rate shown is 35 s^{-1} since stress-strain curves were not available at higher rates for reasons discussed in Section 6.3. Flow curves for strain rates higher than 200 s^{-1} are not shown in Figures 6.29 through 6.31 because uniform strain values were very small for those rates.

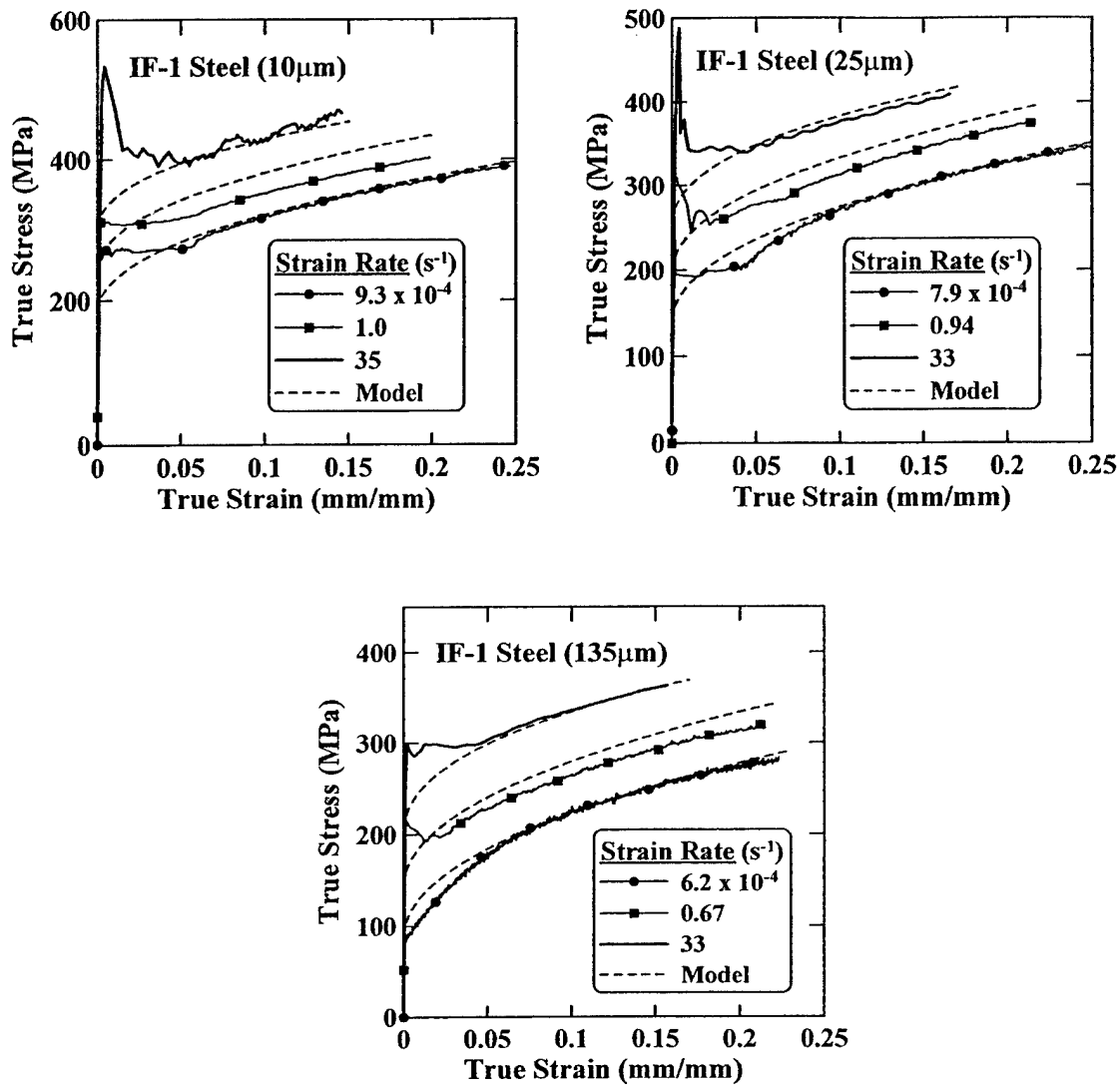


Figure 6.28: True stress-strain curves for IF-1 steel at three different strain rates compared with Modified Zerilli-Armstrong model at same strain rates using the constants shown in Table 6.12. (a) 10 μm grain size, (b) 25 μm grain size, and (c) 135 μm grain size.

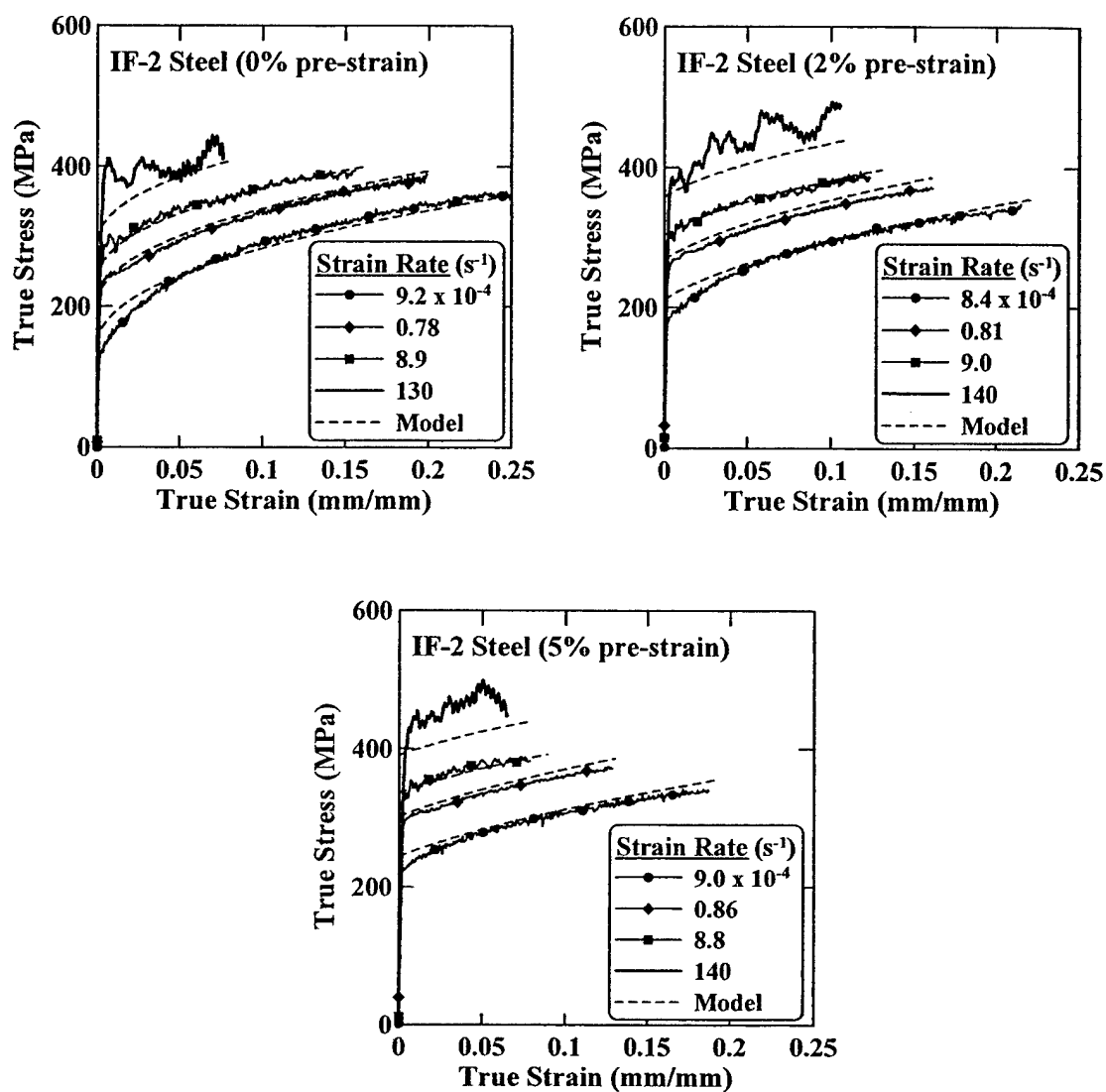


Figure 6.29: True stress-strain curves for IF-2 steel at four different strain rates compared with Modified Zerilli-Armstrong model at same strain rates using the constants shown in Table 6.12. (a) 0% pre-strain, (b) 2% pre-strain and (c) 5% pre-strain.

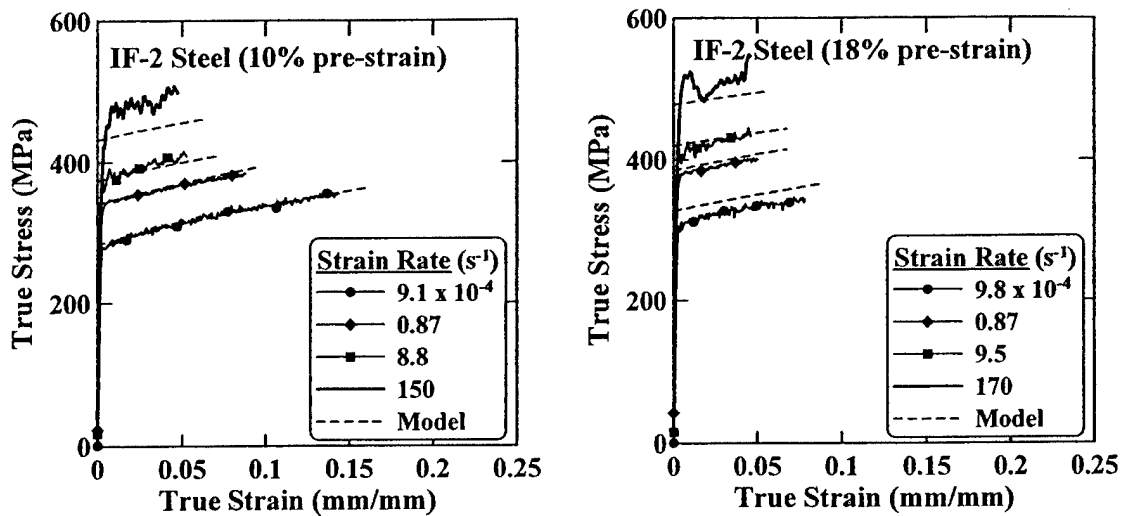


Figure 6.30: True stress-strain curves for IF-2 steel at four different strain rates compared with Modified Zerilli-Armstrong model at same strain rates using the constants shown in Table 6.12. (a) 10% pre-strain and (b) 18% pre-strain.

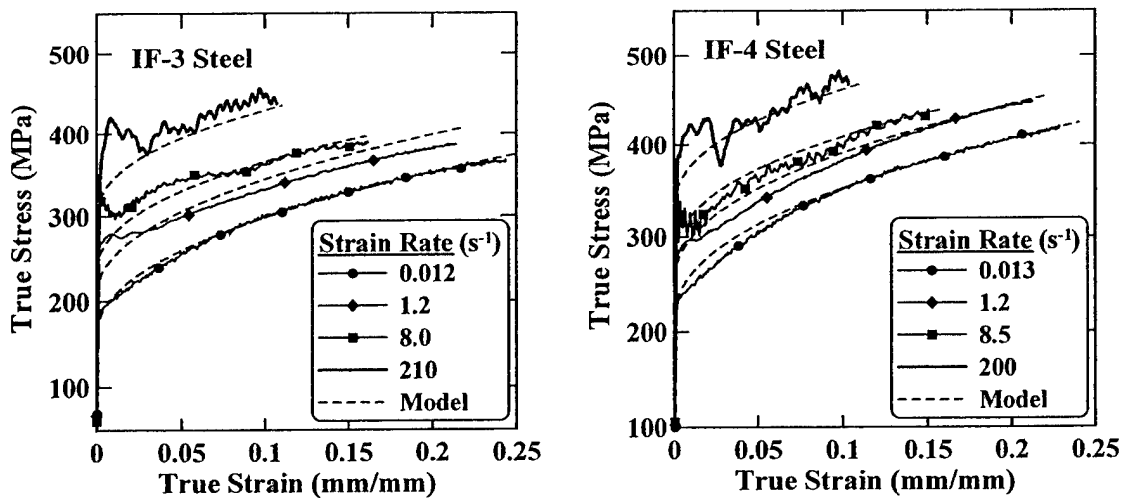


Figure 6.31: True stress-strain curves for (a) IF-3 steel and (b) IF-4 steel at four different strain rates compared with Modified Zerilli-Armstrong model at same strain rates using the constants shown in Table 6.12.

In Figures 6.28 through 6.31, the MZA model generally provides a good fit to the experimental data, although yield strength values are not particularly accurate, especially for materials exhibiting yield point elongation. In addition, for several steels, including IF-3 and IF-1, the model tends to overpredict flow stress values for strain rates of about 1 s^{-1} . This may be due to the fact that the model predicts a continuously increasing strain rate sensitivity, while strain rate sensitivity plots for IF steels typically show a rather sharp transition in strain rate sensitivity around a strain rate of 1 s^{-1} . In addition, the IF-1 tensile samples for grain sizes of 10 and 25 μm were fairly thick (4.1 mm) which may cause adiabatic heating to occur at lower strain rates than for thinner materials.

If yield strength predictions are required for materials with yield point elongation, the Hahn model [104] may be used. However, different Hahn model constants would have to be determined for each specific material. The Hahn model was discussed in Section 3.13.3.2 with the equation given by Equation 3.50, which is presented again here as Equation 6.4, where σ is the flow stress, ϵ is the plastic strain, $\dot{\epsilon}$ is the strain rate, ρ_0 is the initial dislocation density, τ_0 is the shear stress at unit dislocation velocity, b is the Burger's vector, and q , C , β and m are constants.

$$\sigma = 2q\epsilon + 2\tau_0 \left[\frac{2\dot{\epsilon}}{bf(\rho_0 + C\epsilon^\beta)} \right]^{1/m} \quad [6.4]$$

For IF-1 steel with 10 μm grain size, Hahn model constants were determined as shown in Table 6.13. To determine these constants, the constants given by Hahn [104] for 1020 steel (shown in Table 6.13) were used as a starting point. The constants m_L , m_H , and τ_0 were adjusted as needed to provide a good fit. Figure 6.32 shows the results of the model by plotting the experimental values of lower yield stress for IF-1 steel and the lower yield stress values predicted by the Hahn model versus strain rate. The model fits

the data well, which is expected since the experimental data points were used to determine the constants. The Hahn model could also be used to predict the magnitudes of yield drops.

Table 6.13: Constants for the Hahn model for IF-1 steel with 10 μm grain size. m_L was for strain rates up to 1 s^{-1} , while m_H was used for strain rates above 1 s^{-1} . Model constants given by Hahn [104] for 1020 steel are shown for comparison.

Material	f	ρ_0 (cm^{-2})	C (cm^{-2})	β	b (nm)	m_L	m_H	τ_0 (MPa)	q (GPa)
IF-1 (10 μm)	0.1	10^4	1.6×10^9	0.9	0.248	28	22	125	3.44
1020 Steel [104]	0.1	10^4	1.6×10^9	0.9	0.248	33	13	100	3.44

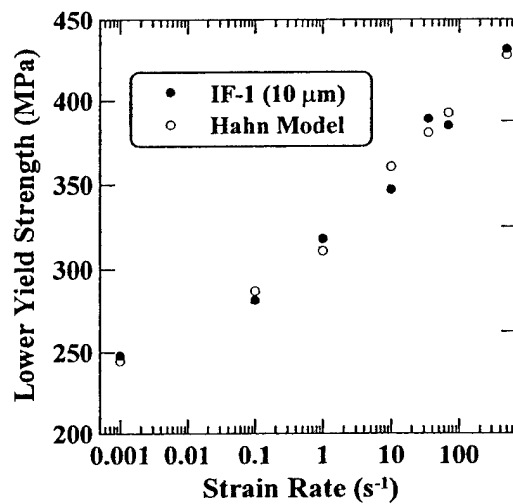


Figure 6.32: Lower yield strength as a function of strain rate for IF-1 (10 μm grain size) steel compared to the Hahn model using the constants shown in Table 6.13.

6.9 Constitutive Equation for HSLA Steels

The Modified Zerilli-Armstrong model developed in Section 6.8 was also used to fit flow curves for the two HSLA steels discussed in Section 6.2.2. Since HSLA steels have pearlite in the microstructure and typically employ precipitation strengthening as a major strengthening mechanism, it was expected that the C_5 constant in Equation 6.2 would need to be increased compared to the IF steel value. Values for σ_{ss} were based upon the solid solution increment calculated using Figure 6.6 in the same manner as discussed in Section 6.8. MZA model constants were determined using the methods discussed in Appendix C for IF steels, except that HSLA-1 steel was used as a starting point. MZA model constants for the HSLA steels are shown in Table 6.14. True stress-strain curves for each HSLA steel at four different strain rates are plotted along with the curves predicted by the MZA model in Figure 6.33. In the MZA model, adiabatic heating was included for strain rates above 1 s^{-1} . The MZA model provides a good fit to post-YPE experimental data.

Table 6.14: Constants for the modified Zerilli-Armstrong (MZA) equation (Equation 6.2) for HSLA steels.

Material	C_1 (MPa)	C_3 (K^{-1})	C_4 (K^{-1})	n	k ($\text{MPa}\sqrt{\text{mm}}$)
HSLA Steel	670	0.00698	0.000415	0.490	14
		β	ρ (kg/m^3)	C_p ($\text{J}/\text{kg}\cdot\text{K}$)	
		0.9	7870	445	

Material	σ_L (MPa)	σ_{ss} (MPa)	C_{ss}	C_5 (MPa)	ϵ_{cw} (mm/mm)	d (mm)
HSLA-1	77	18	1.00	490	0	0.009
HSLA-2	241	57	0.85	550	0	0.009

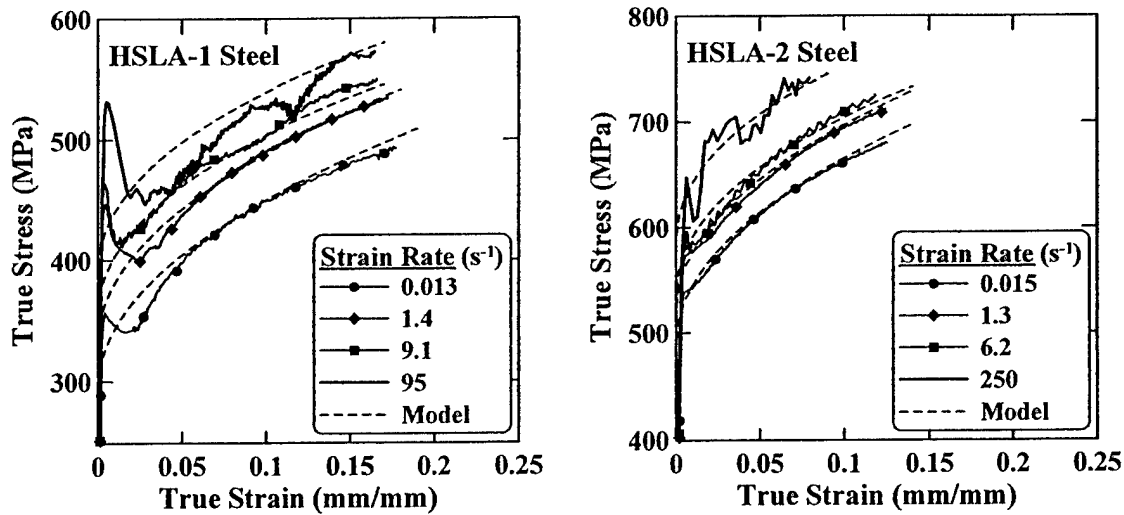


Figure 6.33: True stress-strain curves for (a) HSLA-1 steel and (b) HSLA-2 steel at four different strain rates compared with Modified Zerilli-Armstrong model at same strain rates using the constants shown in Table 6.14.

6.10 Summary of Strengthening Mechanism Results

The investigation of strengthening mechanisms in IF steels has revealed that strengthening provided by cold work or grain refinement is not affected by changes in strain rate, while the strengthening increment due to solute additions decreases with increasing strain rate. Thermally-activated dislocation motion, as discussed in Section 3.13.2, predicts that strengthening provided by long-range obstacles to dislocation motion will not be altered by changes in temperature or strain rate, while strengthening due to short-range barriers will be affected by changes in temperature or strain rate. Therefore, the conclusions were made that grain boundaries and dislocations produced by cold work are long-range obstacles to dislocation motion, while solute atoms are short-range barriers.

The effect of strain rate on solid solution strengthened IF steels was opposite that predicted for short-range obstacles. Resistance to dislocation motion provided by short-range obstacles should increase as strain rate increases due to the decrease in available

waiting time for thermal assistance to overcome those obstacles. This increasing resistance to dislocation motion is manifested in tensile testing by increasing flow stress. The short-range barrier of intrinsic friction stress (Peierl's-Nabarro stress) of BCC metals follows the expected trend and is responsible for the increase in flow stress with increasing strain rate seen in pure iron. The friction stress contribution to increasing flow stress with increasing strain rate was observed in Sections 6.3 and 6.4 where σ_0 in the Hall-Petch equation (Equation 3.11) increased with increasing strain rate. One would also expect the strengthening increment due to solid solution strengthening to increase with increasing strain rate. The fact that the strengthening increment due to solid solution strengthening decreases with increasing strain rate is analogous to other experimental results showing that the strengthening increment in iron due to solute additions decreases with decreasing temperature (for a specific temperature range below room temperature) as discussed in Section 3.6. This observation, together with the results for cold work and grain size, further supports the equivalence of decreasing temperature and increasing strain rate.

A comparison of two HSLA steels showed the same solid solution softening effect with increasing strain rate as seen in IF steels. The magnitude of the softening effect in the HSLA steels could be attributed entirely to the solution strengthening increment. This result suggests that other strengthening mechanisms (such as precipitation strengthening) employed in HSLA steels may be independent of strain rate.

Strengthening in TRIP steels includes an increment created by transformation of retained austenite to martensite, which increases with increasing plastic strain, causing high work hardening rates. At low strain rates, increasing strain rate aids the transformation by a stress-assisted mechanism associated with the increase in flow stress of the matrix ferrite. However, at high strain rates, adiabatic heating becomes important and the transformation is hindered, leading to low strain rate sensitivity values. Low strain rate sensitivity (β) values translate to low strengthening increment at high strain rates, which results in less of an increase in energy absorption capability at high rates,

compared to materials with high β values. Since the deformation behavior of TRIP steels is highly dependent upon the amount and type of retained austenite, the details of these results may not be applicable to all TRIP steels as a class of materials.

The Zerrili-Armstrong constitutive relationship, which contains a variable for grain size, was modified to include terms for cold work and solid solution strengthening so that flow curves could be predicted for IF steels with changes in those three strengthening mechanisms. It is anticipated that more athermal terms could be included to account for precipitation strengthening and possibly volume fraction of martensite for dual phase steels. The model could then be extended to HSLA and dual phase steels.

The primary result of this research is that IF steels (and possibly HSLA steels) may be strengthened by cold work or grain refinement without sacrificing the strength increase due to increased strain rate. However, the benefit of strengthening by solute atoms decreases with increasing strain rate.

6.11 Relationships Between Dynamic Test Methodology and Strengthening Mechanism Investigation

The strengthening mechanism research conducted in this thesis would not have been possible without the development of a reliable method for generating accurate high-rate stress-strain curves. Comparing stress-strain curve shapes between materials at different strain rates was an excellent method for evaluating key differences in material behavior. Significant information can quickly be gathered from visual interpretation of stress-strain curves.

The use of a single test system for obtaining mechanical property data over a very large strain rate range was important. Most reported strain rate dependent data covers only strain rates up to about 1 s^{-1} (typically using conventional hydraulic test machines) and strain rates above about 500 s^{-1} (using Hopkinson bar tests). Not only are data missing in the strain rate range from 1 s^{-1} to 500 s^{-1} , but the possibility for differences in results due to completely different test methods is high. The MTS high-rate tensile test

system allowed tensile tests to be run from quasi-static rates up to about 500 s^{-1} with appropriate sample dimensions. Since all data were gathered using the same test equipment and methods, self-consistency of the results was assured.

While the results obtained for this thesis were sufficient to evaluate the mechanisms studied, there is room for improvement in the test method. Reducing the mass between sample and load measuring device is crucial to improvement in load data. Although the system of using strain gages mounted to sample grip sections to collect load data was effective, it was also extremely time-consuming both in sample preparation and data reduction steps. The development of a load measurement device separate from the test sample that gives useable results will greatly improve the efficiency of testing.

CHAPTER 7

CONCLUSIONS

7.1 Dynamic Tensile Testing Conclusions

- A dynamic tensile testing method was developed that provides accurate and repeatable load and strain measurements for strain rates ranging from 0.001 s^{-1} to 500 s^{-1} .
- Families of stress-strain curves were produced for several different sheet steels over a wide range of strain rates. Results were shown to be independent of tensile sample geometry and demonstrated the ability to distinguish important aspects of material properties, such as continuous- or discontinuous-yielding behavior, up to strain rates of 500 s^{-1} .
- Strain rate sensitivity plots of various material properties, such as yield and tensile strengths, work hardening exponents, and energy absorbed, were used to evaluate the strain rate dependent behavior of several sheet steels.

7.2 Strengthening Mechanisms Conclusions

Conclusions in this section are valid for room temperature and strain rates ranging from 0.001 s^{-1} to 500 s^{-1} .

7.2.1 Single Phase Ferrite Low Carbon Sheet Steels

- Dislocations and dislocation substructures created by cold work are long-range (athermal) obstacles to dislocation motion and therefore the strain rate sensitivity of flow stress is independent of the amount of cold work.
- Solute additions provide short-range barriers to dislocation motion and therefore the strain rate sensitivity of flow stress is highly dependent on the amount of solute.
- Grain boundaries are long-range obstacles to dislocation motion and therefore the strain rate sensitivity of flow stress is independent of grain size.
- A modified version of the Zerilli-Armstrong equation was used to predict flow behavior of IF steels with changes in cold work, grain size or solute additions. With the addition of a method for relating solute content to temperature and strain rate sensitivity, this equation may be used to predict flow curves for other IF steels if the grain size, cold work, solute content, and quasi-static flow curve are known.

7.2.2 Multiphase Transformation Induced Plasticity (TRIP) Steels

- Quasi-static flow behavior of TRIP steels can be altered by heat treating to obtain different carbon contents in the retained austenite phase, which changes the retained austenite stability. However, the differences in behavior diminish with increasing strain rate.
- Strain rate sensitivities of yield and tensile strengths at high strain rates (above 1 s^{-1}) for the TRIP steels analyzed in this thesis were lower than those calculated for all IF, HSLA and dual phase steels investigated. Low strain rate sensitivity values have negative consequences for energy absorption at high strain rates.

7.3 Suggestions for Future Work

- Determine the effects of strain rate on a series of materials with controlled changes in precipitation strengthening.
- Determine the effects of strain rate on strain aging or baking response.
- Develop multiphase dual phase and TRIP steels with controlled microstructure variations to investigate the effects of strain rate on dual phase steels with variations in martensite fraction, and on TRIP steels with differences in type and amount of retained austenite.
- Obtain several IF steels with controlled variations in solute content to establish the effects of the amount of solute on the degree of solid solution softening.

- Conduct another study to verify the effects of strain rate on grain size using an IF steel with very low solute content to minimize effects of precipitation and solute segregation.
- Refine the modified Zerilli-Armstrong model to incorporate variations in strain rate sensitivity for low and high strain rate regimes. Develop a method to predict the solid solution softening coefficient. Extend the model to dual phase and TRIP steels.
- Develop a test method that produces accurate high-rate load information without requiring the use of strain gages mounted to each sample.

CHAPTER 8

REFERENCES

1. Meyers, M.A., Dynamic Behavior of Materials, John Wiley & Sons, New York, New York, 1994.
2. Clark, D.S. and Duwez, P.E., "The Influence of Strain Rate on Some Tensile Properties of Steel," Proc. Am. Soc. Test. Mater., Vol. 50, 1950, pp. 560-576.
3. Hockett, J.E., "Compression Testing at Constant True Strain Rates," Am. Soc. Testing Mater. Proc., Vol. 59, 1959, pp. 1309-1319.
4. Marsh, K.J. and Campbell, J.D., "The Effect of Strain Rate on the Post-Yield Flow of Mild Steel," J. Mech. Phys. Solids, Vol. 11, 1963, pp. 49-63.
5. Lindholm, U.S., "Review of Dynamic Testing Techniques and Material Behavior," Conference of Mechanical Properties of Materials at High Rates of Strain, Oxford, 1974, pp. 3-21.
6. Saxena, A. and Chatfield, D., "High Strain Rate Behavior of Some Hot and Cold Rolled Low Carbon Steels," SAE Technical Paper #760209, 1976.
7. Mansilla, A., Regidor, A., Garcia, D. and Negro, A., "Dynamic Tensile Testing for Determining the Stress-Strain Curve at Different Strain Rate," J. Phys. IV France, Vol. 10, No. 9, 2000, pp. 697-700.
8. Yan, B. and Xu, K., "High Strain Rate Behavior of Advanced High Strength Steels for Automotive Applications," 44th MWSP Conference Proceedings, Vol. XL, 2002, pp. 493-507.
9. Hove, I.H., Andersson, B. and Johnsen, T.E., "High Speed Tensile Testing," J. Phys. IV France, Vol. 7, no. 3, 1997, pp. 229-234.
10. Bleck, W. and Schael, I., "Determination of Crash-Relevant Material Parameters by Dynamic Tensile Tests," Steel Research, Vol. 71, no. 5, 2000, pp. 173-178.

11. Pirttijoki, J. and Peura, P., "Ultra High Strength Steels and Steel Tubes for Automotive Safety Components," Proceedings of FISITA 2002 World Automotive Congress, Helsinki, June 2-7 2002.
12. Peura, P. and Talonen, J., "Formability and Influence of Strain Rate on the Mechanical Properties of Hot Dip Galvanized Ultra High Strength Multi-Phase Steels," Proceedings of FISITA 2002 World Automotive Congress, Helsinki, June 2-7 2002.
13. Moriau, O., Tosai-Martinez, L., Verleysen, P. and Degrieck, J., "Dynamic Mechanical Properties of Cold Rolled TRIP Steels for Crash-Relevant Applications," Int. Conf. on TRIP-Aided High Strength Ferrous Alloys, 2002, pp. 247-251.
14. Masuda, T., Kobayashi, T. and Toda, H., "High Strain Rate Deformation Behavior of Al-Mg Alloys," Impact Engineering and Application, 2001, pp. 363-368.
15. Westvold, F., Andersson, B., Langsrud, Y. and Evensen, J.D., "Effect of Alloying Elements on High-Strain-Rate Behavior in Recycled Al-Fe-Si System Alloys," Japan Institute of Light Metals, Aluminum Alloys, Vol. 2., 1998, pp. 961-966.
16. Andersson, B. and Johnsen, T.E., "Interpretation of Flowstress Curves of Al Alloys at High Rates," 11th Jounées Thematiques Dymat, France, 1998.
17. Andersson, B. and Skjervold, S.R., "Tensile Properties at Low to High Strain Rates of AlMgSi and AlZnMg Alloys," Materials Science Forum, Vol. 242, 1997, pp. 153-158.
18. Puente, I., Sanchez, J.M. and Martin-Meizoso, A., "Experimental Technique for High Temperature and High Strain Rate Testing of CMCs," Key Engineering Materials, vols. 127-131, 1997, pp. 737-744.
19. Aune, T.K., Albright, D., Westengen, H., Johnsen, T.E. and Andersson, B., "Behavior of Die Cast Magnesium Alloys Subject to Rapid Deformation," SAE Technical Paper #2000-01-1116, 2000.
20. Higashi, K., Mukai, T., Kaizu, K., Tsuchida, S. and Tanimura, S., "Strain Rate Dependence on Mechanical Properties in Some Commercial Aluminum Alloys," Journal De Physique IV, Vol. 1, no. 3, 1991, pp. 341-346.

21. Choi, I.D., Bruce, D.M., Kim, S.J., Lee, C.G, Park, S.H., Matlock, D.K. and Speer, J.G., "Deformation Behavior of Low Carbon TRIP Sheet Steels at High Strain Rates," *ISIJ International (Japan)*, Vol. 42, No. 12, 2002, pp. 1483-1489.
22. Clarke, K.D., "Influence of Strain Rate on the Mechanical Properties and Formability of Ferritic Stainless Steels," M.S. Thesis #MT-SRC-002-011, Colorado School of Mines, Golden, CO, July 2002.
23. Gillis, P.P. and Gross, T.S., "Effect of Strain Rate on Flow Properties," *ASM Handbook*, 8th Ed., Vol. 8, 1990, pp. 38-45.
24. Thomson, W.T. and Dahleh, M.D., Theory of Vibration with Applications, 5th Ed., Prentice Hall, Upper Saddle River, New Jersey, 1998.
25. Graff, K.F., Wave Motion in Elastic Solids, Dover Publications, Inc., Mineola, New York, 1991.
26. Kolsky, H., Stress Waves in Solids, Dover Publications, Inc., New York, New York, 1963.
27. Nicholas, T. and Bless, S.J., "High Strain Rate Tension Testing," *ASM Handbook*, 8th Ed., Vol. 8, 1990, pp. 208-215.
28. Davies, E.D.H. and Hunter, S.C., "The Dynamic Compression Testing of Solids by the Method of the Split Hopkinson Pressure Bar," *J. Mech. Phys. Solids*, Vol. 11, 1963, p. 155.
29. Nemat-Nasser, S., "High Strain Rate Tension and Compression Tests," *ASM Handbook*, 9th Ed., Vol. 8, 2000, pp. 429-446.
30. Dieter, G.E., Mechanical Metallurgy, 3rd Ed, McGraw-Hill, Boston, Massachusetts, 1986.
31. Hodowany, J., Ravichandran, G., Rosakis, A.J. and Rosakis, P., "Partition of Plastic Work into Heat and Stored Energy in Metals," *Experimental Mechanics*, Vol. 40, no. 2, 2000, pp. 113-123.
32. Incropera, F.P. and DeWitt, D.P., "Introduction to Heat Transfer," 2nd Ed., John Wiley & Sons, New York, 1990.

33. Bleck, W. and Larour, P., "Measurement of the Mechanical Properties of Car Body Sheet Steels at High Strain Rates and Non-Ambient Temperature," 7th International Conf. on Mechanical and Physical Behavior of Materials Under Dynamic Loading, Porto, Portugal, To Be Held September 2003.
34. Leslie, W.C., The Physical Metallurgy of Steels, Hemisphere Publishing Company, 1981.
35. Miura, K., Takagi, S., Hira, T., Furukimi, O. and Tanimura, S., "High Strain Rate Deformation of High Strength Sheet Steels for Automotive Parts," SAE Technical Paper #980952, 1998.
36. Harding, J., "The Effect of Grain Size and Strain Rate on the Lower Yield Stress of Pure Iron at 288°K", *Acta Metall.*, Vol. 17, 1969, pp. 949-958.
37. Petch, N.J., "The Upper Yield Stress of Polycrystalline Iron," *Acta. Met.*, Vol. 12, 1964, pp. 59-65.
38. Milititsky, M., "Effects of Pre-Strain on the Mechanical Properties of Low-Carbon Steels Tested Over a Wide Range of Strain Rates," M.S. Thesis #MT-SRC-000-021, Colorado School of Mines, Golden, CO, December 2000.
39. Courtney, T.H., Mechanical Behavior of Materials, 2nd Ed., McGraw-Hill, Boston, Massachusetts, 2000.
40. Reed-Hill, R.E. and Abbaschian, R., Physical Metallurgy Principles, 3rd Ed., PWS Publishing Company, Boston, Massachusetts, 1994.
41. Meyers, M.A. and Chawla, K.K., Mechanical Behavior of Materials, Prentice-Hall Inc., Upper Saddle River, New Jersey, 1999.
42. Campbell, J.D. and Ferguson, W.G., "The Temperature and Strain-Rate Dependence of the Shear Strength of Mild Steel," *Phil. Mag.*, Vol. 21, 1970, pp. 63-82.
43. Kojima, N., Nakazawa, Y. and Mizui, N., "Compression Flow Stress of Ultra Low Carbon Mild Steel at High Strain Rate," Impact Engineering and Application, Chiba, A., Tanimura, S. and Hokamoto, K. (Eds.), Elsevier Science Ltd., 2001, pp. 439-444.

44. Spitzig, W.A. and Keh, A.S., "Orientation and Temperature Dependence of Slip in Iron Single Crystals," *Met. Trans.*, Vol. 1, 1970, pp. 2751-2757.
45. Brunner, D. and Diehl, J., "The Use of Stress-Relaxation Measurements for Investigations on the Flow Stress of α -Iron," *Phys. Stat. Sol. (a)*, Vol. 104, 1987, pp. 145-155.
46. Brunner, D. and Diehl, J., "Extension of Measurements of the Tensile Flow Stress of High-Purity α -Iron Single Crystals to Very Low Temperatures," *Zeitschrift Metallkunde*, Vol. 83, 1992, pp. 828-834.
47. Brunner, D. and Diehl, J., "Temperature and Strain-Rate Dependence of the Tensile Flow Stress of High-Purity α -Iron Below 250K," *Phys. Stat. Sol. (a)*, Vol. 124, 1991, pp. 455-464.
48. Brunner, D. and Diehl, J., "Strain-Rate and Temperature Dependence of the Tensile Flow Stress of High-Purity α -Iron Above 250K (Regime I) Studied by Means of Stress-Relaxation Tests," *Phys. Stat. Sol. (a)*, Vol. 124, 1991, pp. 155-170.
49. Honeycombe, R.W.K., The Plastic Deformation of Metals, Edward Arnold, London, 1984.
50. Christian, J.W., "Some Surprising Features of the Plastic Deformation of Body-Centered Cubic Metals and Alloys," *Met. Trans. A*, Vol. 14A, 1983, pp. 1237-1256.
51. Basinski, Z.S. and Christian, *Austral. J. Physics*, 1960, Vol. 13, pp. 299-308.
52. Campbell, J.D., Eleiche, A.M. and Tsao, M.C.C., "Strength of Metals and Alloys at High Strains and Strain Rates," Fundamental Aspects of Structural Alloy Design, Jaffee, R.I. and Wilcox, B.A. (Eds.), Plenum Press, New York, 1977, pp. 545-562.
53. Follansbee, P.S., "Analysis of the Strain-Rate Sensitivity at High Strain Rates in FCC and BCC Metals," *International Conference on Mechanical Properties at High Rates of Strain*, Oxford, 1989, pp. 213-220.
54. Lin, M.R. and Wagoner, R.H., "Effect of Temperature, Strain, and Strain Rate on the Tensile Flow Stress of I.F. Steel and Stainless Steel Type 310," *Scripta Metallurgica*, Vol. 20, 1986, pp. 143-148.

55. Fiore, N.F. and Bauer, C.L., "The Binding of Solute Atoms to Dislocations," Progress in Materials Science, Vol. 13, Chalmers, B. and Hume-Rothery, W. (Eds.), Pergamon Press, New York, 1968, pp. 85-134.
56. Ratka, J.O., Sethi, V.K. and Gibala, R., "The Effects of Solutes on Plastic Flow of Niobium and Niobium Alloys," Mechanical Properties of BCC Metals, Meshii, M. (Ed.), TMS-AIME, Warrendale, PA, 1982, pp. 103-109.
57. Astié, P. Peyrade, J.P. and Groh, P., "Dislocation Relaxation Peaks and Solid Solution Softening in Substitutional Iron Alloy," Scripta Metallurgica, Vol. 16, 1982, pp. 977-980.
58. Pink, E. and Arsenault, R.J., "Low-Temperature Softening in Body-Centered Cubic Alloys," Progress in Materials Science, Vol. 24, 1979, pp. 1-50.
59. Arsenault, R.J., "The Possibility of Irradiation Damage Affecting the Rate-Controlling Mechanism of Slip in BCC Metals and Solid Solutions," Acta. Met., Vol. 15, 1967, pp. 501-511.
60. Hall, E.O., "The Deformation and Ageing of Mild Steel: III Discussion of Results," Proc. Phys. Soc. (London), Vol. 64B, 1951, pp. 747-753.
61. Petch, N.J., "The Cleavage Strength of Polycrystals," J. Iron Steel Inst., Vol. 174, 1953, pp. 25-28.
62. Gladman, T., The Physical Metallurgy of Microalloyed Steels, The Institute of Materials, Cambridge, England, 1997.
63. Matlock, D.K, Bruce, D.M. and Speer, J.G., "Strengthening Mechanisms and Their Applications in Extremely Low C Steels," International Forum for the Properties and Application of IF Steels, Takechi, H. (Ed.), Proceedings of IF Steels 2003, Iron and Steel Institute of Japan, Tokyo, Japan, 2003, pp. 118-127.
64. Cottrell, A.H., "Theory of Brittle Fracture in Steel and Similar Metals," Trans. TMS-AIME, Vol. 212, 1958, pp. 192-203.
65. Embury, J.D., "Strengthening by Dislocation Substructures," Strengthening Methods in Crystals, Kelly, A. and Nicholson, R.B. (Eds.), John Wiley & Sons, New York, 1971, pp. 331-402.

66. Li, J.C.M., "Petch Relation and Grain Boundary Sources," Trans. TMS-AIME, Vol. 227, 1963, pp. 239-247.
67. Ashby, M.F., "The Deformation of Plastically Non-Homogeneous Alloys," Strengthening Methods in Crystals, Kelly, A. and Nicholson, R.B. (Eds.), John Wiley & Sons, New York, 1971, pp. 137-192.
68. Mintz, B., "Importance of k_y (Hall-Petch Slope) in Determining Strength of Steels," Metals Technology, Vol. 11, 1984, pp. 265-272.
69. Hutchison, M.M., "The Temperature Dependence of the Yield Stress of Polycrystalline Iron," Phil. Mag., Vol. 8, 1963, pp. 121-127.
70. Campbell, J.D. and Harding, J., "The Effect of Grain Size, Rate of Strain, and Neutron Irradiation of the Tensile Strength of α -Iron," Response of Metals to High Velocity Deformation, Shewmon, P.G. and Zackay, V.F. (Eds.), Interscience, New York, 1961, pp. 51-76.
71. Heslop, J. and Petch, N.J., "The Ductile-Brittle Transition in the Fracture of α -Iron: II," Phil. Mag., Vol. 3, 1958, pp. 1128-1136.
72. Igata, N., Kawata, K., Itabashi, M., Yumoto, H., Sawada, K. and Kitahara, H., "Plastic Deformation of Iron and Steel at High Strain Rate," Proc. 2nd Japan International SAMPE Symposium, 1991, pp. 1121-1129.
73. Orowan, E., "Symposium on Internal Stresses" (discussion), Institute of Metals, London, 1947, p. 451.
74. Speich, G.R., "Physical Metallurgy of Dual-Phase Steels," Fundamentals of Dual-Phase Steels Conference, Metallurgical Society/AIME, 1981, pp. 3-45.
75. Matlock, D.K., Krauss, G. and Zia-Ebrahimi, F., "Strain Hardening of Dual-Phase Steels: An Evaluation of the Importance of Processing History," Deformation, Processing, and Structure, Krauss, G. (Ed.), ASM, Metals Park, Ohio, 1984, pp. 47-87.
76. Krauss, G., Steels: Heat Treatment and Processing Principles, ASM International, Materials Park, Ohio, 1990.
77. Owen, W.S., "The Effect of Silicon on the Kinetics of Tempering," Trans. ASM, Vol. 46, 1954, pp. 253-264.

78. Krauss, G., De, A.K., Speer, J.G. and Matlock, D.K., "The Mechanical and Physical Metallurgy of Low-Carbon Sheet Steels Produced by Dual-Phase and TRIP Steel Processing," CSM Internal Report, 2002.
79. Sugimoto, K., Misu, M., Kobayashi, M. and Shirasawa, H., "Effects of Second Phase Morphology on Retained Austenite Morphology and Tensile Properties in a TRIP-Aided Dual-Phase Steel Sheet," *ISIJ International*, Vol. 33, 1993, pp. 775-782.
80. Sugimoto, K., Usui, N., Kobayashi, M. and Hashimoto, S., "Effects of Volume Fraction and Stability of Retained Austenite on Ductility of TRIP-Aided Dual-Phase Steels," *ISIJ International*, Vol. 32, 1992, pp. 1311-1318.
81. Tomita, Y. and Morioka, K., "Effect of Microstructure on Transformation-Induced Plasticity of Silicon-Containing Low-Alloy Steel," *Materials Characterization*, Vol. 38, 1997, pp. 243-250.
82. Jacques, P., Furnemont, Q., Mertens, A. and Delannay, F., "On the Sources of Work Hardening in Multiphase Steels Assisted by Transformation-Induced Plasticity," *Phi. Mag. A*, Vol. 81, 2001, pp. 1789-1812.
83. DeArdo, A.J., "Multi-Phase Microstructures and Their Properties in High Strength Low Carbon Steels," *ISIJ International*, Vol. 35, 1995, pp. 946-954.
84. Porter, D.A. and Easterling, K.E., Phase Transformations in Metals and Alloys, 2nd Edition, Chapman and Hall, 1996.
85. Kaufman, L. and Hillert, M., "Thermodynamics of Martensitic Transformations," Martensite, ASM International, 1992, pp. 41-58.
86. Wang, J. and Van der Zwaag, S., "Stabilization Mechanisms of Retained Austenite in Transformation-Induced Plasticity Steel," *Metallurgical and Materials Transactions A*, Vol. 23A, 2001, pp. 1527-1539.
87. Balliger, N.K. and Gladman, T., "Work Hardening of Dual-Phase Steels," *Metal Science*, Vol. 15, 1981, pp.95-108.

88. Lawson, R.D., Matlock, D.K. and Krauss, G., "The Effect of Microstructure on the Deformation Behavior and Mechanical Properties of a Dual-Phase Steel," Fundamentals of Dual-Phase Steels, Kot, R.A. and Bramfitt, B.L. (Eds.), TMS-AIME, Warrendale, PA, 1981, pp. 347-381.
89. Tamura, I. and Wayman, C.M., "Martensitic Transformations and Mechanical Effects," Martensite, ASM International, 1992, pp. 227-236.
90. Olsen, G.B., "Mechanically Induced Phase Transformations in Alloys," Pergamon Press, Encyclopedia of Materials Science and Engineering, Vol. 4, 1986, pp. 2929-2931.
91. Olsen, G.B. and Cohen, M., "Stress-Assisted Isothermal Martensitic Transformation: Application to TRIP Steels," Metallurgical Transactions A, Vol. 13A, 1992, pp. 1907-1914.
92. Brandt, M.L. and Olsen, G.B., "Enhancement of Austenite Stability for Improved Ductility," 36th MWSP Conf. Proc., ISS-AIME, Vol. XXXII, 1995, pp. 367-371.
93. Levistas, V.I., Idesman, A.V. and Olson, G.B., "Continuum Modeling of Strain-Induced Martensitic Transformation at Shear-Band Intersections," Acta Mater., Vol. 47, 1999, pp. 219-233.
94. Onodera, H. and Tamura, I., "Effect of Prestraining on Martensitic Transformation," ICOMAT 1979, Martensitic Transformations, Cambridge, Mass., 24-29 June 1979, pp. 337-342.
95. Bleck, W., Kranz, S., Ohlert, J. and Papamantellos, K., "Effect of the Testing Temperature on the Mechanical Behavior of Low and High Alloyed Steels Showing the TRIP Effect," 41st MWSP Conf. Proc., ISS, Vol. XXXVII, 1999, pp. 295-305.
96. Hecker, S.S., Stout, M.G., Staudhammer, K.P. and Smith, J.L., "Effects of Strain State and Strain Rate on Deformation-Induced Transformation in 304 Stainless Steel: Part I. Magnetic Measurements and Mechanical Behavior," Met. Trans. A, Vol. 13A, 1982, pp. 619-626.
97. Pychmintsev, I.Y., Savrai, R.A., De Cooman, B.C. and Moriau, O., "High Strain Rate Behavior of TRIP-Aided Automotive Steels," Int. Conf. on TRIP-Aided High Strength Ferrous Alloys," Conf. Proc., Ghent, Belgium, 2002, pp. 299-302.

98. Wei, X.C., Li, L., Fu, R.Y., De Cooman, B.C., Wollants, P., Zhu, X.D. and Wang, L., "Influence of the Strain Rate on the Strain-Induced Transformation of Retained Austenite to Martensite in High Strength Low Alloy TRIP Steels," Int. Conf. on TRIP-Aided High Strength Ferrous Alloys," Conf. Proc., Ghent, Belgium, 2002, pp. 373-377.
99. Wei, X.C., Li, L., Fu, R.Y., De Cooman, B.C., Wollants, P., Zhu, X.D. and Wang, L., "Time Dependence of Transformation Process of Si-Mn TRIP Steel During High-Speed Tensile Impact Testing," Int. Conf. on TRIP-Aided High Strength Ferrous Alloys," Conf. Proc., Ghent, Belgium, 2002, pp. 253-258.
100. Fu, R.Y., Wei, X.C., Shi, W., Li, L., De Cooman, B.C., Wollants, P., Zhu, X.D. and Wang, L., "Dynamic Tensile Characteristic of High Strength Low Alloy TRIP Steel and its Modeling," Int. Conf. on TRIP-Aided High Strength Ferrous Alloys, Conf. Proc., Ghent, Belgium, 2002, pp. 287-291.
101. Xu, K., Wong, C., Yan, B. and Zhu, H., "A High Strain Rate Constitutive Model for High Strength Steels," SAE Technical Paper #2003-01-0260, 2003.
102. Campbell, J.D., Dynamic Plasticity of Metals, (lecture notes for course held at University of Oxford), 1970.
103. Saka, H. and Imura, T., "Direct Measurement of Mobility of Edge and Screw Dislocations in 3 Percent Si-Fe by High-Voltage Transmission Electron Microscopy," J. Phys. Soc. Japan, Vol. 32, 1972, pp. 702-716.
104. Hahn, G.T., "A Model for Yielding with Special Reference to the Yield-Point Phenomena of Iron and Related BCC Metals," Acta Met., Vol. 10, 1962, pp. 727-738.
105. Johnson, G.R. and Cook, W.H., "A Constitutive Model and Data for Metals Subjected to Large Strains, High Strain Rates and High Temperatures," Proc. 7th Intl. Sym. Ballistics, The Hague, The Netherlands, Apr 1983, pp. 541-547.
106. Johnson, G.R. and Holmquist, T.J., "Evaluation of Cylinder-Impact Test Data for Constitutive Model Constants," J. Appl. Phys., Vol. 64, 1988, pp. 3901-3910.
107. Zerilli, F.J. and Armstrong, R.W., "Dislocation-Mechanics-Based Constitutive Relations for Material Dynamics Calculations," J. Appl. Phys., Vol. 61, 1987, pp. 1816-1825.

108. Goldthorpe, B.D., Butler, A.L. and Church, P., "A Wide Range Constitutive Equation for Medium and High Strength Steel," *Journal de Physique IV*, Vol. 4, no. C8, 1994, pp. 471-476.
109. Kocks, U.F., Argon, A.S. and Ashby, M.F., "Thermodynamics and Kinetics of Slip," *Progr. Mater. Sci.*, Vol. 19, 1975.
110. Follansbee, P.S. and Kocks, U.F., "A Constitutive Description of the Deformation of Copper Based on the Use of the Mechanical Threshold Stress as an Internal State Variable," *Acta. Met.*, Vol. 36, 1988, pp. 81-93.
111. Goto, D.M., Bingert, J.F., Chen, S.R., Gray, G.T. III and Garrett, R.K. Jr., "The Mechanical Threshold Stress Constitutive-Strength Model Description of HY-100 Steel," *Met. and Mat. Trans. A*, Vol. 31A, 2000, pp. 1985-1996.
112. "Surface Preparation for Strain Gage Bonding," Vishay Micro-Measurements Application Note B-129-8, Document #11129, Revision February 2003.
113. "High-Elongation Strain Measurements," Vishay Measurements Group Tech Tip TT-605, January 1995.
114. "Errors Due to Wheatstone Bridge Nonlinearity," Vishay Measurements Group Tech Note TN-507-1, May 1997.
115. Harding, J., "High-Rate Straining and Mechanical Properties of Materials," Explosive Welding, Forming and Compaction, ed. by Blazynski, T.Z., Applied Science Publishers, New York, New York, 1983, pp. 123-158.
116. Clark, D.S. and Wood, D.S., "The Time Delay for the Initiation of Plastic Deformation at Rapidly Applied Constant Stress," *Proc. Amer. Soc. Test. Mater.*, Vol. 49, 1949, pp. 717-737.
117. Krafft, J.M. and Sullivan, A.M., "Effect of Grain Size and Carbon Content of the Yield Delay-Time of Mild Steel," *Trans. Amer. Soc. Metals*, Vol. 51, 1959, pp. 643-665.
118. Albertini, C., Eleiche, A.M. and Montagnani, M., "Strain-Rate History Effects on the Mechanical Properties of AISI 316 Stainless Steel," *Metallurgical Applications of Shock-Wave and High-Strain-Rate Phenomena*, Murr, L.E., Staudhammer, K.P. and Meyers, M.A. (Eds.), Marcel Dekker, Inc., New York, 1986, pp. 583-603.

119. Eleiche, A.M. and Campbell, J.D., "The Influence of Strain-Rate History and Temperature on the Shear Strength of Copper, Titanium and Mild Steel," Technical Report AFML-TR-76-90, Air Force Materials Laboratory, Wright-Patterson AFB, OH, 1976.
120. Clark, D.S. and Wood, D.S., "The Influence of Specimen Dimension and Shape on the Results in Tension Impact Testing," Proc. Amer. Soc. Test. Mater., Vol. 50, 1950, pp. 577-585.
121. Follansbee, P.S., "High-Strain-Rate Deformation of FCC Metals and Alloys," Metallurgical Applications of Shock-Wave and High-Strain-Rate Phenomena, Murr, L.E., Staudhammer, K.P. and Meyers, M.A. (Eds.), Marcel-Dekker, Inc., New York, 1986, pp. 451-479.
122. Sato, K., Yoshitake, A., Zeng, D. and Liu, S.D., "Crashworthiness of Automotive Stamped Parts Using High Strength Steel Sheets," SAE Technical Report #2002-01-0641, 2002.
123. Nakanishi, E., Tateno, H., Hishida, Y. and Shibata, K., "New Materials Technology for Achieving Both Crashworthiness and Weight Reduction Using Energy-Absorbing Steel with Higher Strain-Rate Sensitivity," SAE Technical Report #980953, 1998.
124. Cornette, D. and Galtier, A., "Influence of the Forming Process on Crash and Fatigue Performance of High Strength Steels for Automotive Components," SAE Technical Report #2002-01-0642, 2002.
125. Fekete, J.R., Stibich, A.M. and Shi, M.F., "A Comparison of the Response of HSLA and Dual Phase Sheet Steel in Dynamic Crush," SAE Technical Report #2001-01-3201, 2001.
126. Bleck, W. and Larour, P., "Effect of Strain Rate and Temperature on the Mechanical Properties of LC and IF Steels," International Forum for the Properties and Applications of IF Steels, Takechi, H. (Ed.), Proceedings of IF Steels 2003, Iron and Steel Institute of Japan, Tokyo, Japan, 2003, pp. 138-147.
127. Ushioda, K., Yoshinaga, N., Koyama, K. and Akisue, O., "Application of Ultra-Low Carbon Steels to the Development of Super-Formable Sheet Steels, Solution-Hardened High Strength Sheet Steels and Bake-Hardenable Sheet Steels," Proc. Intl. Conf. Physical Met. of IF Steels, ISIJ, Tokyo, 1994, pp. 227-244.

128. Honeycombe, R.W.K. and Bhadeshia, H.K.D.H., Steels: Microstructure and Properties, 2nd Ed., Edward Arnold, London, 1995, p. 53.
129. Kouwenhoven, H.J., "The Influence of Ferrite Grain Size and Volume Fraction of Pearlite on the Lower Yield Stress and Luders Strain of Carbon Steel," Trans. ASM, Vol.62, 1969, pp. 437-446.
130. Bouet, M., Root, J., Es-Sadiqui, E. and Yue, S., "The Effect of Mo in Si-Mn Nb Bearing TRIP Steels," 40th MWSP Conf. Proc., ISS, 1998, pp. 675-684.
131. Den Hartog, J.P., Mechanical Vibrations, 4th Ed, Dover Publications, Inc., Mineola, New York, 1985.
132. ASTM E8-00b, Annual Book of ASTM Standards, Section 3, Vol. 03.01, Baltimore, MD, 2001, pp. 56-76.

APPENDIX A

NATURAL FREQUENCY CALCULATION FOR TENSILE SAMPLE

The tensile sample data shown in Figure 4.8 are for a TRIP steel with dimensions shown below, where L_3 is the total sample length not including the portion of the sample contained within the grips.

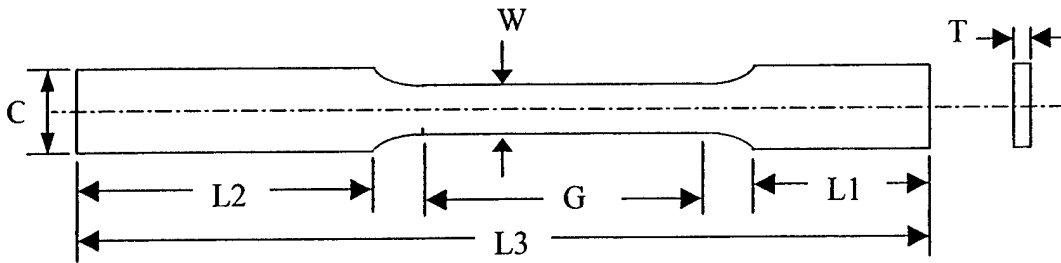
Natural frequency calculations for a single degree of freedom system were discussed in section 2.2.1. For the tensile sample, the calculations are more complex because the sample is fixed on both ends and will vibrate with motion out of the plane of the sample [131 (p.135-140, 431)]. For longitudinal vibration of a uniform beam fixed at both ends, the natural frequency is:

$$f_n = \frac{1}{2} \sqrt{\frac{EA}{L^2 \mu}}, \text{ where } \mu = \text{mass per unit length.}$$

For a uniform steel beam, this equation can be simplified to:

$$f_n = \frac{2,591}{L}, \text{ where } L \text{ is in units of meters}$$

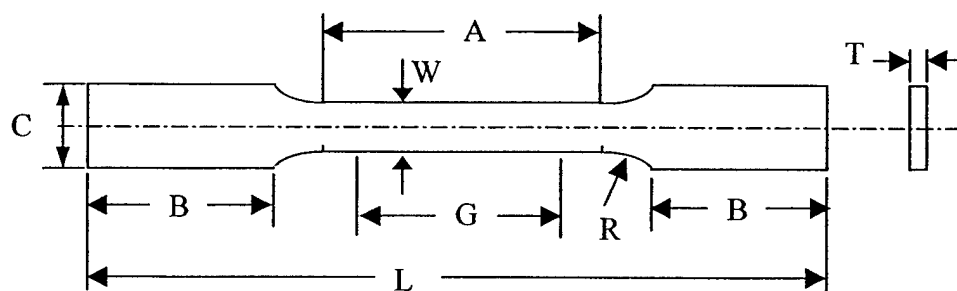
Therefore, by assuming the tensile sample is a uniform beam, the natural frequency of a tensile sample with length (between the grips) of 112 mm, would be about 23 kHz.



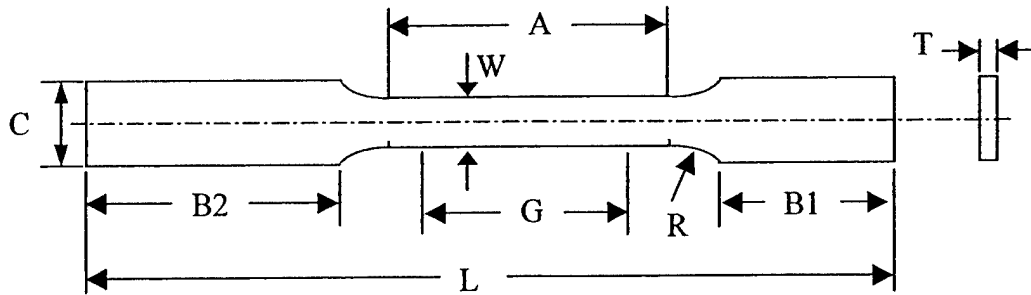
$L1 = 28 \text{ mm}$	$L2 = 50 \text{ mm}$	$L3 = 112 \text{ mm}$	$G = 20 \text{ mm}$
$W = 6.35 \text{ mm}$	$C = 15.9 \text{ mm}$	$T = 1.4275 \text{ mm}$	

APPENDIX B TENSILE SAMPLE DIMENSIONS

B1. ASTM E-8 [132] Tensile Sample Dimensions



	Standard Dimensions (inches)	Subsize Dimensions (inches)
G - Gage Length	2.000 ± 0.005	1.000 ± 0.003
W - Width	0.500 ± 0.010	0.250 ± 0.005
T - Thickness	thickness of material	thickness of material
R - Radius of Fillet, min.	$\frac{1}{2}$	$\frac{1}{4}$
L - Overall Length, min.	8	4
A - Length of Reduced Section, min.	$2 \frac{1}{4}$	$1 \frac{1}{4}$
B - Length of Grip Section, min.	2	$1 \frac{1}{4}$
C - Width of Grip Section	$\frac{3}{4}$	$\frac{3}{8}$

B2. Other Tensile Sample Dimensions

	Dimensions (inches)		
	2" Gage Length	1" Gage Length	½" Gage Length
G - Gage Length	2.000 ± 0.005	1.000 ± 0.003	0.500 ± 0.003
W - Width	0.500 ± 0.010	0.250 ± 0.005	0.250 ± 0.005
T - Thickness	thickness of material		
R - Radius of Fillet	$\frac{1}{2}$	$\frac{1}{4}$	$\frac{1}{4}$
L - Overall Length	8 to 8 ½	6 to 8	6 to 8
A - Length of Reduced Section	$2 \frac{1}{4}$	$1 \frac{1}{4}$	$\frac{5}{8}$
B1 - Length of Short Grip Section	$2 \frac{1}{2}$	$2 \frac{1}{2}$	$2 \frac{1}{2}$
C - Width of Grip Section	$\frac{3}{4}$ to 1	$\frac{3}{8}$ to 1	$\frac{3}{8}$ to 1

APPENDIX C

DETERMINATION OF CONSTANTS FOR THE
MODIFIED ZERILLI-ARMSTRONG EQUATION

The modified Zerilli-Armstrong (MZA) equation was given as Equation 6.2 in Section 6.8, with temperature rise due to adiabatic heating calculated using Equation 6.3.

$$\sigma = \sigma_L + \sigma_{ss} + C_{ss} C_1 \exp[-C_3 T + C_4 T \ln(\dot{\epsilon})] + C_5 (\epsilon + \epsilon_{cw})^n + kd^{-1/2} \quad [6.2]$$

$$\Delta T = \frac{\beta}{\rho C_p} \int_0^{\epsilon} \sigma d\epsilon \quad [6.3]$$

The goal of the MZA equation was to model several different IF steels by writing a single equation with the only variable changes between specific steels being allowed for changes in precipitation or second phase strengthening (σ_L), solid solution strengthening (σ_{ss} and C_{ss}), cold work (ϵ_{cw}), and grain size (d). The starting point for the model was to use the constants given by Zerilli and Armstrong [107] for iron, since the microstructure of IF steel is not much different from pure iron. Those constants were given in Section 3.13.4.2 in Table 3.4, which is shown again here.

Table 3.4: Constants for the Zerilli-Armstrong equation (Equation 3.57) for iron [107].

Material	σ_L (MPa)	C_1 (MPa)	C_3 (K ⁻¹)	C_4 (K ⁻¹)	C_5 (MPa)	n	k (N/mm ^{3/2})
Iron	0	1033	0.00698	0.000415	266	0.289	22

Using Equation 6.2 and 6.3 requires determination of all of the model constants shown in Table 3.4 in addition to the additional terms in Equations 6.2 and 6.3. A table made for all the required constants is shown in Table C1.

Table C1: Constants required for the modified Zerilli-Armstrong (MZA) equation (Equation 6.2) for IF steels.

Material	C_1 (MPa)	C_3 (K^{-1})	C_4 (K^{-1})	C_5 (MPa)	n	k (MPa \sqrt{mm})
IF Steel						
		β	ρ (kg/m ³)	C_p (J/kg·K)		

Material		σ_L (MPa)	σ_{ss} (MPa)	C_{ss}	ϵ_{CW} (mm/mm)	d (mm)
IF-1	10 μm					
	25 μm					
	135 μm					
IF-2	0%					
	2%					
	5%					
	10%					
	18%					
IF-3						
IF-4						

Since all tests for this thesis were conducted at room temperature, it was decided to leave the temperature-dependent constants, C_3 and C_4 , the same. Some of the constants for Table C1, including k , d , ϵ_{CW} , and σ_{ss} , were determined based on material properties and processing history. The value of k was chosen as 14, which was the mean value of k calculated in Sections 6.3 and 6.4 for IF-1 and IF-5 steels. Grain size, d , was

determined by the material microstructure. If the cold work done to the material was known (as it was for the IF-2 steels in this study), it became the ϵ_{CW} term. The quasi-static solid solution strengthening increment term (σ_{SS}) was calculated as explained in Section 6.8. Values for the IF steels to be modeled were shown in Table 6.11, which is shown again here.

Table 6.11: Quasi-static solid solution strengthening increment for several IF steels.

	IF-1	IF-2	IF-3	IF-4
Quasi-Static Solid Solution Strengthening Increment (MPa)	4	10	15	60

For the constants in Equation 6.3, the density of steel is 7870 kg/m^3 and the room temperature value of heat capacity for steel is $445 \text{ J/kg}\cdot\text{K}$. β was chosen as 0.9 because it is a commonly accepted value [1 (p. 377), 30 (p. 303)] for the amount of plastic strain energy converted to heat. Thus far, several of the constants for the MZA model have been decided as shown in Table C2.

Table C2: Constants for the modified Zerilli-Armstrong (MZA) equation (Equation 6.2) for IF steels determined prior to fitting the model to experimental data.

Material	C_1 (MPa)	C_3 (K^{-1})	C_4 (K^{-1})	C_5 (MPa)	n	k (MPa $\sqrt{\text{mm}}$)
IF Steel		0.00698	0.000415			14
		β	ρ (kg/m^3)	C_p ($\text{J/kg}\cdot\text{K}$)		
		0.9	7870	445		

Material		σ_L (MPa)	σ_{SS} (MPa)	C_{SS}	ϵ_{CW} (mm/mm)	d (mm)
IF-1	10 μm		4		0	0.010
	25 μm					0.025
	135 μm					0.135
IF-2	0%		10		0	0.030
	2%				0.022	
	5%				0.051	
	10%				0.100	
	18%				0.178	
IF-3			15		0	0.040
IF-4			60		0	0.033

The remaining variables to be determined are C_1 , C_5 , n , σ_L and C_{SS} . Of these terms, C_1 , C_5 and n must remain constant for all IF steels, and σ_L and C_{SS} will vary by specific material. To find the remaining terms required adjusting them as necessary to fit one set of empirical data. IF-2 steel with 0% pre-strain was chosen as the material to be used for fitting the model constants. The reasons why it was chosen was that it was a commercially produced product with no additional processing and was therefore expected to have constant properties. Also, IF-2 was continuous-yielding and would be easier to fit to the MZA model, since the MZA model is continuous-yielding. Using ExcelTM, true stress-strain curves were plotted for strain rates ranging from $.001 \text{ s}^{-1}$ to 130 s^{-1} . Equations were written in ExcelTM for the MZA model initially using the constants from

Table 3.4 for C_1 , C_5 , n , and σ_L , and using a value of 1.00 for C_{SS} . The model results were plotted on the same chart as the experimental data. The model curves did not fit the magnitudes or strain hardening behaviors of the experimental data, so the C_1 , C_5 , n , and σ_L terms were adjusted as necessary to provide a good fit to all four curves. The numbers determined were $C_1 = 825$ MPa, $C_5 = 415$ MPa, $n = 0.475$ and $\sigma_L = 10$ MPa. The results of this fit are shown in Figure C1.

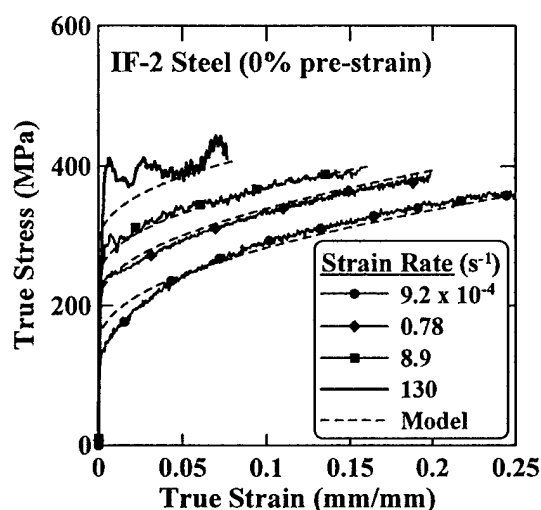


Figure C1: True stress-strain curves for IF-2 steel with 0% pre-strain at four different strain rates compared with Modified Zerilli-Armstrong model at same strain rates.

No further changes to model constants were made for the other pre-strain levels of IF-2 steel (except the already mentioned changes to ϵ_{CW}) and the model continued to fit the data well (as shown in Section 6.8). Next, the model was applied to IF-1 steel for three different grain sizes, with the only change being a small adjustment to change σ_L to a value of 1 MPa, which accounts for quasi-static strength differences such as an unknown amount of prior cold work and precipitation strengthening. Changing the value

of σ_L simply shifts all of the model curves up or down by equal amounts. Finally, the model was applied to IF-3 and IF-4 steels. In addition to changes in σ_L , it was expected that the C_{SS} term for IF-4 steel would be less than 1 due to solid solution softening. Since the solid solution strengthening study in Section 6.2.1 included only two different materials, it was not possible to predict the C_{SS} term and therefore it had to be determined by trial and error. For IF-3 steel, σ_L was found to be 15 MPa, while it was determined to be 25 MPa for IF-4 steel. For IF-4 steel, C_{SS} was determined (by trial and error) to be 0.85.

The final results of fitting constants to the MZA model for IF steels are shown in Table C3.

Table C3: Final constants for the modified Zerilli-Armstrong (MZA) equation (Equation 6.2) for IF steels.

Material	C_1 (MPa)	C_3 (K^{-1})	C_4 (K^{-1})	C_5 (MPa)	n	k (MPa $\sqrt{\text{mm}}$)
IF Steel	825	0.00698	0.000415	415	0.475	14
		β	ρ (kg/m ³)	C_p (J/kg·K)		
		0.9	7870	445		

Material		σ_L (MPa)	σ_{SS} (MPa)	C_{SS}	ϵ_{CW} (mm/mm)	d (mm)
IF-1	10 μm	1	4	1.00	0	0.010
	25 μm					0.025
	135 μm					0.135
IF-2	0%	10	10	1.00	0	0.030
	2%				0.022	
	5%				0.051	
	10%				0.100	
	18%				0.178	
IF-3		15	15	1.00	0	0.040
IF-4		25	60	0.85	0	0.033